Scale Model Testing of Tidal Stream Turbines: Wake Characterisation in Realistic Flow Conditions

Thesis submitted in accordance with the requirements of
the University of Liverpool for the degree of Doctor in Philosophy
by

Siân C. Tedds

February 2014

Acknowledgements

Above all I would like to thank my supervisor, Dr Rob Poole for his invaluable guidance and support throughout this thesis. Thanks to Prof. Ieuan Owen for his expert advice and encouragement. Thank you both for being so patient with all my grammatical errors and spelling mistakes.

I would like to acknowledge the School of Engineering for the DTA award.

Many thanks to the technical support from Steven Bode, Marc Bratley, Emlyn Jones, Martin Jones and Derek Neary. For the design and production of the scale-model turbine I would like to acknowledge Prof. Tim O'Doherty, Dr. Allan Mason-Jones, Dr. Daphne O'Doherty, Ceri Morris, Dr Carl Byrne, Paul Prickett and Dr Roger Grosvenor from Cardiff University.

Thanks to Tiago de Jesus Henriques for the many hours spent in the lab helping me take measurements. Thanks to Dr Richard Whalley for his advice and reading through my thesis. To all other members of my office over the years for all the help and friendship; especially thanks to Dr Adam Yulie, Dr Chris Kaaria, Dan Eddon, Paul Scott, Dr Sean Malkeson, and Whaleed Abed.

To my parents and brother, Liam, thanks for always being so supportive and interested in everything I do.

To my wonderful friends, Anna, Bex, Tom, Kate, Jen and Sarah, thank you for your unlimited friendships, humour and encouragement. To Hannah, your smile and wit will forever be missed, thank you for being my friend.

A special thanks to Jack for all his love, patience and optimism.

Abstract

In this thesis the effect of uniform and profiled (non-uniform) steady flows on a scale-model tidal stream turbine ($0.5m$ diameter) are experimentally investigated using the University of Liverpool high-speed recirculating water-channel. The power and thrust coefficients of the turbine with numbers of blades between two and six and various blade-pitch-angles are measured in uniform flow with low levels of turbulence at velocities ranging from $0.45m/s$ to $1.34m/s$. With a three-bladed turbine at optimum blade-pitch-angle the power and thrust coefficients are compared in three different flow conditions of uniform flow with low turbulence intensity (2%), uniform flow with high turbulence intensity (5%) and non-uniform flow with high turbulence intensity (5%).

Using an Acoustic Doppler Velocimeter (ADV) measurements of three-dimensional velocities are taken, initially, around the three-bladed turbine with optimum blade-pitch-angle. The velocities at five different heights and up to $7D$ downstream are probed where the upstream velocity is uniform with low turbulence levels and mean upstream velocity of $0.9m/s$. Further ADV measurements are taken downstream of the three-bladed turbine through a horizontal centre-plane at lower velocities of $0.45m/s$ and $0.68m/s$ to probe the effect of Reynolds number on the turbine's wake. In addition wake measurements are taken downstream of the two-bladed turbine with optimum and non-optimum blade-pitch-angles to study the effect of differing tip-speed-ratios, thrust and power coefficients. The wake of the turbine

support structure without blades is investigated.

In a flow with high turbulence and mean velocity of $0.9m/s$ the wake of the three-bladed turbine is studied through a centre-plane equal to the turbine hub height. Further in a profiled flow, representative of a $1/5th$ velocity power law and upstream integral average velocity of $0.82m/s$ (over the turbine's swept area), characterisation of the flow downstream of the three-bladed turbine with optimum blade-pitch-angle is taken at five depths up to $5D$ downstream. These velocities are then compared in detail to those in uniform flow.

Finally the ADV technique is used extensively throughout this thesis and, indeed, in most studies concerned with tidal turbine wakes. As issues regarding certain aspects of the ADV came to light during this study, the robustness of this technique is investigated by using two different ADV probe orientations and a comparison to $1D$ Laser Doppler Velocimetry is made.

Contents

Nomenclature

A	=	swept out area of turbine (m^2)
$\mathbf{b}$	=	Reynolds-stress anisotropy tensor (-)
C_P	=	power coefficient ($\frac{P}{1/2\rho A U^3}$)
C_{P_F}	=	free-stream power coefficient (-)
C_{P_T}	=	channel power coefficient (-)
C_T	=	thrust coefficient ($\frac{T}{1/2\rho A U^2}$)
C_{T_F}	=	free-stream thrust coefficient (-)
C_{T_T}	=	channel thrust coefficient (-)
d	=	wire diameter (m)
D	=	rotor diameter (m)
f	=	sampling frequency (Hz)
f_c	=	characteristic frequency (Hz)
Fr_D	=	Froude number based on rotor diameter ($\frac{U}{\sqrt{gD}}$)
Fr_h	=	Froude number based on turbine depth in water column ($\frac{U}{\sqrt{g(H-h)}}$)

g	=	gravitational constant ($9.81 m/s^2$)
h	=	height (m)
H	=	water height (m)
L	=	characteristic length (m)
M	=	mesh spacing (m)
N	=	number of samples
P	=	power (W)
R	=	radius of turbine (m)
Re_F	=	Reynolds number based on upstream flow velocity and turbine radius ($\frac{UR}{\nu}$)
Re_M	=	Reynolds number based on mesh spacing ($\frac{UM}{\nu}$)
Re_ω	=	Reynolds number based on velocity at the blade tip ($\frac{\omega R^2}{\nu}$)
s	=	time step (s)
St	=	Strouhal number ($\frac{f_c L}{U}$)
t_i	=	transit time (s)
T	=	thrust (N)
TI	=	Turbulence Intensity (%)
TKE	=	Turbulence Kinetic Energy (m^2/s^2)
TKE_{MAX}	=	maximum Turbulence Kinetic Energy (m^2/s^2)
u	=	streamwise velocity (m/s)

u_i	=	individual streamwise velocity sample (m/s)
u_{MIN}	=	minimum streamwise velocity (m/s)
u'	=	streamwise normal stress (m/s)
u'_{MAX}	=	maximum streamwise normal stress (m/s)
$\overline{uv}$	=	shear stress in $x-y$ plane (m^2/s^2)
$\overline{uv}_{MAX}$	=	maximum shear stress in $x-y$ plane (m^2/s^2)
$\overline{uw}$	=	shear stress in $x-z$ plane
$\overline{uw}_{MAX}$	=	maximum shear stress in $x-z$ plane (m^2/s^2)
U	=	mean upstream velocity (m/s)
U_F	=	free-stream mean upstream velocity (m/s)
U_T	=	channel mean upstream velocity (m/s)
$\overline{U}$	=	integral average upstream velocity (m/s)
v	=	vertical velocity (m/s)
v_i	=	individual vertical velocity sample (m/s)
$\|v\|_{MAX}$	=	absolute maximum vertical velocity (m/s)
v'_{MAX}	=	maximum vertical normal stress (m/s)
$\overline{vw}$	=	shear stress in $y-z$ plane (m^2/s^2)
$\overline{uw}_{MAX}$	=	maximum shear stress in $y-z$ plane (m^2/s^2)
w	=	spanwise velocity (m/s)
w_i	=	individual spanwise velocity sample (m/s)
$\|w\|_{MAX}$	=	absolute maximum spanwise velocity (m/s)
w'	=	spanwise normal stress (m/s)
w'_{MAX}	=	maximum spanwise normal stress (m/s)
W	=	width of channel (m)

x	=	streamwise distance (m)
y	=	vertical distance (m)
z	=	spanwise distance (m)
λ	=	tip-speed-ratio $(\frac{\omega R}{U})$
λ_F	=	free-stream tip-speed-ratio (-)
λ_T	=	channel tip-speed-ratio (-)
η	=	invariant of Reynolds-stress anisotropy tensor (-)
μ	=	dynamic viscosity of water (m^2/s)
ν	=	kinematic viscosity of water (m^2/s)
ξ	=	invariant of Reynolds-stress anisotropy tensor (-)
ρ	=	density of water(kg/m^3)
$\rho(s)$	=	autocorrelation function (-)
$\overline{\tau_{ii}}$	=	integral timescale (s)
ω	=	angular velocity (rad/s)

Acronyms

ADCP	Acoustic Doppler Current Profiler
ADP	Acoustic Doppler Profiler
ADV	Acoustic Doppler Velocimeter
BEM	Blade Element Momentum
CFD	Computational Fluid Dynamics
FFT	Fast Fourier Transform
FHFA	Flying Hot-Film Anemometry
FHWA	Flying Hot-Wire Anemometry
FKE	Flow Kinetic Energy
HATT	Horizontal Axis Tidal Turbine
LDV	Laser Doppler Velocimetry
MRF	Moving Reference Frame
RANS	Reynolds-Averaged Naiver-Stokes
RSM	Reynolds Stress Model
SNR	Signal-to-Noise Ratio
SHWA	Stationary Hot-Wire Anemometry
SST	Shear Stress Transport
VATT	Vertical Axis Tidal Turbine

Chapter 1

Introduction

Throughout the world there is a growing demand for energy produced from sustainable resources, with many governments setting targets for renewable production of electricity. The UK aims to provide 15% of total energy from renewable sources by 2020, this is a significant increase from 3.3% produced in 2010 and 4.1% in 2012 (Department of Energy and Climate Change, 2013). The UK has some of the best marine energy resources in the world, harnessing this energy is one way renewable energy targets can be met (Hardisty, 2009). Marine energy can be split into two main categories: wave and tidal. One of the main advantages of tidal power is the predictability of the tides. There are two principal ways to harness tidal energy: tidal barrages or lagoons which use the tidal range, and tidal stream turbines that use the tidal current. An advantage of tidal stream turbines over tidal barrages or lagoons is that they minimise the impact on the marine environment as they allow water to pass straight through, and are often fully submerged with no visual impact. The UK has some of the largest tides in the world and is at the forefront of tidal energy device development. Successful prototype devices have been connected to the national grid since 2008 (Marine Current Turbines, 2013). In February 2013 two projects, deploying arrays of tidal turbine devices in Anglesey and the Pentland Firth, were announced by the Depart-

ment of Energy and Climate Change (Department of Energy and Climate Change, 2013). This significant investment in tidal energy projects highlight the timely nature of tidal energy research.

There are a number of different types of tidal turbine devices in development, the main types are detailed in section 1.1. The UK is the forefront of tidal device development due to the large number of potential tidal sites, which are discussed in section 1.2.

Studies of small scale devices have been a key part of research into tidal stream turbine device development. Initial research were concerned with power and thrust characteristics and these studies are discussed in section 1.3. Further, more detailed, investigations have been made into the wake downstream of devices in order to find optimum spacing for arrays of turbines and these studies are discussed in section 1.4. Finally the chapter ends with the aims and objectives of the thesis in section 1.6.

1.1 Types of Tidal Stream Turbine Devices

There are a number of tidal stream devices currently being developed many of which have been adapted from the wind industry. The main types include:

1. **Horizontal Axis Tidal Turbines**
   Horizontal Axis Tidal Turbines (HATTs) are the most common devices and predominately they are three-bladed, axial rotor devices (King & Tryfonas, 2009). In 2008 Marine Current Turbines' (MCT's) SeaGen became the first grid connected turbine. SeaGen, situated in Strangford Lough Northern Ireland, has so far generated over $9GWhr$ (Marine Current Turbines, 2013). An artist's impression of SeaGen is shown in figure 1.1, the device is a HATT with dual two-bladed rotors each $16m$ in diameter.

2. **Ducted Horizontal Devices**
   Ducted Horizontal devices have a rotor within in a duct, which ac-

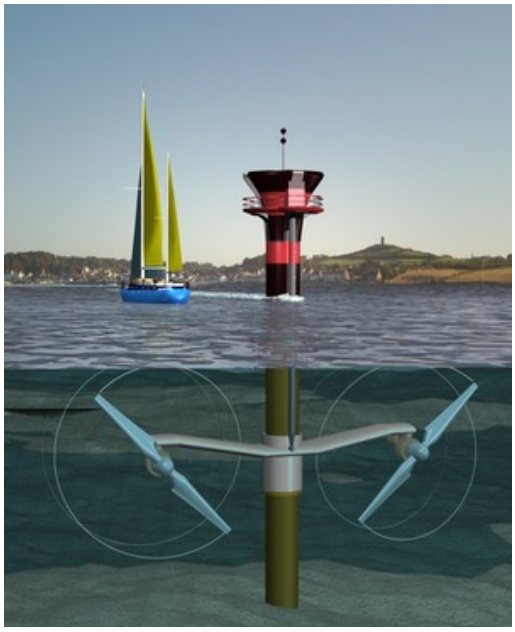

Figure 1.1: Multiple Open Rotor Horizontal Axis Device [Source: Marine Current Turbines' SeaGen (Marine Current Turbines, 2013)]

celerates the flow through the device: see figure 1.2 which has been developed by Lunar Energy. This approach is a more feasible proposal for tidal stream than for wind due to the bi-directionality of the tidal flow compared to wind which can flow in any direction. The main benefits of these types of device is the increase of energy capture per unit of rotor area using the effect of blockage caused by the duct. However, they are more expensive due to the amount of materials required per device. These devices must also incorporate bi-directional rotors (Hardisty, 2009).

3. **Vertical Axis Tidal Turbines**
   An example Vertical Axis Tidal Turbine (VATT) is shown in figure 1.3, designed by Neptune Renewable Energy, which is also a ducted device. VATTs were first developed for the wind industry, but research into this configuration decreased due to the fact they are theoretically less

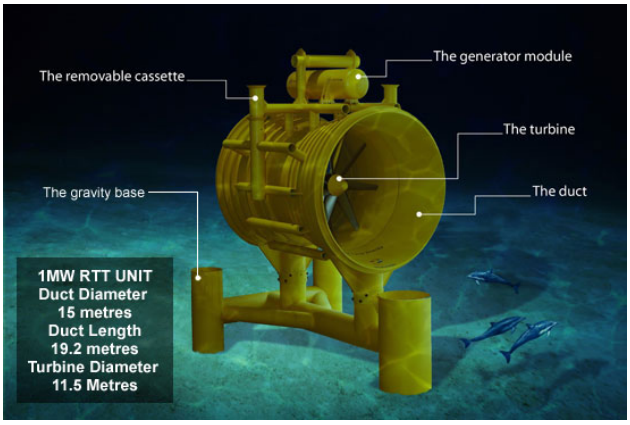

Figure 1.2: Ducted Horizontal Device. [Source: Lunar Energy (2013)]

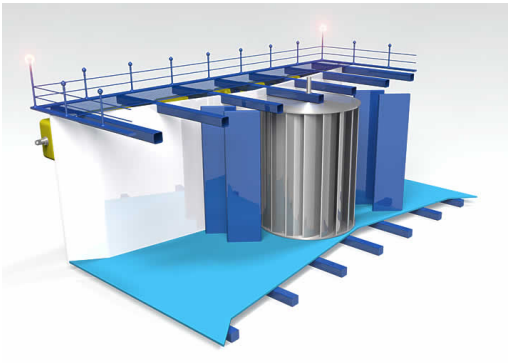

Figure 1.3: Vertical Axis Device. [Source: Neptune Renewable Energy (2013)]

efficient than the horizontal devices (King & Tryfonas, 2009). However, research on VATTs has been revived for the tidal industry because of the number of operational advantages, mainly associated with the fact that all gearing and electrical machinery can be raised above the water surface (Hardisty, 2009).

4. **Oscillating Hydrofoil Devices**
   Oscillating Hydrofoil devices have a hydrofoil attached to an oscillating arm where the motion of the tidal current flows either side of the

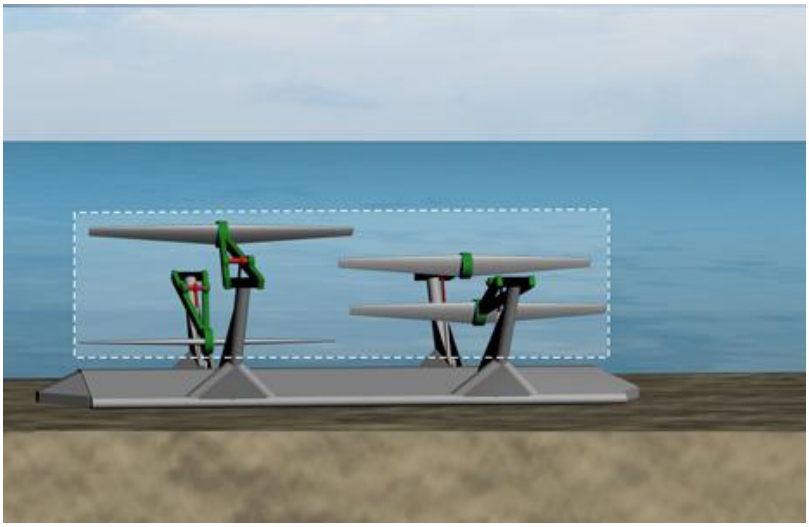

Figure 1.4: Oscillating Hydrofoil Device [Source: Pulse Tidal (2013)]

hydrofoil, which results in lift. This motion can then drive fluid in a hydraulic system which is then converted into electricity (The European Marine Energy Centre Ltd., 2014). Pulse Tidal's design of an oscillating Hydrofoil is shown in figure 1.4.

These are the main four types of tidal devices which are currently under development. Other designs are in development such as a Transverse HATT, where initial testing small-scale testing and design is detailed by McAdam et al. (2009). Table A.1. in Appendix A lists all the known developers of tidal energy devices as of early 2014, and also provides details of the device type and country of development. From the table it is observed that almost half of the devices in development are HATTs, which is most likely due to the adaptation of devices from the wind industry. In addition over a third of developers are based in the UK, highlights that the UK is leading the way in tidal turbine development.

1.2 Sites for Tidal Stream Turbine Devices

The main advantage of tidal devices is the predictability of the tides. Ideal conditions for tidal stream turbines are for a current of $2 - 3m/s$ (Fujita Research, 2011) and a depth of $20 - 30m$ (Soares, 2011). It is predicted that of the UK's $382.5TWh$ energy demand, $15.6TWh$ (or 4%) can be produced using tidal stream turbines alone (Black and Veatch Ltd, 2005). Figure 1.5 shows the predicted average annual power from tides around the UK, where the key areas highlighted for potential sites alongside the Severn estuary and Mersey are in the Orkneys, around Anglesey and Isle of Wight amongst others. In a report published by the Carbon Trust (2005) the UK is spilt into five regions and the potential yield estimated from each site: The Channel Islands ($3.017TWh$ per year), Northern Ireland ($1.045TWh$ per year), North West ($2.033TWh$ per year), Pentland ($8.12\ TWh$ per year) and South West ($1.229TWh$ per year). In the Orkney Islands the European Marine Energy Centre (EMEC) was established in 2003 with 8 developers having deployed or in the process of deploying prototype devices. As stated at the beginning of the chapter in February 2013 two projects were announced by Department of Energy and Climate Change (2013) of farms of devices in Anglesey and the Pentland Firth. In April 2013 Marine Current Turbines (now owned by Siemens) opened the UK's first tidal turbine power test and assembly plant and is planning a $10MW$ tidal array in Wales and an $8MW$ array in Scotland (Department of Energy and Climate Change, 2013). All these developments are aiding growth in the tidal energy sector in the UK, which emphasises the need for understanding of tidal devices in complex flow conditions.

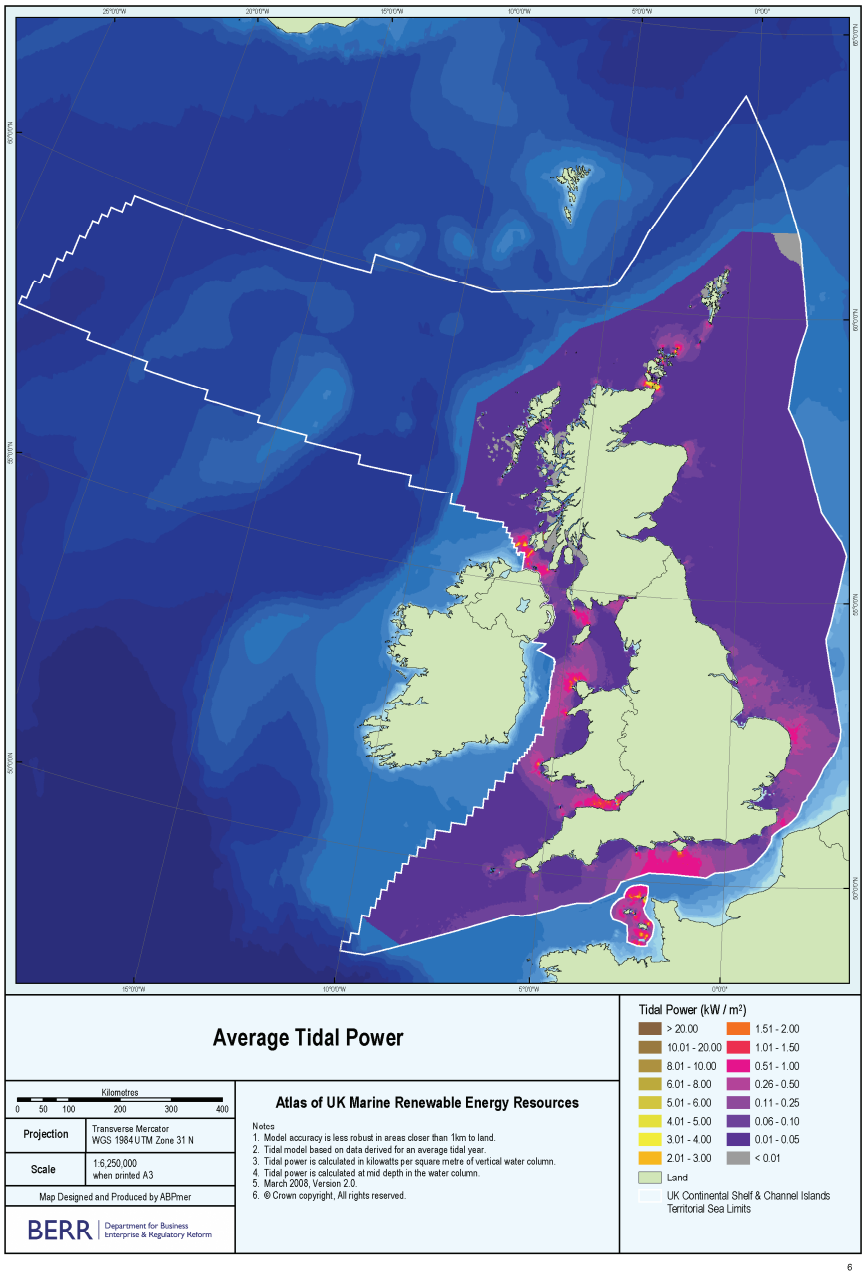

Figure 1.5: UK map of average annual tidal power. Reproduced from `http://www.renewables-atlas.info/` ©Crown Copyright

1.3 Power and Thrust Measurements

There have been a number of tests of model HATTs in water-channels and towing tanks, e.g. Bahaj et al. (2006), Myers & Bahaj (2006), Maganga et al. (2009), and O'Doherty et al. (2009). Initial tests within water channels were at various uniform steady velocities, in most cases three-bladed turbines were tested. In addition a number of studies have investigated the use of Blade Element Momentum (BEM) theory and Computational Fluid Dynamics (CFD) to predict the thrust and power output of a turbine (e.g. Malki et al., 2013 and Mason-Jones et al., 2013). In an attempt to make clear the link between the same research groups' studies, where more than a single paper is discussed, in the following discussion the research institutions where the research originates is provided. One of the first experimental studies was conducted by Myers & Bahaj (2006), from the University of Southampton (UoS), to characterise the power output of a scale model turbine. The power output of a $\frac{1}{30}th$ scale ($0.4m$ diameter) turbine was measured in a channel with a channel length of $4.4m$, width $1.4m$ and depth of $0.84m$. Different blade-pitch-angles were investigated and the angle at which the turbine was aligned to the flow (yaw) was changed over a number of increments from 0^o to 30^o were investigated (n.b. optimum yaw at 0^o is when the turbine is set facing the water flow directly). With an optimum blade-pitch-angle (20^o) it was found that with a 0^o yaw angle the peak power output was $220W$,which was much greater than peak power of $180W$ at yaw angles $10 - 30^o$. This study was mostly interested in stall effects of the turbine and no thrust measurements were taken. The UoS group have since conducted further experiments of a larger scale-model turbine, whereby Bahaj et al. (2006) altered the blade pitch angle and yaw. All tests were carried out using a three-bladed $0.8m$ diameter HATT in a cavitation tunnel (5 x 2.4 x 1.2 m) and a towing tank (60 x 3.7 x 1.8 m). Free-stream velocities ranged from 0.8 to $2m/s$, where the velocity in the cavitation tunnel was measured using a pitot-static tube and the velocity of the carriage was computer-controlled in the towing-tank

tests. These tests gave insights into the operation of a single rotor turbine. For HATTs it is often desirable to discuss non-dimensional performance characteristics. For example power coefficient, defined as:

$$C_P = \frac{P}{\frac{1}{2}\rho A U^3}, \tag{1.1}$$

where P is the power output, ρ is the water density, U is the upstream velocity, and A is the swept area of the turbine. Additionally the thrust coefficient, defined:

$$C_T = \frac{T}{\frac{1}{2}\rho A U^2}, \tag{1.2}$$

where T is the loading on the turbine. These quantities are often plotted against tip-speed ratio, defined:

$$\lambda = \frac{\omega R}{U}, \tag{1.3}$$

where ω is the angular velocity and R is the turbine radius in Bahaj et al. (2006). The optimum blade-pitch-angle was found to be 20^o, where peak C_P was equal to 0.46 and further details of the twist and taper design are tabulated by Bahaj et al. (2006). The main difference between the cavitation tunnel and the towing tank was the effect of thrust, which was greater in the towing tank because of the presence of the free-surface in this case which meant waves were produced. As the yaw angle increases C_T and C_P both decrease. At maximum yaw angle tested (30^o), for an optimum blade-pitch-angle (20^o) setting, C_P decreased by 30% and C_T decreased by 15% compared to the yawed case.

Similarly Wu et al. (2012) designed, using BEM theory and a commercial CFD package Fluent using the isotropic $k-\epsilon$ turbulence model, and built a rotor in which the number of blades could be altered between two and four. Experimental studies were completed in a $5m$ wide channel (the depth was not given) to validate the CFD model predictions of torque and power on

the turbine. In addition to different numbers of blades, various turbine radii of $0.3m, 0.4m$ and $0.6m$ were considered. It was found that with a radius of $0.6m$ the power coefficients are $10 - 15\%$ higher compared to those with the smaller radii. The difference in power coefficients could be due to the increased blockage (Bahaj et al., 2006, Whelan et al., 2009 and Consul et al., 2013) caused by the turbine in the channel causing an acceleration of the flow, but no blockage ratio could be obtained to confirm this assertion as no water depth was provided in Wu et al. (2012). In addition it was found that with 3 or 4 blades the peak power was similar but with 2 blades the maximum power coefficient was lower by 16%.

Furthering the studies of blade-pitch-angles and yaw effects on a turbine by the UoS group, Bahaj et al. (2007) compared their previous experimental results from towing tank and cavitation tunnel experiments (Bahaj et al., 2006), already discussed, with two different numerical studies based on BEM theory (GH-Tidal and SERG-Tidal). At different blade-pitch-angles agreement was observed for the thrust coefficient between both the numerical studies and experiments. Peak power coefficient was found to be the same with the SERG-Tidal model and the experimental results, but GH-Tidal showed an increase in power at blade-pitch-angles equal to and above the design case, but lower for below the optimum condition. At higher tip-speed-ratios both numerical studies over-predicted the power coefficients of the experimental results. More recent studies at the Univesity of Swansea by Chapman et al. (2013) have extended the BEM theory to include a modified Buhl correction which is a high induction, semi-empirical correction. The Buhl correction gave better agreement with experimental power results for the turbine in this thesis (to be discussed in chapter 2) than the BEM theory alone as the correction works in conjunction with tip/hub losses.

In addition to investigating the effects of the different blade-pitch-angles Batten et al. (2008), again the UoS group, used BEM theory to calculate the thrust and power coefficients of the turbine at different yaw angles

($15^o, 20^o, 25^o$ and 27^o). The BEM theory slightly over-predicted the power coefficient but under-predicted the thrust coefficient. As the theoretical results from BEM theory from Bahaj et al. (2007) and Batten et al. (2008) gave reasonable approximations to the experimental results, they scaled up their numerical models to investigate the thrust and power on a $20m$ diameter turbine in a tidal flow profile (non-uniform velocity profile represented by a power-law). They discovered that the non-uniform flow effected the fluctuations on blade loading. Alongside these calculations, Batten et al. (2007) expanded their BEM theory model to investigate more realistic site conditions to calculate the blade loading and possible power extraction over a one-month period. They were able to show that not only optimising the energy yield but additionally assessing the loading on a turbine is an important factor for device costing over its lifetime.

Further simulations using a coupled BEM and CFD model, and a $k - \epsilon$ turbulence model, were conducted by Malki et al. (2013) (from the University of Swansea) to evaluate the power and thrust coefficients of a turbine. This model was compared to the towing-tank tests conducted by Bahaj et al. (2006) and to a BEM model. When plotted alongside the blockage-corrected results of Bahaj et al. (2006), the BEM-CFD model over-predicts both the power and thrust coefficients when the domain had the same volume as that of the towing tank. Therefore the domain volume was tripled, increasing the cross-sectional area, to reduce the blockage effect in the simulations, and this resulted in the BEM-CFD model matching the experimental power and thrust coefficients and gave a better approximation than the BEM model alone. The coupled BEM-CFD model, in addition to providing a good match to experimental power and thrust coefficients, also enabled simulations of the flow field and turbulent structure around the turbine, which is not possible with a BEM model alone.

In addition to the studies discussed above there have been a number of CFD simulations of tidal stream devices, one that relates most to this the-

sis are those by a group at Cardiff University (CU) (Mason-Jones, 2010, O'Doherty et al., 2009 and Mason-Jones et al., 2013) who modelled the same turbine as used in this thesis. These studies concentrated mainly on a three-bladed device, both at full-scale ($10m$ diameter) and model ($0.5m$ diameter) conditions. The power and thrust coefficients were characterised in detail for different blade-pitch-angles. The optimum blade pitch angles were found for 2, 3 and 4 bladed turbines as 3^o, 6^o and 9^o respectively. Details of C_P and C_T were found in these cases for various velocities for all possible tip speed ratios. Simulations were verified with small scale tests using the University of Liverpool (UoL) high-speed water-channel (details of which are provided in section 2.1). Initial simulations detailed by O'Doherty et al. (2009) were conducted to investigate the grid dependency and to calculate the optimum blade-pitch-angle for the three-bladed turbine design. To simulate the turbine rotation in the channel the turbine volume was modelled using a cylindrical 'Moving Reference Frame' (MRF) with the axis of rotation centred at the centre of the hub of the turbine, where the blades meet. Different domain sizes were used, one to match the UoL water-channel exactly and another much larger to avoid effects of blockage. A Reynolds Stress Model (RSM) was found to be the best approximation to experimental results and they suggested this is due to the introduction of turbulence anisotropy by the turbine rotation which is considered in this model. Using CFD the optimum blade-pitch-angle for the three-bladed turbine was found to be 6^o which is confirmed by the experimental results to be shown later in chapter 2. Further investigations of the effect of velocity profile and support structure on the turbine performance were performed by Mason-Jones et al. (2013). A $\frac{1}{7}th$ power-law velocity profile was used as an inlet condition as this was representative of what was measured in the Severn estuary by an Acoustic Doppler Current Profiler (ADCP) and this profile slightly reduced the power coefficient compared to those in the uniform flow when normalised by the average upstream velocity. Five different stanchions of different cross-sectional shape were modelled: hydrofoil,

elliptical, circular, diamond and square which were the length of the whole depth of the domain. All stanchions increased, as expected, the thrust on the whole turbine structure corresponding to the unsupported case. Due to the lower drag coefficients the ellipse and hydrofoil stanchions had the smallest thrust and the square, because of its larger drag coefficient, had the greatest. With and without a circular stanchion, the axial thrust on each blade was shown through 360^o of rotation and it was found that as a blade passes the stanchion the thrust increases by 5%. Therefore to calculate the thrust on the whole turbine structure a simple linear addition of forces on blades and stanchion alone cannot be used as the stanchion impacts the axial thrust on the blades.

To investigate realistic conditions akin to the work conducted by Mason-Jones et al. (2013), Fleming et al. (2013), from the University of Oxford (UoO), studied the effect of the performance of a tidal turbine in a sheared flow. This numerical work was conducted using ANSYS Fluent with a $k-\omega$ Shear Stress Transport (SST) turbulence model (see Menter (1994) for details of this model). A log-law velocity profile was used to approximate the shear flow through the depth of a channel which replicated experimental conditions in a recirculating water flume $80m$ long, $1.5m$ wide with a water depth of $0.8m$ and a mean flow velocity of $0.55m/s$. The three-bladed turbine used in the study had a diameter of $0.6m$, resulting in an area blockage ratio of 24% and vertical height blockage of 75%. Initially the computation lift and drag coefficients over different angles of attack were compared to experimental results obtained by Miley (1982). The lift coefficient was slightly over-predicted by the numerical simulation and for angles of attack $\leq 4^o$ the drag coefficient was under-predicted. For the whole turbine it was found that the simulation over-predicted the thrust coefficients but matched the power coefficients to those experimentally measured. It was then possible to scale-up the numerical model so as to represent a full-scale tidal device, along with the use of ADCP data to estimate realistic flow conditions. The thrust and

power coefficients were calculated with the turbine placed at three different heights in the sheared flow. When C_P was normalised by the area-average of velocity-cubed ($C_P = \frac{P}{1/2\rho A \int U^3 dA}$) and C_T by the area-average of velocity-squared ($C_T = \frac{T}{1/2\rho A \int U^2 dA}$) the data were found to collapse showing that the sheared flow does not effect the power and thrust coefficients. (In chapter 2 we test this idea experimentally).

Experimental studies have been conducted to investigate the power and thrust on scale tidal turbines in uniform steady flows e.g. Bahaj et al. (2006, 2007) and O'Doherty et al. (2009) and non-uniform steady flows e.g. Mason-Jones et al. (2013) and Fleming et al. (2013). Furthermore investigation has been conducted into more realistic flow conditions on HATTs, such as the effect of wave-current interactions which add unsteady orbital motions into the flow. The majority of studies concerned with the effects of waves on tidal turbines have been conducted in towing-tanks such as those by Barltrop et al. (2006, 2007), Galloway et al. (2013), Luznik et al. (2013). In these towing-tank experiments both two- and three-bladed HATTs with a range of wave conditions (different wave-heights and -frequencies). The means of the power and thrust were equal to the current alone conditions however the power and thrust fluctuated with frequencies matching those of the waves. These towing tank tests provided a wide range of wave-current conditions with a small blockage ratio, however they are limited in the time period of data collection (e.g. $30s$ in Luznik et al. (2013)). Alongside characterising the power and thrust on a turbine in a number of different flow conditions another important factor is to investigate the velocity and turbulent flow field around the turbine, which is now discussed.

1.4 Wake Characterisation

As turbines are likely to be placed in farms or arrays to make them commercially viable, wake recovery length is crucial for the appropriate spacing

between turbines. Also, knowledge of the wake is important so that potential effects on the sea bed can be investigated. The earliest research into tidal turbine wakes was conducted using an absorption disk to represent the turbine, both experimentally (Myers & Bahaj (2010)) and using CFD (Sun et al. (2008), Harrison et al. (2010) and Batten et al. (2013)). Experimental studies into the characterisation of the wake of model turbines were conducted by Myers & Bahaj (2009) Stallard et al. (2011, 2013), Rose et al. (2011a) and Maganga et al. (2010). Further studies to compare experimental wake data to CFD were completed by Mycek et al. (2011, 2013b) and Rose et al. (2011b). Table 1 includes relevant details, such as model size, Reynolds number and blockage ratio, of studies undertaken to date.

As a first approach absorption disks were used as an approximation to a tidal device in that the momentum extracted by the device is captured but the swirl effects are neglected. An absorption disk is a disk with various holes which allow the water to flow through, the size and number of these holes are variable, which defines the porosity of the disk. The first to use this method was Sun et al. (2008) using both two- and three-dimensional commercial CFD (ANSYS Fluent). The computational domain used replicated a laboratory water channel, which was $1.5m$ wide, $10m$ long and had a water depth of $1m$. A volume-of-fluid approach was used to simulate the free surface and a no-slip wall boundary condition was used on the bed. The turbulence model used was the $k - \varepsilon$ model which assumes isotropic turbulence. In the two-dimensional simulations, Sun et al. (2008) used an absorption zone centred at a height of $0.5m$. When the water passed through the absorption disk approximately 38% of kinetic energy was dissipated. Results from this solution showed a substantial drop in the free-surface behind the absorption disk, reducing to roughly half the initial water height. The two-dimensional domain was extended to a three-dimensional domain, where a square disk was used which had an area ratio to the flume cross-section of 17%, this resulted in a 10% overall loss of kinetic energy in the flow. The results showed

that as the water flow reaches the disk it accelerates as it flows through, then velocity drops directly behind the disk. Similar to the two-dimensional solution, there was a free-surface drop behind the disk, however the drop was smaller for the three-dimensional model. These simulations gave a first simple approach for the characterisation of the wake and were concentrated on the near-wake and effects on the free-surface close to the disk. Similarly, Myers & Bahaj (2010) from the UoS group investigated experimentally an absorption disk approach. The experiments were conducted in a $21m$ tilting flume, which had a width of $1.35m$ and depth of $0.4m$. The vertical velocity profile produced in the flume resembled a modified $\frac{1}{7}$th power law which was more uniform closer to the surface and approximated a profile measured at a full scale site reported by the Carbon Trust (2005). Artificial bed roughness was added to the flume to reduce the velocity and increase the shear stress in the bottom third of the water column, creating conditions that were as realistic as possible. The absorption disks (mesh disks) used by Myers & Bahaj (2010) were $100mm$ in diameter (resulting in a blockage ratio of 6%) and had porosity (ratio of opened-to-closed area) varying between 0.48 and 0.35. To measure the thrust a load cell was attached to each disk, and it was found that the porosity alone did not influence the thrust coefficient. Four disks with equal porosity were tested, those with a larger number of small holes had a greater thrust than disks with fewer large holes. A Nortek Vectrino, Acoustic Doppler Velocimeter (ADV) device, with a sample rate of $50Hz$ and sampling volume of $0.15cm^3$, was used to map the wake up to 20 disk diameters (D) downstream. For all disks tested, it was found that at $10D$ downstream the mean velocity profiles were virtually identical and any effects of the disk had dissipated. Using a disk with thrust coefficient, $C_T \approx 0.9$, Myers & Bahaj (2010) investigated four different disks depths, with the disk centred at $0.33D$, $0.5D$, $0.66D$ and $0.75D$ above the floor of the flume. It was found that as the disk was placed closer to the floor, the mean velocity deficit was longer. The turbulent kinetic energy (TKE) was

also measured, where TKE is expressed as:

$$TKE = \frac{1}{2}(u'^2 + v'^2 + w'^2), \tag{1.4}$$

where

$$u' = \sqrt{(\frac{1}{N}\sum_{i=1}^{N}(u_i - u)^2)}, \tag{1.5}$$

$$v' = \sqrt{(\frac{1}{N}\sum_{i=1}^{N}(v_i - v)^2)}, \tag{1.6}$$

$$w' = \sqrt{(\frac{1}{N}\sum_{i=1}^{N}(w_i - w)^2)}, \tag{1.7}$$

where N is the number of samples at a particular point, u_i, v_i and w_i are the individual velocity samples and u, v and w are the mean velocities at a particular location. As the distance between the floor and the disk was increased, the TKE levels in the wake increased. To simulate a rocky seabed in the flume artificial rocks, with lengths between 6.7 and 10 mm ($0.067D$ and $0.1D$) over a length of 4 m, were placed in the flume as this bed type was expected to have the greatest effect on the turbulence levels. Again as the distance between the disk and the floor decreased, the wake velocity deficit downstream increased; in turn this increase of the velocity deficit was larger than that with the smoother bed. As a consequence, Myers & Bahaj (2010) suggested that a rocky seabed is less suitable for placing tidal turbines than a smoother bed. However, due to the limitations of the disk in that swirl is not accounted for this can only be taken as an idealised conclusion. The absorption disk experiments provide useful information on the far wake. The changes in wake length with the height of the turbine provides a good indication of where a turbine should be placed in relation to the bed to minimise the effect of the bed on the wake.

Harrison et al. (2010), again from the group at UoS, compared three-dimensional CFD simulations to the experimental absorption disk results conducted by Myers & Bahaj (2010) discussed above. The approach by Harrison et al. (2010) was more sophisticated than Sun et al. (2008) as the free-surface was simulated using a homogeneous coupled volume-of-fluid approach and the flow was calculated using the $k-\omega$ shear stress transport (SST) model. This model, an extension of the $k-\varepsilon$ model, was used as preliminary studies indicated that the $k-\varepsilon$ model did not accurately replicate the flow conditions. The model domain represented the flume in which the experiments were conducted, including a water depth of $0.3m$ and air to a height of $0.15m$ above the water. The disk was matched to the one used experimentally with a diameter of 0.1 m and thickness of 0.001 m and was located in the centre of the water column. To enable direct comparison with the experimental results, the thrust coefficient was matched. The measured inlet velocity distribution of the flume was used to set the inlet velocity. Both the far-wake and the near-wake were compared. The near-wake had some limitations in its accuracy, in that the effects of swirl were not taken into account, but this, the authors argued, was a reasonable method to estimate the effects of the far wake. The trend and wake recovery of the far wake was found to be similar in the two approaches and the turbulence levels in the wake were comparable.

Myers & Bahaj (2009) (UoS group) measured the wake of a turbine and support structure with a diameter of $0.8m$, using an Acoustic Doppler Velocimeter (ADV), in a recirculating water channel which was $18m$ long, $4m$ wide and $2m$ deep, giving a blockage ratio of 6.3% and had an upstream velocity of $0.8m/s$. The wake of the turbine support structure without the rotor was measured and was found to be significant, especially near the free-surface. The support structure increased the turbulence intensity, again near

to the free-surface, by $5D$ downstream the Turbulence Intensity, defined:

$$TI = \sqrt{\frac{2}{3}TKE}/U^2 \times 100, \tag{1.8}$$

was 10% which was still much higher than the upstream level of 6%. The wake of the support structure and rotor was measured at $5D$ downstream through the width of the channel at five different heights ($-0.2D, -0.1D$, centre, $0.1D$, $0.2D$). The largest deficit was found to be at a height of $-0.1D$ due to the presence of the support structure and the rotation of the blades. The smallest deficit was found at the deepest point measured ($-0.2D$) as the support structure was not present here. The streamwise velocity was also measured from $3D$ to $10D$ downstream of the centre of the turbine, it was found that by $10D$ downstream the velocity was still less than 80% of the upstream velocity. Overall it was clear that the support structure in this particular set-up had a dominant effect on the overall wake.

Batten et al. (2013) (UoS group), furthering the study by Harrison et al. (2010), investigated the use of the actuator disk Reynolds-average Navier-Stokes (RANS) approach of predicting the wake of a tidal turbine. The RANS results were compared to the experiments conducted by Myers & Bahaj (2009), discussed above, therefore the turbine diameter, size of channel and velocity and TI was matched. Two different computational models were investigated, firstly, a RANS actuator disk approach + blade element (BE) approach and RANS + disk approach where turbulence is injected artificially at the disk through source terms. The RANS + BE can be used to predict the power coefficient (C_P) and thrust coefficient (C_T), this model under-predicted the C_P for tip-speed-ratios greater than 6.5 compared to the results from BEM theory but gave a reasonable approximation to the experimental results. The thrust coefficient was over-predicted by the RANS + BE approach compared to both the BEMT and experimental results. The time averaged velocity and TI downstream of the turbine at the centreline of

both the RANS + BE and the RANS + disk approaches showed a reasonable agreement to experimental data of Myers & Bahaj (2009) between $5D$ and $10D$ downstream. At $5D$, $8D$ and $10D$ downstream time average velocities and TI of the two computational approaches and experimental data were analysed through the depth of the channel. At $5D$ downstream the TI from the RANS + BE model was greater than that of the experimental data, but further downstream the TI levels of the model were in reasonable agreement with the experimental data. Batten et al. (2013) concluded that the RANS + BE model was a better method of modelling a turbine compared to the RANS + disk model as the wake measurements showed a better agreement to that of the experiments and it removed the pragmatic approach of turbulence source terms added at the centre of the disk. In addition, as discussed in detail in chapter 5, there are some issues related to turbulence measurements using ADV (Khorsandi et al., 2012) so this method of adding a turbulent source term in the CFD so as to match experimental ADV results, which may themselves not be correct, is difficult to justify.

Although absorption disks give a reasonable approach to the far wake, the effect of the blades and rotation are not considered. Therefore it is important to investigate the wake effects using a rotating scale-model device in well controlled conditions. The wake of three devices were measured by Rose et al. (2011a) from the University of Strathclyde (UStrath). The wake of a four-bladed, $0.14m$ diameter, turbine, with Reynolds number $Re_F = \frac{UR}{\nu} = 80,000$, was measured. A particle imaging velocimetry (PIV) system was used to measure the downstream velocities, which acquired images at $100Hz$ with a total of 1000 image pairs taken for each test. This experiment was undertaken in a flume which was $20m$ long, $0.75m$ wide and $0.52m$ deep, at a velocity of $0.57m/s$. The second experiment took place in a flume $35m$ x $0.4m$ x $0.92m$ (length x width x depth) at a mean velocity of $0.42m/s$. A two-bladed turbine with a diameter of $0.25m$, at a Reynolds number of 1.05 x10^5, was placed $0.23m$ below the surface. A Nortek ADV

was used to measure the velocities downstream of the turbine, sampling at $25Hz$ for $33s$ at each location, therefore collecting a total of 825 samples per location. A third, larger scale experiment was undertaken in a lake by towing a turbine. The site, Montgomery Lough, is a lake of approximately $400m$ x $133m$. The turbine used was four-bladed with a diameter of $1.5m$, with a Reynolds number of $1.8\text{x}10^6$; it was placed $1.285m$ below the water surface. An ADV system was again used which had a sampling rate of $64Hz$, collecting for $170s$ therefore producing $10,000$ samples per point. Measurements were taken between $0.5D$ and $3D$ in the longitudinal direction and $1D$ laterally. It is difficult to compare these three results produced by Rose et al. (2011a) because of the differing thrust coefficients for each turbine, combined with the sparse data sets. As other work has suggested that the wake is strongly effected by the thrust on the turbine and C_T is not matched in these cases (Myers & Bahaj (2010), Harrison et al. (2010)) it is not entirely unexpected for the wakes to be different. The general pattern produced by the three experiments are consistent as the centreline always has the maximum velocity deficit, but little detailed insight was provided.

More detailed wake measurements of a single turbine was conducted by Chamorro et al. (2013) from the University of Minnesota (UMin). An ADV, with a sampling frequency of $200Hz$, was used to measure the wake of a $0.5m$ diameter turbine in a flume $85m$ long and $2.75m$ wide with a water depth of $1.15m$. The upstream velocity was non-uniform with a mean of $0.4m/s$ at the turbine hub-height. Wake measurements were taken up to $15D$ downstream through the water depth of the centre of the turbine with a tip-speed-ratio of 5.8. The spanwise velocities show the effect of swirl due to the turbine rotation and are of the order of 15% of the mean streamwise velocity. The swirling motion induced into the flow by the turbine rotation is also highlighted by the power spectra of the velocities which show a clear peak equal to the rotational frequency. The streamwise turbulence intensity increases downstream, at a height above the turbine to around, 20% and this increase expands through

the depth after $2D$ downstream until $4D$ downstream, where the TI is then reduced. Further wake measurements were taken downstream of the turbine at different tip-speed-ratios, $\lambda = 2.9, 3.8, 5.8$ and 7.7 at a depth equal to the central hub-height. It is observed that the lower the tip-speed-ratio the lower the streamwise velocity deficit, this difference between $\lambda = 2.9$ and 7.7 is around 5% of the mean streamwise velocity. Neary et al. (2013) (from the UMin group) continued the work of Chamorro et al. (2013) by comparing ADV wake measurements with Acoustic Doppler Profiler (ADP) measurements. These measurements were taken in a centre-plane through the depth of the channel. The mean streamwise velocity showed reasonable agreement between the two techniques in the main wake region. However, the velocity fluctuations were found to be much greater when measured using ADP and at some distances downstream the qualitative trends were found to differ, highlighting concerns over the use of acoustic Doppler techniques for wake measurements downstream of tidal turbines. Chapter 5 attempts to address some of the issues surrounding acoustic Doppler measurements in highly turbulent flows.

Another experimental test of the wake downstream of a single device was undertaken by Maganga et al. (2010) (from IFREMER), where the wake from a three-bladed turbine was measured, with a diameter of $0.7m$ in a flume $18m$ long, $4m$ wide and $2m$ deep, giving a blockage ratio of 5%. Tests were conducted with velocities between $0.5m/s$ and $1.5m/s$, and with different upstream turbulence intensity levels of 4.6% and 14.4% where turbulence intensity is defined in equation 1.8. The claimed increase of turbulence intensity to a very high value of 14.4% by the simple removal of the honeycomb used to straighten the flow raises questions on the uniformity of this turbulence level. This value is far higher than the maximum TI of 5% that could be produced using conventional methods, by means of a grid for example (Pope, 2011) as is shown in chapter 2. Different yaw angles of the turbine were investigated; $0^o, -10^o, 10^o, 15^o$ and 20^o. Power and thrust were

also measured at these yaw angles, and it was found that as the yaw angle increased from the optimum position (i.e. correctly aligned (0^o)), the thrust decreased. Theses results on yaw agree with work conducted earlier by Bahaj et al. (2006) as discussed previously (see section 1.3). It was also noticed at the higher turbulence intensity level, 14.4%, both C_p and C_T decreased in comparison to the base case (4.6% TI). A two-dimensional Laser Doppler Velocimetry (LDV) system was used to measure the velocities behind the turbine, with a sampling rate of $50Hz$ for $100s$. Measurements were taken every diameter in the streamwise direction behind the turbine, up to $10D$ downstream; measurements were also taken in the spanwise direction between $-1.7D$ and $1.7D$ with a spacing of $100mm$ between points. Results from the study showed that with the higher turbulence intensity level there is a much faster wake recovery and that after $5D$ downstream the deficit is almost negligible. At the lower turbulence intensity level (4.6%) the mean velocity deficit is still clearly visible $10D$ downstream and the turbulence intensity levels in the wake remained higher than upstream levels. These results are in broad agreement with a number of experimental studies conducted on the influence of ambient turbulence intensity on the near wake of different structures: a wind turbine, a circular cylinder and prisms (Adaramola et al. (2006), Vermeer et al. (2003), Devarakonda & Humphrey (1996), Wussow et al. (2007)).

Mycek et al. (2011, 2013b) (also from IFREMER group) furthered the work of Maganga et al. (2010) by studying the interaction between two tidal turbines placed in series. Firstly by measuring the wake of a single turbine and then the interaction of wakes of two turbines one placed downstream of the other; this was achieved both experimentally, using two-dimensional LDV and numerically using CFD. The turbines investigated were three-bladed with a diameter of $0.7m$ ($\frac{1}{30}$th scale). The water channel used was the same as that of Maganga et al. (2010), with a flow velocity of $0.8m/s$ and upstream turbulence intensity levels of 2.9% and 14.4% (note these were previously

calculated from Maganga et al. (2010) as 4.6% and 14.4% respectively for exactly the same facility and settings). The velocities and turbulence intensities were measured with a two component LDV system and were collected at each point for $100s$ with a frequency of $7 - 17Hz$ (therefore $700 - 1700$ samples per point). The measurements were taken up to $10D$ downstream of the turbine and 25 measurements were taken in the spanwise direction across the width of the flume every $100mm$. For the wake behind a single turbine with TI of 14.4% it was found that by $7D$ downstream the wake had recovered to 90% of its upstream turbulence intensity level and its uniformity had returned. Whereas with a TI of 2.9% even after 10 diameters the profile was still non-uniform and the TI was still much greater than the 14.4% level. It was suggested by the authors that the high upstream turbulence levels significantly reduce the wake by enhancing the transfer of momentum between the free stream and the wake regions. The numerical study conducted by Mycek et al. (2011) investigated a flow with 0% TI upstream, using a Lagrangian vortex particle method with a large eddy simulation turbulence model. A comparison of these results with experimental data was undertaken at $1.2D$ behind the turbine. The results showed a qualitatively similar profile, however the mean velocity was underestimated by the computational model. Experimental work with two turbines in both flow conditions, also reported by Mycek et al. (2011), compared the power output of the second turbine at $4D$, $6D$, $8D$ and $10D$ downstream from the first turbine. As expected, because of the velocity deficit, there was a drop in maximum power coefficient, C_P, for the downstream turbine (based on the velocity upstream of the first turbine). The further downstream the second turbine was placed from the first, the higher the maximum C_P of the downstream turbine but by $10D$ downstream the C_P was still lower than that of the upstream turbine.

The numerical study by Mycek et al. (2011) was furthered by Pinon et al. (2012) (IFREMER group), whom investigated the sensitively of different mesh sizes in their CFD model. For tip-speed-ratios less than 3.5, power

and thrust coefficients were found to match both BEM models of a single turbine used by Bahaj et al. (2007). The streamwise velocity downstream of a turbine was found to be qualitatively similar for the simulations and experimental studies. However, the mean axial velocity deficit downstream of the turbine was consistently lower for all the numerical models compared with the experimental data by around 5%. Continuing the experimental study of Mycek et al. (2011, 2013b), velocity measurements were taken by Mycek et al. (2013a) downstream of two axially-aligned scale model turbines ($0.7m$ diameter). These measurements were again conducted at two different ambient turbulence intensity levels, 3% and 15% (presumably the same as the previous studies but were defined differently in all three papers). The axial velocity in the wake downstream of the turbines echoes that of the single turbine, where the recovery is found to be much quicker with increased turbulence intensity. The wake downstream of the second turbine was found to be similar regardless of the distance between the two turbines. The only difference, at low ambient TI, is that the turbulence intensity of the wake merges much faster behind a second turbine, within $4D$, than behind a single device where the merging zone, i.e. where the two individual wakes become indistinguishable, is around $6D$ downstream. This difference is likely due to the velocity fluctuations created by the rotation of the upstream turbine and the resulting trend is more similar to that of single rotor in a higher ambient TI. If the average (mean) TI, over the disk area, is calculated then agreement is found after $4D$ for both single and two turbine configurations. This result indicates that rotors may always have similar far-wake characteristics even if placed directly downstream of another device which is a useful result for the planning of arrays/farms of turbines.

Extending the research of wakes of single devices by Rose et al. (2011a), Maganga et al. (2010) and two devices placed in series by Mycek et al. (2011, 2013b,a), Stallard et al. (2011, 2013), from the University of Manchester (UoM), probed the effect of a series of turbines on the wake structure. All

turbines were three bladed and had a diameter of $0.27m$ (corresponding to an estimated $\frac{1}{70}$th scale), with a Reynolds number based on the blade chord of 1.2x10^5. These experiments were conducted in a flume with a water depth of $0.45m$, width of $5m$ and length of $12m$, the flow had a turbulence intensity (TI) of approximately 10% and a mean velocity of $0.45m/s$. Thus, although area blockage is small (2%) the turbine takes up, similarly to our turbine in the UoL water-channel, 60% of the vertical column and so some acceleration above and below the turbine may be expected. The number of turbines tested at a time were 1, 2, 3, 5, 6, 7 and 10. The turbines in the arrays were configured into one, two, and three rows. The lateral spacing between the devices was 1.5, 2 or $3D$, the longitudinal spacing of devices considered was between 4 and $10D$. The wake was measured using an ADV, sampling at $200Hz$ for $60s$ at each location (i.e. collecting $12,000$ samples per spatial point). For a single turbine, the wake was measured directly downstream of the centreline of the turbine. Rapid recovery of the wake was observed for the first $5D$ downstream. Further downstream the recovery was much slower and by $20D$ downstream the wake still had a velocity deficit of just under 20%. It was found that with the 2, 3 and 5 turbine configurations the individual deficit was identifiable up to $4D$ downstream but further downstream all the wakes merged into a single structure. The effect of waves was briefly investigated, with a wave-height of $50mm$ and a peak period of $1.25s$ (frequency $0.8Hz$). These waves increased the velocity fluctuations to around 25%, defined more clearly in the later study by Olczak et al. (2013), at the surface but these fluctuations decayed through the depth. The wake recovery in these conditions was similar over a range of $5D$ to $10D$ downstream, however the turbulence intensity remains above 12% at $10D$ downstream.

In extension of the work conducted by Stallard et al. (2011, 2013), using the same turbine and facilities, Olczak et al. (2013), from the UoM group, investigated the effect of opposing waves on the wake of a single device. The upstream streamwise velocity was fairly uniform with a mean of $0.46m/s$ and

waves with frequencies of $0.5, 0.6, 0.7$, and $0.8Hz$ were tested. An ADV was used initially to characterise the velocity in the channel and it was found that the Flow Kinetic Energy (defined $FKE = \frac{1}{2}\sum_{i=1}^{3}\overline{(\tilde{u}_i(t) + u_i'(t))^2}$ where $\tilde{u}$ denotes the periodic waves induced fluctuations and u' is the turbulent fluctuations), increased near to the water surface with waves present. Detailed measurements through the depth of the channel were taken at $2D$ and $4D$ downstream with the current alone and three different wave conditions. It was observed that the maximum velocity deficit occurs at a depth equal to the centre of the turbine and was greatest in the current alone case. When the velocity deficit was plotted at the centreline downstream of the turbine the wake recovery was found to be similar in the current alone and different wave cases after $6D$ downstream. At this location the velocity was recovered to 80% of the upstream value, showing that the opposing waves have the largest impact on the near-wake region.

Other comparisons of CFD and experimental work have been conducted by Rose et al. (2011b), in which a single rotor with a diameter of $0.3m$ was used. The turbine had interchangeable blades and 2 and 3 blade configurations were tested at different blade pitch angles (0^o, 2^o, 4^o and 6^o). The experiments were conducted in a tank which was $0.92m$ wide, $0.42m$ deep and $35m$ long, therefore giving a blockage ratio of 18%, where the turbine takes up 70% of the vertical water column. An ADV was used to measure the three-dimensional velocities and TI, which were sampled at $25Hz$ for $33s$ at each location (i.e ≈ 825 points per location). The results showed that there was a rapid and significant recovery between $2D$ and $8D$ downstream, however the wake had not fully returned to the mean upstream velocity by $25D$ downstream. The increase in blade pitch angles showed a smaller wake impact and the three-bladed turbine had a higher deficit than the two-bladed due to the corresponding higher C_T. The CFD comparison conducted by Rose et al. (2011b), used a three-dimensional RANS simulation using the same width and height of the flume in which the experiments were conducted, but they

made the channel longer. A $k-\omega$ turbulence model was used near the walls and $k-\epsilon$ was used in the main flow. The assumptions of isotropic turbulence in this latter model meant that it was under-predicting the wake compared to that measured in the experimental study.

Following the review of studies to date showing the scope for this study the aims and objectives are now discussed.

Table 1.1: Overview of previous tidal stream turbine wake studies

Author / Year	CFD / Experimental	Turbine diameter	Blockage ratio	T.I.	Reynolds Number	C_T	Conclusions
Sun et al. (2008)	CFD	$0.5m$	17%				First approach at estimating the far wake.
Myers & Bahaj (2009)	Exp	$0.8m$	6.3%	$\approx 6\%$	$3.2\text{x}10^{5}$*	0.9	Support structure had a large influence up to $5D$ downstream. By $10D$ the velocity had recovered to 80% of the upstream velocity.
Myers & Bahaj (2010)	Exp	$100mm$ - mesh disks	1.5%	$\approx 5\%$	$2.5\text{x}10^{4}$*	≈ 0.9	When disk was placed closer to the floor the velocity deficit persisted for longer.
Harrison et al. (2010)	CFD	$100mm$ - mesh disks	1.5%	$\approx 5\%$	$2.5\text{x}10^{4}$*	≈ 0.9	The trend of the wake recovery and turbulence levels are qualitatively similar in the CFD and experimental results.
Maganga et al. (2010)	Exp	$0.7m$	5%	4.6% and 14.4%	$3.5\text{x}10^{5}$*		with 14.4% TI after $5D$ downstream the deficit was almost neligible, with 4.6% TI at $10D$ downstream the TI was still higher and the velocity deficit still visible.

Author / Year	CFD / Experimental	Turbine diameter	Blockage ratio	T.I.	Reynolds Number	C_T	Conclusions
Rose et al. (2011a)	Exp	$0.14m$, $0.25m$ and $1.5m$	3.9%, 13.3%		$80,000$*, $1\text{x}10^5$* and $1.8\text{x}10^6$*	0.959, 0.373 and 0.567	Centreline measurements of velocity are consistent for the three devices, the maximum deficit was always the centreline.
Rose et al. (2011b)	CFD and Exp	$0.3m$	18%		$1.2\text{x}10^5$*		Rapid recovery between $2D$ and $8D$ but by $25D$ still not recovered. The CFD results underpredicted the experimental results of the wake.
Mycek et al. (2011, 2013b)	Exp and CFD	$0.7m$	5%	2.9% and 14.4% experimentally and 0% in CFD	$3.5\text{x}10^5$*		With 14.4% TI at $7D$ downstream the TI was 90% of the initial TI With the TI levels of 2.9% at $10D$ downstream the flow was still non-uniform and TI levels are still much greater. The CFD results were similar for the velocity measurements but underestimate the TI

Author / Year	CFD / Experimental	Turbine diameter	Blockage ratio	T.I.	Reynolds Number	C_T	Conclusions
Pinon et al. (2012)	CFD	$0.7m$	5%	0%	$3.5\text{x}10^{5}$*		Compared to Mycek et al. (2013b) the mean axial velocity deficit was qualitatively similar but underestimated by around 5%.
Stallard et al. (2011), Stallard et al. (2013)	Exp	$0.27m$	2.5%	10% and 25% with waves	based on blade chord $30,000$, $1.2\text{x}10^{5}$*	0.82	Rapid recovery up to $5D$ downstream with a recovery of 70% of upstream velocity, but by $20D$ downstream the velocity was 80% of the upstream velocity. With two or more turbines the individual wakes of the devices can be seen up to $4D$ downstream but after the wakes merge to a single defecit. The effect of waves on the wake had a similar velocity trend to the uniform flow between $5D$ to $10D$ but the TI remained a lot higher downstream.
Batten et al. (2013)	CFD	$0.8m$	6.3%	5%	$3.2\text{x}10^{5}$	0.9	RANS + BE model gives a better agreement to experimental data than the disk model. Results showed that by $22D$ downstream the velocity had not returned to the upstream value.

Author / Year	CFD / Experimental	Turbine diameter	Blockage ratio	T.I.	Reynolds Number	C_T	Conclusions
Mycek et al. (2013a)	Exp	$0.7m$	5%	3% and 15%	3.5x10^5*		Velocity deficit behind two axial aligned turbines found to equivalent to the wake behind a single device. The TI downstream equivalent to that of a single device in high ambient TI.
Chamorro et al. (2013)	Exp	$0.5m$	6%	10%	1.7 x 10^5 based on turbine diameter, 1.5 x 10^4 based on blade chord		Swirl induced by blade rotation was a prominent feature in the wake. The lower the tip-speed-ratio the lower the velocity deficit downstream of the turbine.
Neary et al. (2013)	Exp	$0.5m$	6%	10%	1.7 x 10^5 based on turbine diameter, 1.5 x 10^4 based on blade chord		Different techniques ADV and ADP were used to measure the wake of a single turbine, both measurements agreed for mean quantities but disagreed for fluctuating velocities.
Olczak et al. (2013)	Exp	$0.27m$	2.5%		$200,000$		Opposing waves impact the wake up to $8D$ downstream but further downstream the wake was similar to current alone flow conditions.

*based on the radius and upstream velocity which is estimated by present authors based on limited data provided in the original papers.

1.5 Conclusions from the literature

The following are found to be the keys points from the literature survey.

- Power and thrust coefficients of turbines have been well documented for a number of turbine configurations and flow conditions.
- Absorption disks provide useful information of the far-wake turbines however, because they lack the production of swirl they do not represent the flow characteristics of a turbine's near-wake. Therefore it is important to use a rotor when investigating the near-wake of a turbine.
- Support structures can have a large impact on the the flow downstream, therefore it is important to consider the size in relation to that of the rotor.
- Reynolds number is a very important parameter to consider when conducting small scale experiments so to produce results which are consistent with full-scale devices.

1.6 Aims and Objectives

As the previous studies have made clear, a great deal of preliminary work has been conducted on scale-model turbines in uniform flow. However it is apparent that little in-depth experimental studies have been made in more realistic conditions. Therefore the aim of this this is to address this gap by completing a detailed study on turbine wake characteristics in a number of different flow conditions along with power and thrust measurements. Not only will these experiments provide physical insight, but they will represent a comprehensive benchmarking data set for comparison to numerical models.

Using CFD, Mason-Jones (2010) calculated the power and thrust coefficients of a turbine, the one used in this thesis, with different numbers of blades and blade-pitch-angles and compared them to a limited experimental

data set. An initial objective will there be to verify these CFD calculations by conducting detailed experimental measurements of the turbine with between two and six blades at different blade-pitch-angles in uniform flow.

In a non-uniform flow, such as a power-law or a log-law velocity profile numerical simulations (e.g. Mason-Jones et al. (2013) and Fleming et al. (2013)) found that by using an area-averaged velocity there is collapse of power and thrust coefficients, however this has not been confirmed experimentally. A secondary objective will be to investigate the effect of a non-uniform flow experimentally, to do so a flow which approximates a $1/5th$ velocity power-law profile, is produced in the UoL water-channel. Power and thrust coefficients of a three-bladed turbine with optimum blade-pitch-angle (6^o) are taken in non-uniform and are compared to those in uniform flow.

The studies to date which have investigated the wakes of tidal stream turbines have mostly been concerned with the mean streamwise flow and turbulence intensity in single planes downstream of the turbine, with measurements confined to a centre-plane through the turbine or planes normal to the flow. In the experimental studies the number of locations at which the flow has been characterised has been fairly sparse or been concerned with the far-wake effects. The third objective is to produce a more detailed three-dimensional data set than has hitherto been reported. In this study the near-wake of a single turbine in uniform flow with a low TI is characterised by means of an ADV. Initially the near-wake velocities, at 5 different height up to $7D$ downstream, of a three-bladed turbine with optimum blade-pitch-angle are measured with upstream mean velocity of $0.9m/s$. As a number of studies have been conducted at low Reynolds numbers such as Rose et al. (2011b), Stallard et al. (2013) and Chamorro et al. (2013), to investigate any Reynolds number effects, the near-wake of the turbine is measured with upstream mean velocities of $0.45m/s$ and $0.68m/s$. These velocity measurements were taken through a centre-plane at a depth equal to the centre of the turbine and compared with the wake of the turbine at an upstream velocity

of $0.9m/s$. Harrison et al. (2010) and Myers & Bahaj (2010) suggested that the thrust coefficient was the main influence on the wake structure. Therefore a further objective will be to investigate this hypothesis in section 3.3 by measuring the near-wake downstream of a two bladed-turbine with optimum (3^o) and non-optimum (9^o) blade-pitch-angles, therefore with different λ, C_T, and C_P.

After investigating the wake of the turbine in uniform flow conditions, another objective of this thesis is to investigate it in more complex flows. Although there have been some limited studies in more complex flows the conditions have not been well characterised and the wake measurements are sparse. Here, turbulence is generated in the channel, while keeping the mean flow uniform, by means of a upstream grid creating higher TI levels. The wake of the three-bladed turbine through a centre-plane is measured using ADV in this flow with higher TI. Additionally the velocities in the wake of the three-bladed turbine in non-uniform steady flow at five different heights up to $5D$ downstream is measured and compared with the wake in both uniform flow conditions.

Along with the work in this thesis, most studies investigating the flow field around a tidal turbine have used ADV (e.g. Maganga et al., 2009, Stallard et al., 2013 and Neary et al., 2013). Using this velocity measurement technique recently Khorsandi et al. (2012) found that some of the velocity fluctuations were overestimated compared to other measurement techniques. Therefore the final objective is to study the robustness of the use of ADV measurements to characterise the near-wake of a tidal turbine and in chapter 5 ADV measurements are presented with different probe orientations and compared to LDV measurements.

Chapter 2

Experimental Technique and Turbine Characterisation

All experimental work was conducted at the University of Liverpool, using the high-speed recirculating water-channel. A scale-model turbine, which was designed and built at Cardiff University (Mason-Jones, 2010), was tested and the experimental arrangement is detailed here.

2.1 Description of University of Liverpool Water Channel

Testing was undertaken in the University of Liverpool high-speed re-circulating water-channel, a schematic of which is shown in figure 2.1. The channel uses a $75kW$ motor-driven axial-flow impeller to circulate $90,000$ litres of water. The water flows into the working section which is $3.7m$ long by $1.4m$ wide and can provide a depth range of between $0.15m$ and $0.85m$. This provides the possibility of a uniform velocity profile ranging between $0.03m/s$ and $6m/s$. On leaving the impeller the flow is passed through the lower section, then up through brass honeycomb which straightens the flow. The flow is

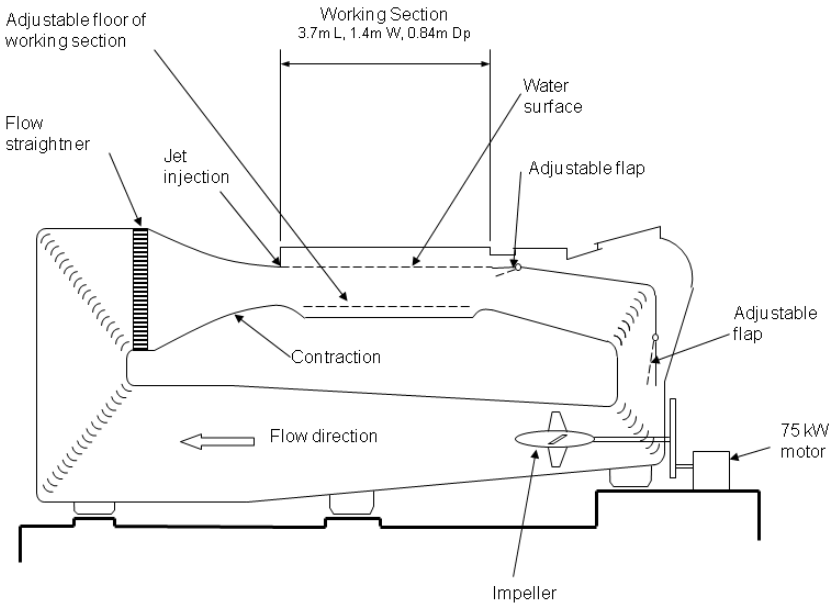

Figure 2.1: Schematic of the University of Liverpool water channel

accelerated by the contraction into the working section providing uniform flow where all measured mean streamwise velocities agree to within 1%. The jet injection, which can be adjusted according to the mean flow speed, at the start of the working section adds flow to the surface to compensate for the velocity deficit at the free-surface which is caused by the boundary layer on the contraction wall. The splitter flap at the the end of the working section separates the topmost layer of the flow from the main flow, this is necessary to remove any air bubbles added to the flow in the working section, this splitter flap was kept constant throughout the testing at 76 on the scale. To reintroduce the separated flow there is another adjustable flap, set constant to 82 on the scale, further down the channel. More details of the high-speed water-channel can be found in Millward (2002).

The conditions under which the experimental tests were made were $0.8m$ water depth with uniform velocity in the range 0.45 - $1.34m/s$ with an average turbulence intensity (TI) of 2% measured by an Acoustic Doppler Velocime-

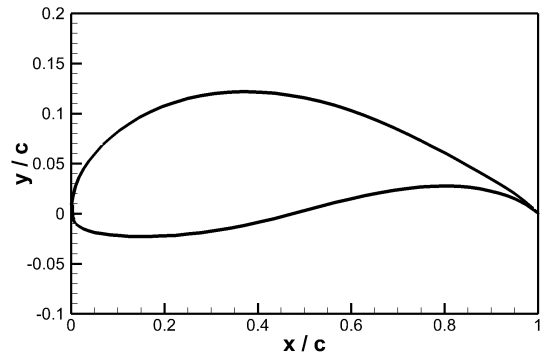

Figure 2.2: Normalised blade profile

ter (ADV) throughout the channel. Where TI is defined in equation 1.8. The turbine was located with its centreline at a depth of $0.42m$, giving a swept area blockage ratio of approximately 18% (Mason-Jones et al., 2012) and takes up 62% of the vertical water column.

2.2 Description of Turbine

The original Horizontal Axis Tidal Turbine (HATT) blade profile, a variant on the Wortmann FX 63-137, was selected by Egarr et al. (2004) using methods suggested by the National Advisory Committee for Aeronautics (NACA) for aerofoil sections, and subsequently optimised using Blade Element Modelling theory. The normalised blade profile is plotted in figure 2.2. Figure 2.3 shows an image of the assembled $0.5m$ diameter, three-blade configuration HATT with the stanchion attachment point and nose cone that has been used in this study. The turbine has been designed such that the number of blades can be varied from 2 up to a maximum of 6 blades. The blade-pitch-angle

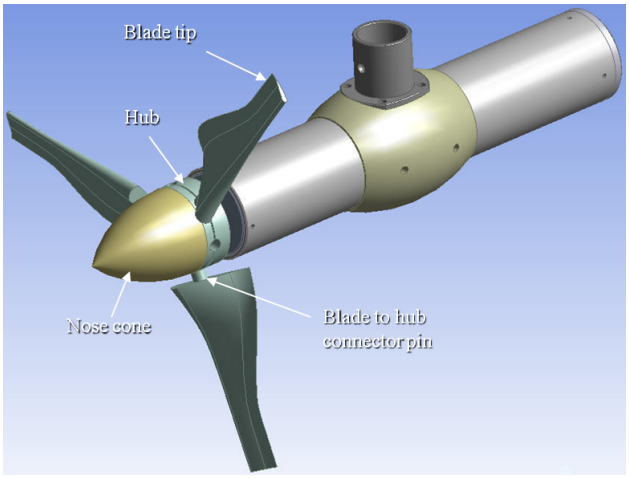

Figure 2.3: Horizontal Axis Tidal Turbine

is adjustable and was set by hand using a jig as shown in the photograph in figure 2.4, where positive angle is to feather. Complete details of the turbine, such as taper and twist of the blades, can be found in Mason-Jones (2010). Investigation of the power and thrust coefficients were undertaken at various arrangements to confirm the optimum found using CFD by Mason-Jones (2010); this is discussed in section 2.8.

The turbine was connected to a Baldor brushless AC servomotor in order to measure/calculate the torque, angular velocity and power generated. A regen-resistor or dynamic brake was used to apply an opposing torque to that developed by the hydrodynamic forces on the turbine. This motor was combined with a control system which in turn was programmed via Workbench V5 (O'Doherty et al., 2009 and Mason-Jones et al., 2012. Workbench allows up to 1000 data points to be collected over any set time period, therefore for each torque setting at least 5 measurements of torque and angular velocity over a $10s$, period were taken resulting in a minimum of 5000 points per torque setting.

A constant torque was applied which was proportional to the maximum drive rate current, in this case the maximum was $10.1A$, which is related to

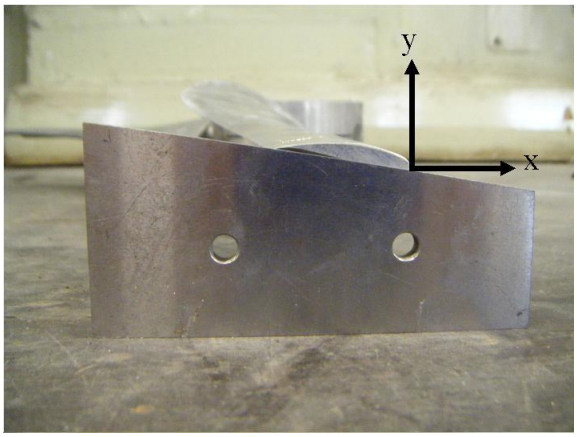

Figure 2.4: Photograph of setting the blade pitch angle

the torque by a proportionality constant of $0.82Nm/A$. The torque throughout the measurements of the wake was set to 20% of the current limit. The rotational speed of the motor was measured as a percentage of the rated rotational velocity for the motor ($500rpm$). Therefore, the angular velocity of the turbine was calculated from:

$$\omega = \frac{speed(\%)}{100} \times \frac{500}{60} \times 2\pi = speed \times \frac{\pi}{6}. \tag{2.1}$$

Thus from the angular velocity and torque, the power is calculated.

2.3 Force Blocks

To determine the thrust on the whole turbine structure and support, a $50kg$ strain gauge dynamometer was attached to the stanchion mounting, the design of which is described in detail by Millward & Rossiter (1983). The force block was calibrated by applying a variable load from $1kg$ to $25kg$ in steps of $1kg$, where the weights were found to be accurate to $\pm 1\%$. It is estimated that this produced a calibration which is accurate to about 1%, as shown in figure 2.5.

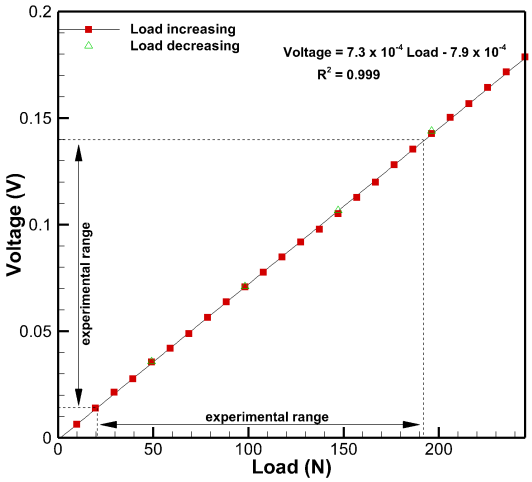

Figure 2.5: Force block calibration

2.4 Acoustic Doppler Velocimeter (ADV)

An Acoustic Doppler Velocimeter (Nortek Vectrino+) was used to measure velocities and turbulence statistics. ADV is a well known technique (Lohrmann et al., 1994 and Voulgaris & Trowbridge, 1998) for simultaneously measuring velocity components in three dimensions using the acoustic Doppler principle. The ADV used in this study had four $10MHz$ receiving elements positioned around a $10MHz$ transmitter. The probe was submerged in the flow and focused on a location $50mm$ away from the probe head to minimise flow interference. The ADV had a cylindrical sampling volume set to $198mm^3$ (height of $7mm$ and diameter of $6mm$). Data was collected at a sampling rate of $200Hz$ and at least $10,000$ individual velocities were measured to ensure the mean velocities and turbulence statistics converged. Data was filtered using the WinADV software using the de-spiking methods of Wahl (2003), which was adapted from Goring & Nikora (2002). The ADV had two different interchangeable probe heads: probe A has a fixed stem with

the downwards-looking head shown in figure 2.6(a) and the other, probe B, has a flexible cable with a sideways head orientation as shown in figure 2.6(b) in the sideways position and in figure 2.6(c) with the downwards-looking set-up. These different heads enable different orientations, such that the control volume can be either set with the jth component (see figure 2.6 (d)) in the vertical or in the spanwise direction.

The ADV (probe A) was used to characterise the three-dimensional velocities and turbulence statistics in the various flow conditions produced in the high-speed water-channel, this same probe arrangement was used throughout chapters 2-4. Figure 2.7 shows the relationship between the dial setting of the water-channel and the streamwise velocity measured at the centre of the channel, showing that there is a linear relationship between dial setting and velocity which is consistent with the measurements of Sutcliffe (1995) and Millward (2002). Figure 2.8 shows the spanwise and vertical velocities at different mean streamwise velocities; these velocities are always less than 5% of the streamwise component, showing that the flow is essentially one-dimensional. The standard deviations of the velocities, figure 2.9, show that the fluctuations are very small and that the free-stream flow has low turbulence levels. Figure 2.10 shows the ADV measured turbulent kinetic energy at different mean streamwise velocities, which akin to the fluctuating velocities are constantly low but increase linearly with increased streamwise velocity resulting in a constant TI. As well as characterising the flow in the channel, the flow field in the near-wake downstream of the turbine was also characterised using the ADV is discussed in chapters 3-5.

(a) ADV probe A - downwards looking

(b) ADV probe B - sideways looking

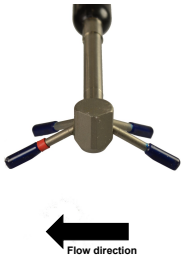

(c) ADV probe B - downwards looking

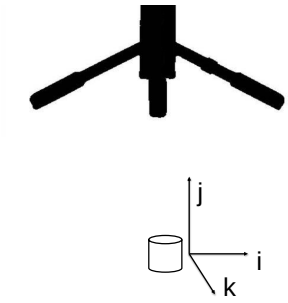

(d) ADV control volume orientation

Figure 2.6: ADV probe set-ups

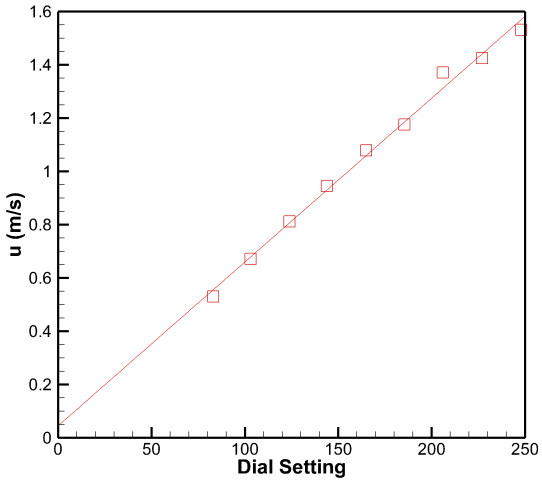

Figure 2.7: ADV measured streamwise velocity in the centre high-speed water-channel

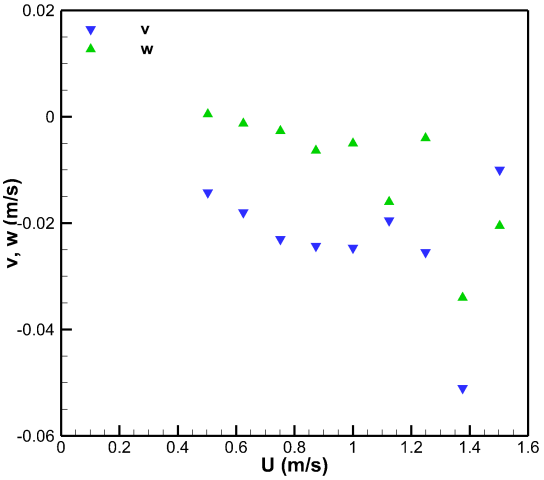

Figure 2.8: ADV measured vertical (v) and spanwise (w) velocities in the centre in the high-speed water-channel

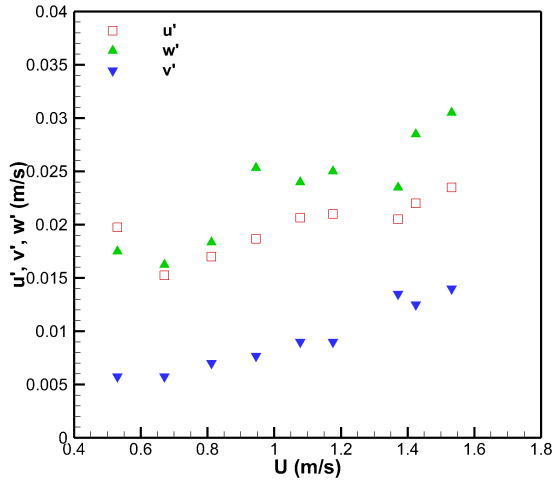

Figure 2.9: ADV measured standard deviations of streamwise, vertical and spanwise velocities in the centre of the high-speed water-channel

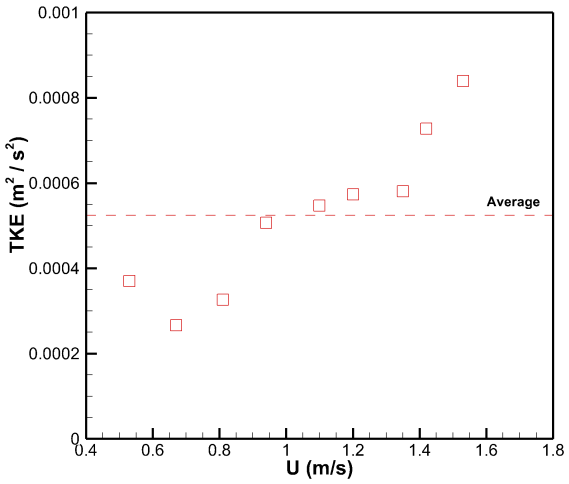

Figure 2.10: ADV measured TKE in the centre of the high-speed water-channel

2.5 Laser Doppler Velocimetry

Laser-Doppler Velocimetry (LDV) is widely known as one of the most accurate flow measuring techniques, having small control volumes and being unobtrusive (Tropea, 1995). The LDV system used in this study was a Dantec $1D$ FlowLite with a focal length of $400mm$, operating in back-scatter with velocity realisations obtained in burst mode at an average sampling frequency of $4Hz$. The control volume for the LDV ($2.3mm^3$) is 100 times smaller than the ADV ($198mm^3$) measuring volume. For each measurement at least $10,000$ velocity samples were collected, which was found to be enough for convergence of the mean and standard deviation. To avoid issues associated with velocity biasing, all measurements of the mean ($\hat{u}$) and standard deviation (u') were calculated using transit-time weighting (Bucchave et al., 1979 and Tropea, 1995):

$$\hat{u} = \sum_{i=1}^{N} \frac{t_i}{\sum t_i} u_i, \tag{2.2}$$

and

$$u' = \sqrt{\sum_{i=1}^{N} \frac{t_i}{\sum t_i} (u_i - \hat{u})^2}, \tag{2.3}$$

where u_i are the individual velocity samples, t_i is the transit time (the time the tracer particle in the flow takes to pass the control volume) and N is the number of samples i.e. $10,000$.

2.6 Grid Generated Turbulence - Characterisation of Flow

Tidal turbines will be placed in marine currents which are highly turbulent, it is therefore important to consider flows with higher turbulence levels

than those naturally found in the water channel. As a first approach in the high-speed water-channel a grid was placed upstream in the working section, which produced a steady uniform flow with an increased turbulence level. Using a grid to increase the turbulence is a well-known technique and has been researched in depth by Uberoi & Wallis (1967) and Murzyn & Belorgey (2005). Murzyn & Belorgey (2005) investigated the decay downstream of a grid in a open water-channel using a $2D$ LDV system and found that when $15 < x/M < 60$, where M is the mesh spacing, x is the distance downstream of the grid, the flow is isotropic and homogeneous for Reynolds number based on M ($Re_M = \frac{UM}{\nu}$) between 7400 and 11000. A number of grids were therefore tested within the high-speed water-channel to analyse the effect on both the turbulence levels and the effect on the uniformity of the flow. The grids tested were:

- $M = 11.5mm$, $d = 1.5mm$, $Re_M = 10350$,
- $M = 22mm$, $d = 3mm$, $Re_M = 19800$,
- $M = 50mm$, $d = 4mm$, $Re_M = 45000$,

where d is the wire diameter. For all grids tested velocity measurement were taken across the channel and through the depth.

The spanwise measurements were taken at a depth of $0.4m$ in the centre of the channel, the mean streamwise velocities are shown in figure 2.11. It can be seen that the velocities with the meshes where $M = 11.5mm$ and $22mm$, varied between $\pm 1\%$ of the mean across the channel, showing that the grid had little effect on the uniformity of the flow. However, the velocities for the mesh with $M = 50mm$ varied $3 - 4\%$ across the channel, even though the measurement was further downstream than for the other meshes as close to the grid the variations were much greater. These variations correspond to the wire causing a blockage and reducing the mean flow directly downstream and the flow being greater where the wire is not present, this is more prominent with larger wire diameters. The vertical and spanwise mean

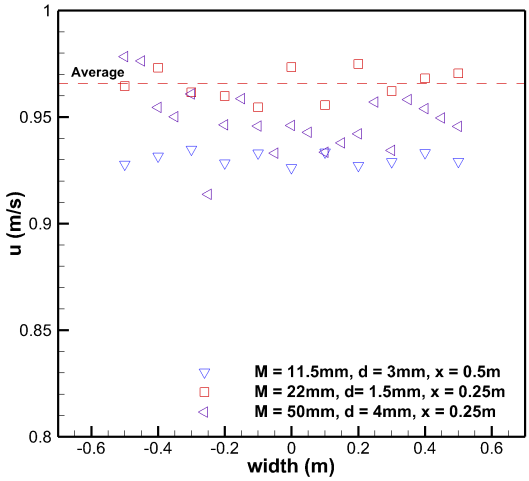

Figure 2.11: The streamwise velocity downstream of grids of various spacings

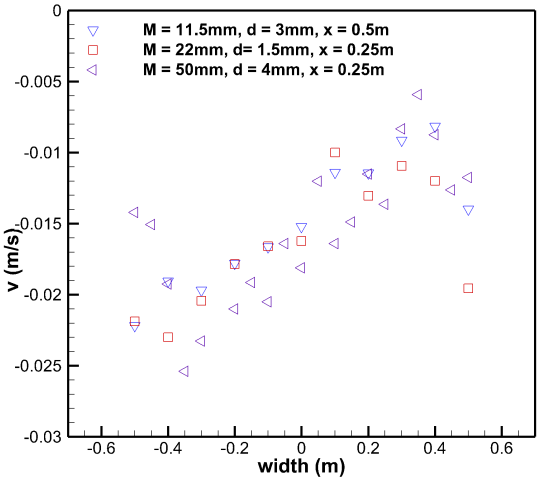

Figure 2.12: The vertical velocity downstream of grids of various spacings

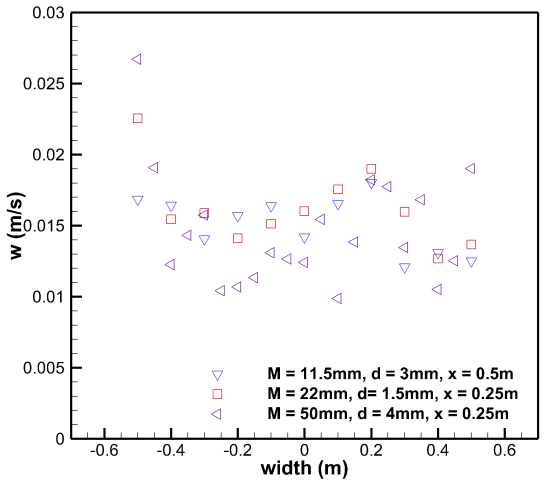

Figure 2.13: The spanwise velocity downstream of grids of various spacings

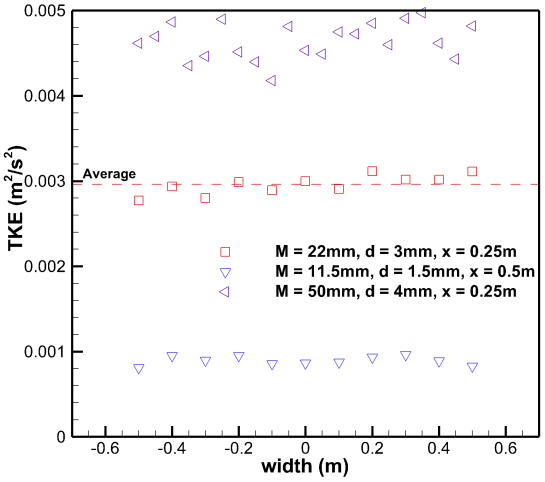

Figure 2.14: The TKE at downstream of grids of various spacings

velocities, shown in figures 2.12 and 2.13 respectively, are always less than 2.5% of the streamwise flow, showing that the flow is still essentially one-dimensional (i.e. one mean velocity component is much larger than the other two components) across the width of the channel (cf. figure 2.9 in uniform flow). The variation across the channel width of these components is very small and is a consequence of the impeller creating the flow in the channel and is observed without the grid in place too. The TKE downstream of the grids are shown in figure 2.14; the values for the grids where $M = 11.5mm$ and $M = 22mm$ do vary up to 10% of the average TKE value which is reasonable due to the combination of the measuring technique, the nominal differences in the channel and the effects of the grid, whereas the mesh with $M = 50mm$ varies three times more than the other meshes across the width. In addition to measurements across the channel, the ADV was used to take velocity measurements through the water depth downstream of the meshes. The mean streamwise velocity, shown in figure 2.15, is uniform through the depth for all the meshes. This result is in agreement with the streamwise velocity measurements across the width of the channel shown in figure 2.11. However, it is noted that there are some free-surface effects, which caused the velocity to be greater near the surface for the grids with $M = 22mm$ and $M = 50mm$ at $0.25m$ downstream, and slower for the other conditions. This free-surface effect can be explained by the formation of a standing wave by the large blockage of the grid; to try to combat this the velocity at the surface was decreased by reducing the jet-box flow setting to 200 and the results shown are with the optimum channel set-up for all the meshes. The flow is seen to be essentially one-dimensional as both the vertical and spanwise velocities, shown in figures 2.16 and 2.17, were less than 2.5% of the streamwise velocities. It is observed in figure 2.18 that there is some variation of the TKE through the depth of the channel. The TKE, in figure 2.18, is always greater near to the floor of the channel, this variation is small when $M = 11.5mm$ and $22mm$, but the variation is greater for $M = 50mm$, which

has a bigger impact on the flow. From these results it was decided that the grid to be used was the $M = 22mm$ grid as this increased the levels of turbulence within the flow without effecting the uniformity, particularly at the position where the turbine is placed at $0.25m$ downstream of the grid. This grid increased the turbulence intensity to approximately 5% from the nominal channel level of 2%, where TI is defined in equation 1.8. The spanwise measurements were taken at a depth of $0.4m$ in the centre of the channel, the mean streamwise velocities are shown in figure 2.11. It can be seen that the velocities with the meshes where $M = 11.5mm$ and $22mm$, varied between $\pm 1\%$ of the mean across the channel, showing that the grid had little effect on the uniformity of the flow. However, the velocities for the mesh with $M = 50mm$ varied $3 - 4\%$ across the channel, even though the measurement was further downstream than for the other meshes as close to the grid the variations were much greater. These variations correspond to the wire causing a blockage and reducing the mean flow directly downstream and the flow being greater where the wire is not present, this is more prominent with larger wire diameters. The vertical and spanwise mean velocities, shown in figures 2.12 and 2.13 respectively, are always less than 2.5% of the streamwise flow, showing that the flow is still essentially one-dimensional (i.e. one mean velocity component is much larger than the other two components) across the width of the channel (cf. figure 2.9 in uniform flow). The variation across the channel width of these components is very small and is a consequence of the impeller creating the flow in the channel and is observed without the grid in place too. The TKE downstream of the grids are shown in figure 2.14; the values for the grids where $M = 11.5mm$ and $M = 22mm$ do vary up to 10% of the average TKE value which is reasonable due to the combination of the measuring technique, the nominal differences in the channel and the effects of the grid, whereas the mesh with $M = 50mm$ varies three times more than the other meshes across the width. In addition to measurements across the channel, the ADV was used to take velocity measurements through the water

depth downstream of the meshes. The mean streamwise velocity, shown in figure 2.15, is uniform through the depth for all the meshes. This result is in agreement with the streamwise velocity measurements across the width of the channel shown in figure 2.11. However, it is noted that there are some free-surface effects, which caused the velocity to be greater near the surface for the grids with $M = 22mm$ and $M = 50mm$ at $0.25m$ downstream, and slower for the other conditions. This free-surface effect can be explained by the formation of a standing wave by the large blockage of the grid; to try to combat this the velocity at the surface was decreased by reducing the jet-box flow setting to 200 and the results shown are with the optimum channel set-up for all the meshes. The flow is seen to be essentially one-dimensional as both the vertical and spanwise velocities, shown in figures 2.16 and 2.17, were less than 2.5% of the streamwise velocities. It is observed in figure 2.18 that there is some variation of the TI through the depth of the channel. The TI levels are always greater near to the floor of the channel, this variation is fairly small when $M = 11.5mm$ and $22mm$, but the variation is greater for $M = 50mm$, which has a bigger impact on the flow. From these results it was decided that the grid to be used was the $M = 22mm$ grid as this increased the levels of turbulence within the flow without effecting the uniformity, particularly at the position where the turbine is placed at $0.25m$ downstream of the grid. This grid increased the turbulence intensity to approximately 5% from the nominal channel level of 2%. It is however noted that with the method of turbulence production the turbulence does decay downstream rapidly other methods to produce turbulence that does not decay so rapidly require longer channels which allow turbulence to develop were not possible for the channel used in this study.

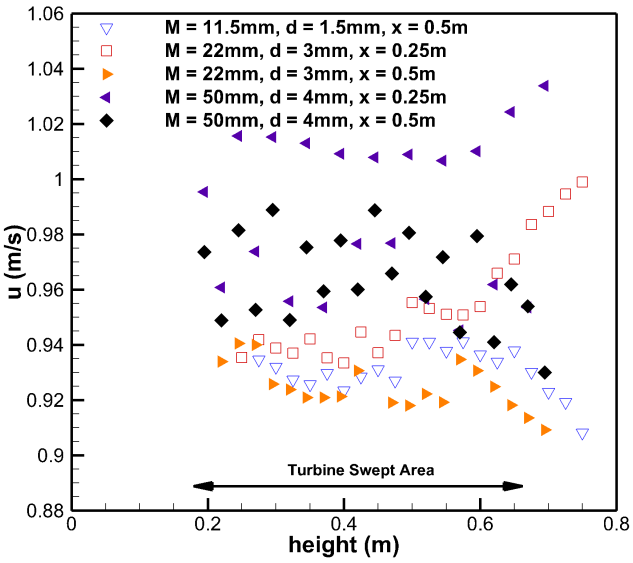

Figure 2.15: The streamwise velocity downstream of the grid through the depth of the channel

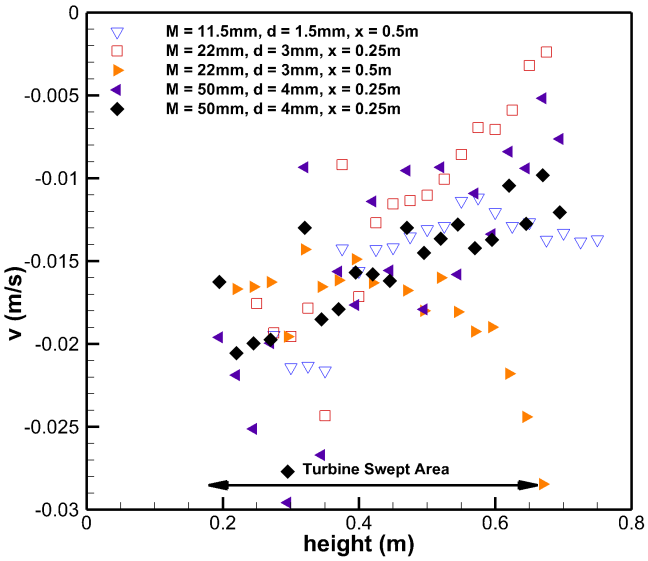

Figure 2.16: The vertical velocity downstream of the grid through the depth of the channel

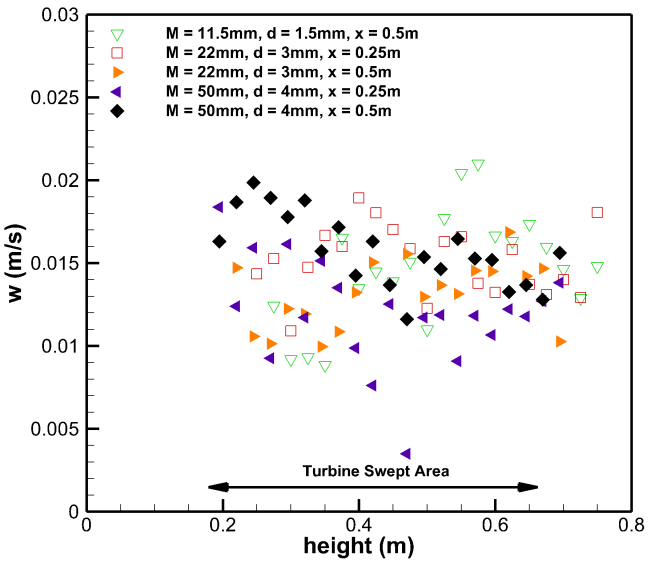

Figure 2.17: The spanwise velocity downstream of the grid through the depth of the channel

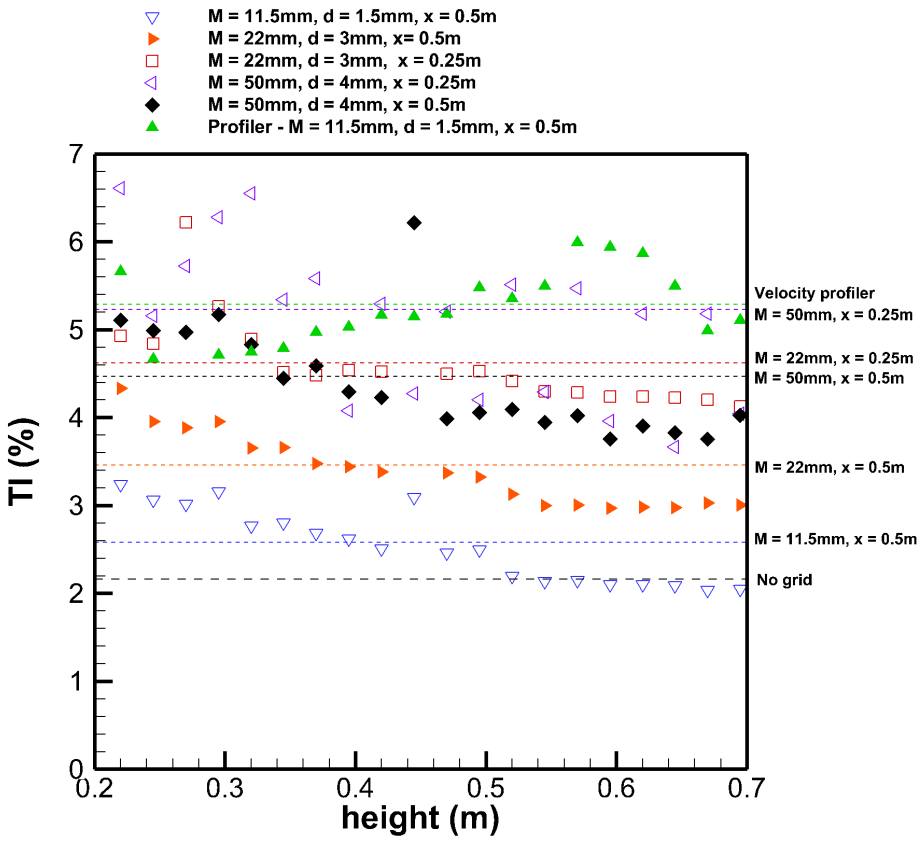

Figure 2.18: The TI levels downstream of the grid through the depth of the channel (dashed lines denote average through the depth)

2.7 Velocity Profiler - Characterisation of Flow

To represent more realistic 'at-sea' flow conditions it is important to investigate the effects of a non-uniform steady flow. A $\frac{1}{5}th$ power-law profile was therefore produced within the high-speed water-channel and is now discussed.

2.7.1 Design of velocity profiler

A velocity profile within the high-speed water-channel was produced by placing a series of horizontal bars at differing depths using the method used by Cockrell & Lee (1966) from wind tunnel experiments. This method arises from basic theory by Elder (1959). A discussion on how this velocity profile is produced can be found in Appendix B.

2.7.2 Characterisation of flow downstream of the flow profiler

To reduce the wakes shed by the individual bars in the flow profiler, a mesh was placed across the channel directly downstream of the horizontal bars. Four different meshes (different wire spacing, M, and wire diameter, d) were tested and the resulting flow was measured using the ADV. The four square meshes tested were:

- $M = 19mm$, $d = 3mm$,
- $M = 12.4mm$, $d = 1.6mm$,
- $M = 6mm$, $d = 0.71mm$,
- $M = 1.75mm$, $d = 0.5mm$.

Figure 2.19 shows the velocity measured through the depth of the channel at $1m$ downstream of the flow profiler with different meshes. It can be seen that the mesh alters the power law produced by the flow profiler and change

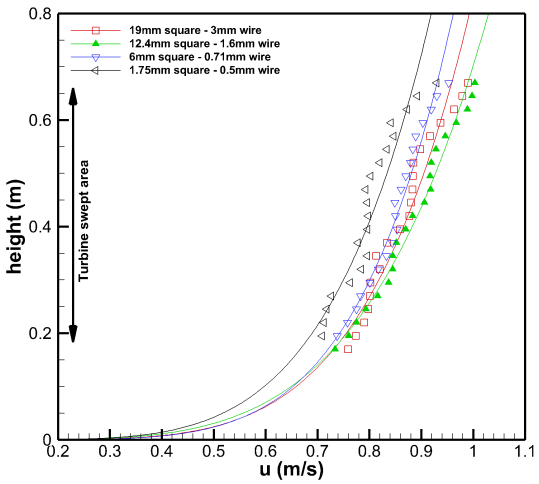

Figure 2.19: Measured velocity profiles $1m$ downstream of the flow profiler with different size meshes (dial setting constant)

the average velocities due to the difference in blockage by each mesh (note that these were all measured with the same water-channel settings). The flow profiler was designed to fitted by a $\frac{1}{7}th$ power law, but the mesh had an impact on the downstream measured profile that slightly modified the power-law velocity profile measured. The mesh with $M = 6mm$ and $d = 0.71mm$ was chosen as it had the best resemblance to a power law, a photograph of the final set-up of the flow profiler is shown in figure 2.20.

Figure 2.21 shows the measured streamwise velocity at five different spanwise locations $1m$ downstream of the flow profiler allowing the wakes from the individual bars to be minimal. The streamwise velocity profiles were measured across the width of the channel at the centre of the channel and at ± 0.5 and ± 1 turbine diameters (D) across the channel. These results confirm that the flow is the same across the width of the channel and therefore essentially two-dimensional (i.e. changes only through the depth of the channel). The measured streamwise velocity profile is fitted with a 1/5th

Figure 2.20: Photograph of the flow profiler

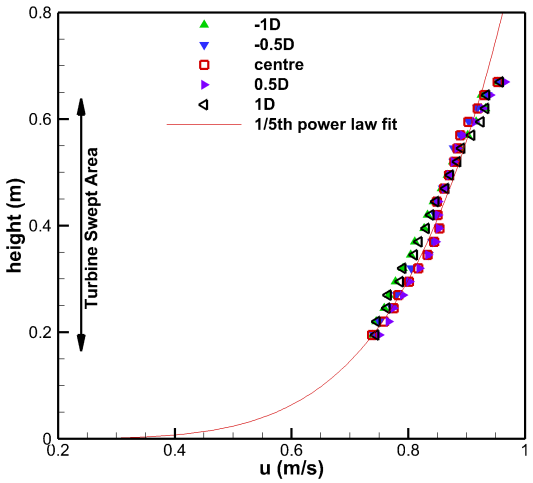

Figure 2.21: Measured velocity at various distances across the channel $1m$ downstream of the flow profiler

power-law and has an integral average upstream velocity of $0.82m/s$ over the swept area of the turbine, which is defined by;

$$\bar{U} = \int_{H-R}^{H+R} \frac{2U(h)\sqrt{R^2 - (h-H)^2}}{\pi R^2} dh. \tag{2.4}$$

The average Turbulence Intensity (equation 1.8) at $1m$ downstream of the flow profiler,with the selected grid $M = 6mm$ and $d = 0.71mm$, was found to be $\approx 5\%$, which is similar as the TI produced downstream of the grid, which was seen previously in figure 2.18.

2.8 Power and Thrust Measurements

Power and thrust measurements were taken in all three flow conditions:

- uniform flow with low TI ($\approx 2\%$),
- uniform flow with high TI ($\approx 5\%$),
- and non-uniform flow with high TI ($\approx 5\%$).

In uniform flow with low TI the number of blades is altered between two and six and different blade-pitch-angles were tested. Before proceeding onto a discussion of these results it is firstly shown how the non-dimensional quantities given in chapter 1 arise (equations 1.1 - 1.3).

2.8.1 Non-dimensional analysis

Considering any HATT with a characteristic radius R, rotating with an angular velocity ω, which is submerged in a fluid with dynamic viscosity μ, density ρ and is moving with a characteristic velocity of U. The power output from the turbine is therefore a function, f, of these variables:

$$P = f(R, \omega, \mu, \rho, U), \tag{2.5}$$

Using the Buckingham Pi theory the relationship between power and the variables can be expressed through three non-dimensional groups:

$$\frac{P}{\rho R^2 V^3} = f\left(\frac{\rho U R}{\mu}, \frac{\omega R}{U}\right). \tag{2.6}$$

These groupings are more conventionally expressed as the power coefficient:

$$C_P = \frac{P}{\frac{1}{2}\rho A U^3}, \tag{2.7}$$

Reynolds number:

$$Re_F = \frac{UR}{\nu}, \tag{2.8}$$

where $\nu = \frac{\mu}{\rho}$ is the kinematic viscosity, and tip-speed-ratio is defined:

$$\lambda = \frac{\omega R}{U}. \tag{2.9}$$

A second definition of the Reynolds number can be identified by using the relationship $\lambda Re_F = Re_\omega$, resulting in Reynolds number based on the velocity at the blade tip as:

$$Re_\omega = \frac{\omega R^2}{\nu}. \tag{2.10}$$

It is important to note that the inclusion of constants e.g. $1/2$ and π do no change the dimensionless form of the groups, but just allow for conventional engineering forms. Therefore the relationship, from equation 2.5, is equivalent to:

$$C_P = f(Re_F, \lambda), \tag{2.11}$$

In a similar manner the non-dimensional thrust coefficient is:

$$C_T = \frac{T}{\frac{1}{2}\rho A U^2}, \tag{2.12}$$

and has the relationship:

$$C_T = f_1(Re_F, \lambda). \tag{2.13}$$

Usually for turbomachines, as long as the Reynolds number is sufficiently high, a weak dependence on Reynolds number is assumed (Wright, 1999) and then C_P and C_T are assumed to be functions of λ alone. In such cases data on model turbines can be used directly for estimations of full-scale turbines even in the absence of exact Reynolds number matching (which is necessary for full dynamic similarity). The Reynolds number ranges for the model experiments reported here are shown in Table 2.1 where it can be seen that based on upstream velocity they are of the order of 10^5 and of the order of 10^6 based on tip speed ratio. The limited data available to date for HATTs (Bahaj et al., 2006) would seem to indicate that Reynolds number effects at these values are small.

In addition when waves or free-surface effects are significant the Froude number is considered, this can be based on the diameter of the turbine,

$$Fr_D = \frac{U}{\sqrt{gD}}, \tag{2.14}$$

or on the depth $(H - h)$ at which the turbine is placed,

$$Fr_h = \frac{U}{\sqrt{g(H-h)}}. \tag{2.15}$$

In a confined channel blockage must also be considered as this can alter the tip-speed-ratio, power and thrust coefficients depending on the ratio of the turbine swept area to the channel area. Methods can be applied to correct for blockage, e.g. Bahaj et al. (2006) and Garrett & Cummins (2007), to calculate the estimated power and thrust in an unconfined channel.

Table 2.1: Comparison of Reynolds number and Froude number for different turbine arrangements

Number of Blades	Blade Pitch Angle	$U(m/s)$	Re_ω	Re_F	Fr_D	Fr_h
2	$3^o, 6^o, 9^o$	0.45-1.34 m/s	3×10^5- 3.1×10^6	1.1×10^5- 3.4×10^5	0.20 - 0.61	0.22 - 0.66
3	$3^o, 6^o, 9^o$	0.45-1.34 m/s	4.7×10^5-2.7×10^6	1.1×10^5- 3.4×10^5	0.20 - 0.61	0.22 - 0.66
4	9^o	0.45-1.34 m/s	6.6×10^5-2.4×10^6	1.1×10^5- 3.4×10^5	0.20 - 0.61	0.22 - 0.66
6	12^o	0.9-1.1 m/s	9.3×10^5-1.7×10^6	2.2×10^5- 2.8×10^5	0.41 - 0.50	0.44 - 0.54

2.8.2 Power Measurements in Uniform Flow

A number of experiments have been undertaken to investigate the performance of the model HATT, where the number of blades and blade pitch angle were varied. The initial experiments were undertaken at various mean velocities in uniform flow with a low turbulence intensity. Although experiments such as these have been well documented for HATTs of similar scale (e.g. Bahaj et al., 2006), as a first step this set-up is important to ensure controlled and accurate data was obtained. These experiments also provided a data-set which can be compared to the well developed CFD model of the HATT (Mason-Jones, 2010). From the CFD results of Mason-Jones (2010) the optimum pitch-angles for 2, 3 and 4 bladed versions were shown to be 3^o, 6^o and 9^o respectively. For each experiment the water channel was set to the desired free-stream velocity (U) and the turbine was allowed to free-wheel, where no torque was applied, before a resistive current was applied and the rotational speed and current was logged five times for $10s$, giving 5000 samples at each torque. The torque was increased incrementally until the turbine rotated backwards or motor cut-out occurred ($2.82A$ or a peak torque $\approx 2.3Nm$). This meant that the experiments started with high tip speed ratio and as the torque increased, tip speed ratio and Re_ω ($= \lambda \times Re_F$) decreased. Due to motor cut out, for higher water velocities peak power extraction was not always possible, therefore in some cases peak C_P was not always reached.

As the blockage ratio is 18% and resulting power coefficients are found to be close to the Betz limit, it is common for a correction to be applied, such as the methods of Bahaj et al. (2006) and Garrett & Cummins (2007). Due to non-physical results, as discussed in section 2.8.4, no correction for blockage is applied to any of the data presented in this thesis. Despite the lack of blockage correction this study has provided a benchmarking data-set that was compared directly to CFD models of the turbine in the channel (Mason-Jones et al., 2012).

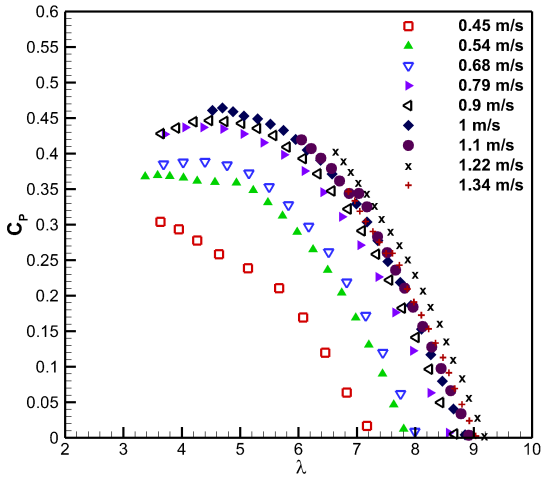

Figure 2.22: Comparison of the effect of velocity on power coefficient of a two-bladed turbine with optimum blade pitch angle (3^o)

Figure 2.22 shows the power coefficient data for the two-bladed configuration with the optimum 3^o blade-pitch-angle, at a series of different velocities. C_P collapses for $U > 0.79m/s$ (corresponding to $Re_F > 2 \times 10^5$) this represents the threshold at which the Reynolds number effect is small. In this case the peak power coefficient is approximately 0.47, which is considered high but this is due to the effect of blockage. For the two bladed turbine with a higher blade-pitch-angles, 6^o and 9^o, shown in figure 2.23, the peak power is lower (≈ 0.44) in both cases. At off-optimum blade-pitch-angle of 6^o there is more scatter in this data, any Reynolds number effect is essentially negligible beyond $0.45m/s$. However for the 9^o blade-pitch-angle there is considerably more spread of the data, suggesting that Reynolds number has a greater effect at the higher blade-pitch-angle.

For the three-bladed set-up, three different configurations were used, with blade pitch angles of 3^o, 6^o (optimum) and 9^o. At the optimum condition, figure 2.24, a Reynolds number effect can be seen below $U = 0.79\ m/s$, for

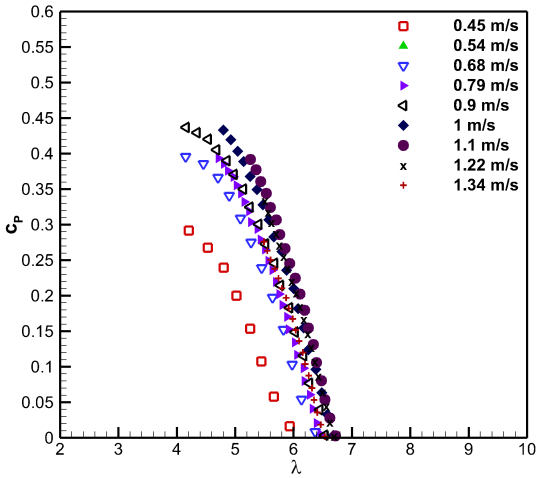

(a) 6^o blade pitch angle

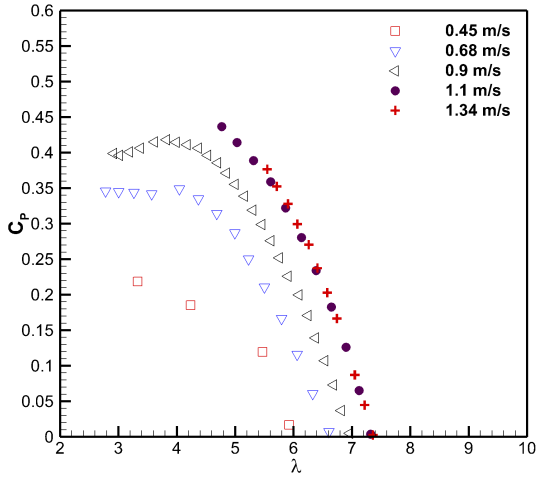

(b) 9^o blade pitch angle

Figure 2.23: Comparison of the effect of velocity on power coefficient of a two-bladed turbine

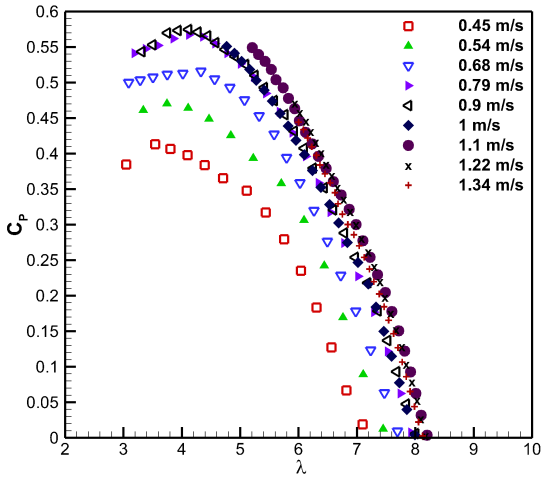

Figure 2.24: Comparison of the effect of velocity on power coefficient of a three-bladed turbine with optimum blade pitch angle (6^o)

data above this Reynolds number collapse of the data can be seen. This data indicates that the model HATT used in this study should be tested at $Re_F > 2 \times 10^5$ for any Reynolds effect to be small. The maximum power coefficient of approximately 0.56 is higher than previous studies (e.g. Bahaj et al. (2006)) because of effects of blockage (18%). Moving to non-optimum conditions, figure 2.25 indicate, as expected, a reduced power extraction.

Figures 2.26 and 2.27 show the power coefficient for the four- and six-bladed configuration with optimum blade-pitch-angles (9^o and 12^o respectively). The trends are similar to those of the two- and three-bladed configurations at optimum angles.

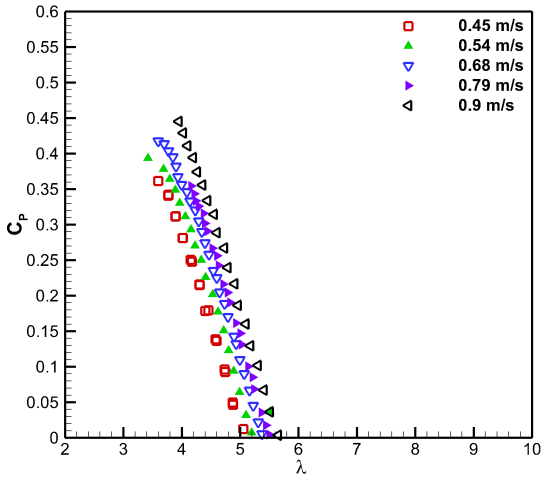

(a) 3^o blade pitch angle

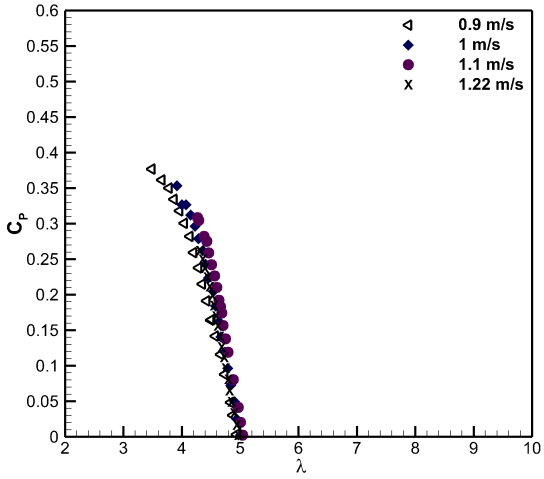

(b) 9^o blade pitch angle

Figure 2.25: Comparison of the effect of velocity on power coefficient of a three-bladed turbine

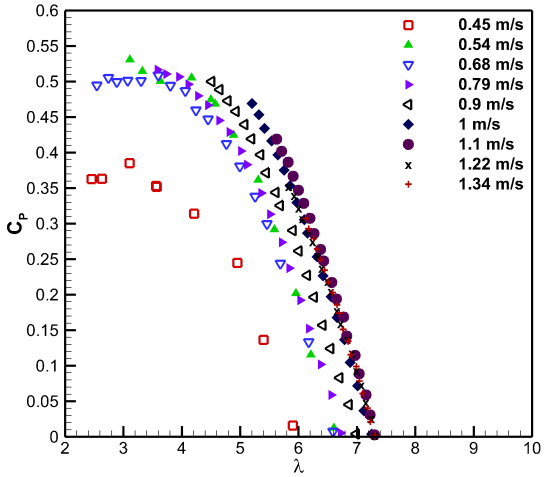

Figure 2.26: Comparison of the effect of velocity on power coefficient of a four-bladed 9^o blade pitch angle

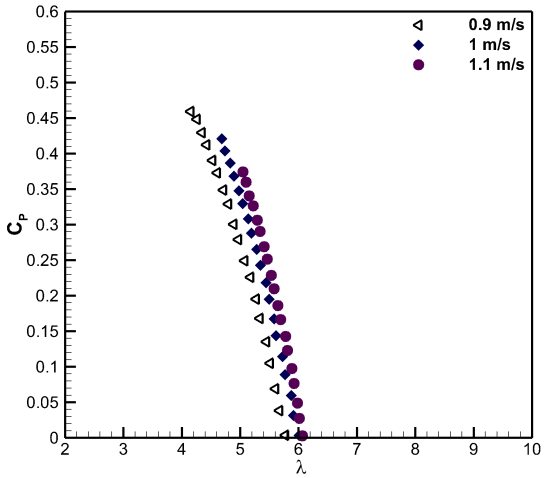

Figure 2.27: Comparison of the effect of velocity on power coefficient of a six-bladed 12^o blade pitch angle

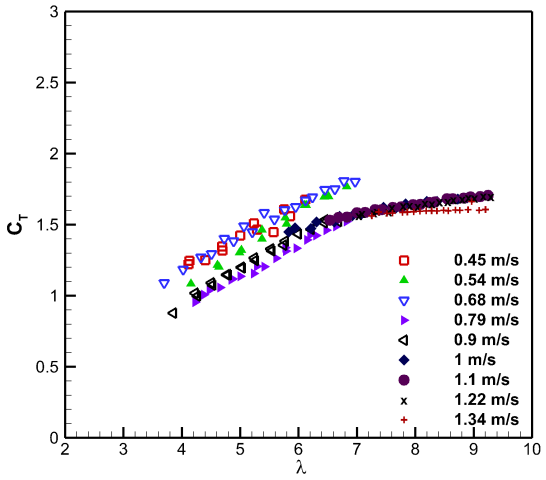

Figure 2.28: Comparison of the effect of velocity on thrust coefficient of a two-bladed turbine with optimum (3^o) blade pitch angle

2.8.3 Thrust Measurements

In addition to power measurements, thrust on tidal turbines have been extensively studied (e.g. Bahaj et al., 2006). Again these tests were completed to compare with CFD simulations by Mason-Jones (2010) and have not been corrected for blockage. The same configurations were tested to that of the power measurements. It is important to note that the force measured was that of the whole turbine structure including the support stanchion, turbine body and hub. Therefore care should be taken when comparing directly to other studies in the literature where C_T is measured directly from forces on the blades (Bahaj et al., 2006).

Figures 2.28 and 2.29 show the thrust coefficients for the two bladed turbine. The data collapses in both these cases and there are no obvious Reynolds number trends. For the optimum angle (3^o, figure 2.28), the thrust coefficient is lower at approximately 1.5 at its peak at free wheeling, whereas at 6^o (figure 2.29(a)) there is a higher thrust coefficient (approximately 2.5)

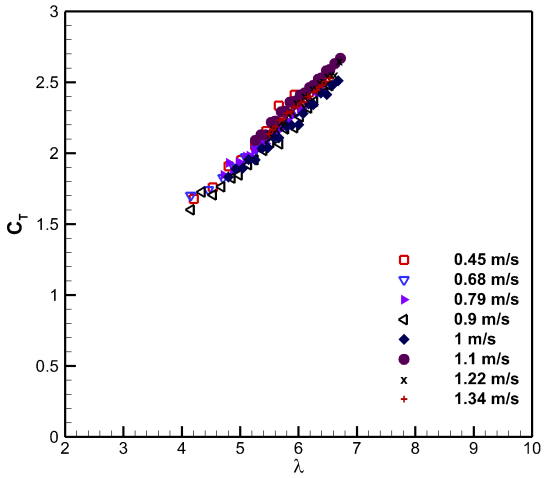

(a) 6^o blade pitch angle

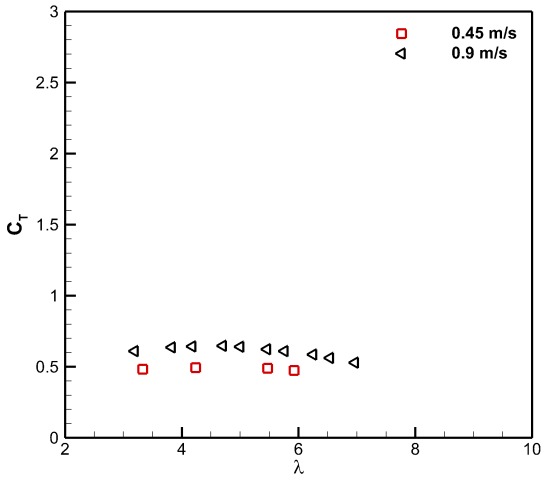

(b) 9^o blade pitch angle

Figure 2.29: Comparison of the effect of velocity on thrust coefficient of a two-bladed turbine at non-optimum blade pitch angles

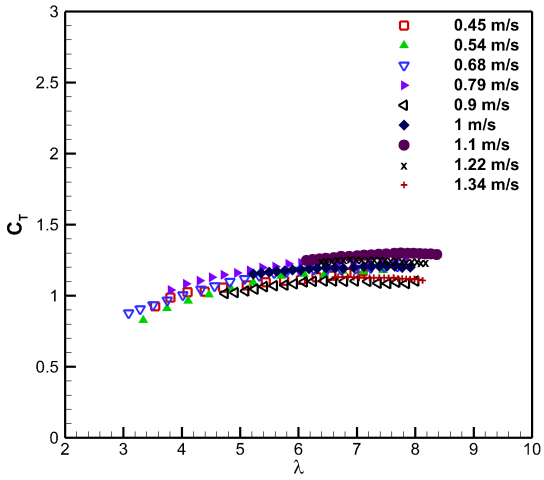

Figure 2.30: Comparison of the effect of velocity on thrust coefficient of a three-bladed turbine with optimum blade pitch angle (6^o)

at free-wheeling. There is a reduction in thrust at 9^o, which is consistent with the study by Mason-Jones (2010) using CFD, shown in figure 2.29(b) where at $0.9m/s$ the thrust coefficient is reduced to a peak at approximately 0.5.

Figures 2.30 and 2.31 show the thrust coefficients for the three bladed turbine. Similarly to the two bladed, the three bladed turbine at optimum angle has a lower thrust coefficient – around 1.2 – compared to around 2 at 3^o and 9^o. The thrust coefficient for the four- and six-bladed turbine are shown in figures 2.32 and 2.33, the data has some scatter but are consistent with the two- and three-bladed turbine.

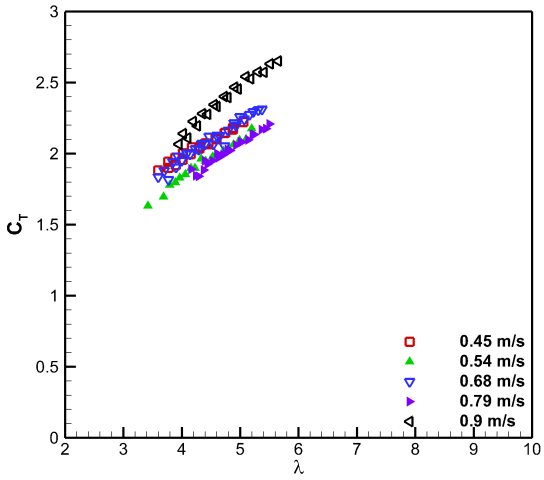

(a) 3^o blade pitch angle

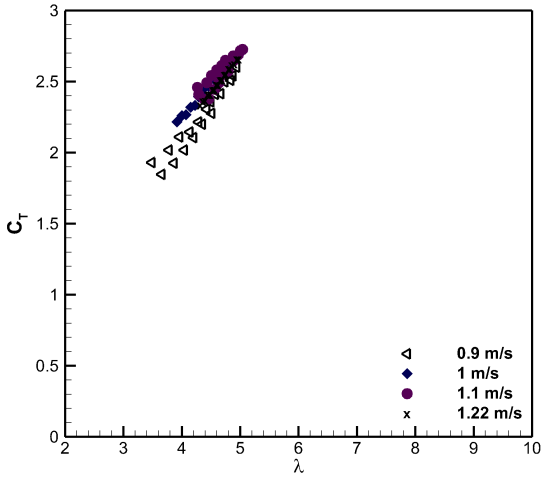

(b) 9^o blade pitch angle

Figure 2.31: Comparison of the effect of velocity on thrust coefficient of a three-bladed turbine

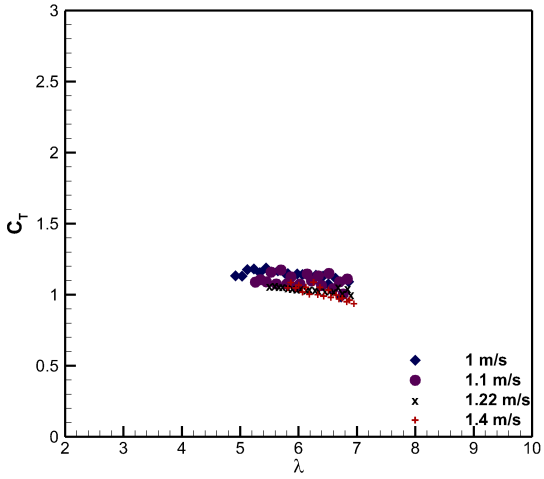

Figure 2.32: Comparison of the effect of velocity on thrust coefficient of a four-bladed 9^o blade pitch angle

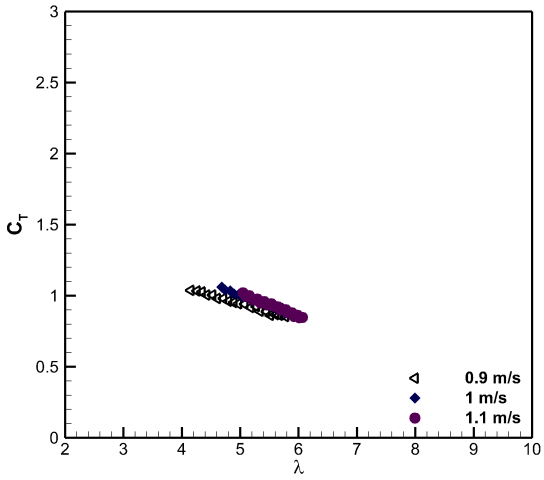

Figure 2.33: Comparison of the effect of velocity on thrust coefficient of a six-bladed 12^o blade pitch angle

2.8.4 Blockage Correction

The $0.5m$ diameter turbine with swept out area $0.2m^2$ and channel area $1.12m^2$ causes a blockage ratio of 0.18. A number of studies have been conducted to resolve issues surrounding blockage effect on power and thrust coefficients in a restricted channel (Bahaj et al., 2006, Garrett & Cummins, 2007, Whelan et al., 2009, Chen & Liou, 2011 and Consul et al., 2013. These blockage corrections are shown as an analytical approach, where they have been applied to numerical studies (BEM and CFD) and experimental results of porous discs (Whelan et al., 2009) primarily. Bahaj et al. (2006) applied this method to measurements of a tidal turbine in a cavitation tunnel and the same method used here: details are given in Appendix C. All of these methods use the assumption of an actuator disc model of the flow through the turbine where the velocity and pressure far upstream are presumed to be uniform across the channel. In addition the velocity through the turbine and directly downstream is taken to be uniform; which indeed is incorrect as swirling components are neglected (Garrett & Cummins, 2007) and as demonstrated in the next chapter, the flow directly downstream of the turbine is far from uniform and contains swirling motions from the rotation of the blades. Following the methods of Bahaj et al. (2006) (shown in Appendix C) the blockage factor $\frac{U_T}{U_F}$ (the ratio of free-stream water-channel velocity, U_T, to the unbounded free-stream velocity, U_F) was calculated using the principles of continuity, momentum and energy by means of an iterative process. Using this calculated blockage factor the corrected tip-speed-ratio, power coefficient and thrust coefficient for the two- and three-bladed turbine configurations

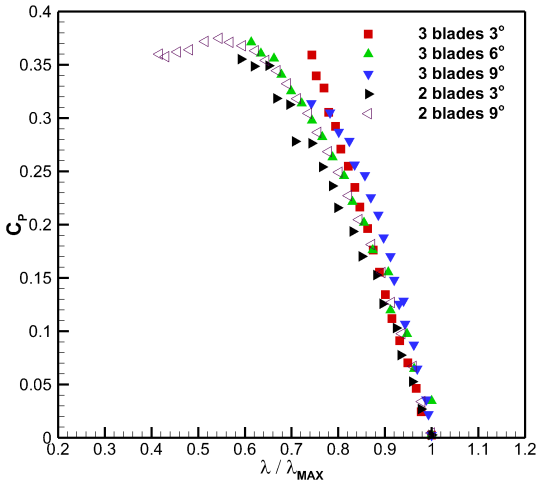

Figure 2.34: Power coefficient for different turbine configurations with blockage correction applied

were corrected as following:

$$C_{P_F} = C_{P_T} \left(\frac{U_T}{U_F} \right)^3, \tag{2.16}$$

$$C_{T_F} = C_{T_T} \left(\frac{U_T}{U_F} \right)^2, \tag{2.17}$$

$$\lambda_F = \lambda_T \left(\frac{U_T}{U_F} \right). \tag{2.18}$$

In figure 2.34 the corrected power coefficient is plotted in terms of normalised (by its maximum) tip-speed-ratio at $0.9m/s$ for all turbine blade configurations. By normalising the tip-speed-ratio by its maximum the data is seen to collapse for all turbine configurations and there is no difference in peak power. In fact it is observed that for the two-bladed turbine at 9^o blade-pitch-angle (non-optimum) peak C_P is greater than with a 3^o blade-pitch-angle (optimum). From these results one could conclude that the blade-

pitch-angle does not effect the power output, however we know that this is not correct and this result suggests that this method fails for non-optimum blade-pitch-angles. Therefore it is concluded that this method for correcting for blockage is unsuitable for a turbine set with non-optimum conditions as it does not take into consideration the blade shape. Given this issue, all the results in this thesis are shown without a blockage correction applied.

2.8.5 Power and thrust in uniform and non-uniform steady flows

The power and thrust of the turbine were measured in uniform and non-uniform flow. Both inlet conditions had an average velocity ($\bar{U}$) of $0.82m/s$; mean for uniform flow conditions and integral average over the turbine swept area for non-uniform flow conditions. When plotted non-dimensionally, using the integral average velocity, the output power and thrust in both the uniform flows ($TI \approx 2\%$ and 5%) and the non-uniform flow are seen to collapse reasonably well onto single characteristic curves in figures 2.35(a) and 2.36(a). This data collapse is an important and useful result and is not shown when using the mean velocity at hub height in figures 2.35(b) and 2.36(b). It shows that in non-uniform flows the power output and thrust of the turbine can be obtained from known characteristics, obtained in either uniform or non-uniform flows, by using the integral area averaged velocity, defined in equation 2.4. Additionally it was found that using the integral average definition of Fleming et al. (2013), which integrates over the velocity squared and cubed for the thrust coefficient and power coefficient respectively, was in agreement to 0.1% with using the integral average velocity to calculate C_P and C_T. The observation of this collapse is consistent with the computational results obtained independently by both Mason-Jones et al. (2012) and Fleming et al. (2013). It is also seen in figures 2.35 and 2.36 that the additional turbulence in the flow does not have a significant effect on the power and thrust at these levels ($TI \approx 2\%$ and 5%).

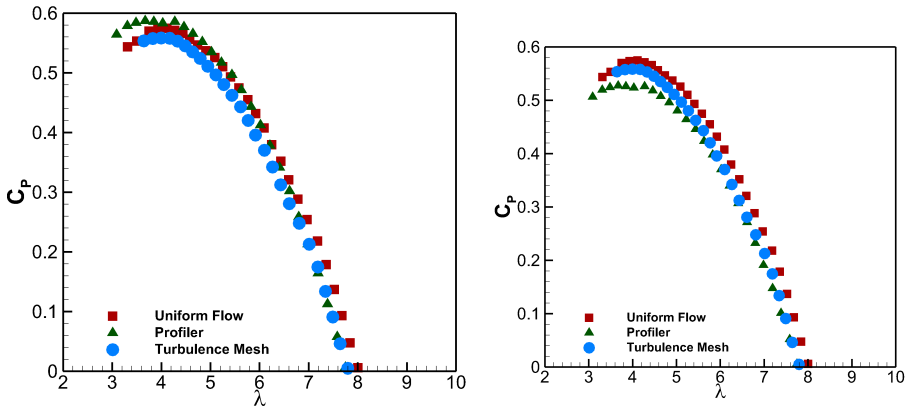

(a) Integral average (b) Mean

Figure 2.35: Comparison of power coefficient in uniform and non-uniform steady flow

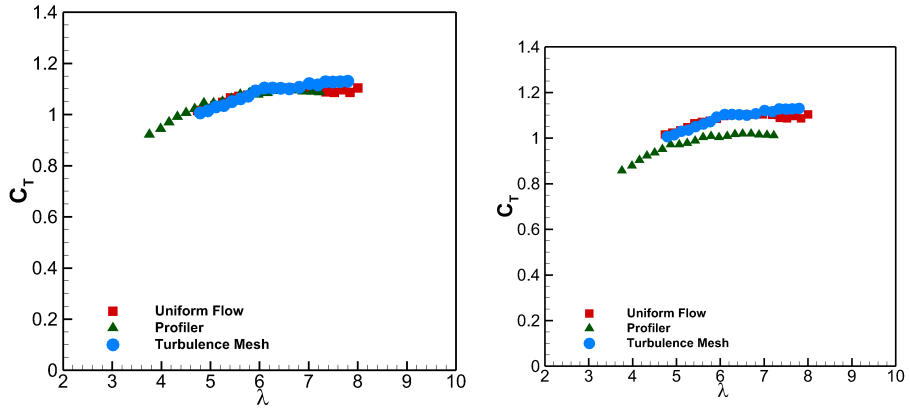

(a) Integral average (b) Mean

Figure 2.36: Comparison of thrust coefficient in uniform and non-uniform steady flow

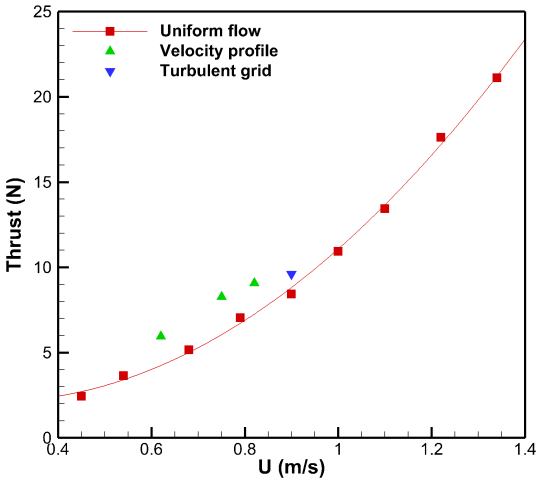

Figure 2.37: Comparison of thrust on turbine without blades in uniform and non-uniform steady flow

2.8.6 Thrust on turbine structure with no blades

To estimate the contribution of the support structure and hub of the turbine thrust measurements were taken without blades. These thrust measurements were taken in the three different flow conditions at different velocities; the results are shown in figure 2.37 . For the three flow conditions there is agreement, showing that the thrust on the turbine body and support increases with a squared relationship with velocity (suggesting a drag coefficient of approximately 0.9 - i.e. 10% of C_T at optimum blade-pitch-angle).

2.9 Chapter Summary

In this chapter the experimental arrangement has been detailed including all facilities and instrumentation used in this thesis. A number of different flow conditions were produced in the high-speed water-channel and the three-dimensional velocities were characterised using ADV. Furthermore power and

thrust measurements on the turbine were completed, initially in uniform flow conditions with low turbulence intensity ($\approx 2\%$), for different numbers of blades and blade-pitch-angles. Optimum blade-pitch-angles were found confirming CFD results of Mason-Jones (2010). It was also found that at velocities $< 0.78m/s$ the power coefficient was dependent on Reynolds number and is therefore suggested that experimental studies should be conducted at Reynolds numbers above $2\text{x}10^5$. Additionally measurements were collected of power and thrust on the three-bladed turbine with optimum blade-pitch-angle (6^o) in the three different flow conditions, uniform with low TI (2%), high TI (5%) and non-uniform flow with high TI (5%). Collapse of power and thrust coefficients were found when plotted non-dimensionally using the upstream integral average velocity. Having characterised the power and thrust on the turbine the next step is to characterise the flow field around the turbine.

Chapter 3

Characterisation of Wake in Uniform Flow

Having characterised the power and thrust coefficients for the different turbine configurations, a crucial next step is to characterise the effect of the turbine on the surrounding flow. In this chapter the wake downstream of the turbine is characterised in uniform flow with a low turbulence intensity (of 2% measured using the ADV). The first approach investigated the wake downstream of the three bladed turbine with optimum blade pitch angle (6^o) at a velocity at which the power coefficient is not Reynolds number dependent (i.e. $U = 0.9m/s$) (see section 2.8.2). Further, the effect of low Reynolds number on the wake is considered as many studies to date have investigated wake characteristics at low Reynolds number (e.g. Harrison et al., 2010 and Stallard et al., 2013). In addition, the effect of number of blades and blade-pitch-angles on the wake is considered, to examine the difference of off- and on-optimum blade-pitch-angles arrangements.

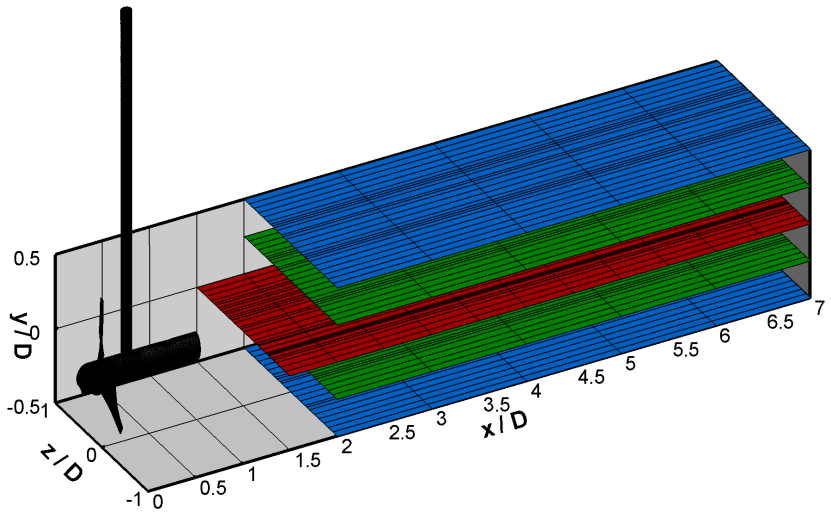

Figure 3.1: Wake measurement locations downstream of the turbine

3.1 Three-Bladed Turbine

The three-bladed turbine arrangement, which is considered the most common set-up for tidal stream turbines (see chapter 1), was used to characterise the surrounding flow. Firstly, it was important to characterise the flow field that the turbine is subject to, thus flow velocity measurements using the ADV (detailed in 2.4). The near-wake was measured at five different depths (transverse distances) at a number of streamwise distances behind the turbine; from $1.5D$ behind the turbine to $7D$, and across the width of the channel at least every $50mm$, where the origin is defined at the point where the blades meet in the centre of the hub. These downstream measurement locations and the origin are illustrated in Figure 3.1.

For all the measurements of the flow surrounding the three-bladed turbine, the optimum blade pitch angle was set (6^o). The torque was set to 20% of the motor's maximum torque and the upstream streamwise velocity to $0.9m/s$. These conditions resulted in power coefficient $C_P = \frac{P}{1/2\rho AU^3} = 0.34$, tip-speed-ratio $\lambda = \frac{\omega R}{U} = 6.15$, thrust coefficient $C_T = \frac{T}{1/2\rho AU^2} = 1.00$ (this

value was determined by measuring the force on the whole turbine structure - including body and support - and then subtracting the drag of the body and support alone without blades at identical upstream velocities and will be stated in this manner throughout the wake sections of this thesis) and Reynolds number based on the turbine radius $Re_F = \frac{UR}{\nu} = 2.22$ x 10^5.

3.1.1 Upstream of the turbine

Upstream measurements were taken at distances of $0.25m$ ($0.5D$), $0.5m$ ($1D$) and $1m$ ($2D$) in the spanwise direction across the width of the flume every $50mm$ and at $1m$ ($2D$) through the depth. to determine any potential blockage effect on the velocity, and to confirm the uniformity and low turbulent nature of the flow. Measurements at the centreline are shown across the width at $0.5D$, $1D$ and $2D$ upstream in figure 3.2 and through the depth at $2D$ upstream in figure 3.3. At $1D$ and $2D$ upstream of the turbine mean velocities in the streamwise, vertical and spanwise directions are constant across the width of the channel and are within 1% of the mean streamwise velocity. However, at $0.5D$ upstream the turbine causes the flow to decrease slightly at the centre of the channel and accelerate around the outside of the turbine, this is most visible in the mean streamwise component. The mean vertical and spanwise velocities, shown in figures 3.2 (b) and (c), are near to zero and are, at most 7% of the streamwise component across the channel width where small velocities can be attributed to the pre-swirl in front of the turbine.

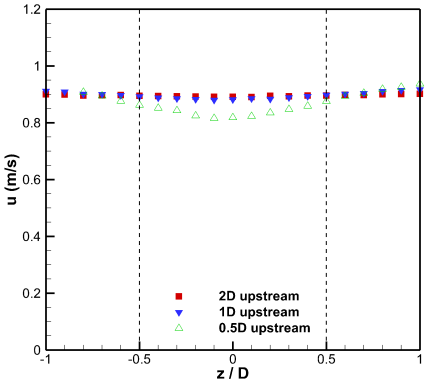

(a) Streamwise velocity upstream of turbine at centre height

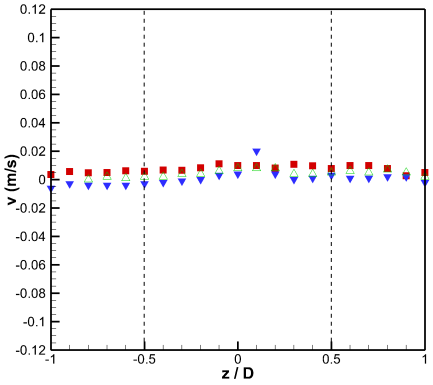

(b) Vertical velocity upstream of turbine at centre height

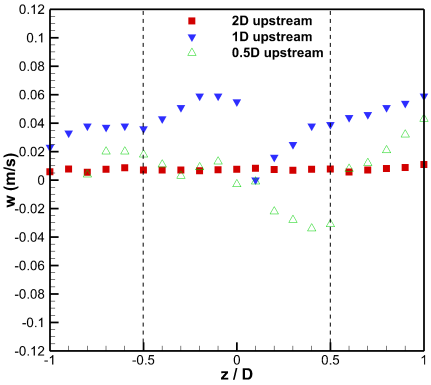

(c) Spanwise velocity upstream of turbine at centre height

Figure 3.2: Three-dimensional velocities upstream of turbine, dashed lines denote edges of turbine

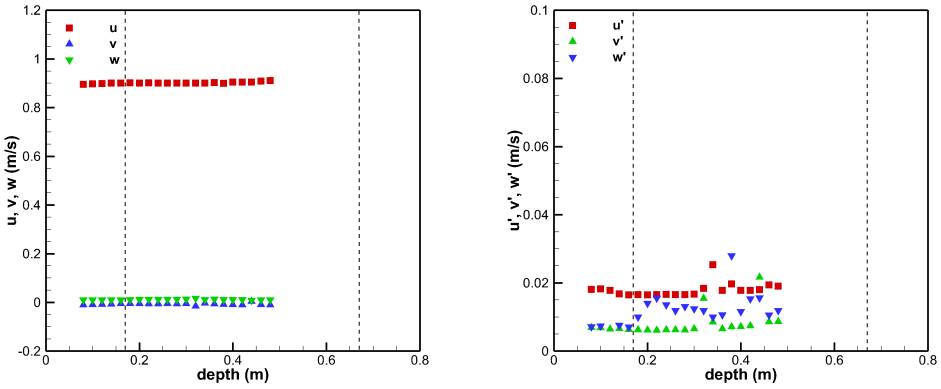

(a) Velocities

(b) Reynolds normal stresses

Figure 3.3: Velocities and Reynolds normal stresses through the depth $2D$ upstream of the three-bladed turbine, dashed lines denote edge of turbine

The Reynolds normal stresses (standard deviations of velocities), defined in equations 1.5, 1.6 and 1.7, are shown in figure 3.3 (b) through the depth of the channel, where 0 is the water free-surface. This data shows that the turbulence levels upstream are very low and uniform throughout the depth. The streamwise Reynolds normal stress appears to be slightly greater than the vertical and spanwise, this could be due to the inherent issues with the ADV to be discussed in chapter 5, but does give a good indication that the levels are very low and are in agreement with previous studies conducted in the channel e.g. Millward (2002).

3.1.2 Three-Dimensional Velocity Contours

Figure 3.4 shows the mean streamwise velocities behind the three-bladed turbine measured in horizontal planes. The largest velocity deficit is at the tip of the blades, in figure 3.4(a) this can be seen at $z/D = \pm 0.5$ and in figures 3.4(d), 3.4(e) at the centre (i.e. $z/D = 0$). By seven diameters

downstream there is an overall recovery of the streamwise velocity to about 80% of the upstream velocity. There is a small asymmetry in the results due to the free-surface effects and the presence of the support structure. This asymmetry in figures 3.4 (b) and (c) can be observed by noting that the velocities are larger at $y/D = -0.25$ than at $y/D = +0.25$, similarly it can be seen at $y/D = -0.5$ the velocities are greater than at $y/D = +0.5$ in figures 3.4(d) and (e).

The mean vertical velocities in figure 3.5 show the effect of the swirl induced by the turbine blade rotation, this is clearest in figure 3.5(a) where there are both negative velocities and positive velocities corresponding to the clockwise rotation of the blades; this same trend can be seen at $\pm 0.25D$ depths, again, asymmetry due to the free-surface effects can be seen between $y/D = +0.5$ and $y/D = -0.5D$. Significant transverse velocities are still evident at the edge of the measurement window (i.e. $6 - 7$ diameters downstream).

Figure 3.6 shows the mean spanwise (side-to-side) velocities, which are all less than 10% of the streamwise velocities, the regions of high absolute velocities occur generally at the higher turbulent regions at the edge of the blades. These higher turbulent regions alter between negative and positive velocities, in particular when we look at figure 3.6(b) between 2 and $3D$ downstream there are negative values on one side and positive on the other, further downstream this is reversed, showing the effect of two rotations of the large-scale swirling motions. The observation of the swirling motions concur with the results of Chamorro et al. (2013) who found regions of negative and positive spanwise velocities directly downstream of their turbine.

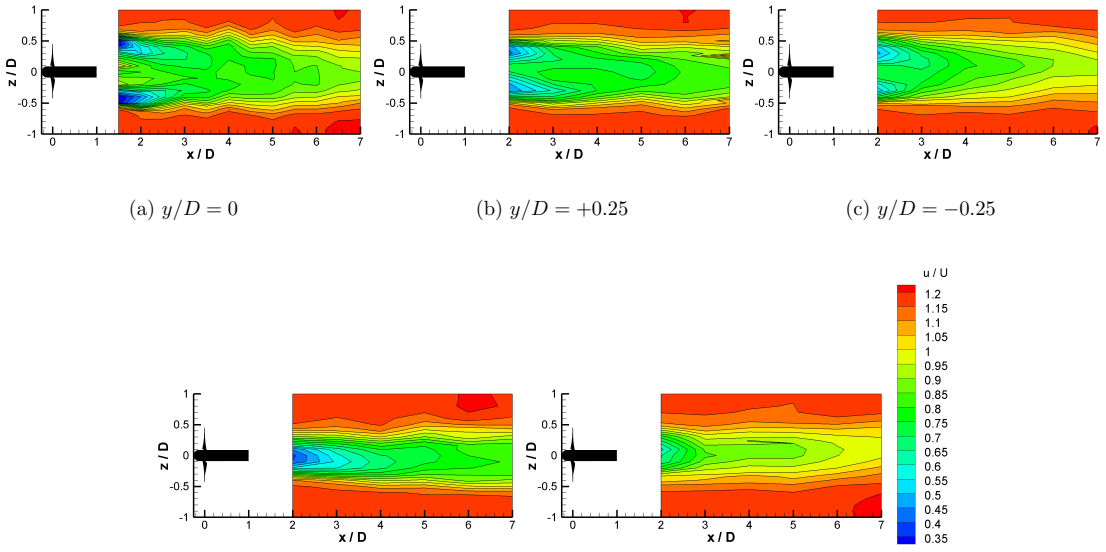

(a) $y/D = 0$ (b) $y/D = +0.25$ (c) $y/D = -0.25$

(d) $y/D = +0.5$ (e) $y/D = -0.5$

Figure 3.4: Contours of the mean streamwise velocities behind a turbine

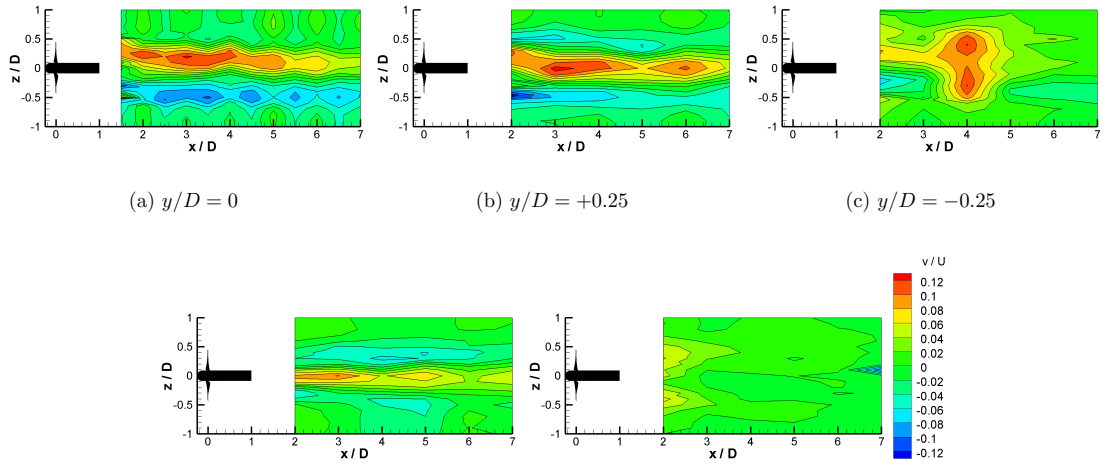

(a) $y/D = 0$ (b) $y/D = +0.25$ (c) $y/D = -0.25$

(d) $y/D = +0.5$ (e) $y/D = -0.5$

Figure 3.5: Contours of the mean vertical velocities behind a turbine

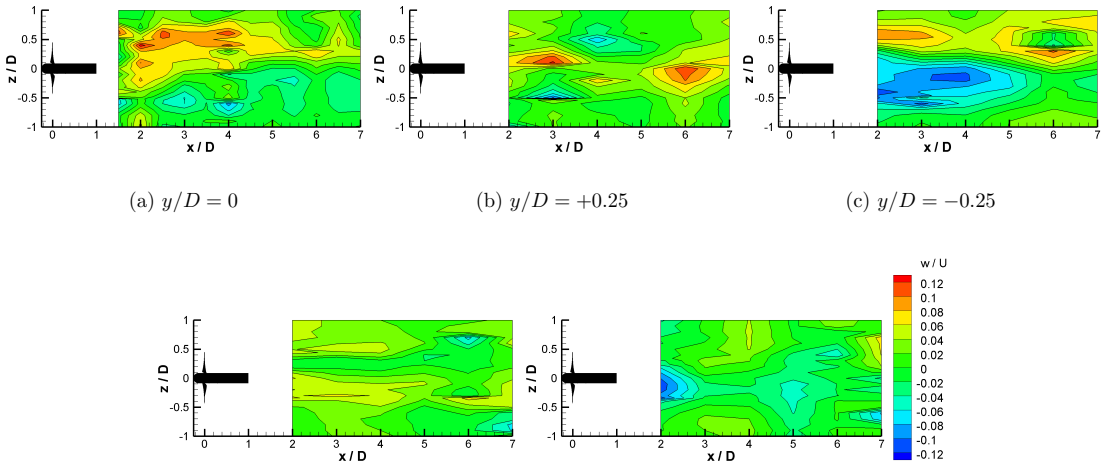

(a) $y/D = 0$ (b) $y/D = +0.25$ (c) $y/D = -0.25$

(d) $y/D = +0.5$ (e) $y/D = -0.5$

Figure 3.6: Contours of the mean spanwise velocities behind a turbine

3.1.3 Reynolds Normal Stresses and Turbulent Kinetic Energy

Figure 3.7 show the Reynolds normal stress (standard deviation) of the streamwise velocity (u') at the centre height and up to seven diameter distances downstream. The key point to take from the data for the Reynolds normal stresses is that there is a maximum effect around the tip of the blades ($z/D = \pm 0.5$, denoted by the dotted lines) and this effect can be seen up to $7D$ downstream showing the turbine still has an impact on the flow field. The standard deviation of the velocity components emanating from the blade tip can be expected to be higher due to the blade speed being maximum at this point and the generation of tip vortices. Figures 3.8 - 3.11 show the streamwise Reynolds shear stresses at heights $0.5D$ and $0.25D$ above and below the central hub height, where dashed lines denote the edge of the blades at these heights. At $y/D = \pm 0.25$ and $y/D = 0$ the maximum Reynolds normal stresses occur at the edge of the blades. However, at $y/D = 0.5$ peaks are not found at the centre of the figure, at the blade edges, but at $z/D \approx \pm 0.2$ which shows that the wake is growing away from the turbine swept area in the vertical directions and is particularly noticeable nearer to the surface. To find the edge of the wake, measurements would be required near to the surface, which was not possible with the experimental arrangement in this study. The reason why the wake expands vertically upwards could be due to a combination of the blockage in this direction as the water height ($0.8m$) is smaller than the width of the channel ($1.4m$), combined with free-surface effects and the presence of the stanchion at these heights.

Similarly for the vertical Reynolds normal stresses in figures 3.12 - 3.15 there is a very similar trend to that found in the streamwise Reynolds normal stress where peak levels are found at the edge of the blades, which is a maximum at $2D$ downstream. By $7D$ downstream the levels are still 10 times higher than the upstream value, showing that the wake has yet to recover. In addition, the expansion of the Reynolds normal stress in the

vertical direction is again visible at $y/D = 0.5$ where the peak value occurs not at the blade edges but at $z/D \approx \pm 0.2$ as shown in figure 3.16

Likewise to the streamwise and vertical Reynolds normal stresses the spanwise Reynolds normal stresses, shown in figures 3.17-3.21, peaks occur at the edges of the blades at $y/D = 0, -0.5, -0.25$ and 0.25 and at $y/D = 0.5$ the wake expansion is visible. In addition, the spanwise Reynolds normal stresses are still ten times greater than the upstream value at $7D$ downstream.

Figure 3.22 show spanwise distributions of the normalised turbulent kinetic energy (TKE) downstream of the three bladed turbine, where TKE is defined in equation 1.4. In figure 3.22, it can be seen that the TKE levels peak at the edges of the blades at $z/D = \pm 0.5$ and can be seen in all measurements up to seven diameters downstream. In figure 3.22(a), it can be seen that at $1.5D$ downstream there is a third smaller peak at $z/D = 0$, which is probably due to the presence of the stanchion, and this issue is addressed in section 3.4.

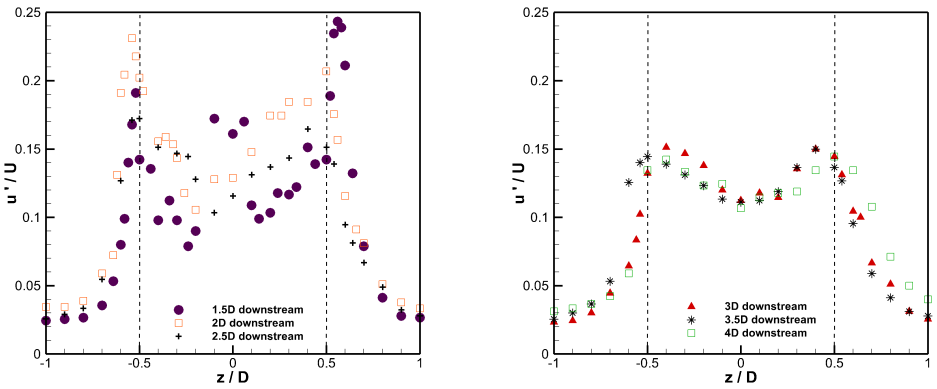

(a) u' at $1.5 - 2.5D$ downstream

(b) u' at $3 - 4D$ downstream

(c) u' at $4.5 - 5.5D$ downstream

(d) u' at $6 - 7D$ downstream

Figure 3.7: Streamwise Reynolds normal stress at $y/D = 0$, dashed lines denote edge of turbine

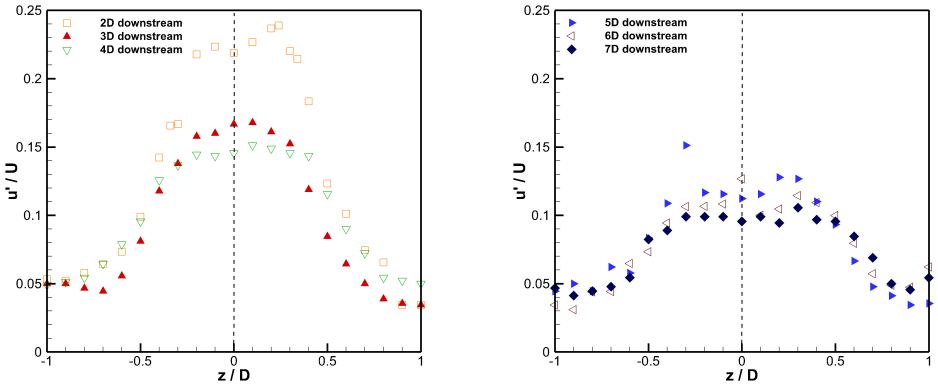

(a) u' at $2-4D$ downstream (b) u' at $3-4D$ downstream

Figure 3.8: Streamwise Reynolds normal stress at $y/D = -0.5$, dashed lines denote edge of turbine

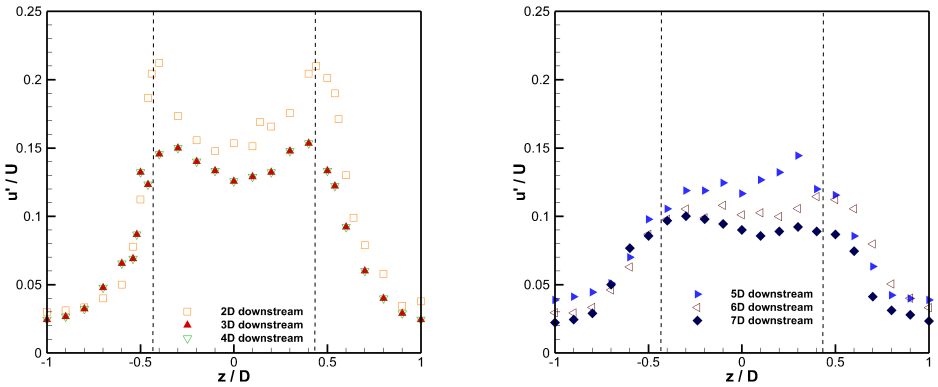

(a) u' at $2-4D$ downstream (b) u' at $3-4D$ downstream

Figure 3.9: Streamwise Reynolds normal stress at $y/D = -0.25$, dashed lines denote edge of turbine

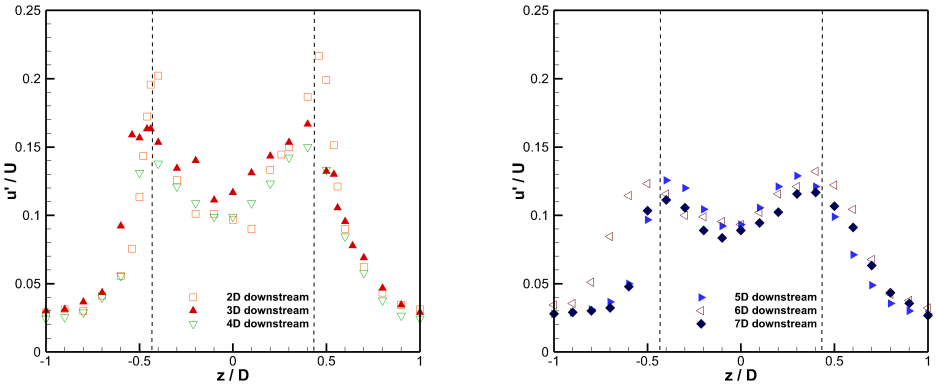

(a) u' at $2-4D$ downstream (b) u' at $3-4D$ downstream

Figure 3.10: Streamwise Reynolds normal stress at $y/D = 0.25$, dashed lines denote edge of turbine

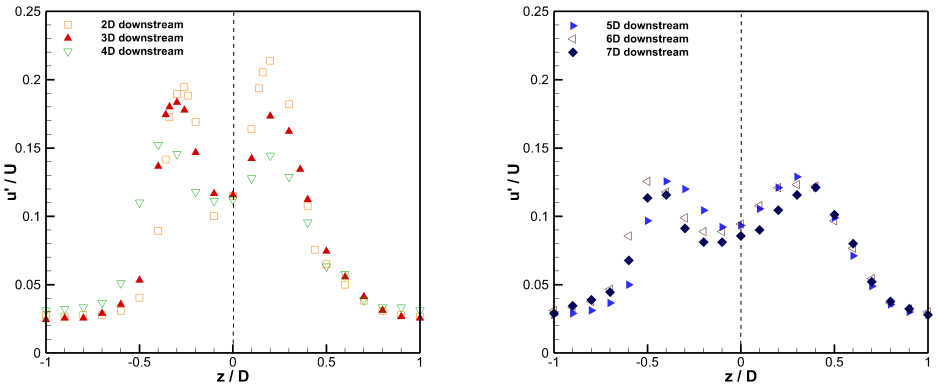

(a) u' at $2-4D$ downstream (b) u' at $3-4D$ downstream

Figure 3.11: Streamwise Reynolds normal stress at $y/D = 0.5$, dashed lines denote edge of turbine

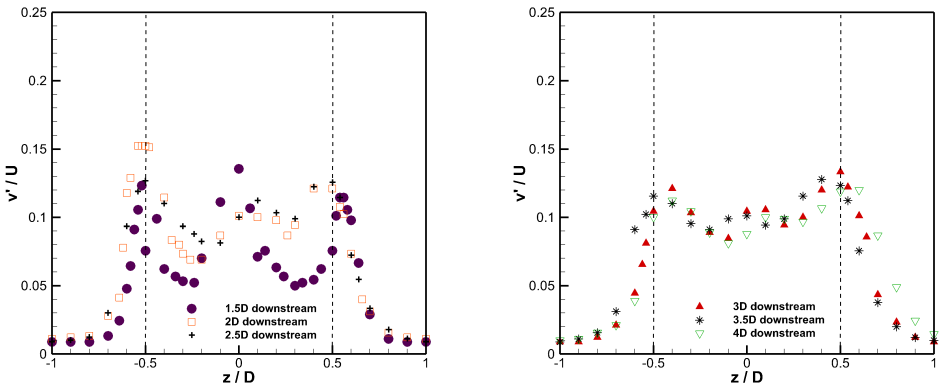

(a) v' at $1.5 - 2.5D$ downstream

(b) v' at $3 - 4D$ downstream

(c) v' at $4.5 - 5.5D$ downstream

(d) v' at $6 - 7D$ downstream

Figure 3.12: Vertical Reynolds normal stress at $y/D = 0$, dashed lines denote edge of turbine

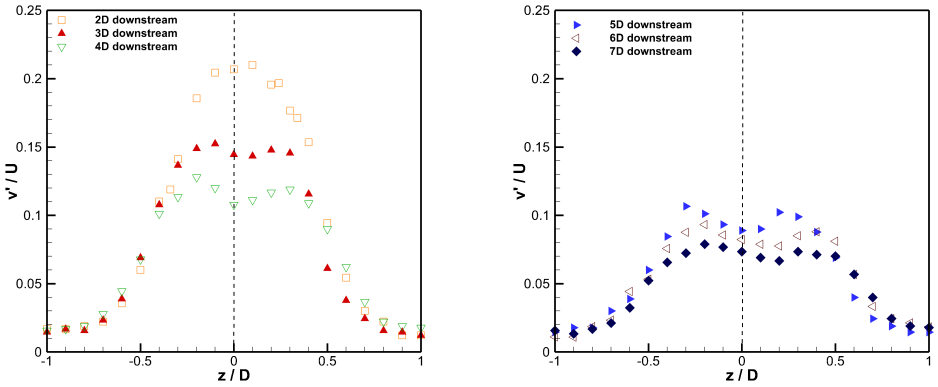

(a) v' at $2-4D$ downstream (b) v' at $3-4D$ downstream

Figure 3.13: Vertical Reynolds normal stress at $y/D = -0.5$, dashed lines denote edge of turbine

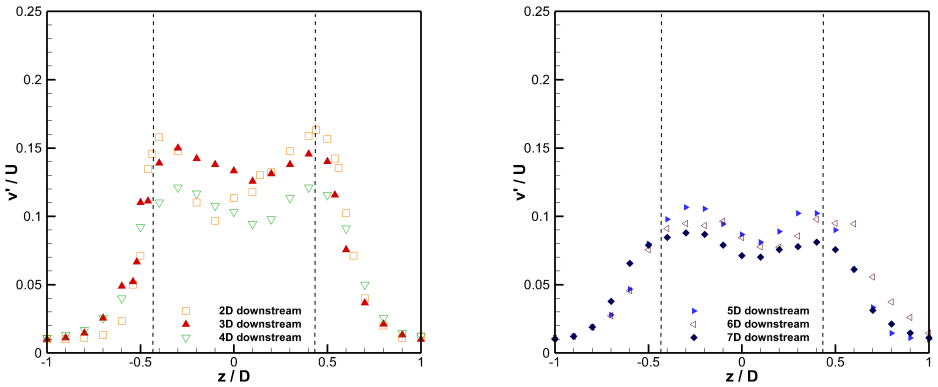

(a) v' at $2-4D$ downstream (b) v' at $3-4D$ downstream

Figure 3.14: Vertical Reynolds normal stress at $y/D = -0.25$, dashed lines denote edge of turbine

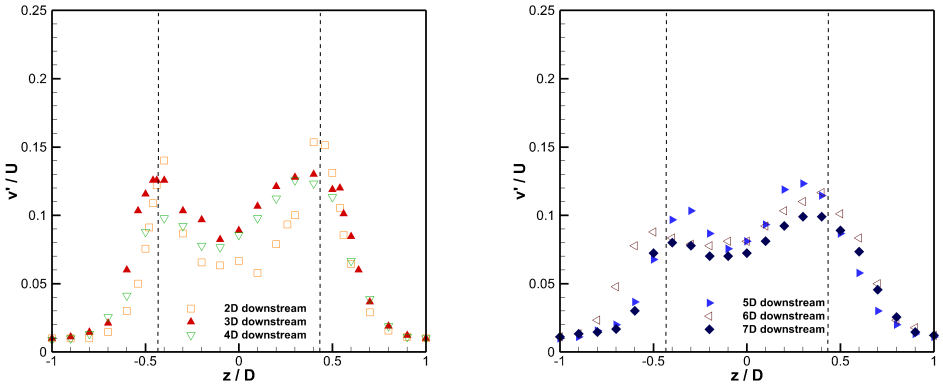

(a) v' at $2-4D$ downstream (b) v' at $3-4D$ downstream

Figure 3.15: Vertical Reynolds normal stress at $y/D = 0.25$, dashed lines denote edge of turbine

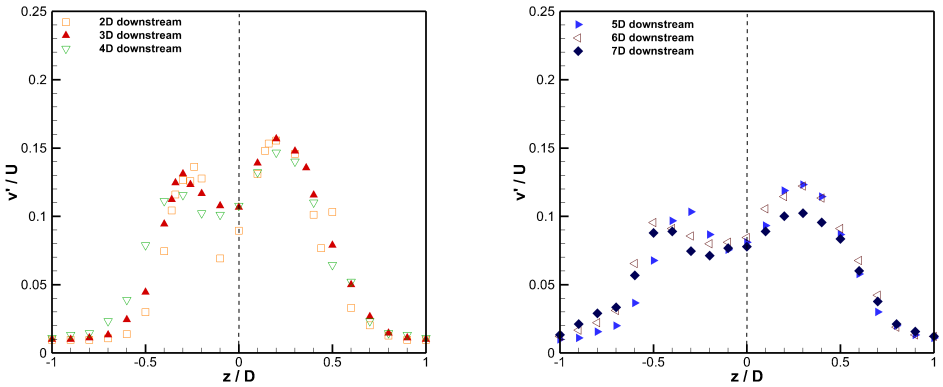

(a) v' at $2-4D$ downstream (b) v' at $3-4D$ downstream

Figure 3.16: Vertical Reynolds normal stress at $y/D = 0.5$, dashed lines denote edge of turbine

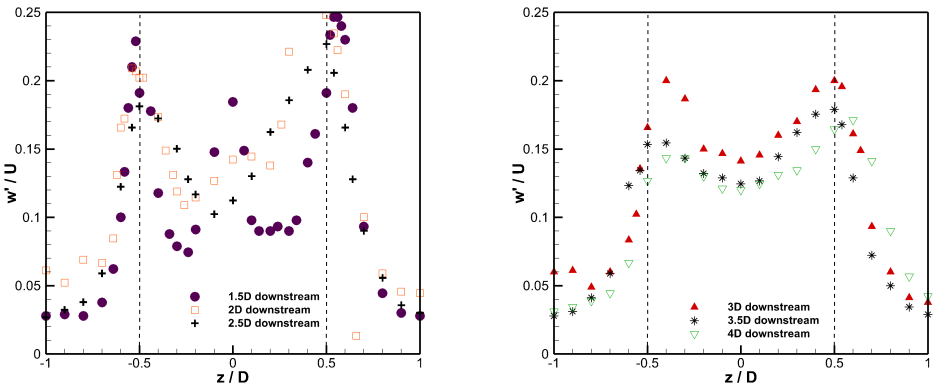

(a) w' at $1.5 - 2.5D$ downstream

(b) w' at $3 - 4D$ downstream

(c) w' at $4.5 - 5.5D$ downstream

(d) w' at $6 - 7D$ downstream

Figure 3.17: Spanwise Reynolds normal stress at $y/D = 0$, dashed lines denote edge of turbine

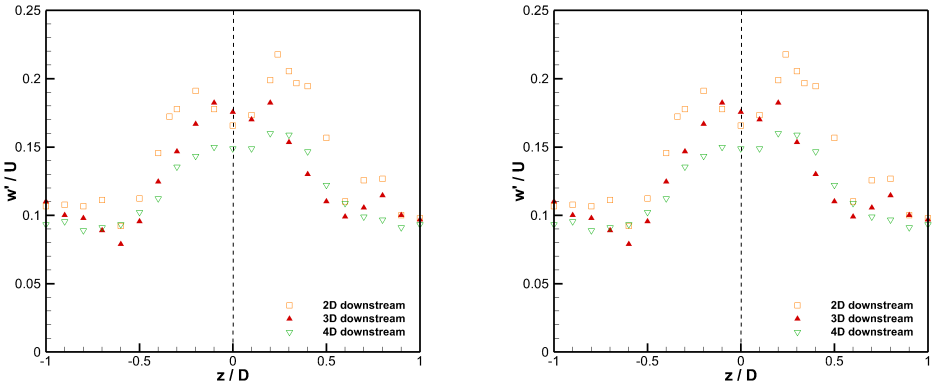

(a) w' at $2-4D$ downstream (b) w' at $3-4D$ downstream

Figure 3.18: Spanwise Reynolds normal stress at $y/D = -0.5$, dashed lines denote edge of turbine

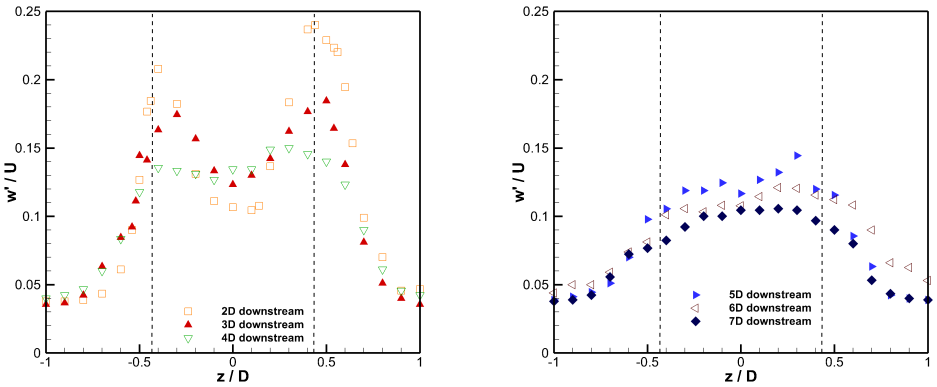

(a) w' at $2-4D$ downstream (b) w' at $3-4D$ downstream

Figure 3.19: Spanwise Reynolds normal stress at $y/D = -0.25$, dashed lines denote edge of turbine

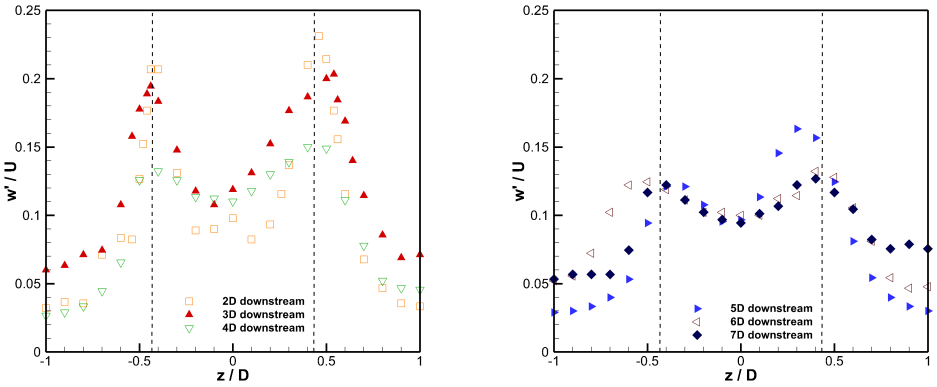

(a) w' at $2-4D$ downstream (b) w' at $3-4D$ downstream

Figure 3.20: Spanwise Reynolds normal stress at $y/D = 0.25$, dashed lines denote edge of turbine

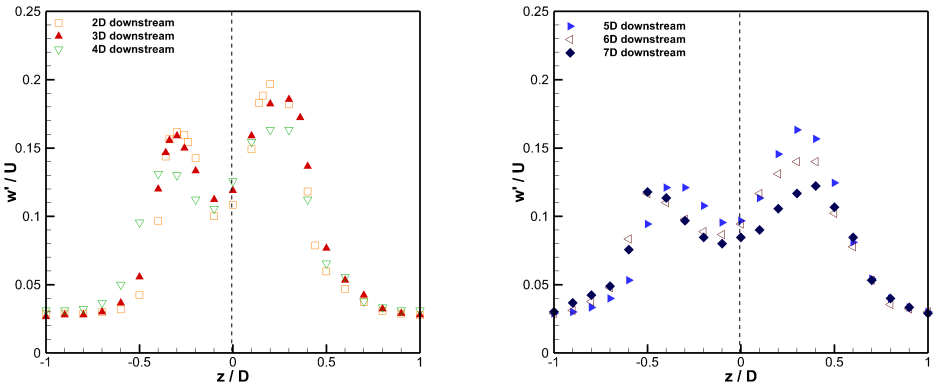

(a) w' at $2-4D$ downstream (b) w' at $3-4D$ downstream

Figure 3.21: Spanwise Reynolds normal stress at $y/D = 0.5$, dashed lines denote edge of turbine

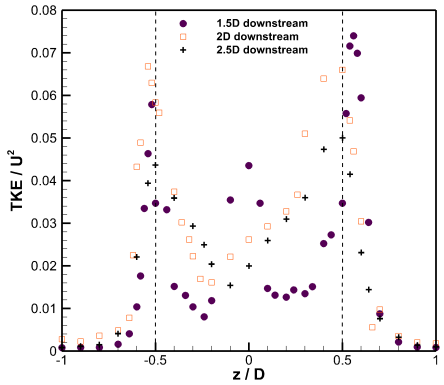

(a) TKE at $1.5 - 2.5D$ downstream

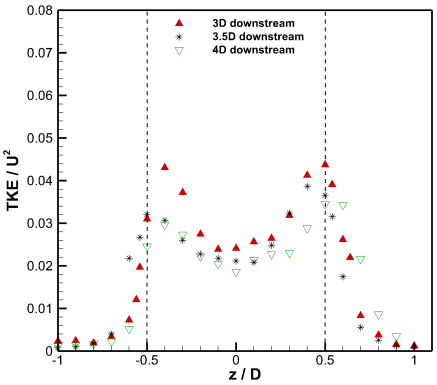

(b) TKE at $3 - 4D$ downstream

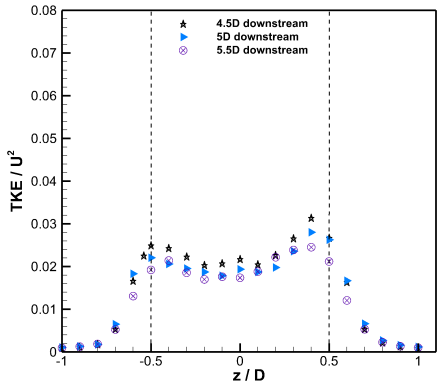

(c) TKE at $4.5 - 5.5D$ downstream

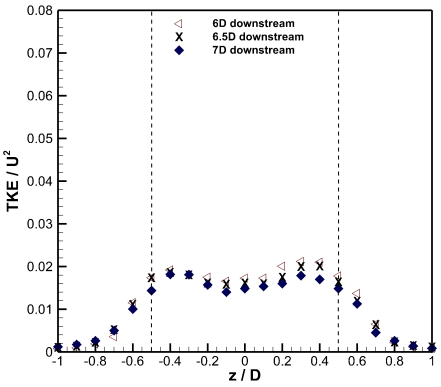

(d) TKE at $6 - 7D$ downstream

Figure 3.22: The turbulent kinetic energy at a depth corresponding to the centre of the turbine (dashed lines denote edge of turbine)

3.1.4 Reynolds Shear Stresses

One of the advantages of ADVs is the ability to measure three-dimensional velocities simultaneously allowing the Reynolds shear stresses to be calculated. The Reynolds shear stresses are defined:

$$\overline{u'v'} = \frac{1}{N}\sum_{i=1}^{N}((u_i - u)(v_i - v)), \tag{3.1}$$

$$\overline{u'w'} = \frac{1}{N}\sum_{i=1}^{N}((u_i - u)(w_i - w)), \tag{3.2}$$

$$\overline{v'w'} = \frac{1}{N}\sum_{i=1}^{N}((v_i - v)(w_i - w)), \tag{3.3}$$

where N is the number of samples at a particular point and u, v and w are the mean velocities at a particular location.

The normalised $u - v$ Reynolds shear stresses at hub height are shown in figure 3.23; between 1.5 and $5D$ downstream peaks occur at the edge of the blades as a result of the rotation. After $6D$ downstream $\overline{u'v'}$ is not varying across the channel as the turbine is having less of an impact on the flow after this point. For $\overline{u'w'}$, the normalised $u - w$ Reynolds shear stresses shown in figure 3.24, the maximum levels occur at $z/D = 0.5$ and a minimum at $z/D = -0.5$ which relate to the clockwise rotation of the turbine and can be seen for all distances downstream. Similarly the normalised $v - w$ Reynolds shear stresses, $\overline{v'w'}$, shown in figure 3.25, have maximum and minimums occurring at the blade edges due to the rotation. It is clear that the rotation of the blades inducing swirl downstream has the greatest impact on the downstream turbulence and is visible in all the Reynolds shear stresses and normal stresses, this shows the importance of scale-model testing of turbines compared to use of porous disks which many previous studies have investigated such as Myers & Bahaj (2010) and Harrison et al. (2010).

The swirling motions are therefore shown to be the greatest influence on the turbulent wake length/recovery.

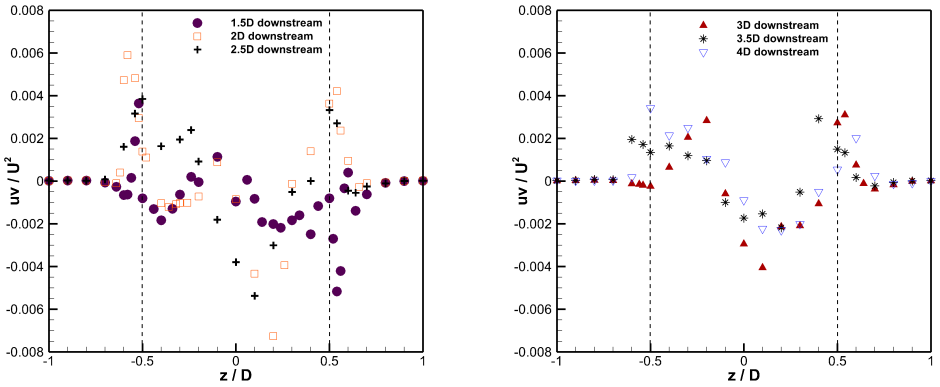

(a) $\overline{u'v'}$ at $1.5 - 2.5D$ downstream

(b) $\overline{u'v'}$ at $3 - 4D$ downstream

(c) $\overline{u'v'}$ at $4.5 - 5.5D$ downstream

(d) $\overline{u'v'}$ at $6 - 7D$ downstream

Figure 3.23: The Reynolds shear stresses at a depth corresponding to the centre of the turbine behind a turbine, dashed lines denote edge of turbine

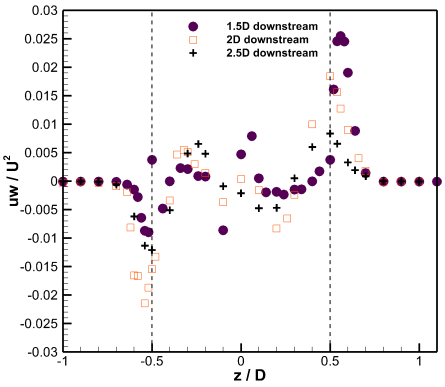

(a) $\overline{u'w'}$ at $1.5 - 2.5D$ downstream

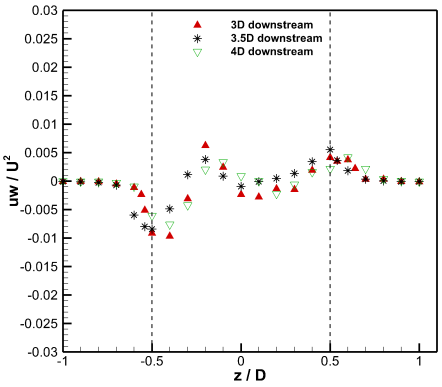

(b) $\overline{u'w'}$ at $3 - 4D$ downstream

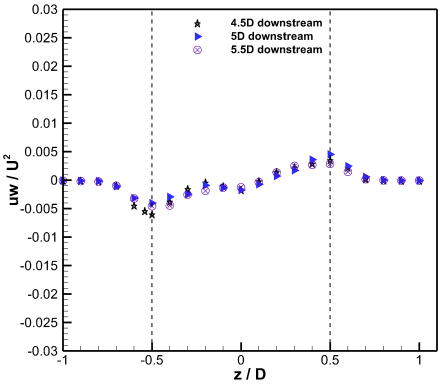

(c) $\overline{u'w'}$ at $4.5 - 5.5D$ downstream

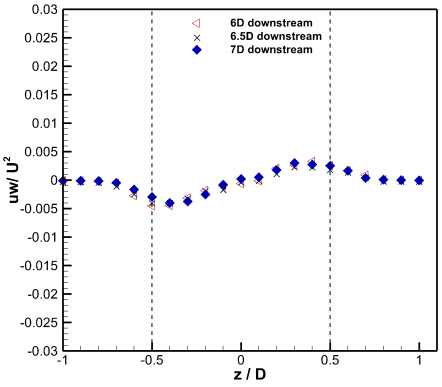

(d) $\overline{u'w'}$ at $6 - 7D$ downstream

Figure 3.24: The Reynolds shear stresses at a depth corresponding to the centre of the turbine behind a turbine, dashed lines denote edge of turbine

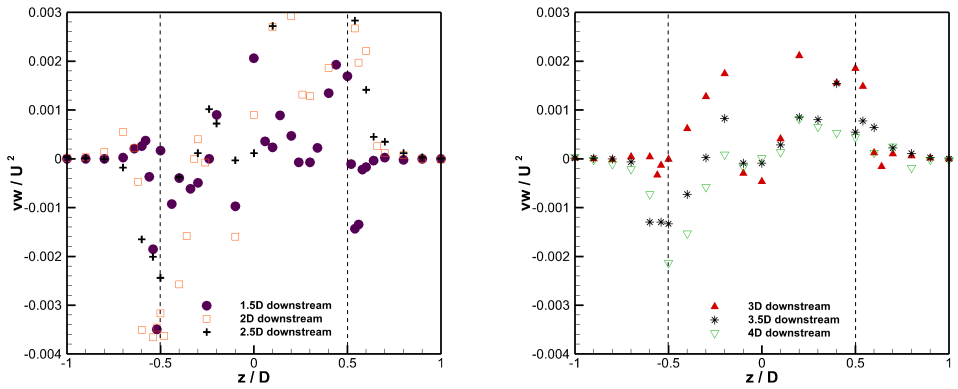

(a) $\overline{v'w'}$ at $1.5 - 2.5D$ downstream

(b) $\overline{v'w'}$ at $3 - 4D$ downstream

(c) $\overline{v'w'}$ at $4.5 - 5.5D$ downstream

(d) $\overline{v'w'}$ at $6 - 7D$ downstream

Figure 3.25: The Reynolds shear stresses at a depth corresponding to the centre of the turbine behind a turbine, dashed lines denote edge of turbine

3.1.5 Decay of turbulence anisotropy downstream of the turbine

As discussed in section 1.4, most studies have modelled the turbine wake using turbulence models which assume isotropic turbulence. Therefore knowledge of the degree of turbulence anisotropy induced by the turbine and the rate of return to isotropy is important. To investigate the anisotropy of the turbulent flow field behind the turbine the Reynolds-stress anisotropy tensor **b** can be used and is defined by Choi & Lumley (2001):

$$b_{i,j} = \begin{pmatrix} \frac{u'^2}{u'^2+v'^2+w'^2} - \frac{1}{3} & \frac{\overline{u'v'}}{u'^2+v'^2+w'^2} & \frac{\overline{u'w'}}{u'^2+v'^2+w'^2} \\ \frac{\overline{u'v'}}{u'^2+v'^2+w'^2} & \frac{v'^2}{u'^2+v'^2+w'^2} - \frac{1}{3} & \frac{\overline{v'w'}}{u'^2+v'^2+w'^2} \\ \frac{\overline{u'w'}}{u'^2+v'^2+w'^2} & \frac{\overline{v'w'}}{u'^2+v'^2+w'^2} & \frac{w'^2}{u'^2+v'^2+w'^2} - \frac{1}{3} \end{pmatrix}. \tag{3.4}$$

The Reynolds-stress anisotropy can be more simply, and is commonly, characterised by a pair of invariants, η and ξ, defined by;

$$6\xi^2 = b_{ii}^2 = b_{ij}b_{ji}, \tag{3.5}$$

$$6\eta^2 = b_{ii}^3 = b_{ij}b_{jk}b_{ki}, \tag{3.6}$$

(Lumley, 1978, Choi & Lumley, 2001, Pope, 2011 and Simonsen & Krogstad, 2005). At any point and time in any turbulent flow these invariants can be defined from the Reynolds-stresses, and are restricted with respect to the realisability of the flow to the anisotropy invariant map, which is often referred to as the 'Lumley triangle' (Lumley, 1978) which is shown in figure 3.26. At the origin when both invariants are zero, i.e. $\xi = \eta = 0$, this corresponds to isotropic turbulence: all three diagonal components of the Reynolds stress tensor are equal and therefore $u' = v' = w'$. Emanating from this isotropic origin there are two limiting sides of the triangle which are said to be axisymmetric. The side of the 'Lumley triangle' when $\xi > 0$, is where

a single diagonal component of the Reynolds stress tensor is dominating over the other two components and the shape of the tensor can be said to be 'rod-shaped'. As ξ increases further this side leads up to the limit point where two fluctuating components have tended to zero resulting in a one-component state of turbulence. The other limiting line of the 'Lumley triangle' when $\xi < 0$, is where two equal diagonal components of the Reynolds stress tensor are dominating over the third smaller diagonal component, and the shape of the tensor is said to be 'disc-shaped'. As η increases along this side until the smallest diagonal component has tended to zero the limit point at the side's end corresponds to a two-component state of turbulence. The line connecting the one- and two-component axisymmetric turbulence is all other possible states of the Reynolds stress tensor where there are only two non-zero diagonal components of the tensor. To aid in the visualisation of the eight turbulence anisotropy shapes (i.e. rod-shaped, disc-shaped etc) a graphic representation of the different possible ellipsoid shapes formed by the diagonal components of the Reynolds-stress tensor are shown in figure 3.27.

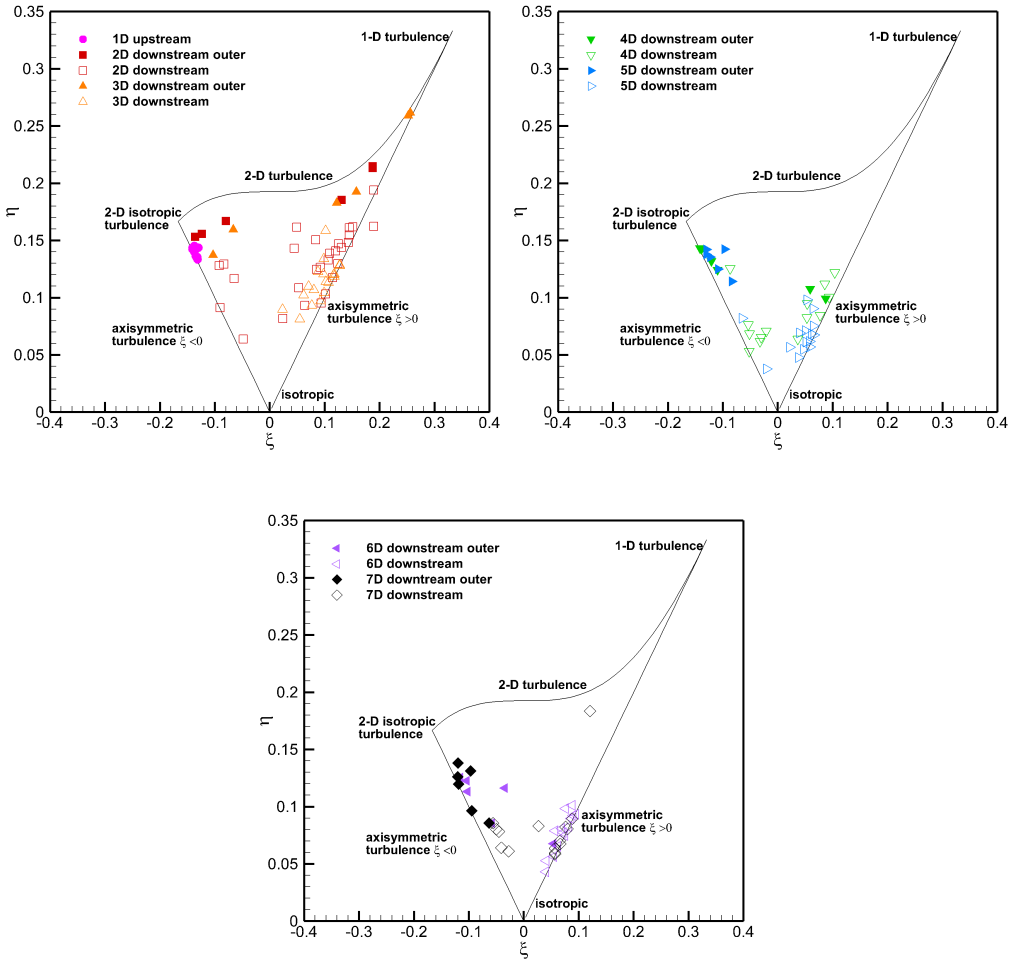

Figure 3.26: The Lumley triangle showing the turbulence anisotropy downstream of the turbine

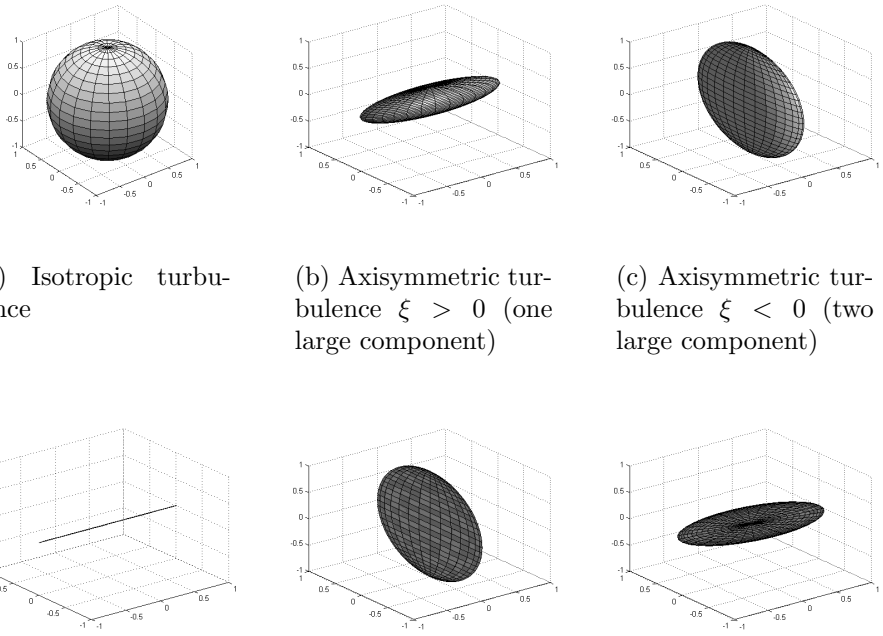

(a) Isotropic turbulence

(b) Axisymmetric turbulence $\xi > 0$ (one large component)

(c) Axisymmetric turbulence $\xi < 0$ (two large component)

(d) One component turbulence

(e) Two-component turbulence (axisymmetric)

(f) Two-component turbulence

Figure 3.27: Illustrations of the shapes formed in different regions of the flow field by the Reynolds-stress anisotropy tensor (after Simonsen & Krogstad (2005))

The Reynolds stress anisotropy data in figure 3.26, has been plotted to compare the effect of the turbine and the outer areas to see the effect around the 'outside' of the turbine. Plotted in this way it can be seen that the upstream (inlet) velocity and 'outside' regions have two dominant turbulent components (u' and w'), shown in figure 3.26(a) which is consistent with channel flows. Figure 3.26(a) shows the downstream data closest to the turbine, and there are larger values for ξ and η, showing the flow is highly anisotropic, further downstream and the figures 3.26(b-c) show that the flow is mainly in the so-called 'disc-shaped' region, where two of the diagonal components of the tensor are dominant, but further downstream the flow gradually becomes, as expected, more isotropic as the two dominant axisymmetric components decrease (i.e. u' and w' become smaller). However at $7D$ the turbulence is still strongly anisotropic and the effect of the turbine is still being felt. These results suggest that turbulence models which assume turbulent anisotropy, such as the $k - \epsilon$, will always fail to capture the near-wake turbulent flow field correctly.

3.1.6 Wake Decay Characteristics

Figure 3.28(a) shows the maximum velocity deficit in the streamwise direction at the five different heights behind the turbine; also shown is data from Harrison et al. (2010) who measured the wake downstream of a porous disc. The data for different heights exhibit a similar trend; the first three diameters behind shows a rapid velocity recovery, further downstream the recovery is much slower. The centreline component of the streamwise velocity can been seen to be recovering with a power law with a decay exponent ≈ 1.2, which is a slightly greater than the power law decay found by Harrison et al. (2010) which shows that there is faster recovery downstream of the turbine. The maximum of the transverse and spanwise velocities (figures 3.28(b-c)) can be seen to decrease essentially linearly at the different heights, but there is no general trend to the heights which have the maximum deficit.

The maximum standard deviation of the three-dimensional velocity field is shown in figure 3.29 and shows a decrease in the maximum values further downstream. In the streamwise and spanwise directions (figures 3.29(a) and (c)), the maximum standard deviations decay at a similar rate with a power-law decay exponent of approximately 0.5, where the values closest to the turbine are approximately double in magnitude to that of the furthest measurement ($7D$ downstream).

The maximum of the Reynolds shear stresses and turbulent kinetic energy is shown in figure 3.30. All the shear stresses decay with a power law, in the $u - v$ plane and $v - w$ plane, and by four disc diameters downstream have decayed to a minimum level of around 20% of the maximum level at two disc diameters downstream. The maximum turbulent kinetic energy decays with a power law with an exponent of ≈ 0.9, which is a slower rate than that of isotropic grid-generated (or mesh generated) turbulence which has a decay exponent most commonly found to be around 1.3 (Pope, 2011). Such differences would indicate that simplified methods to model the wake characteristics of tidal stream turbines, such as the absorption disc approach (Sun et al., 2008, Myers & Bahaj, 2010 and Harrison et al., 2010), may significantly overpredict the rate of decay of the maximum turbulent kinetic energy downstream of a model HATT. The experimental data of Harrison et al. (2010), when replotted as TKE (TI $=\sqrt{\frac{2}{3}TKE/U^2}$) as shown in figure 3.30(d), exhibit power-law decay rates of 1.3 to 1.6 dependent on exact C_T value for example. Thus at identical C_T they predict a TKE decay rate almost twice as high as that measured here.

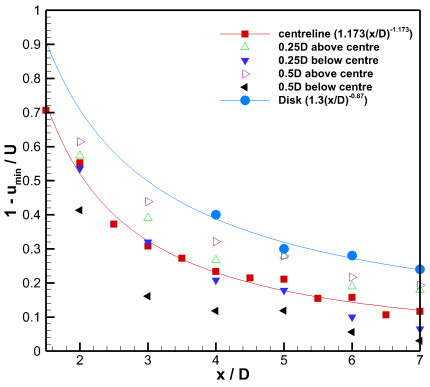

(a) The maximum streamwise velocity deficit at various heights behind a turbine

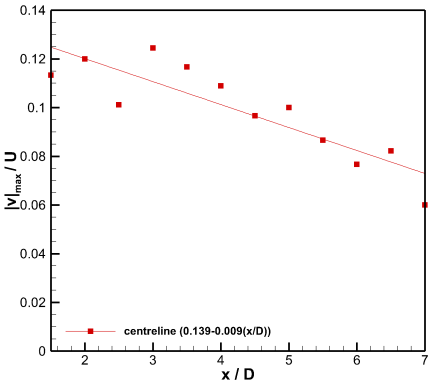

(b) The maximum vertical velocity at hub height

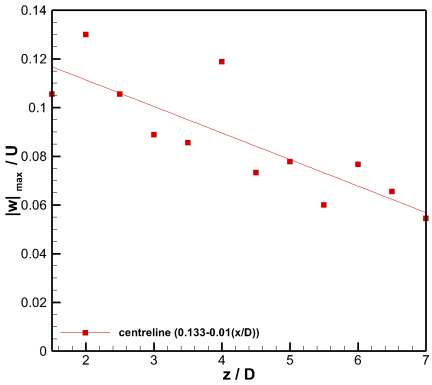

(c) The maximum spanwise velocity at hub height

Figure 3.28: The decay of maximum mean velocities downstream of the turbine, disk - Harrison et al. (2010) ($C_P \approx 0.9$)

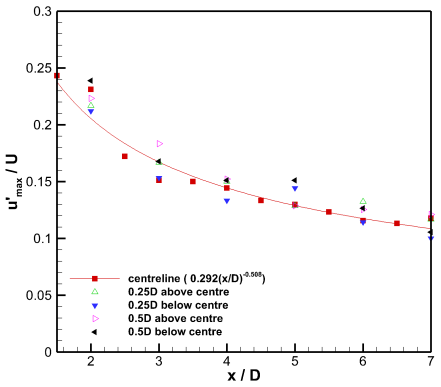

(a) The maximum streamwise Reynolds normal stresses at various heights behind a turbine

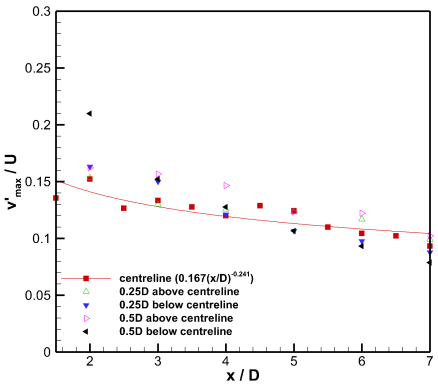

(b) The maximum vertical Reynolds normal stresses at various heights behind a turbine

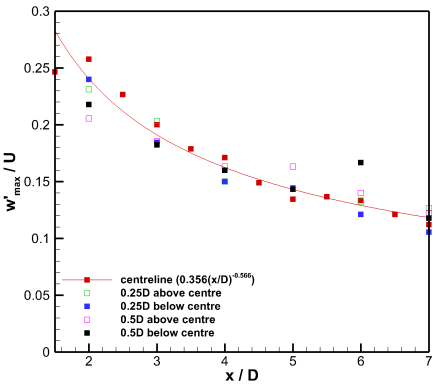

(c) The maximum spanwise Reynolds normal stresses at various heights behind a turbine

Figure 3.29: The decay of the maximum Reynolds normal stresses downstream of the turbine

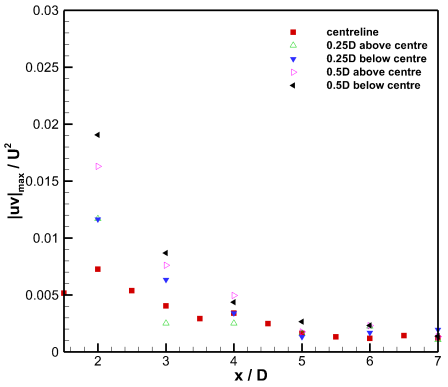

(a) The maximum Reynolds shear stress in the x-y plane deficit at various heights behind a turbine

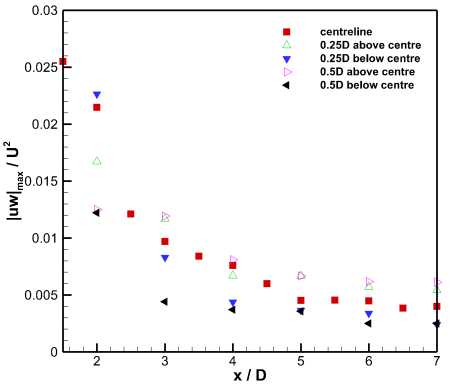

(b) The maximum Reynolds shear stress in the x-z plane deficit at various heights behind a turbine

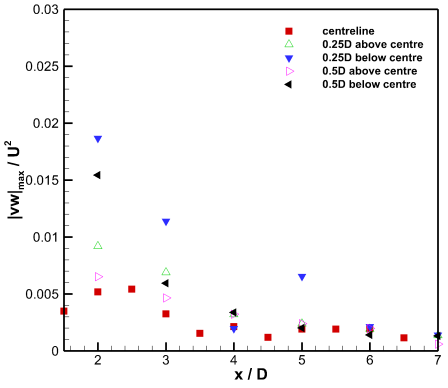

(c) The maximum Reynolds shear stress in the y-z plane deficit at various heights behind a turbine

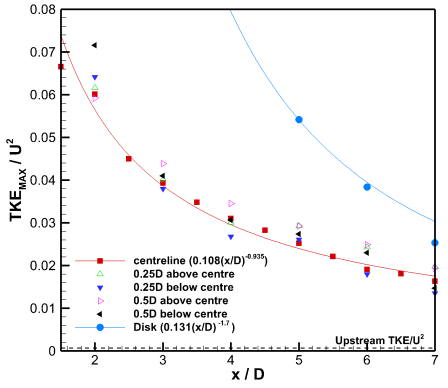

(d) The maximum turbulent kinetic energy deficit at various heights behind a turbine

Figure 3.30: The decay of the maximum Reynolds shear stresses and TKE deficits downstream of the turbine , disk - Harrison et al. (2010) ($C_P \approx 0.9$))

3.2 Reynolds Number Dependence of Wake Structure

Many previous studies have investigated the wake at low Reynolds numbers (e.g. Harrison et al., 2010 and Stallard et al., 2013), it is therefore important to investigate the effect of Reynolds number on the wake not least because it was observed in section 2.8.2 that Reynolds number has an effect on the power coefficient. Having characterised the wake at a flow velocity which was in the Reynolds independent range, the wake structure was measured downstream of the turbine at lower velocities, $0.45m/s$ (Re_F = 1.1 x 10^5) and $0.68m/s$ (Re_F = 1.7 x 10^5). At these velocities there is a difference in power coefficient at the various tip speed ratios, therefore the tip speed ratio was matched to the previous case (i.e. $\lambda = 6.15$) with power coefficients, 0.18 and 0.32 and thrust coefficients of 1.00 for both.

As a first comparison, the three-dimensional velocity contours are plotted in figures 3.31 and 3.32 at $0.45m/s$ and $0.68m/s$ respectively. Similar to the wake at $0.9m/s$ (figure 3.4 (a)) the wake at $0.45m/s$ has the largest deficit in the streamwise component at the edge of the blades, however at $0.45m/s$ the maximum deficit is about 50% of the upstream which is a much smaller deficit than that found at $0.9m/s$. Another difference in the normalised streamwise velocity is that the acceleration at the edge of the channel is less in the data set at $0.45m/s$ than at $0.9m/s$. In addition, the recovery by $7D$ downstream is about 70% of the upstream value, which is less than that recovered by $7D$ at $0.9m/s$. The slower recovery is contrary to what is expected due to the lower power extraction, suggesting that the Reynolds number does indeed have an effect on the wake recovery. In the vertical velocities at $0.45m/s$ (figure 3.31 (b)) there is a strong resemblance to the results at $0.9m/s$ (figure 3.5 (a)) where swirl effects, due to the blade rotation, are visible up to $5D$ downstream. The effects of the swirl is seen by the positive velocities, which are about 10% of the upstream streamwise component, on the left-hand-

side looking downstream and the negative velocities on the right-hand-side looking downstream. In the spanwise velocities (figure 3.31 (c)) there is again some effects of swirl; however it is not as clear as the effects seen in the vertical velocities, but this corresponds to what is seen at $0.9m/s$.

Figure 3.32 shows the velocity contours downstream of the turbine at $0.68m/s$. In the streamwise component (figure 3.32 (a)), akin to the wake at $0.45m/s$ and $0.9m/s$ the maximum deficit is at the edge of the blades ($z/D = \pm 0.5$), and is recovered to 70% of the upstream component by $7D$ downstream. The main difference in the streamwise component at $0.68m/s$, is that the maximum deficit reduces to about 55% of the upstream, which is significantly less than at $0.9m/s$ where it is 70%. In addition at $7D$ downstream the wake has recovered less, to 80% rather than $85 - 90\%$ at $0.9m/s$. These differences must be attributed to the Reynolds number effects rather than power and thrust coefficients as these are essentially the same as those at $0.9m/s$.

To show these differences more clearly for all three upstream velocities, the maximum streamwise velocity deficit has been plotted in figure 3.33, where the initial recovery at $0.9m/s$ is seen to be more rapid than that of the other upstream velocity settings, where the power-law decay exponent is half for $0.45m/s$ than that at $0.9m/s$. In addition the data for the wake downstream of an absorption disk by Harrison et al. (2010) ($Re_F = 2.4$ x 10^4) and the centreline data downstream of the $0.27m$ diameter rotor ($Re_F \approx 1.2$ x 10^5) measured by Stallard et al. (2013) is shown. A similar mean velocity recovery is found between the disc, the $0.27m$ diameter rotor and the data for our turbine at $0.45m/s$ and $0.68m/s$ showing that the disk is more representative of the streamwise mean flow behind a turbine at lower Reynolds number. This means that the differences between the mean streamwise velocity recovery downstream of the absorption disk and the turbine discussed in the previous section can be attributed to the effect of Reynolds number and it highlights the importance of being in the Reynolds independent range

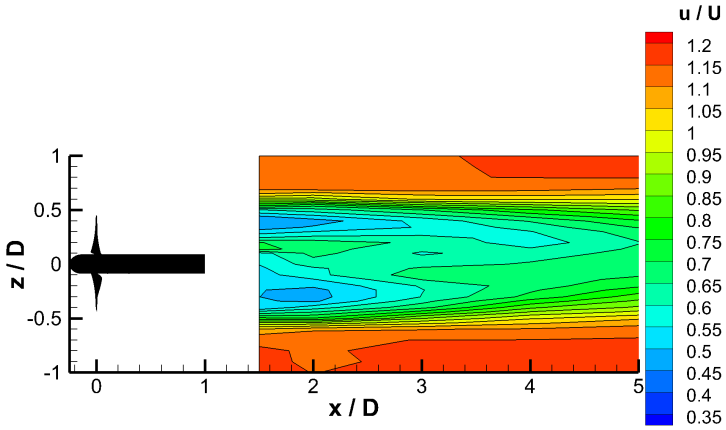

(a) streamwise velocity

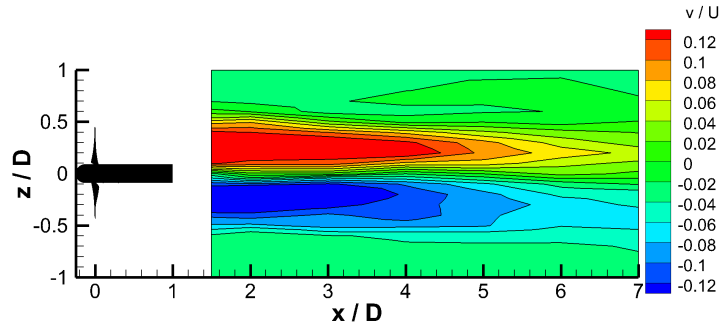

(b) vertical velocity

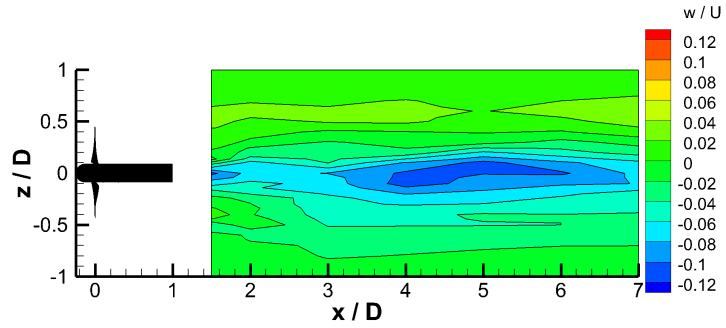

(c) spanwise velocity

Figure 3.31: Three-dimensional velocity contours downstream of a three-bladed turbine at $U = 0.45m/s$

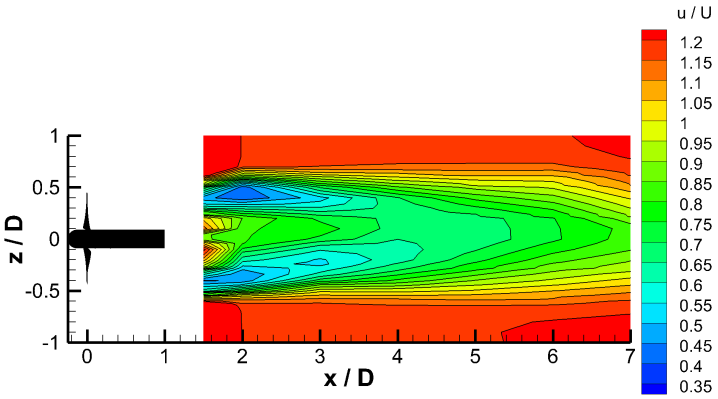

(a) streamwise velocity

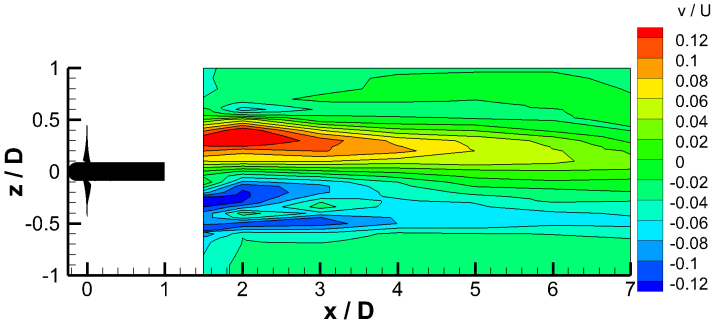

(b) vertical velocity

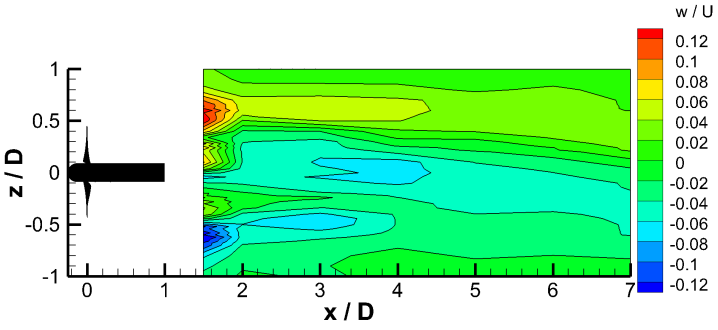

(c) spanwise velocity

Figure 3.32: Three-dimensional velocity contours downstream of a three-bladed turbine at $U = 0.68m/s$

especially for small rotors at low velocities.

To further investigate the effect of the different upstream velocities, the maximum measured TKE downstream of the turbine with different upstream velocities is shown in figure 3.34, it can be seen that at $0.9m/s$ and $0.68m/s$ the TKE decay is fairly similar. With an upstream velocity of $0.45m/s$ TKE is much lower near to the turbine than at higher velocities, which is most probably due to the reduction in power extraction and therefore resulting in lower TKE downstream of the turbine. However, by $4D$ downstream the TKE levels are similar to those in the other flows, showing that after $4D$ downstream Reynolds number effects on the turbine are no longer contributing to the TKE recovery. Although it has been found that the Reynolds number affects the very near-wake, it can be seen that after $4D$ downstream for all velocities that the maximum TKE collapses and the minimum streamwise velocity recovers at the same rate suggesting that it might be possible to characterise the far-wake with low Reynolds number flows. However caution must be taken as although the minimum streamwise velocity recovers similarly after $4D$ the minimum mean velocities are significantly higher at lower Reynolds numbers. In addition, the maximum TKE downstream of the absorption disk measured by Harrison et al. (2010) and the TKE at the centreline by Stallard et al. (2013) with a rotor ($D = 0.27m$ and $U = 0.45m/s$) are shown in figure 3.34. The trend is different downstream of the disk compared to the turbines, even after $4D$ downstream, this shows that the swirling motion induced by the turbine rotation is the most important contributor to the TKE in the flow especially further downstream. The TKE downstream of the turbine measured by Stallard et al. (2013) exhibits a similar trend to that downstream of our turbine after $3D$. The difference in trends in the very near-wake could be due to the fact that only the centreline data was provided rather than the maximum TKE across the channel, as the swirling motions cause more dominant effects on the TKE at the blade edges.

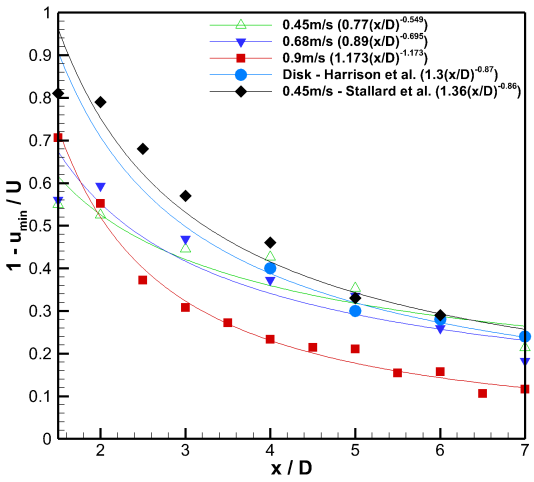

Figure 3.33: The maximum streamwise velocity deficit downstream of a three-bladed turbine at different upstream velocity (disk - (Harrison et al., 2010) ($C_P \approx 0.9$))

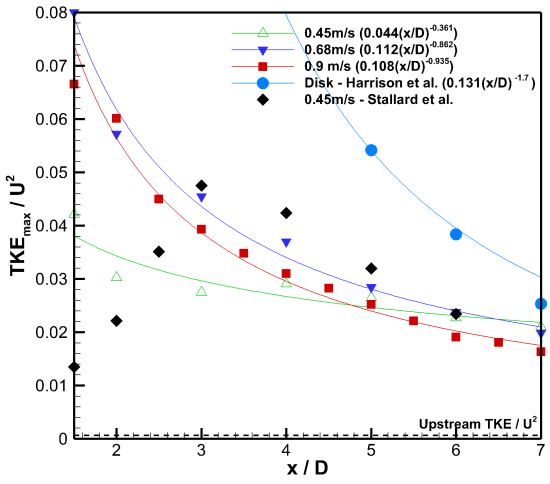

Figure 3.34: The maximum TKE downstream of a three-bladed turbine at different upstream velocity (disk - (Harrison et al., 2010) ($C_P \approx 0.9$))

3.3 Two-Bladed Turbine

The wake downstream of a three-bladed turbine at optimum blade pitch angle has been characterised in the previous sections, subsequently the wake downstream of a two-bladed turbine was investigated to see if the blade number has an impact on the near-wake. Firstly the two-bladed turbine was set with optimum blade pitch angle of 3^o, and the wake measured in the centre-plane, across the width up to $7D$ downstream. Then the turbine was set to an off-optimum angle of 9^o and the wake again measured in the centre-plane. To enable direct comparison with the three-bladed results, the upstream uniform velocity was set to $0.9m/s$ and had measured TI levels of 2%.

3.3.1 Two-bladed turbine with optimum blade pitch angle

The upstream flow was set to $0.9m/s$ and torque to 20% of the motor's maximum level which resulted in a tip speed ratio of 6.4, thrust coefficient of 1.4 (once again this value was determined by measuring the force on the whole turbine structure and then subtracting the drag of the body and support alone without blades at identical upstream velocities) and power coefficient of 0.35. It should be noted that the C_T value does differ from that of the three-bladed turbine measured in section 3.1 and studies have shown that the thrust coefficient may be important in the wake downstream of a turbine (Harrison et al., 2010).

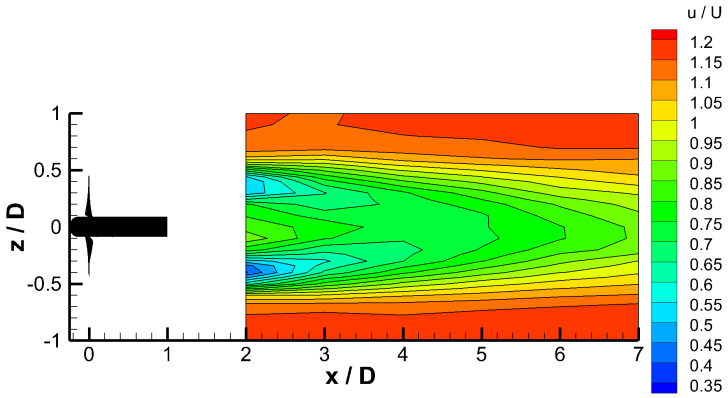

(a) Mean streamwise velocity

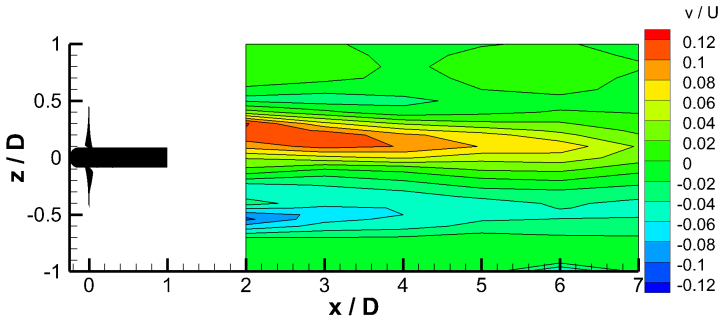

(b) Mean vertical velocity

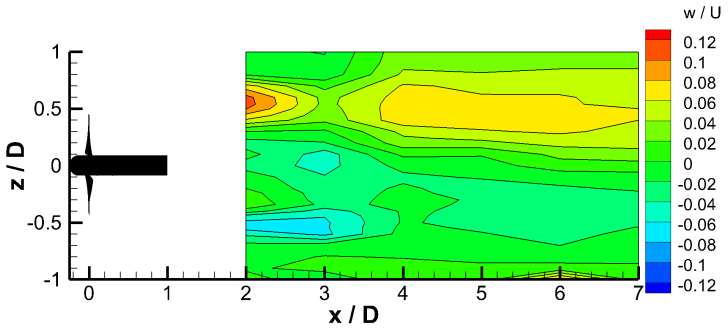

(c) Mean spanwise velocity

Figure 3.35: Three-dimensional velocity contours downstream of two-bladed turbine with 3^o blade pitch angle

Figure 3.35 shows the three-dimensional velocities downstream of the two-bladed turbine with optimum blade pitch angle (3^o). In all three mean velocity components the contour plots are essentially identical to the flow downstream of the three-bladed turbine at optimum blade pitch angle. In the u velocity component (figure 3.35 (a)) the maximum velocity deficit is again at the blade edges and reduces to $\approx 45\%$ of the upstream value at $1.5D$ downstream; the velocity has recovered by $7D$, again, to around 75% of the upstream. The swirl in the wake is also prominent in the v and w (figures 3.35 (b) and (c)) components, similar to what was observed downstream of the three-bladed turbine.

The streamwise Reynolds normal stresses are shown in figure 3.36. Likewise to the three-bladed turbine, the maximum Reynolds normal stresses are observed at the edge of the blades, the trend across the width of the channel is quantitatively similar to that downstream of the three-bladed turbine. In addition, the vertical and spanwise Reynolds normal stresses, shown in figures 3.37 and 3.38, match those downstream of the three-bladed turbine at optimum blade pitch angle. The TKE downstream of the two-bladed turbine is shown in figure 3.39, similar to the other flow statistics these values also match the results for the three-bladed turbine shown in figure 3.22. It can be concluded that the number of blades (2 or 3) set to optimum blade pitch angle has little effect on the wake, in addition this shows that the 40% change in thrust coefficient - from 1.0 with three-blades to 1.4 with two-blades - on the wake is minimal, which contradicts studies by Harrison et al. (2010), who showed that the thrust coefficient of porous discs greatly effected the wake recovery.

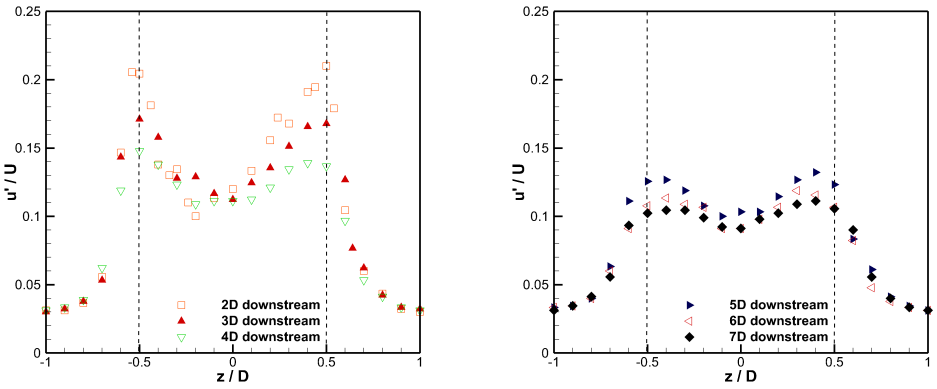

(a) $2-4D$ (b) $5-7D$

Figure 3.36: Streamwise Reynolds normal stresses downstream of a two-bladed turbine with 3^o blade pitch angle (dashed lines denote edge of turbine)

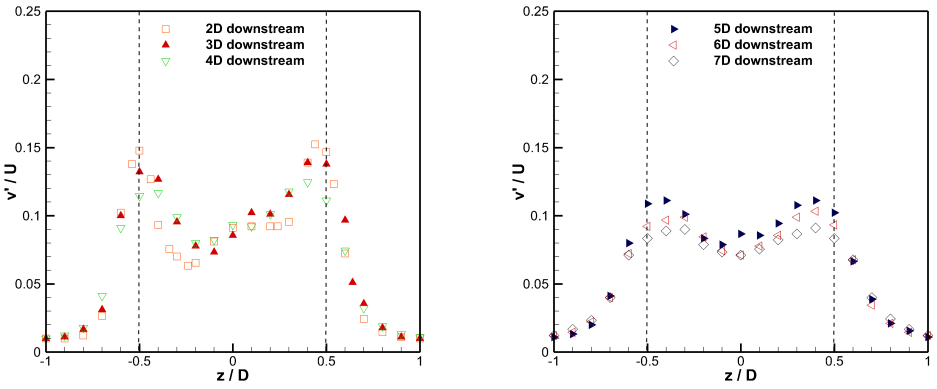

(a) $2-4D$ (b) $5-7D$

Figure 3.37: Vertical Reynolds normal stresses downstream of a two-bladed turbine with 3^o blade pitch angle (dashed lines denote edge of turbine)

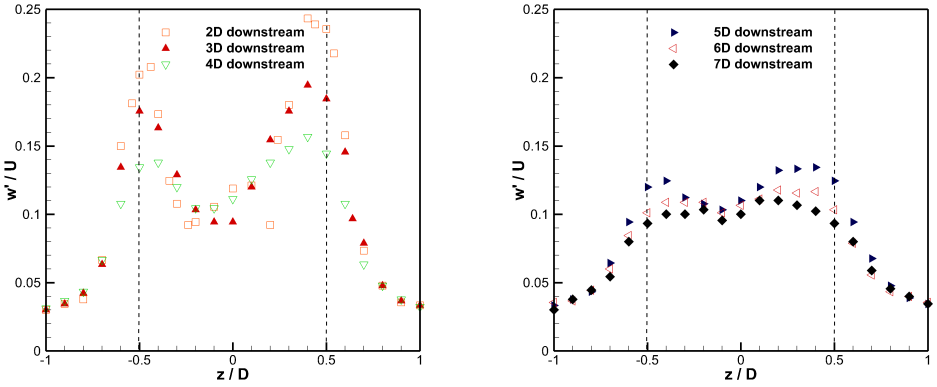

(a) $2-4D$ (b) $5-7D$

Figure 3.38: Spanwise Reynolds normal stresses downstream of a two-bladed turbine with 3^o blade pitch angle (dashed lines denote edge of turbine)

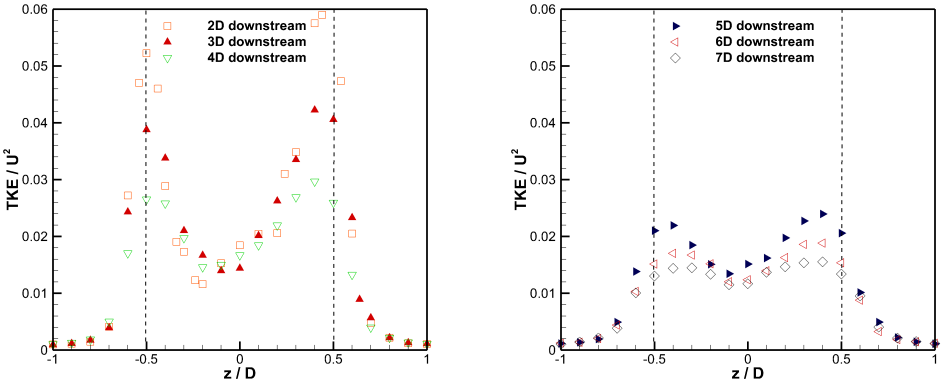

(a) $2-4D$ (b) $5-7D$

Figure 3.39: Turbulent kinetic energy downstream of a two-bladed turbine with 3^o blade pitch angle (dashed lines denote edge of turbine)

3.3.2 Two-bladed turbine with off-optimum blade pitch angle

To investigate the wake of a turbine at off-optimum blade-pitch-angle conditions, the turbine was set with two-blades with blade pitch angles of 9^o. This arrangement, along with the mean upstream streamwise velocity of $0.9m/s$ and the torque of the motor set to 20% of the maximum, resulted in a tip speed ratio $\lambda = 5.5$, thrust coefficient $C_T = 0.5$ and power coefficient $C_P = 0.3$. In contrast to the two- and three-bladed turbines at optimum blade pitch angles, the wake downstream of the two-bladed turbine with off-optimum blade pitch angle is seen to be significantly different. For instance, in the streamwise component (figure 3.40(a)) although the largest deficit is at the blade edges ($z/D = \pm 0.5$), the velocity does not decrease to as large as deficit as at optimum blade pitch angle (figure 3.35(a)), to 70% rather than 45% of the upstream velocity, this reduced deficit also means that by the end of the channel ($7D$ downstream) the wake has recovered slightly more to around 85% of the upstream velocity. In the vertical velocity (figure 3.40(b)) the swirl effects are still visible but the extreme values are around 6% of the streamwise component, rather than $10 - 12\%$ at the optimum blade pitch angle (figure 3.35(b)). In addition to this reduction in the vertical swirl components, the swirl is also not visible in the spanwise velocity (figure 3.40(c)) which was visible at optimum blade-pitch-angle in figure 3.35(c). These differences in mean velocities can be attributed to the differing power and thrust coefficients on the two turbine configurations, showing that a turbine with a lower power output and lower thrust has a smaller impact on the surrounding mean flow. Which contradicts what was found downstream of a porous disk by Harrison et al. (2010), who found that a 35% lower C_T caused a 10% increase of velocity in the near-wake. Another reason for this difference could be due to the differing tip-speed-ratios, Chamorro et al. (2013) observed that the lower the tip-speed-ratio the lower the downstream mean velocity.

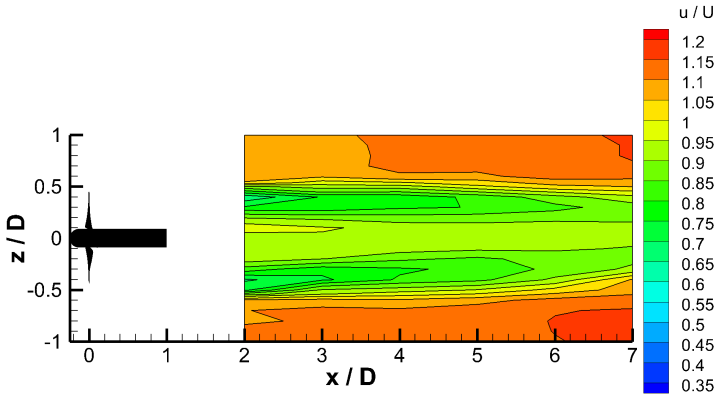

(a) streamwise velocity

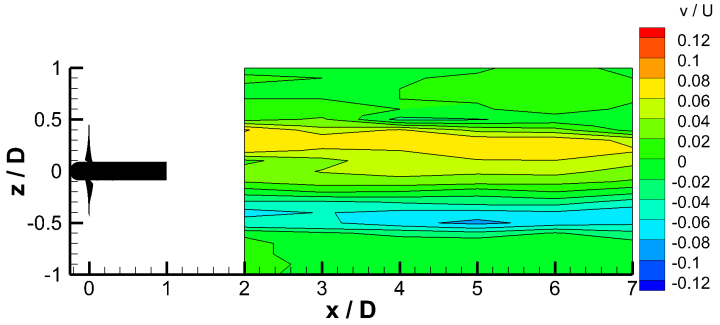

(b) vertical velocity

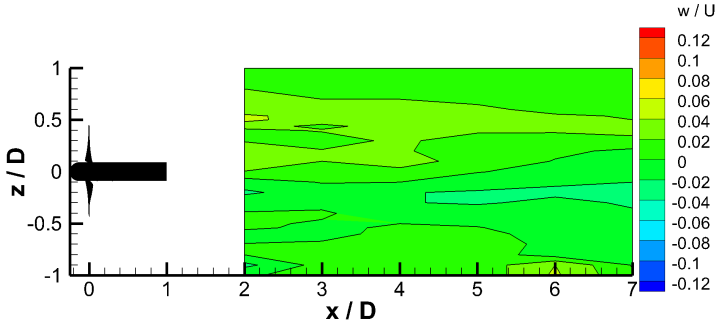

(c) spanwise velocity

Figure 3.40: Three-dimensional velocity contours downstream of a two-bladed turbine with 9^o blade pitch angle

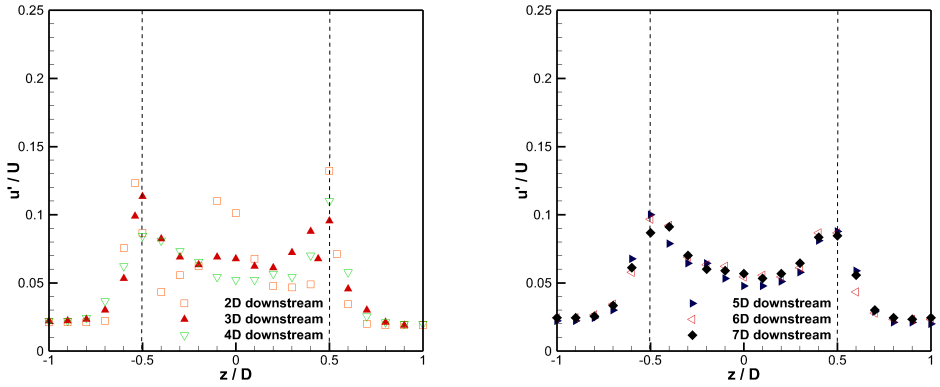

(a) $2-4D$ (b) $5-7D$

Figure 3.41: Streamwise Reynolds normal stresses downstream of a two-bladed turbine with 9^o blade pitch angle (dashed lines denote edge of turbine)

The streamwise, vertical and spanwise Reynolds normal stresses shown in figures 3.41, 3.42 and 3.43 respectively, show decreased peak values at the edge of the blades compared to those at optimum blade-pitch-angle. This reduction is ≈ 0.1 for u'/U and w'/U and ≈ 0.08 for v'/U, showing flow is less turbulent. In figure 3.44 the TKE downstream of the two bladed turbine with 9^o blade pitch angle is shown, likewise to the other velocity statistics shown the peak at $2D$ downstream is reduced to less than a third of that behind the turbine at optimum blade-pitch-angle. These decreases in Reynolds normal stresses and TKE with a turbine with off-optimum blade pitch angle (9^o) can again be attributed to the reduction in power extraction and decrease in thrust.

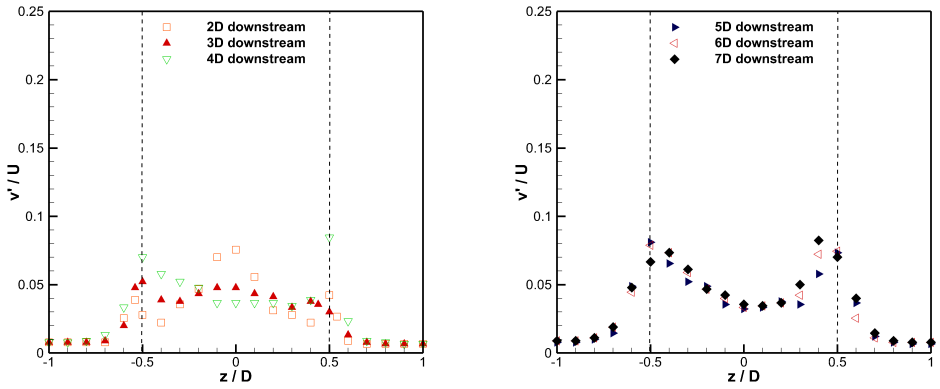

(a) $2-4D$ (b) $5-7D$

Figure 3.42: Vertical Reynolds normal stresses downstream of a two-bladed turbine with 9^o blade pitch angle (dashed lines denote edge of turbine)

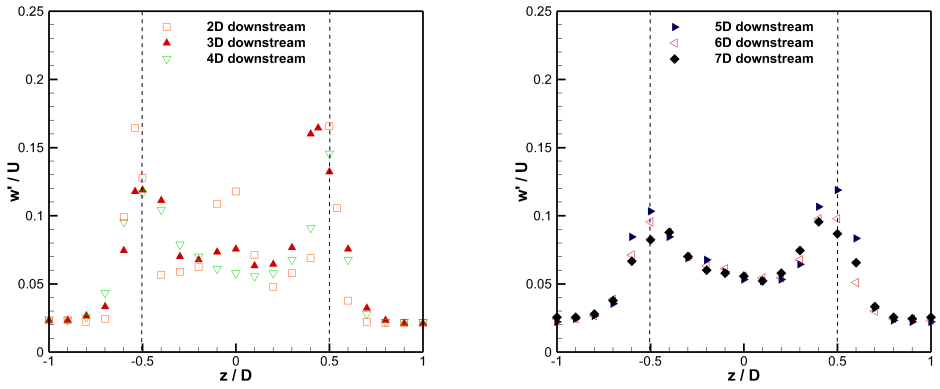

(a) $2-4D$ (b) $5-7D$

Figure 3.43: Spanwise Reynolds normal stresses downstream of a two-bladed turbine with 9^o blade pitch angle (dashed lines denote edge of turbine)

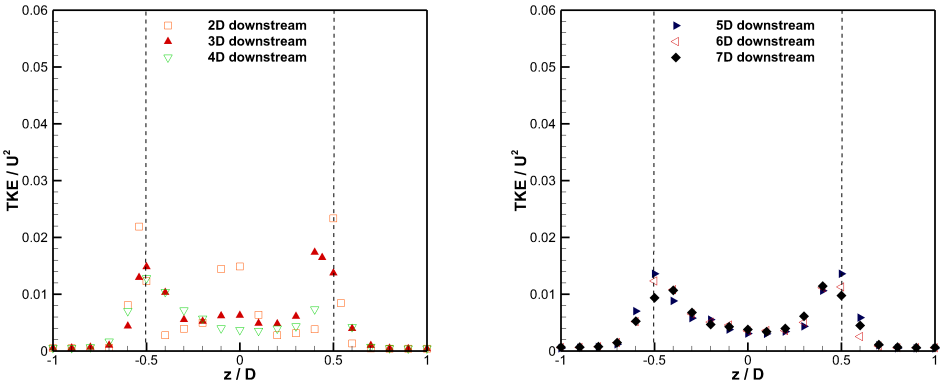

(a) $2-4D$ (b) $5-7D$

Figure 3.44: Turbulent kinetic energy downstream of a two-bladed turbine with 9^o blade pitch angle (dashed lines denote edge of turbine)

Plotting the maximum velocity deficit downstream of the turbine has been found to be useful for a simple comparative measure of the wake downstream of a turbine. This maximum velocity deficit is shown in figure 3.45 (a), where the data is plotted for the two-bladed with blade-pitch-angles of 3^o (optimum) and 9^o (non-optimum), and the three-bladed turbine with blade pitch angle of 6^o all of which are fitted with power laws. Plotted in this way it can be seen more clearly what was observed in the contour plots of the streamwise velocities above, where the off-optimum condition has a smaller deficit initially than when the turbine is set with the optimum blade-pitch-angle. This initial reduction in velocity deficit could be due to the reduction in power extraction and differing tip-speed-ratio which also corresponds to the wake at optimum conditions but with lower upstream velocities seen in section 3.2. However, after $4D$ the maximum velocity deficit in all conditions seem to be very similar with the two-bladed turbine with off-optimum blade pitch angle and the three-bladed turbine. The two-bladed and three-bladed

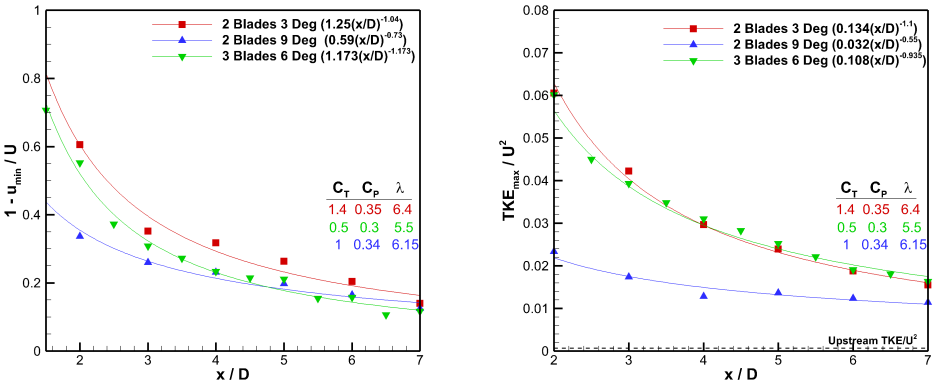

(a) Maximum streamwise velocity deficit

(b) Maximum TKE

Figure 3.45: The maximum streamwise velocity deficit and TKE downstream of a two-bladed turbines with on- and off-optimal blade pitch angles

turbine at optimum blade-pitch-angles decay at a similar rate but there is a constant small difference between them attributed to the uncertainty with the measurement, which could be attributed to the differing thrust coefficients, but this highlights differences that were not so visible in the comparison of mean velocity contour plots.

The normalised maximum TKE for both two-bladed and three-bladed turbines is plotted in figure 3.45 (b), where the data is fitted with a power-law. From the power-law fit it is observed that the wake of the turbines with the optimum blade-pitch-angle has a power-law decay rate twice that of the wake of the off-optimum turbine. The maximum TKE downstream of the turbine with 9^o blade pitch angle is fairly constant through the wake, by $7D$ downstream the TKE levels are becoming similar to the levels at optimum blade-pitch-angle. These results show that setting the blade pitch angle to off-optimum reduces the turbine's effect on the surrounding flow. The reduction in turbulence levels and velocity deficit could be a consequence

of either the decreased power extraction, the reduced thrust, change in tip-speed-ratio or a combination of both.

3.4 Wake Downstream of Turbine Structure without Blades

The wake of the turbine has been characterised in the uniform flow condition; however it important to assess the effect of the turbine support as the data presented by Myers & Bahaj (2009) shows that this may have a large impact on the wake downstream of some turbine designs. The three-dimensional velocities downstream of the turbine assembly without blades are shown in figure 3.46 at hub height. In all three velocity components the only effects of the turbine structure is seen at $1.5D$ and $2D$ downstream and in the region directly downstream of the structure. The effect on the mean velocities is that the streamwise component is reduced and in the vertical and spanwise mean velocities are increased slightly which could be due to vortex shedding from the structure but no peaks were found from spectral analysis. The decay characteristics are consistent to what was found with the turbine blades, where minima were seen at the centre of the channel up to $2D$ downstream (figure 3.4). In comparison Myers & Bahaj (2009) found that their turbine support structure had a greater impact on the downstream flow, where velocity deficit was visible up to $3.5D$ downstream showing that the shape and size of the turbine support structure is important especially to consider its impact on the near-wake.

Turbulence statistics, u'/U, v'/U, w'/U and TKE are shown downstream of the the turbine structure with no blades in figures 3.47-3.50. Similar to the mean velocities, there is an increase in velocity fluctuations directly behind the structure between $1.5D$ and $3D$ at the centre of the channel. Further downstream the turbine structure without blades is having little effect, this shows that the wake effects behind the rotating blades have the greatest

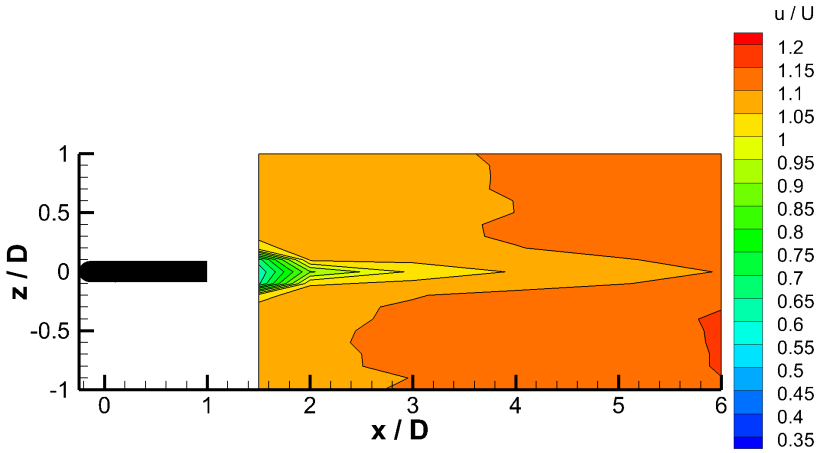

(a) streamwise velocity

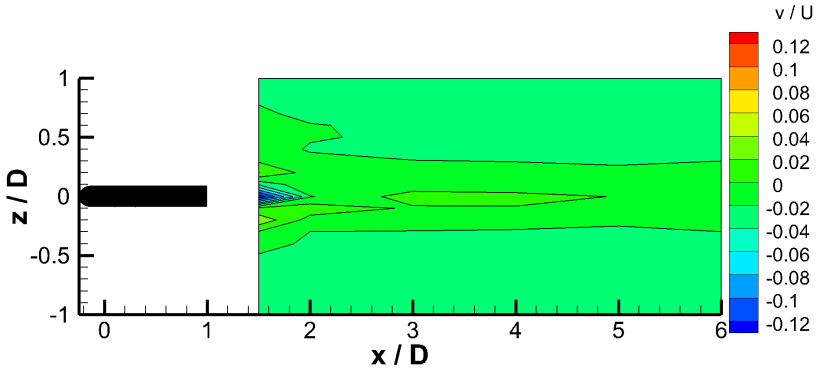

(b) vertical velocity

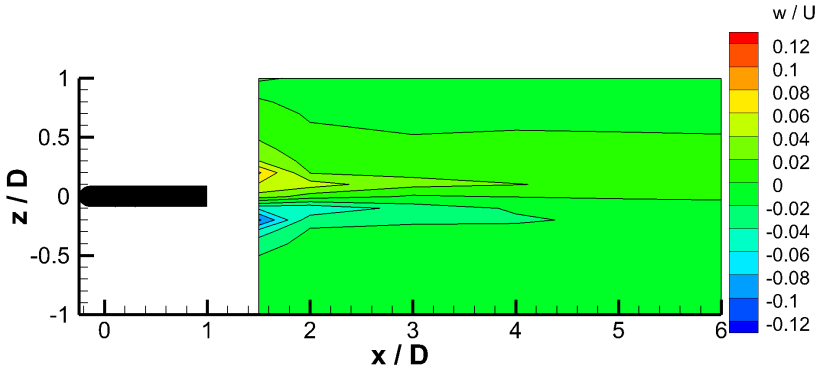

(c) spanwise velocity

Figure 3.46: Three-dimensional velocity contours downstream of the turbine structure without blades

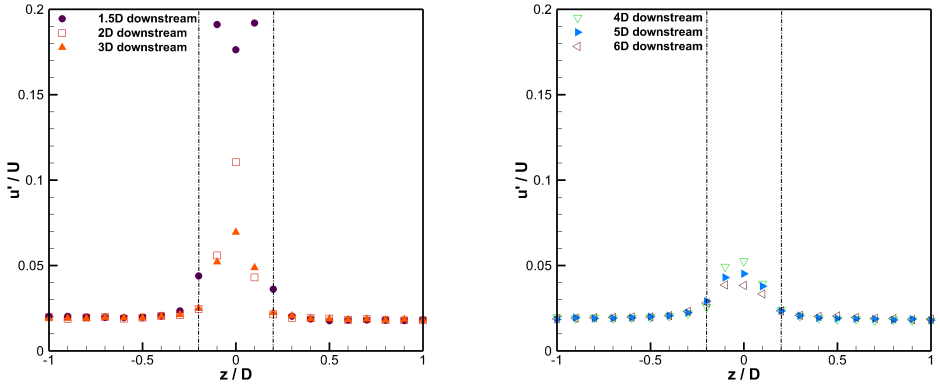

(a) $2-4D$ (b) $5-7D$

Figure 3.47: Streamwise Reynolds normal stresses downstream of the turbine structure without blades (dashed-dot lines denote edge of turbine structure)

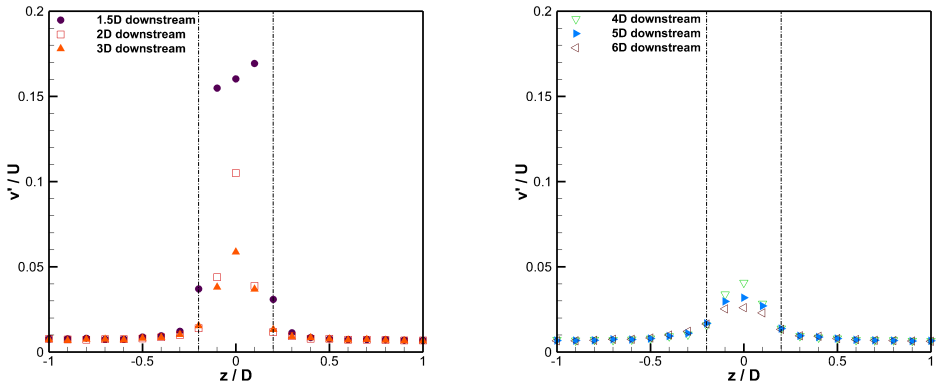

(a) $2-4D$ (b) $5-7D$

Figure 3.48: Vertical Reynolds normal stresses downstream of the turbine structure without blades (dashed-dot lines denote edge of turbine structure)

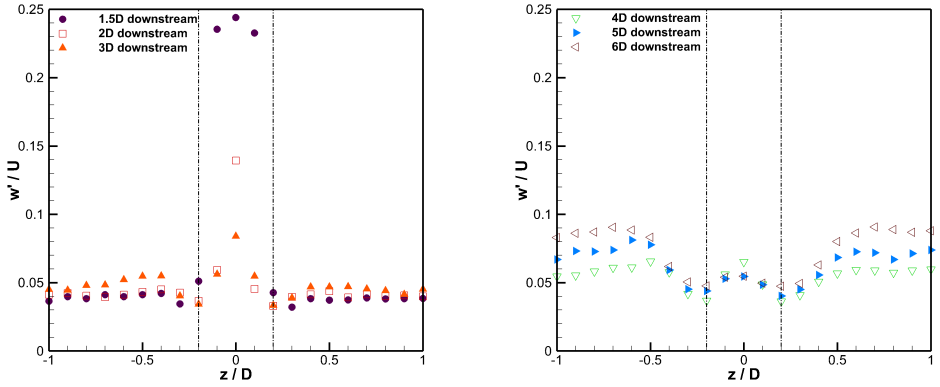

(a) $2-4D$ (b) $5-7D$

Figure 3.49: Spanwise Reynolds normal stresses downstream of the turbine structure without blades (dashed-dot lines denote edge of turbine structure)

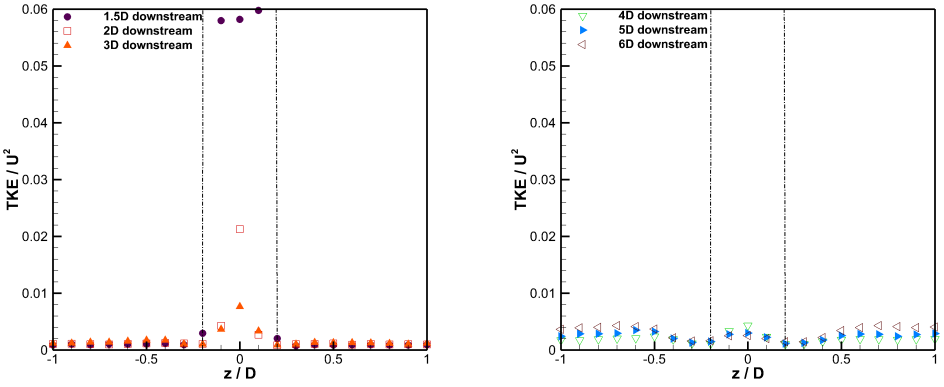

(a) $2-4D$ (b) $5-7D$

Figure 3.50: Turbulent kinetic energy downstream of the turbine structure without blades (dashed-dot lines denote edge of turbine structure)

impact on the flow for this turbine design. Also this is consistent to the peaks seen at the centre of the channel for the first couple of diameters downstream of the three-bladed turbine, in section 3.1, and for the two-bladed turbine, in section 3.3.

3.5 Chapter Summary

Initially the flow downstream of the three-bladed turbine with optimum blade-pitch-angle was measured, the upstream flow was uniform with low TI (2%) and a mean velocity of $0.9m/s$. These wake measurements were taken at five different heights up to $7D$ downstream. The dominant features of the wake were the effects of the swirling motions created from the rotation of the turbine which were visible in the mean spanwise and vertical velocities. It is suggested that the reason for the difference to the absorption disk, measured by Harrison et al. (2010), in TKE downstream is because these swirling features are not present downstream of the disk. The Reynolds stress anisotropy of the wake of the turbine was calculated, which highlighted the anisotropic nature of the flow suggesting that numerical models should not assume isotropic turbulence.

Further velocity measurements were taken with lower upstream velocities, of $0.45m/s$ and $0.68m/s$, with identical tip-speed-ratios ($\lambda = 6.15$) which showed that Reynolds number affected the wake structure. At both lower upstream velocities the mean velocity deficit was reduced. However the maximum TKE at $0.68m/s$ was similar to that downstream of the turbine at $0.9m/s$, but the maximum TKE at $0.45m/s$ was consistently lower in the very near-wake.

To compare the effects of different blade numbers on the wake, velocity measurements were taken downstream of a two-bladed turbine. At optimum blade-pitch-angles there was little difference between the two- and three-bladed turbine wakes, but at a non-optimum blade-pitch-angle (two blades

with 9^o angle) the fluctuating velocities downstream were much lower. Finally in the uniform flow with low TI (2%) the wake of the turbine support structure (without blades) was measured and it was found that the wake-effects were minimal after $2D$ downstream. Having characterised the wake in this uniform, low TI flow it now important to consider the wake effects in more realistic conditions. In the next chapter the wake of the turbine will be measured in a uniform flow with higher TI (5%) and then in a non-uniform flow at identical TI.

Chapter 4

Wake Characterisation in Grid Generated Turbulent and Non-Uniform Steady Flow

In this chapter tidal stream turbine wakes are investigated in more realistic flows. Firstly, the level of turbulence within the high-speed water-channel is increased by means of a grid upstream of the working section, while keeping the mean flow uniform. Further, the velocity profiler was placed upstream of the working section, creating a non-uniform velocity profile with similar levels of turbulence to the tests with the grid. The near-wake downstream of the three-bladed turbine with optimum blade pitch angle was measured using ADV in both flow conditions.

4.1 Grid Generated Turbulence

To increase turbulence levels in the channel a grid was placed upstream of the working section which created a flow with $TI \approx 5\%$ as described in section 2.6. The flow downstream of the three-bladed turbine, set to the optimum blade-pitch-angle of 6^o and placed $0.5m$ downstream of the grid, the flow

characteristics were measured using ADV as described in section 2.4. To compare the wake characteristics to those in the undisturbed channel flow (in section 3.1) the mean upstream velocity was set to $0.9m/s$ and the torque was set to 20% of the motor's maximum torque resulting in a tip-speed-ratio, $\lambda = 6.15$, power coefficient, $C_P = 0.34$, and thrust coefficient, $C_T = 1$. It was observed from the work in chapter 3 that the centre-plane measurements were sufficient to characterise the near-wake, and hence velocity measurements were taken at a height equal to the centre of the turbine, across the width at least every $50mm$, and at downstream distances of $1.5D$, $2D$, $3D$, $4D$, $5D$ and $6D$. Physical restrictions in the water-channel, due to the positioning of the grid within the working section, meant that it was not possible to take measurements any further downstream than $6D$, whereas in the uniform flow with low TI it was possible to measure the wake up to $7D$ downstream.

4.1.1 Three-Dimensional Mean Velocity Contours

Figure 4.1 shows the three-dimensional mean velocities normalised by the mean upstream streamwise velocity. The greatest shear is found to be directly downstream of the blade edges (i.e. at $z/D = \pm 0.5$). The mean streamwise velocity decreases to around 35% of the mean upstream velocity close to the turbine at the edge of the blades. By $6D$ downstream the mean streamwise velocity has recovered to 70% of the upstream. These results in the streamwise mean velocities are consistent with the results in the channel with a lower upstream TI of approximately 2%. Similar to the wake of the three-bladed turbine in low TI conditions, discussed in section 3.1, there is an acceleration of the flow at the edges of the channel due to the effect of blockage. The mean vertical velocities shown in figure 4.1(b) are also consistent with the previous wake results, where the effect of swirl is visible in the near-wake. The swirl can be seen by the positive velocities on the LHS and the negative velocities on the RHS, of the turbine looking downstream, corresponding to the clockwise rotation of the turbine blades. These velocities are

of the order of 10% of the mean upstream streamwise velocity. Additionally these swirling velocities are seen to drift slightly to the RHS of the channel the further downstream, one explaination is that the clockwise rotation is causing the wake to move in this manner. Correspondingly the spanwise velocities, figure 4.1(c), show the swirl effects but these effects are only seen for the first few diameters downstream and this result is consistent with the study by Chamorro et al. (2013). The mean spanwise velocities in the grid-generated turbulent flow are similar to those in the channel alone discussed in section 3.1, thus it can be concluded that the increase in the turbulence intensity from 2% to 5%, has little qualitative effect on the three-dimensional mean velocities downstream of the turbine.

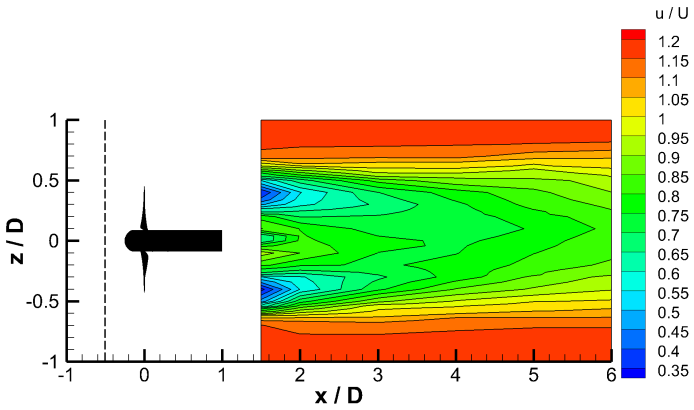

(a) streamwise velocity

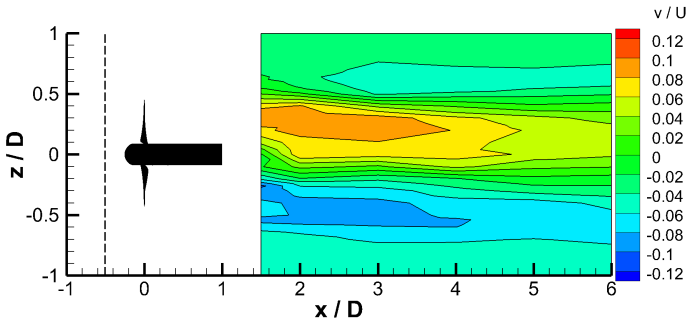

(b) vertical velocity

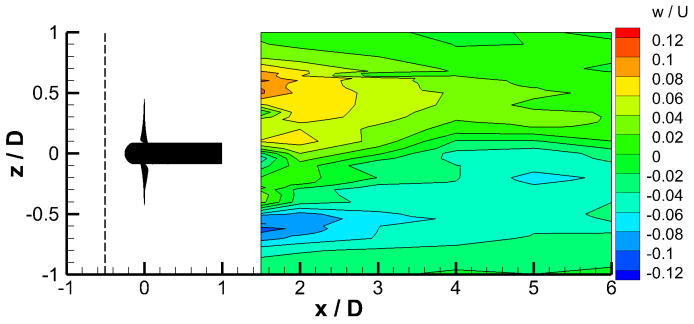

(c) spanwise velocity

Figure 4.1: Three-dimensional mean velocity contours downstream of the three-bladed turbine in 5% TI flow on the centre-plane ($y/D = 0$)

4.1.2 Reynolds Normal Stresses

To investigate the effect of the velocity fluctuations downstream of the turbine, the normalised (by the mean upstream streamwise velocity) Reynolds normal stresses (defined in equations 1.5 - 1.7) are plotted in figures 4.2 - 4.4. In the streamwise Reynolds normal stresses, shown in figure 4.2, peaks occur at the edge of the blades ($z/D = \pm 0.5$ - denoted by dashed lines) corresponding to the points at which the velocity shear is maximum and are as a consequence of the blade rotation. These peaks are greatest near to the turbine, where at $1.5D$ they are around 0.25, by $6D$ downstream the peaks are still visible, but are reduced to 0.15. In addition to the peaks at the blade edges, at $1.5D$ downstream there is a peak at the centre which is a result of the presence of the stanchion, as was highlighted in section 3.4). The peaks at the blade edges in the streamwise Reynolds normal stress decay rapidly in the first few diameters downstream, then the fluctuations remain fairly constant after $4D$. Around the outside of the wake of the turbine ($|z/D| > 0.7$) the normalised Reynolds normal stress is equal to that of the upstream measured values as shown in section 2.6. The streamwise velocity fluctuations in the region directly downstream of the turbine (i.e. $-0.5 < z/D < 0.5$) are identical to those in the low TI flow showing that at these levels the increased free-stream turbulence (from $TI \approx 2\%$ to 5%) is insufficient to affect the turbulence levels in the wake. Around the outside of the turbine however, the Reynolds normal stresses are greater due to the downstream effects of the grid.

The normalised vertical Reynolds normal stresses, shown in figure 4.3, show similar trends to those of the streamwise component, with the peaks always occurring approximately at the blade edges ($z/D = \pm 0.5$) and an additional central peak at $1.5D$ downstream due to the stanchion. Again around the outside of the wake ($|z/D| > 0.7$) the fluctuations are equal to those upstream of the turbine, directly downstream of the grid (shown in section 2.6). The normalised spanwise Reynolds normal stresses, in figure

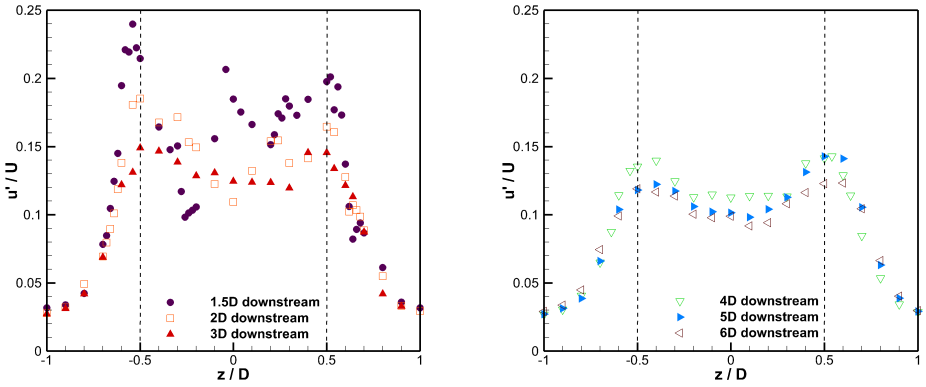

(a) $1.5 - 3D$ downstream

(b) $4 - 6D$ downstream

Figure 4.2: Streamwise Reynolds normal stress at $y/D = 0$ (dashed lines denote edge of turbine)

4.4, show a similar trend with peaks always occurring at the blade edges. At $1.5D$ downstream there is again a third peak at the centre of the channel due to the presence of the stanchion, in addition there is a reduced fluctuation between $z/D = -0.1$ and $z/D = -0.4$ which is much lower than at other distances downstream, it is unknown why this occurred and an FFT of the data in this region shows no visible peaks suggesting that it is not due to any large scale eddies i.e. vortex shedding from the stanchion. It is also seen that outside the turbine wake ($|z/D| > 0.7$) the values are much higher than in the other components, which could be a consequence of the increase in fluctuations caused by the grid or as a result of the uncertainties in the ADV technique. From these results it is observed that the distributions of the Reynolds normal stresses are both qualitatively and quantitatively the same in both low TI (2%) and high TI (5%) free-stream turbulence conditions after $2D$ downstream.

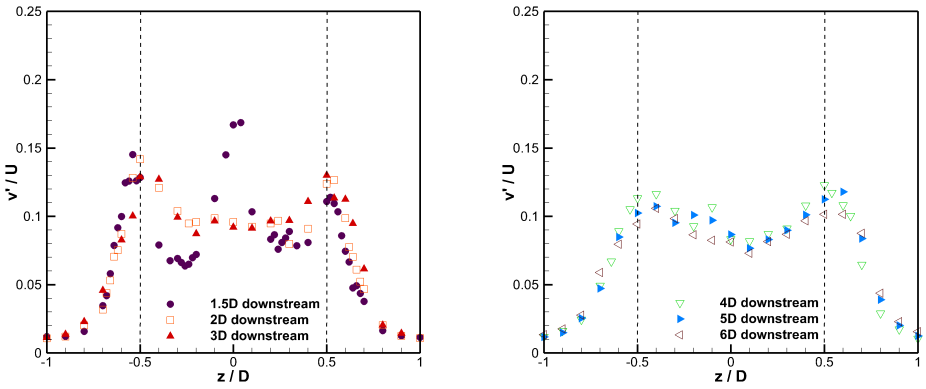

(a) $1.5 - 3D$ downstream (b) $4 - 6D$ downstream

Figure 4.3: Vertical Reynolds normal stress at $y/D = 0$ (dashed lines denote edge of turbine)

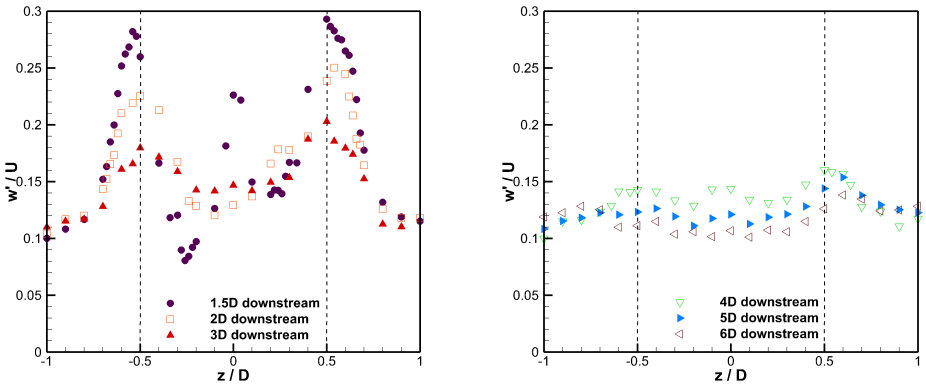

(a) $1.5 - 3D$ downstream (b) $4 - 6D$ downstream

Figure 4.4: Spanwise Reynolds normal stress at $y/D = 0$ (dashed lines denote edge of turbine)

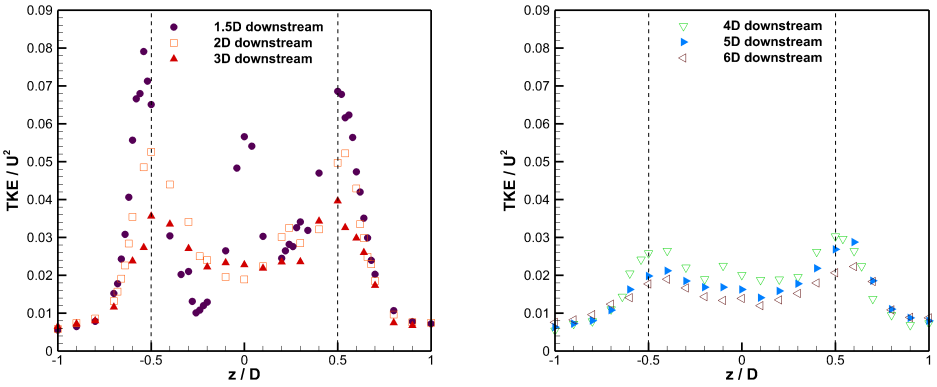

(a) $1.5 - 3D$ downstream

(b) $4 - 6D$ downstream

Figure 4.5: TKE at $y/D = 0$ (dashed lines denote edge of turbine)

4.1.3 Turbulent Kinetic Energy

The normalised Turbulent Kinetic Energy, defined in equation 1.4, downstream of the turbine is shown in figure 4.5. Corresponding to the Reynolds normal stresses, the highest levels of TKE is at the edges of the blades ($z/D = \pm 0.5$ - denoted with dashed lines) with a third central peak at $1.5D$ downstream caused by the turbine support structure. Further downstream the peak TKE levels decrease rapidly in the first $4D$ downstream but afterwards they decrease much more slowly, with peaks still three-times greater than the free-stream levels visible at the edge of the blades even at $6D$ downstream. These results for the TKE are essentially identical to those in the channel-alone case, the only difference is that the free-stream levels outside of the turbine wake are greater due to the upstream conditions as a result of the grid.

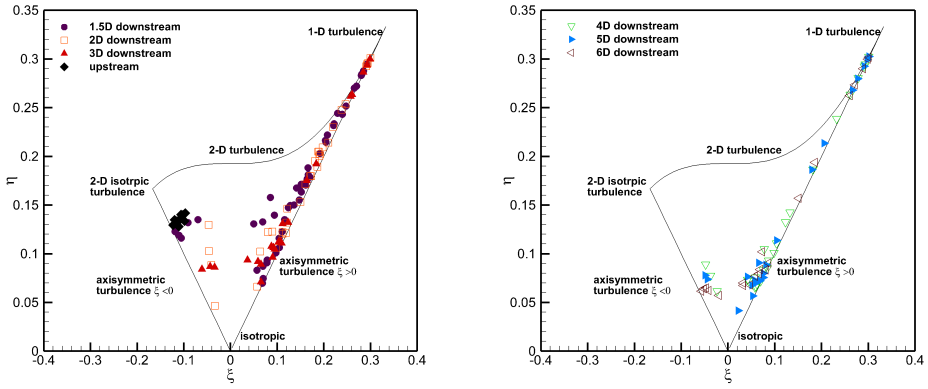

(a) $1.5 - 3D$ downstream

(b) $4 - 6D$ downstream

Figure 4.6: The Lumley triangle showing the turbulence anisotropy downstream of the turbine

4.1.4 Reynolds Stress Anisotropy

To investigate the anisotropy of the turbulent flow field downstream of the turbine the Reynolds stress anisotropy tensor is calculated and the invariants ξ and η are plotted in figure 4.6, details of how these are determined were provided in section 3.1.5. These invariants are calculated to see how anisotropic the turbulence is, for a flow to be isotropic $\xi = \eta = 0$, where all the Reynolds normal stresses are equal i.e. $u' = v' = w'$ and the Reynolds shear stresses are zero. Corresponding to the uniform flow results in section 3.1.5, it is observed that in both flow conditions the upstream turbulent flow field is initially two-dimensional. It can be seen in figure 4.6 that directly downstream of the turbine the flow is axisymmetric but further downstream the flow is becoming either one-dimensional turbulence in the outer region of the channel, or isotropic directly downstream of the turbine. These results replicated those in the uniform stream flow conditions with no grid, showing that the upstream turbulence levels has little impact on the anisotropy of

the near-wake. Again this result highlights the need for any numerical-based wake studies to take into account the anisotropy of the turbulence and not to consider it to be isotropic.

These results of the near-wake downstream of the grid are indistinguishable from the previous results in section 3.1, therefore now more complex non-uniform flows are investigated to see how the near-wake may be affected.

4.2 Non-Uniform Steady Flow

To produce a more complex flow a flow profiler was designed and built and placed upstream of the working section, details can be found in section 2.7. This flow profiler produced a steady flow with a $\frac{1}{5}th$ power law velocity profile through the depth of the channel which was measured at $1m$ downstream of the profiler with turbulence intensity of approximately 5% matching the levels found downstream of the grid. It was found in section 2.7 that with the turbine placed at $1m$ downstream of the flow profiler and by using the integral average velocity across the turbine swept area, to be $0.82m/s$, both the thrust and power coefficients collapse with tip-speed-ratio for both uniform and non-uniform flows. Experimental parameters were set, therefore, the motor's torque was set to 20% of its maximum resulting in tip speed ratio, $\lambda = 6.15$, power coefficient, $C_P = 0.34$ and, thrust coefficient, $C_T = 1$. Wake measurements were taken on five horizontal planes at depths of $-0.5D$, $-0.25D$, $0D$, $0.25D$ and $0.5D$, where $0D$ is the centre of the hub height, as it is expected that the flow profiler will have a different effect on the wake at various heights compared to the results in the uniform flow. The measurements were taken up to $5D$ downstream, which was the maximum distance downstream possible due to the physical limitations of the working section with the 'flow profiler' in place.

4.2.1 Three-Dimensional Mean Velocity Contours

Mean velocities in the non-uniform flow in $x-y$ planes are shown at $2D$ and $5D$ downstream, alongside measurements in uniform flow. Figures 4.7 and 4.8 show the normalised mean streamwise velocity contours at $2D$ and $5D$ downstream in both the uniform with low turbulence intensity, as described in chapter 3, and non-uniform flows, which are plotted in this manner for ease of comparison. In addition to the contours of the velocities in figures 4.7 - 4.12 a silhouette of the turbine is also included to highlight where the turbine is relative to the velocities plotted. At $2D$ downstream, for both flow conditions, the main region of the streamwise velocity deficit is seen to be contained within a roughly circular area which is approximately 10% larger than the swept area of the turbine. The smallest streamwise velocities, shown by the blue regions, are observed to occur at the tips of the blades, these regions are found above the centreline and is likely to be due to the blockage caused by the stanchion which is supporting the turbine from above. By $5D$ downstream the streamwise velocity has recovered to 70% of the upstream velocity. For the flow profile results the non-uniformity of the upstream flow is still visible downstream, at both distances shown; this can be observed by the different contour levels around the outside of the main wake area. In contrast in the uniform flow the velocity levels are constant in the region outside the turbine wake.

The mean vertical velocity contours are shown in figures 4.9 and 4.10 at $2D$ and $5D$ downstream. In both flow conditions the swirl effect is observed, with the negative velocities on the right-hand-side looking downstream and the positive velocities on the left-hand-side, resulting from the clockwise rotation of the turbine blades. At $2D$ downstream in the non-uniform flow there is a downward flow above the turbine (figure 4.9(b)), this is most likely due to the large standing surface wave being produced directly downstream of the stanchion in the profiled flow because of the higher velocities at the top of the water column.

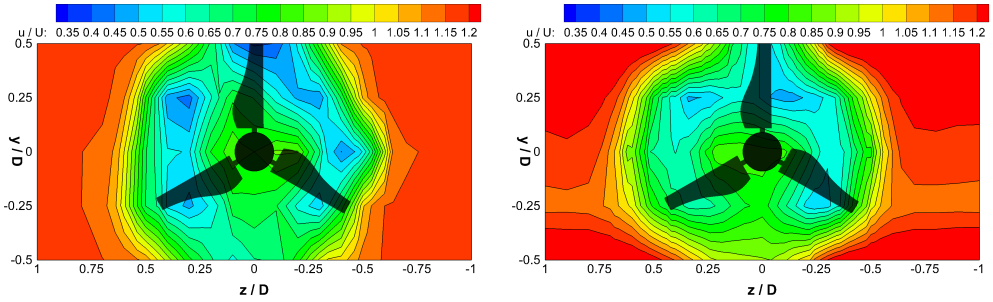

(a) Uniform flow (b) Non-uniform flow

Figure 4.7: Contours of the mean streamwise velocity $2D$ downstream of a turbine

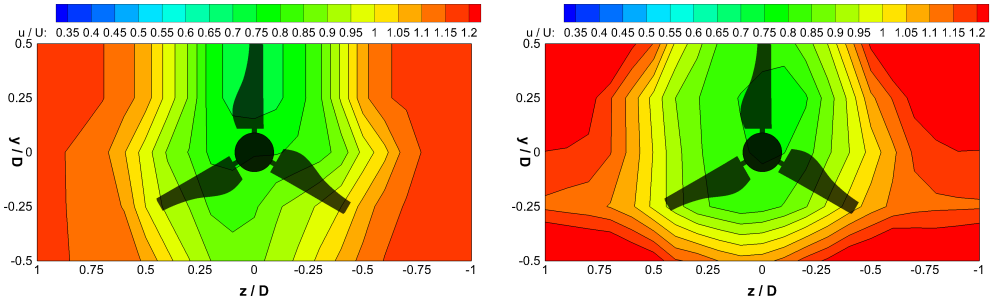

(a) Uniform flow (b) Non-uniform flow

Figure 4.8: Contours of the mean streamwise velocity $5D$ downstream of a turbine

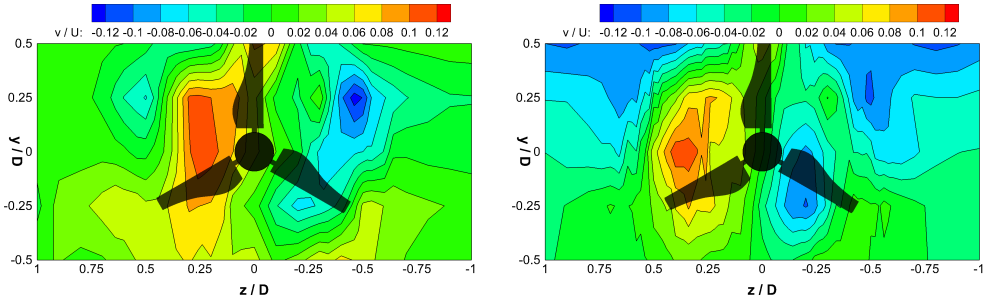

(a) Uniform flow (b) Non-uniform flow

Figure 4.9: Contours of the mean vertical velocity $2D$ downstream of a turbine

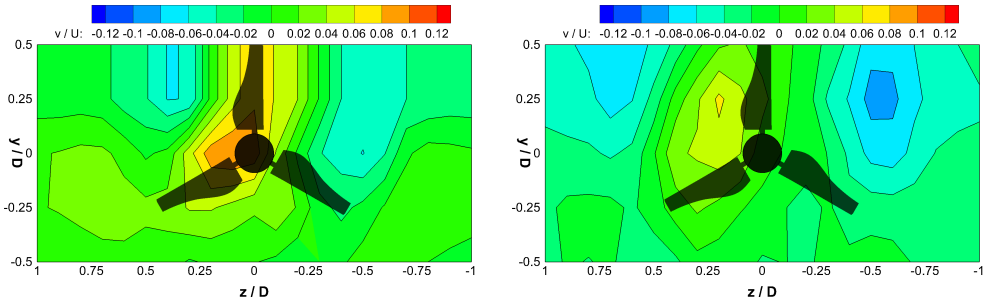

(a) Uniform flow (b) Non-uniform flow

Figure 4.10: Contours of the mean vertical velocity $5D$ downstream of a turbine

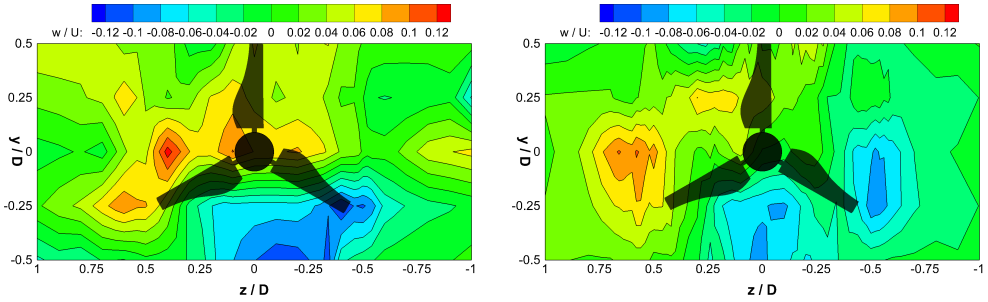

(a) Uniform flow (b) Non-uniform flow

Figure 4.11: Contours of the mean spanwise velocity $2D$ downstream of a turbine

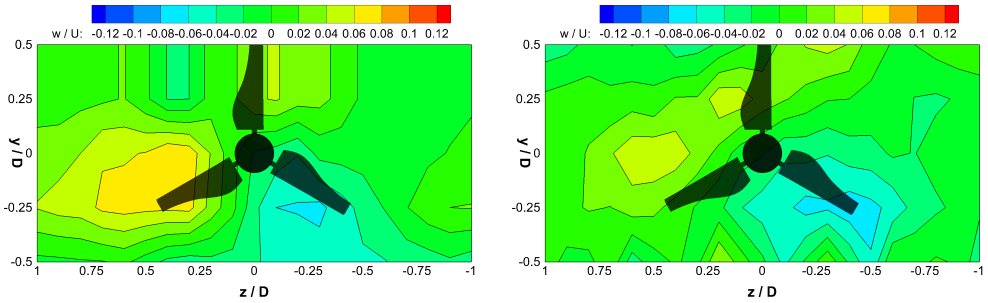

(a) Uniform flow (b) Non-uniform flow

Figure 4.12: Contours of the mean spanwise velocity $5D$ downstream of a turbine

The mean spanwise velocity contours are shown in figures 4.11 and 4.12 at $2D$ and $5D$ downstream. Similar to the vertical velocity component, the swirl effects are visible up to $5D$ downstream in the spanwise mean velocity, where the positive velocities show the flow moving from right to left looking downstream. Again the mean vertical velocities are seen to be slightly smaller in the non-uniform flow compared to those in the uniform flow.

The mean velocity contours plotted in $x - z$ planes at various heights are shown in figures 4.13 - 4.15. Figure 4.13 shows the normalised mean streamwise velocity downstream of the turbine in non-uniform flow. The non-uniformity of the flow is still present downstream of the turbine and is more visible when plotted in this manner. This difference is illustrated in the lower mean streamwise velocities (u/U) at $y/D = -0.5$ and $y/D = -0.25$ compared to the higher velocities in $y/D = 0.5$ and $y/D = 0.25$. The non-uniformity is not present in uniform flow conditions, shown in chapter 3, as the downstream streamwise velocities are symmetrical about the $x - z$ centreline plane. The maximum velocity deficit, which occurs at the blade edges ($z/D = \pm 0.5$ at the centre of the turbine), is around 35% of the upstream velocities which is the same as in the other two flow conditions of uniform flow with low and high free-stream turbulence levels. The mean streamwise velocities at heights below the centre of the turbine, in figures 4.13(a) and (b), show that the maximum deficit is lower than that in the uniform flow at heights above the centre of the turbine. In figures 4.13(d) and (e), the maximum deficit is greater, this is due to the effect of the mean flow caused by the flow profiler, which has a small impact on the wake at different heights. Overall any impact of the velocity profiler appears to be minimal in the streamwise velocities, it would be important to consider flows with a greater shear to see if this had a larger impact on the flow, however, in the facilities used in this study, this was the largest shear flow that could be produced using this approach whilst maintaining a smooth velocity profile.

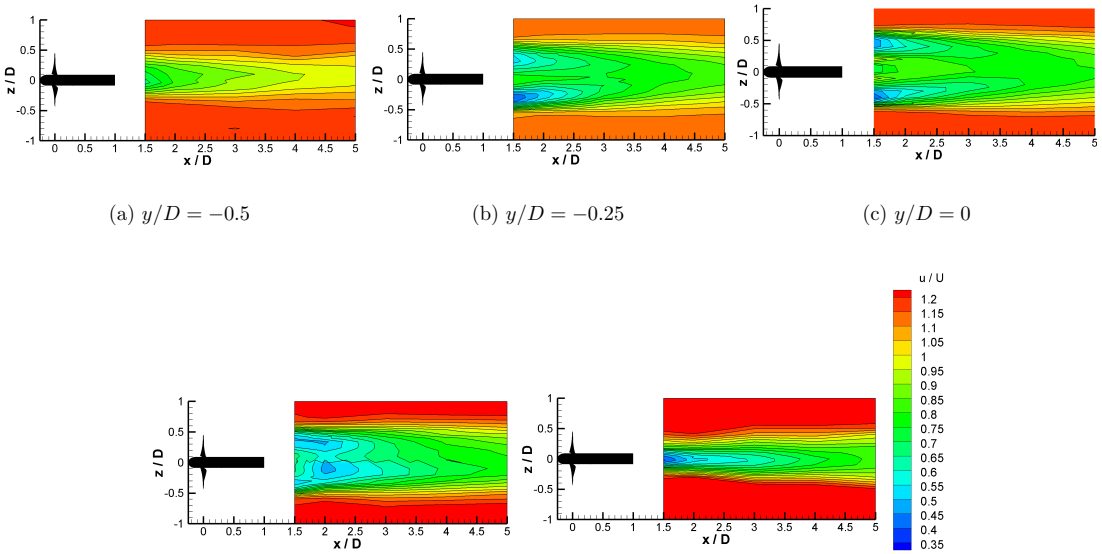

(a) $y/D = -0.5$ (b) $y/D = -0.25$ (c) $y/D = 0$

(d) $y/D = +0.25$ (e) $y/D = +0.5$

Figure 4.13: Contours of the mean streamwise velocities behind a turbine

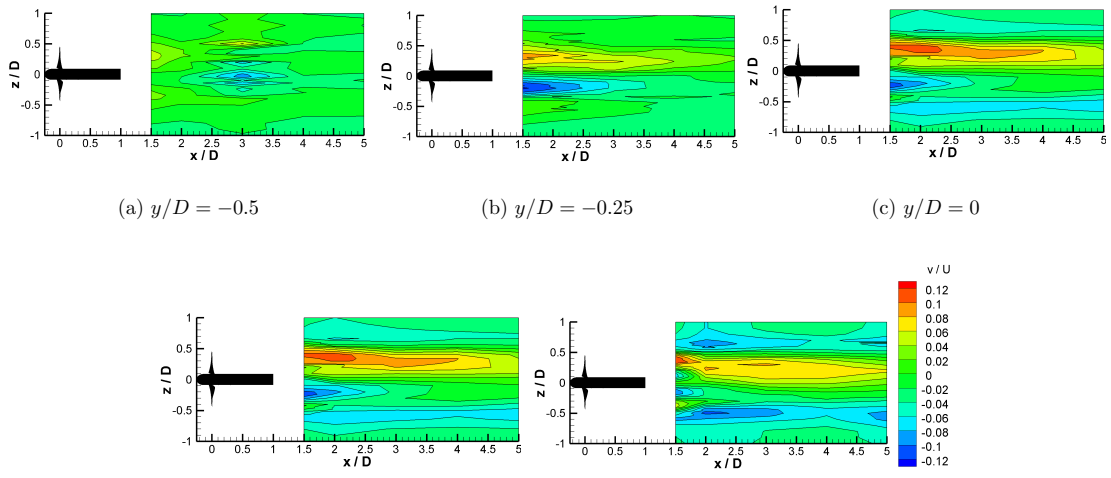

(a) $y/D = -0.5$ (b) $y/D = -0.25$ (c) $y/D = 0$

(d) $y/D = +0.25$ (e) $y/D = +0.5$

Figure 4.14: Contours of the mean vertical velocities behind a turbine

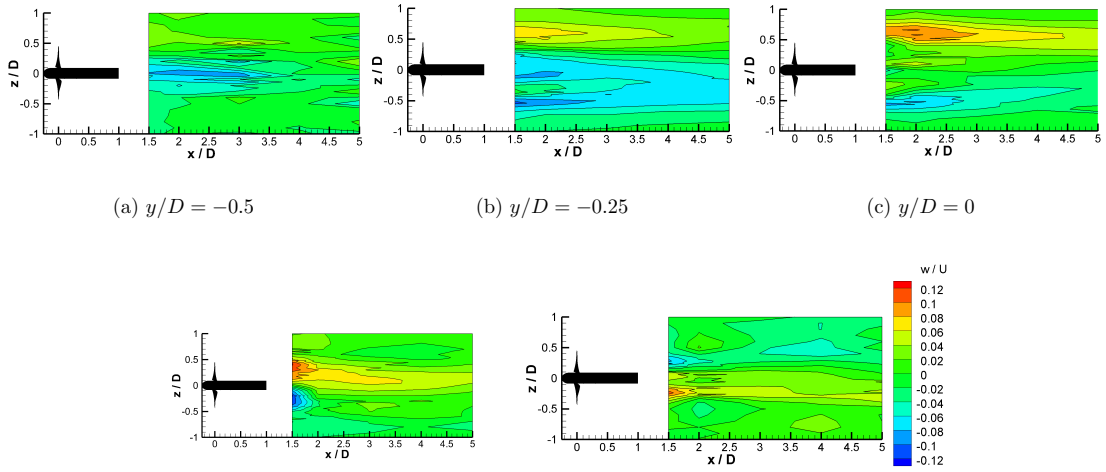

(a) $y/D = -0.5$ (b) $y/D = -0.25$ (c) $y/D = 0$

(d) $y/D = +0.25$ (e) $y/D = +0.5$

Figure 4.15: Contours of the mean spanwise velocities behind a turbine

Figure 4.14 shows the mean vertical velocity contours downstream of the three-bladed turbine in non-uniform flow. Similar to the vertical velocities in uniform flow, the effect of swirl is prominent with the maximum mean velocities being of the order of 10% of the average upstream velocity. These swirl effects are visible at all heights but are most visible at $y/D \geq 0$, which is likely to be a result of the way they are plotted - normalised by the integral average velocity over the turbine swept area - whereas the mean flow is significantly greater ($\approx 25\%$) nearer to the surface as a consequence of the flow profile. Furthermore in figure 4.15 the swirl, caused by the rotation and akin to the study by Chamorro et al. (2013), is observed in the mean spanwise velocities. The swirl is seen at all depths, but again is more prominent at $y/D \geq 0$, due to the increased upstream velocities at these heights and the manner in which they are normalised by the integral average velocity.

4.2.2 Reynolds Normal Stresses

Notwithstanding the subtle differences observed in the mean wake flow downstream of the turbines, illustrated in figures 4.7 - 4.15, the flows were generally similar and this is believed to be due to the dominant effect of the swirl imparted by the turbine to both the uniform and non-uniform inlet flows. Therefore the turbulence statistics within the wake are investigated. First, figures 4.16, 4.17 and 4.18 show the Reynolds normal stresses in the streamwise, vertical and spanwise directions respectively in both uniform ($TI \approx 2\%$ - red symbols) and non-uniform ($TI \approx 5\%$ - green symbols) flow conditions. The Reynolds normal stresses are shown at different heights at all measurement locations in the non-uniform flow in figures 4.19 - 4.21. The Reynolds normal stresses shown in figures 4.16 - 4.18, are similar in both flow conditions. The only differences can be seen at the measurement edges, where in the non-uniform flow the Reynolds normal stresses are slightly greater than those in the uniform flow. In the spanwise component this is the most prominent, however some of this increase could be an effect of ADV noise,

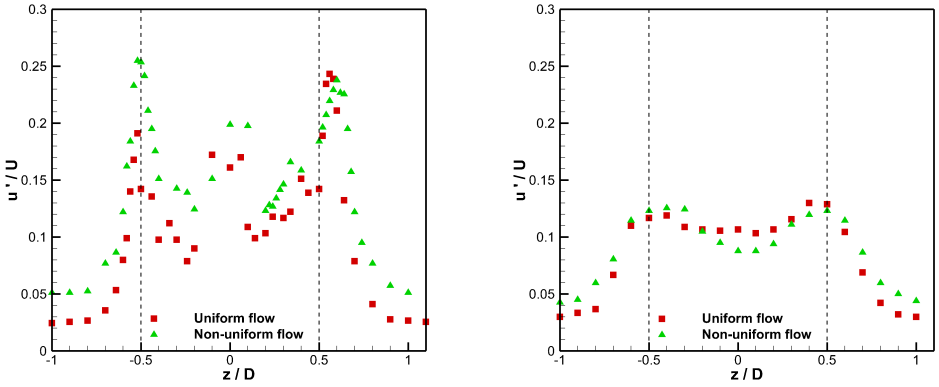

(a) 1.5D downstream (b) 5D downstream

Figure 4.16: Streamwise Reynolds normal stress at $y/D = 0$ (dashed lines denote edge of turbine)

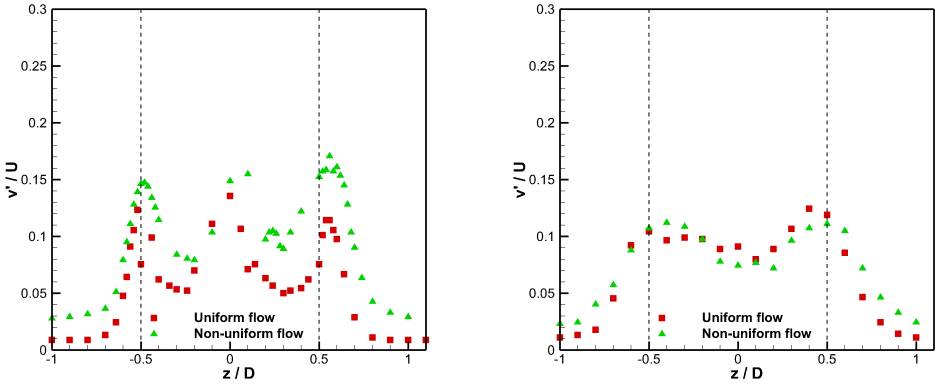

(a) 1.5D downstream (b) 5D downstream

Figure 4.17: Vertical Reynolds normal stress at $y/D = 0$ (dashed lines denote edge of turbine)

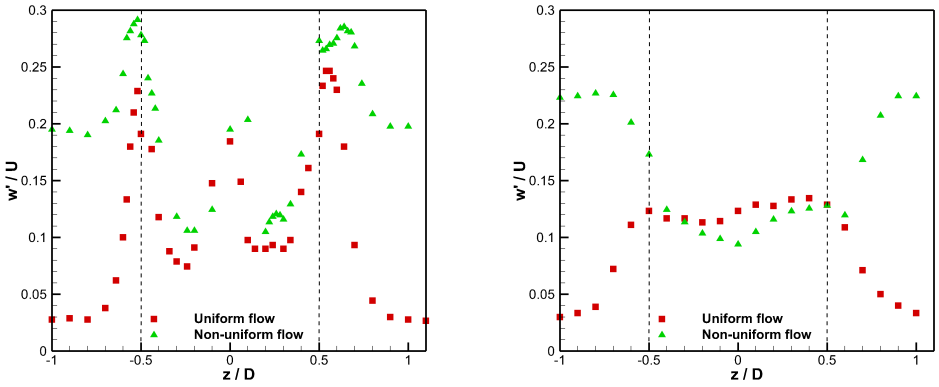

(a) 1.5D downstream (b) 5D downstream

Figure 4.18: Spanwise Reynolds normal stress at $y/D = 0$ (dashed lines denote edge of turbine)

discussed in the following chapter. At 2D downstream when $y/D = 0$, the maximum normal stresses are seen to occur downstream of the edge of the blades and have a third maximum peak at the centre caused by the effect of the hub and stanchion (discussed in section 3.4). There is an increase in the normal stresses in the non-uniform flow at 2D downstream than in the uniform flow which is most likely due to the increased upstream turbulence. By 5D downstream all three Reynolds normal stresses have a maximum of about 0.12, i.e. 12% of the upstream streamwise component, and are of similar magnitude across the entire swept area of the turbine.

The Reynolds normal stresses are plotted at five measurement depths at five distances downstream of the turbine in figures 4.19 - 4.21. The streamwise Reynolds normal stresses, shown in figure 4.19, show peaks occurring at the edge of the blades. These peaks are visible at all depths and are still visible at 5D downstream. Unlike the mean streamwise velocities, in the streamwise Reynolds normal stresses some symmetry is observed at a height

equal to the centre of the turbine. This symmetry is clearest at $1.5D$ and $2D$ downstream where collapse is seen at $y/D = 0.25$ and $y/D = -0.25$. At $y/D = 0.5$ there is some symmetry with $y/D = -0.5$ in the regions where $|z/D| > 0.25$, but not in the central region as the stanchion is present at $y/D = 0.5$ but not at $y/D = -0.5$. This symmetry is observed in the Reynolds normal stresses rather than mean velocities because of the upstream flow conditions where the mean velocities vary through the depth; the velocities change but the Reynolds normal stresses are generally constant and the normalisation by using the integral average velocity over the turbine swept area is more reasonable (see section 2.7 for a discussion of measurements of the flow directly downstream of the profiler). At $3D$ downstream the Reynolds normal stresses are much greater at $y/D = 0.5$, this is probably due to a combination of ADV noise and vibrations of the ADV device at this depth as the ADV body is submerged, it is unclear why this is only occurring at this location and not at other points downstream. At the outer regions of the channel, where $|z/D| > 0.7$, u'/U is constant at all depths and distances downstream (apart from the discussed case at $3D$ downstream for $y/D = 0.5$) showing that the increase in streamwise Reynolds normal stresses by the 'flow profiler' is constant through the depth of the channel at all measurement locations.

In accordance with the streamwise Reynolds normal stresses, the vertical normal stresses shown in figure 4.20 are also symmetric in a similar manner around the central hub height, where there is collapse at $y/D = -0.25$ and $y/D = 0.25$. Beyond $|z/D| \approx 0.7$, i.e. outside of the wake, the standard deviations are equal to those upstream.

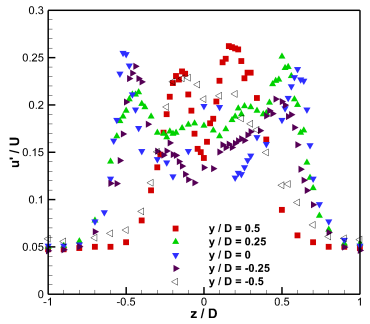

(a) 1.5D downstream

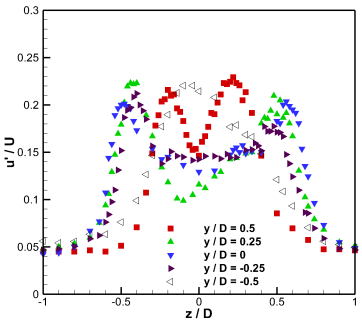

(b) 2D downstream

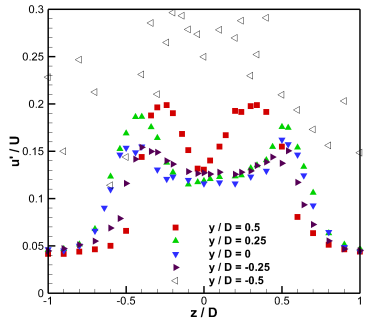

(c) 3D downstream

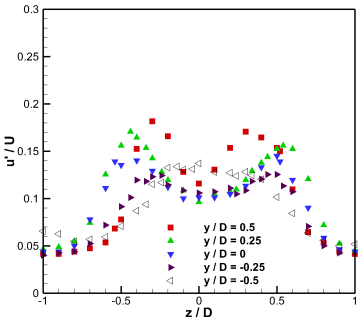

(d) 4D downstream

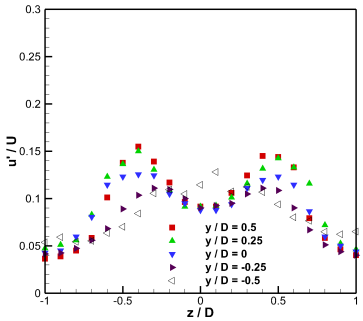

(e) 5D downstream

Figure 4.19: Streamwise Reynolds normal stress downstream of the three-bladed turbine

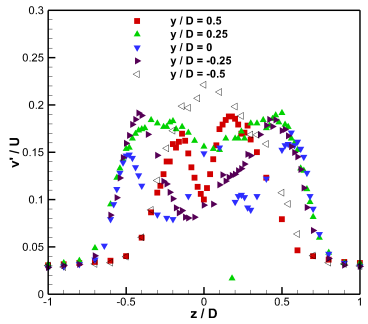

(a) 1.5D downstream

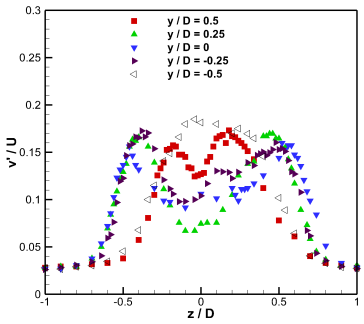

(b) 2D downstream

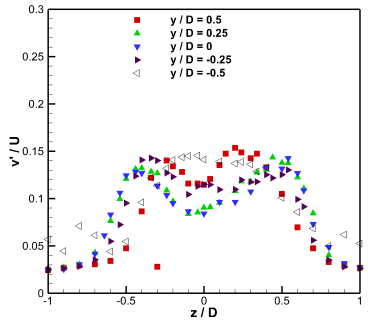

(c) 3D downstream

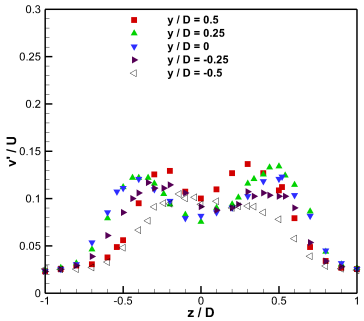

(d) 4D downstream

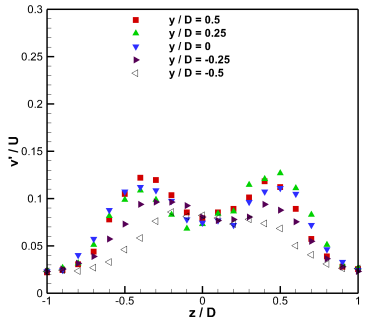

(e) 5D downstream

Figure 4.20: Vertical Reynolds normal stress downstream of the three-bladed turbine

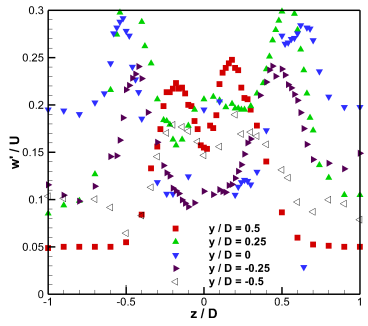

(a) 1.5D downstream

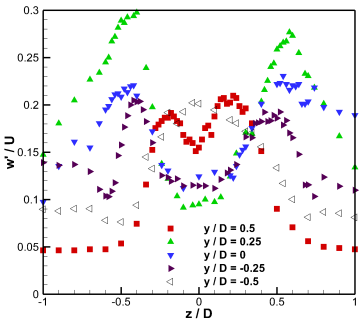

(b) 2D downstream

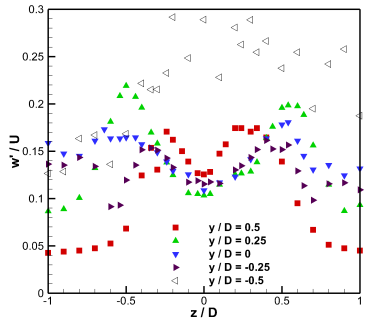

(c) 3D downstream

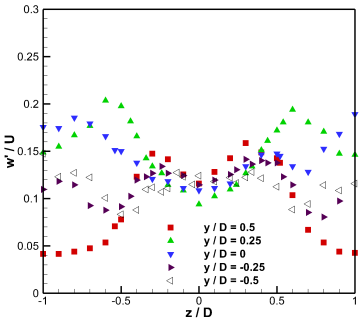

(d) 4D downstream

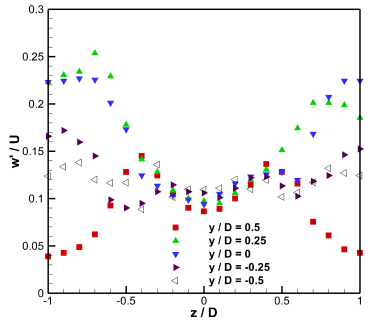

(e) 5D downstream

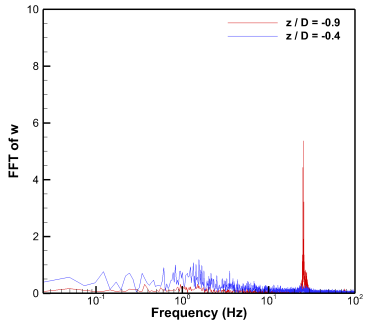

(f) FFT of w at $z/D = 0.9$ at 5D downstream

Figure 4.21: Spanwise Reynolds normal stress downstream of the three-bladed turbine

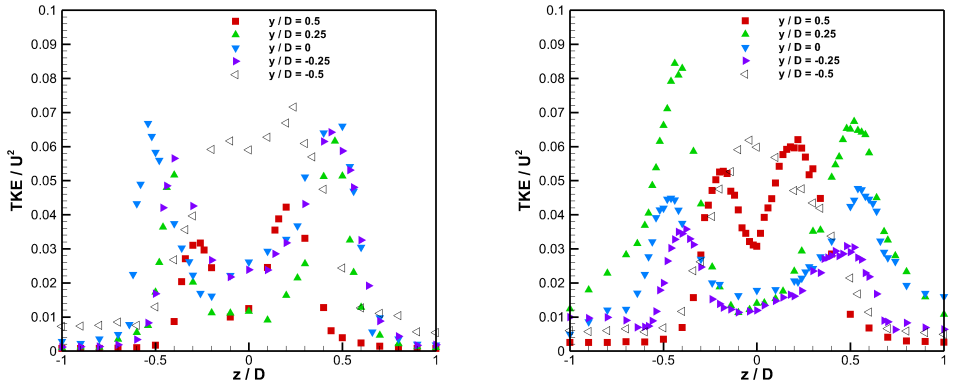

(a) Uniform steady flow (b) Non-uniform steady flow

Figure 4.22: TKE downstream of the turbine at $x/D = 2$

The spanwise Reynolds normal stresses, shown in figure 4.21, are more complex in appearance but this is mostly due to the inherent ADV noise issues, which are found to be greatest in this component for this ADV arrangement (Khorsandi et al., 2012). Because of this issue with noise, the results should be viewed in a qualitative rather than quantitative manner; that is, it can be observed that there are peaks occurring at the edge of the blades but the precise values should be treated with caution. As the results in chapter 5 indicate, the maximum TKE is a much more robust measure of wake recovery.

4.2.3 Turbulent Kinetic Energy

In figures 4.22 - 4.25 the normalised TKE downstream of the turbine is presented at five different depths in both the uniform flow and non-uniform flow. In the uniform flow at $2D$ downstream, figure 4.22, the TKE is symmetric about the horizontal centreplane, in particular it is symmetric at

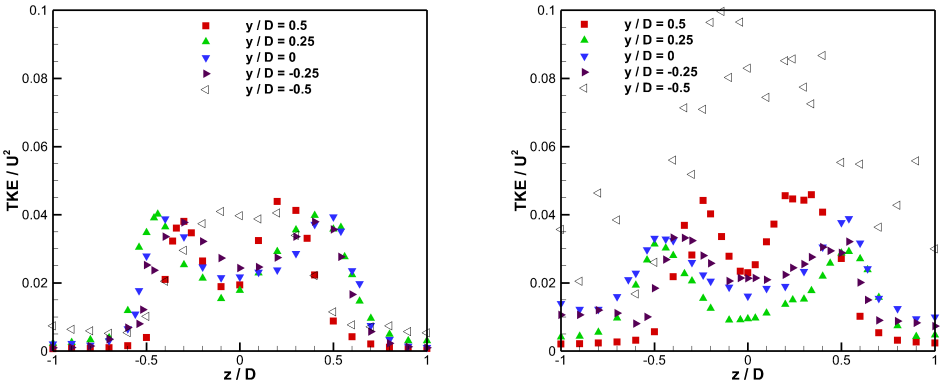

(a) Uniform steady flow (b) Non-uniform steady flow

Figure 4.23: TKE downstream of the turbine at different heights at $x/D = 3$

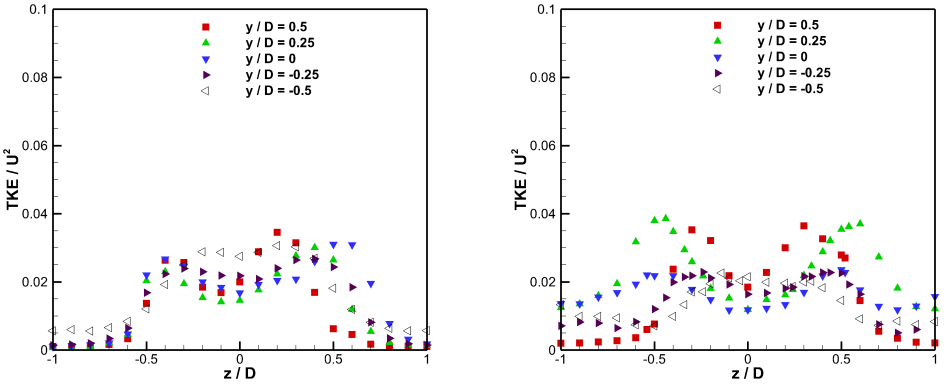

(a) Uniform steady flow (b) Non-uniform steady flow

Figure 4.24: TKE downstream of the turbine at different heights at $x/D = 4$

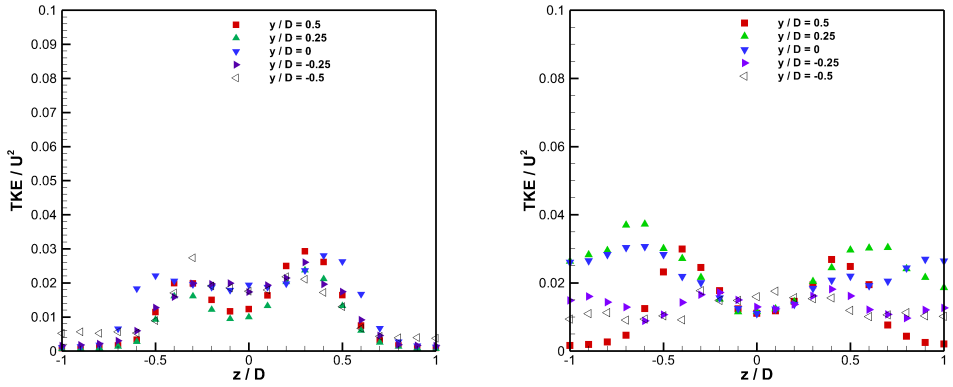

(a) Uniform steady flow

(b) Non-uniform steady flow

Figure 4.25: TKE downstream of the turbine at different heights at $x/D = 5$

$y/D = \pm 0.25$, with the horizontal plane of the turbine axis having the greatest TKE levels. In the non-uniform flow the TKE levels are not symmetric about the horizontal centreplane because of the impact of the upstream flow (shown in figure 4.22(b)). At $0.25D$ above the centre observed maximum TKE levels are 30% greater than that observed in the uniform flow. Similar to the uniform flow at $2D$ downstream, maximum TKE levels occur at the tip of the blades. At $3D$ and $4D$ downstream in the uniform flow conditions at heights $y/D = -0.25, 0$ and 0.25 the TKE collapses, at $y/D = 0.5$ there is only a single peak rather than two peaks that occur at the other heights because the turbine blades only pass at the centre at these heights. In the non-uniform flow at $3D$, at $y/D = -0.25, 0$ and 0.25 the TKE characteristic becomes similar but does not collapse as fully as the profiled flow in the uniform flow. For $y/D = -0.5$ the TKE is much greater, this is probably due to the ADV body being submerged in the flow and vortex shedding from the device (confirmed by a peak in the FFT of the spanwise velocity shown in figure 4.21(f)) causing vibrations of the device and giving erroneous results.

At $4D$ downstream, the TKE peaks at the blade edges, unlike in the uniform flow there is no symmetry about the central hub height because of the non-uniformity of the upstream flow and the normalisation using the integral average velocity. The peak TKE occur at $y/D = 0.25$ which is an effect of the increased upstream velocity at this height compared to $y/D = -0.25$. At $5D$ downstream the TKE levels in the uniform flow (figure 4.25(a)) are similar at all depths whereas in the non-uniform flow (figure 4.25(b)) the effects of the non-uniform upstream flow is visible, where nearer the surface the TKE levels are higher in the faster flow. These results are consistent with those in other flow conditions discussed in this thesis where the largest determining factor in the wake seems to be the swirl induced by blade rotation.

4.2.4 Reynolds Shear Stresses

In addition to mean flow velocities and Reynolds normal stresses, as the ADV measures all three components at once it is possible to calculate the Reynolds shear stresses, which are defined in equations 3.1, 3.2 and 3.3. Reynolds shear stresses are important as they transfer momentum in turbulent flows (Pope, 2011). The Reynolds shear stresses are plotted downstream of the three-bladed turbine in figure 4.26 at a height equal to the central hub height in both non-uniform flow ($TI \approx 5\%$) and uniform flow ($TI \approx 2\%$) . The normalised Reynolds shear stress in the $x - y$ plane, $\overline{u'v'}/U^2$, show similar trends to those in uniform flow after $3D$ downstream. At $1.5D$ and $2D$ downstream the Reynolds shear stress varies much more across the width of the channel in both flow conditions. The absolute maximum Reynolds shear stresses in the $x - y$ plane occur in both flow conditions (non-uniform flow ($TI \approx 5\%$) and uniform flow ($TI \approx 2\%$)) at the edge of the blades ($z/D = 0.5$) however when the Reynolds shear stress is negative in the uniform flow it is positive in the non-uniform flow and vice-versa. These maxima are related to mean shear flow caused by the swirling motion from the rotation of the blades and the difference in the two cases is a consequence

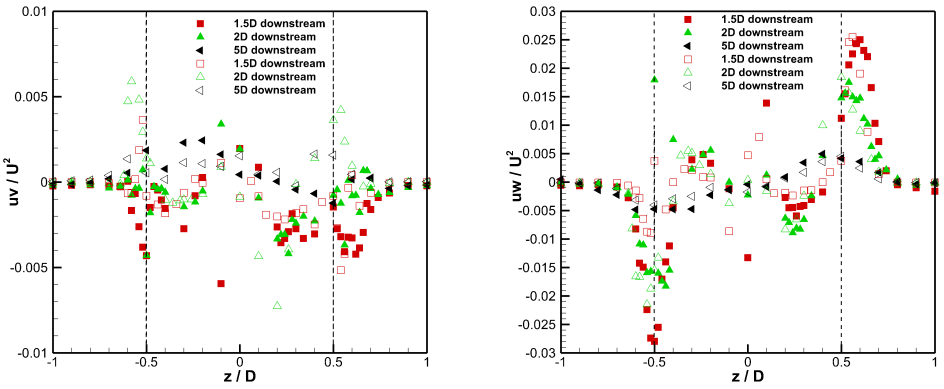

(a) $x - y$ plane

(b) $x - z$ plane

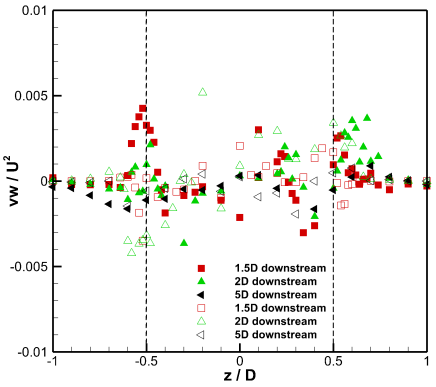

(c) $y - z$ plane

Figure 4.26: The Reynolds shear stresses in the centreline downstream of the three-bladed turbine - filled symbols non-uniform flow ($TI \approx 5\%$) , open symbols uniform flow ($TI \approx 2\%$), dashed lines denote edge of turbine

of the upstream shear flow impacting the wake too. After $3D$ downstream the change in shear stresses across the channel is purely down to the swirl induced from the turbine rotation and effects due to the mean-flow shear have dissipated.

The normalised Reynolds shear stress in the $x-z$ plane, $\overline{u'w'}/U^2$, is again similar to those in both non-uniform and uniform flow after $3D$ downstream where non-zero values occur at the blade edges as a result of the rotation. At $1.5D$ and $2D$ downstream, as well as peaks at the blade edges, $|z/D| = 0.5$, there are opposing peaks at $|z/D| = 0.25$, which is a result of a combination of the effect of blade rotation, the presence of the stanchion and turbine body and the upstream shear profile.

The Reynolds shear stress in the $y-z$ plane $\overline{v'w'}/U^2$, in figure 4.26 (c), in the non-uniform flow are similar at all downstream distances to those in uniform flow except in the region $-0.7 < z/D < 0.3$ at $1.5D$ and $2D$ downstream there are positive peaks compared to slight negative values at other downstream locations and in the wake in uniform flow. The Reynolds shear stress results show that the flow is similar to that in the uniform flow, shown in section 3.1.4, after $3D$ downstream, therefore the profiler has little impact on the flow compared to the effect of the swirl induced by the turbine rotation after this location. These results show that the profiler has an effect in the very near-wake, $< 3D$ downstream, on the Reynolds shear stresses but further downstream the change in Reynolds shear stresses across the channel width are a result of large-scale swirling motions due to blade rotation.

4.2.5 Reynolds Stress Anisotropy

In addition to plotting measurements such as Reynolds normal stresses and Turbulent Kinetic Energy, for the uniform flow it was found that plotting the Reynolds stress anisotropy by means of calculating ξ and η (defined in section 3.1.5) is useful. The constants ξ and η are plotted within the so-called 'Lumley triangle' in figure 4.27 for the flow surrounding the three-bladed turbine in the non-uniform steady flow. Akin to the upstream flow in the uniform flow conditions it was found that upstream of the turbine in non-uniform flow, in figure 4.27(a), was close to two-dimensional turbulence. Corresponding to the uniform flow conditions, in the regions directly behind the turbine the flow field becomes more isotropic further downstream. The regions around the outside of the wake where $|z/D| > 0.7$ the flow is always one-dimensional, due to the acceleration of the flow in the streamwise direction caused by the blockage effect of the turbine. From this calculation of the anisotropy of the flow, along with Reynolds shear stresses, it can be concluded that the velocity profiler has only a small effect on the turbulence in the flow field downstream of the turbine, again suggesting that the swirl induced by the turbine has the largest impact on the turbulence statistics in the flow field downstream of the turbine.

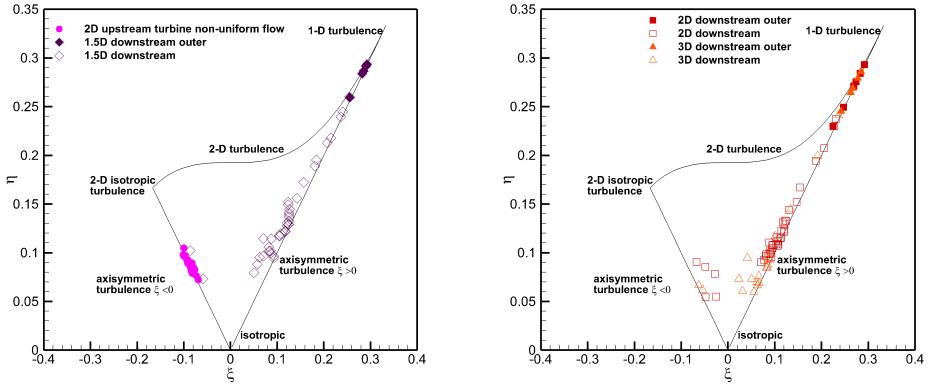

(a) Upstream and $1.5D$ downstream

(b) $2-3D$ downstream

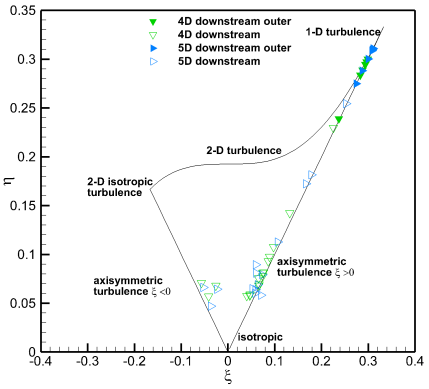

(c) $4-5D$ downstream

Figure 4.27: The Lumley triangle showing the turbulence anisotropy downstream of the turbine

4.3 Decay Characteristics in Uniform and Non-Uniform Steady Flows

Here the decay characteristics are plotted in order to compare the near-wake in different flow conditions and with previous wake studies. Figure 4.28(a) shows the maximum normalised streamwise velocity deficit downstream of the turbine in uniform (both $TI \approx 2\%$ and 5%) and non-uniform flow. At a depth equal to the turbine axis, the maximum mean streamwise velocity deficit in non-uniform flow is similar to that in uniform flow. Also shown is the centreline velocity deficit for a turbine in a higher TI flow (10%) with an upstream velocity of $0.4m/s$ (Re_F = 1.7 x 10^5) by Chamorro et al. (2013). For similar λ it can be seen that the streamwise velocity deficit in the highest TI flow is much greater but decays at a similar rate, that by $7D$ downstream the difference in deficit is similar to the difference at $2D$. This increased velocity deficit in the wake could be due to the increased TI, the reduced upstream velocity and that the measurement is at the centreline and the support structure of Chamorro et al. (2013) is having a larger impact on the flow. This comparison to studies within higher TI flows, suggest that possibly the increase in TI from 2% to 5% is not sufficient to have an impact on the wake and therefore this study cannot conclusively say that increasing TI does not affect the wake.

Figures 4.28(b) and (c) show the maximum mean vertical and spanwise velocities downstream of the three-bladed turbine in the three different flow conditions. It can been seen that in all three conditions the decay is approximately linear over the whole downstream distance where measurements have been obtained. When the free-stream turbulence intensity is $\approx 5\%$ the maximum mean vertical and spanwise velocities are found to identical, however when $TI \approx 2\%$ they are constantly slightly greater (by around 2% of the average upstream velocity). This subtle may be because in the upstream flow the vertical and spanwise velocities have been slightly modified by the

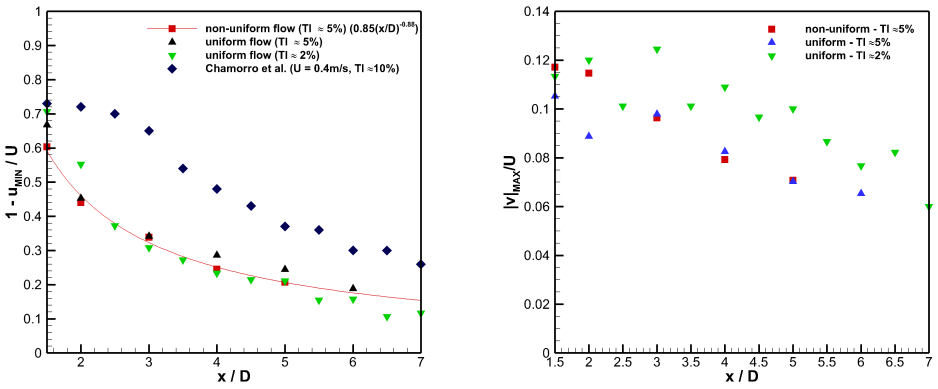

(a) Streamwise velocity deficit

(b) Maximum vertical velocity

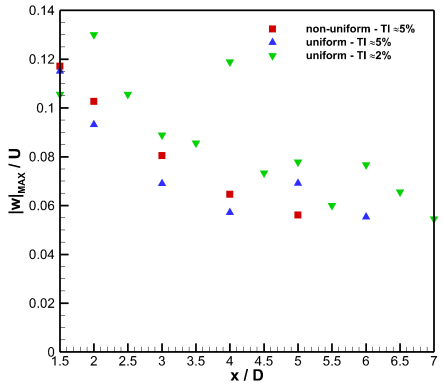

(c) Maximum spanwise velocity

Figure 4.28: The mean velocity decays downstream a three-bladed turbine in uniform and non-uniform steady flows at a height equal to the centre of the turbine (including data from - Chamorro et al. (2013), $\lambda = 5.8$)

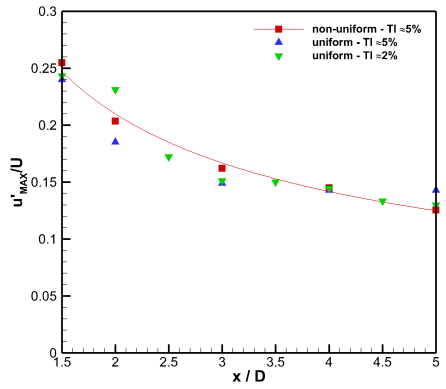

(a) Maximum u'

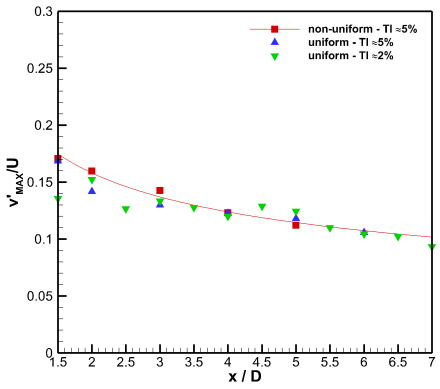

(b) Maximum v'

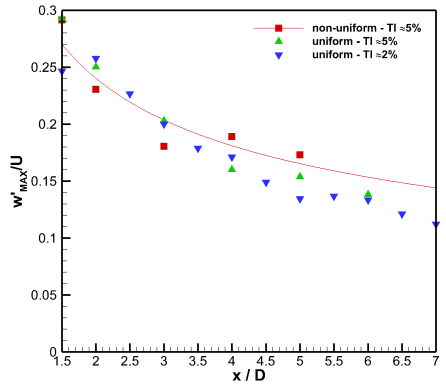

(c) Maximum w'

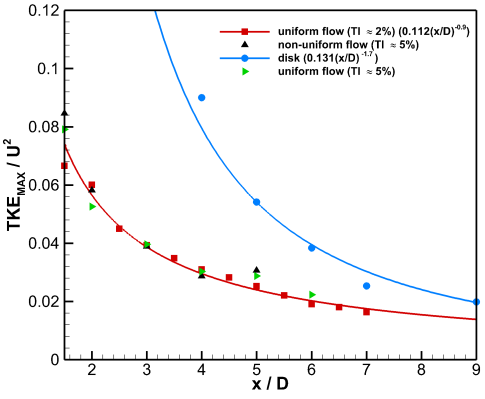

(d) Maximum TKE

Figure 4.29: The maximum standard deviations of velocities and TKE downstream a three-bladed turbine in uniform and non-uniform steady flows at a height equal to the centre of the turbine (disk - Harrison et al. (2010))

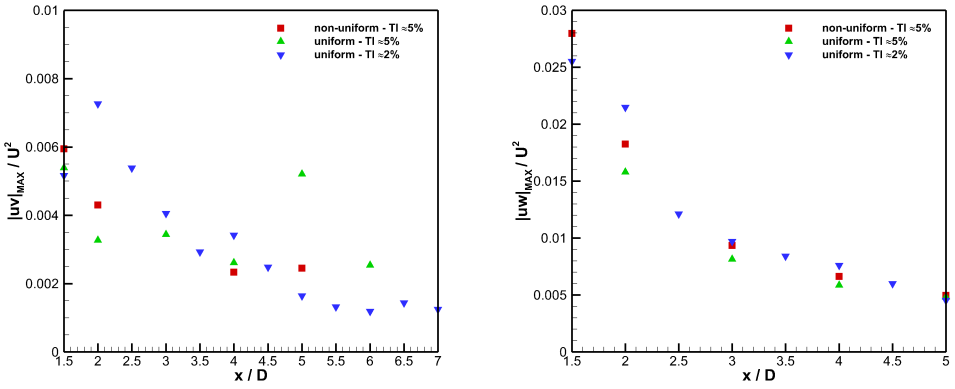

(a) $x-y$ plane

(b) $x-z$ plane

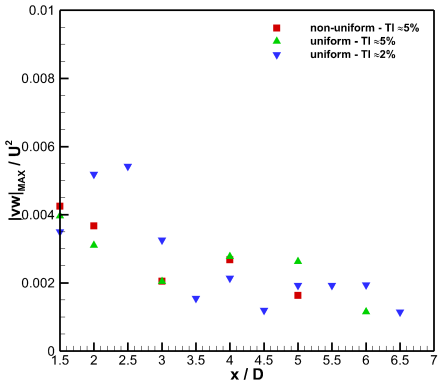

(c) $y-z$ plane

Figure 4.30: The maximum Reynold shear stress downstream a three-bladed turbine in uniform and non-uniform steady flows at a height equal to the centre of the turbine

grid and the 'flow profiler'.

The maximum Reynolds normal stresses are plotted in figures 4.29(a), (b) and (c) in both uniform and non-uniform flow conditions. These maximum values are found at the blade edges and are a result of the mean shear from the swirling motion caused by the turbine rotation. In all three flow conditions at the centre height the maximum Reynolds normal stresses appear to be equivalent showing that the swirl effect is the same and is not determined by the upstream flow conditions. In figure 4.29(d) the turbulent kinetic energy downstream of the turbine is shown for uniform and non-uniform flow. The TKE in non-uniform flow is quantitatively the same as in uniform flow at the centreline depth. The TKE levels decrease more rapidly than the mean velocities downstream with a power law decay of 0.9. This difference in the disk and turbine TKE decay is due to the addition of the swirl into the flow by rotation of the turbine. This shows that the disk, although very good at showing the mean flow deficit, is less representative of the turbulent characteristics downstream of a turbine as it produces much greater TKE levels in the immediate wake which decay very rapidly.

The maximum Reynolds shear stresses are shown in figure 4.30, like the Reynolds normal stresses the data essentially collapses in the three flow conditions (within some larger scatter). Again this highlights that the swirl is the dominant factor in the near-wake and is important for the determination of the wake recovery downstream of turbine.

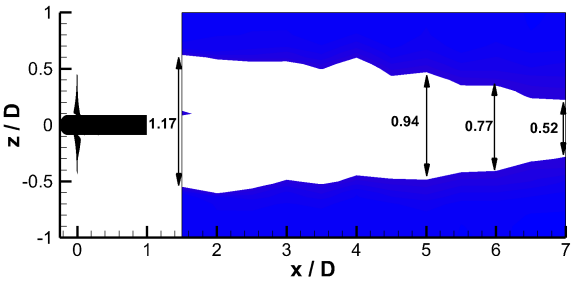

(a) 95% recovery

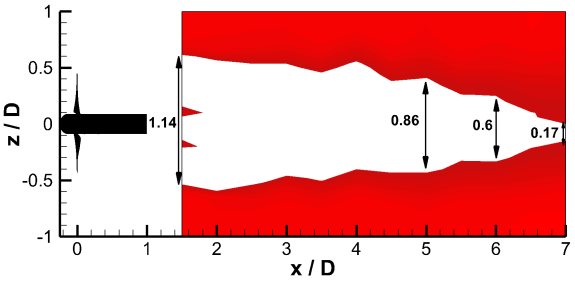

(b) 90% recovery

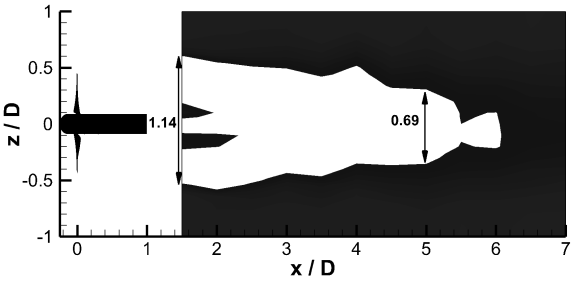

(c) 85% recovery

Figure 4.31: Wake recovery downstream of the three-bladed turbine in uniform flow ($TI \approx 2\%$)

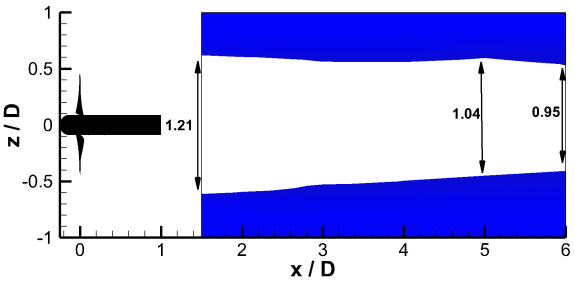

(a) 95% recovery

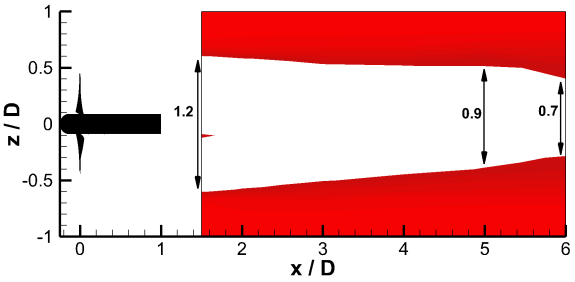

(b) 90% recovery

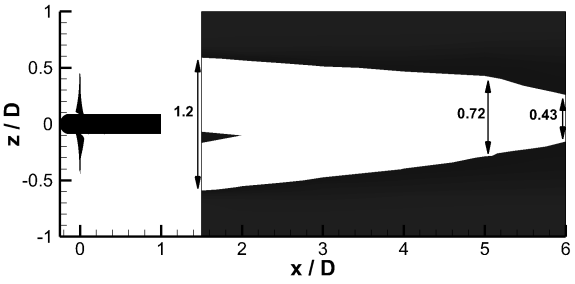

(c) 85% recovery

Figure 4.32: Wake recovery downstream of the three-bladed turbine in uniform flow ($TI \approx 5\%$)

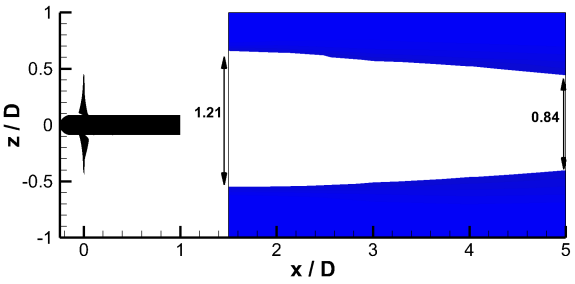

(a) 95% recovery

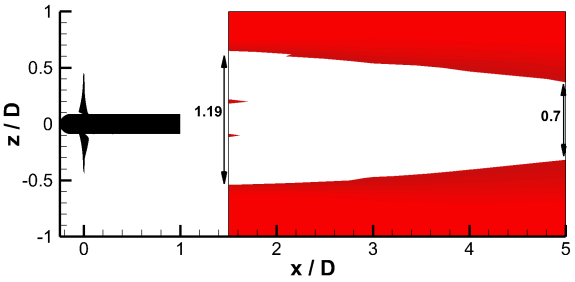

(b) 90% recovery

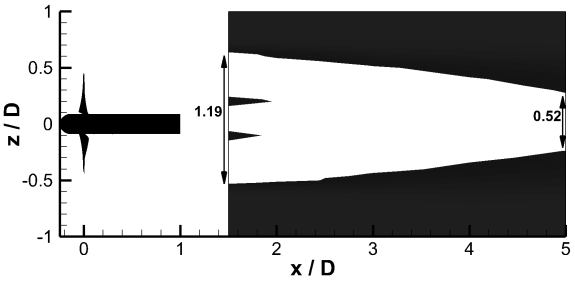

(c) 85% recovery

Figure 4.33: Wake recovery downstream of the three-bladed turbine in non-uniform flow ($TI \approx 5\%$)

4.3.1 Wake recovery

To investigate the recovery of the wake, the regions in which the wake has recovered to 95%, 90%, and 85% of the mean upstream streamwise velocity is plotted in figures 4.31 - 4.33 for both uniform flow conditions ($TI \approx 2\%$ and $TI \approx 5\%$) and non-uniform flow conditions ($TI \approx 5\%$). It is observed that the recovery, is slightly quicker in the non-uniform flow ($TI \approx 5\%$) than in both the uniform flow conditions, this is probably due to the combination of mean shear velocity and increased turbulence intensity. The wake in the uniform flow with low turbulence intensity is found to have recovered slightly more ($\approx$ 20% at 95% recovery) by $6D$ downstream than the wake in the uniform flow with high turbulence intensity. However it is important to note that at the end of the wake measurements were more sparse across the channel than in the very near-wake, i.e. every $50mm$ rather than every $10mm$, and the measurement locations will have an impact on these recovery plots.

4.4 Chapter Summary

In this chapter the wake downstream of the three-bladed turbine with optimum blade-pitch-angle was measured, initially in uniform flow with high TI (5%) through the $x - z$ centre-plane and further in non-uniform steady flow with high TI (5%) at five different heights. The wake in all three conditions were found to be similar, highlighting that a key feature in the wake is the large scale swirling motions caused by rotation. During this chapter and previous chapters questions have emerged about the characteristics of ADV measurements, therefore the final chapter the robustness of the ADV technique for turbine wake measurements.

Chapter 5

Use of Acoustic Doppler Velocimetry in Tidal Energy Research

Acoustic Doppler velocimetry has been a key research tool in this thesis. It has a number of advantages in that is relatively inexpensive, easy to set-up, able to measure all three velocity components simultaneously and has a relatively high sampling rate, enabling data to be collected quickly. For example to collect the data at a set height and distance across the width of the high-speed water-channel (around 70 locations) where $20,000$ samples are taken at each location would typically take $3-4$ hours. Not only has ADV been used extensively in the current research, but it is also used in the majority of studies that have focused on wake measurements of tidal devices (such as Myers & Bahaj, 2009, Stallard et al., 2013 and Neary et al., 2013). During the course of the research being reported here, questions emerged about the characteristics of ADV measurements (Khorsandi et al., 2012). In this chapter ADV is used in different probe orientations to see the effect on the measured velocities, along with a comparison to laser Doppler velocimetry (LDV).

One issue is the difference observed in the levels of velocity fluctuations when the probes are used in sideways or downwards orientations. Therefore two orientations of the ADV probe have been used to repeat measurements in the three flow conditions from chapters 3 and 4 to gain a more accurate and complete data set.

5.1 Previous Studies using ADV

Acoustic Doppler Velocimetry (ADV) was developed in 1992 by SonTek for the U.S. Army Engineer Waterways Station as an alternative to measurement devices such as Laser Doppler Velocimetry (LDV) systems, micro-propellers, electromagnetic current meters and pitot tubes (Lohrmann et al., 1994). All ADV devices since have been based on this design and concept with early devices having a downwards-looking probe, more recently Nortek introduced a sideways-looking ADV probe. The principle of ADV is to emit an acoustic pulse (usually at $10MHz$) from a transmitter. The acoustic waves propagate through the water and are scattered by seeding particles in the flow. The echo received by the ADV transducers show a Doppler shift which is used to calculate the velocity within the sampling volume. There are many different ADV devices where the sampling volume (size and location) and the sampling frequency vary depending on the device characteristics, but the same underlying principles apply.

Initial studies using ADV were conducted in wave basins and towing-tanks where measurements were compared directly to LDV. Lohrmann et al. (1994) present studies in a wave channel which had a still-water depth of $0.3m$. The sampling volumes of both the ADV and LDV were located at a depth of $0.15m$. Good agreement, within 1% was shown between the LDV and ADV in the mean velocity over time. The work by Lohrmann et al. was an extension of the study by Kraus et al. (1994) who compared velocity measured over time by an ADV to a $2D$ LDV system in a $2D$ wave channel and a $3D$ wave

basin. Again results exhibited good agreement in the horizontal velocity component under wave conditions with the peak and troughs of the ADV and LDV data sets matching well. It is important to note however, that in both these studies (Lohrmann et al., 1994 and Kraus et al., 1994) lines of best fit were shown and not a point-by-point comparison. However, the main conclusion from these studies was that ADV can accurately measure mean water flow velocities.

Further investigations comparing ADV with a $2D$ LDV system were undertaken by Voulgaris & Trowbridge (1998). Experiments were conducted in an open channel, $17m$ long, which investigated the flow in a turbulent boundary layer, results being compared to various empirical models derived by Nezu & Rodi (1986). Voulgaris and Trowbridge used ADV with a downwards-looking probe which had the control volume located $108mm$ below the transmitter with a sampling volume of $250mm^3$. The $2D$ LDV system was used in forward-scatter mode and had a sampling volume of $0.07mm^3$. The LDV system was arranged so that two orthogonal velocity components orientated at $\pm 42.5\%$ to the flow were measured simultaneously using a three-beam probe and a subsequent decomposition made into streamwise and vertical velocity components. No mention was made of any correction for velocity biasing (Tropea, 1983). A number of experiments were conducted with various mean flow velocities, water heights and measurement locations. The mean of the two velocity components measured by ADV agreed within 1% of those measured by LDV, with the differences between the measurements attributed to the uncertainty in alignment of the probes (Voulgaris & Trowbridge, 1998). Analysis of the fluctuating velocity results showed that the ADV can measure the variance (standard deviation squared) of the vertical component accurately but tends to overestimate the variance of the streamwise component. This discrepancy was also suggested to be a result of the ADV geometry (Voulgaris & Trowbridge, 1998). To reduce the noise of the ADV measurements corrections were applied to the signal, but these cor-

rections reduced the fluctuating component to below that of the empirical value obtained experimentally by Nezu & Rodi (1986) using LDV measurements in open channels. However, Voulgaris & Trowbridge (1998) observed that the overestimated fluctuations measured by ADV still followed the trend predicted by Nezu & Rodi (1986).

Khorsandi et al. (2012) compared ADV measurements in turbulent jets to flying hot-film anemometry (FHFA). The ADV used was a Nortek Vectrino which sampled at $25Hz$ and had a sampling volume of $260mm^3$ centred $50mm$ from the transmitter. At least $100,000$ samples were taken to ensure convergence of up to fourth order statistics, so that the differences in the measurements taken were not due to the sample size. The FHFA used by Khorsandi et al. measured the streamwise velocity and was validated using stationary hot-wire anemometry (SHWA) and LDV data from the study performed by Hussein et al. (1994), to which a good agreement was found. The results of the streamwise velocity measured by the ADV compared well with results from the FHFA in the mean values; however, the ADV standard deviation values were higher ($\approx 10\%$) than those from the FHFA. Since no measurements of the vertical velocity component were taken using the FHFA, the ADV results were compared with flying hot-wire anemometry (FHWA) data from a study performed by Panchapakesan & Lumley (1993) using turbulent air jets. The standard deviation of the vertical component measured by ADV showed good agreement with FHWA results of Panchapakesan & Lumley (1993). This set of values were lower than the standard deviation values of the vertical velocity in the study by Hussein et al. (1994) by approximately 5%, which could indicate a small underestimation of the standard deviation of the vertical velocity measured with ADV. The results of Khorsandi et al. (2012) are therefore consistent with the study by Voulgaris & Trowbridge (1998) which indicated that there was noise present in the streamwise velocity component measured by ADV. This so-called 'Doppler noise' is not present in the vertical component. Analysis of the power spectrum obtained

with ADV by Khorsandi et al. (2012) showed that the spanwise component also contains 'Doppler noise' and it was present in all measured frequencies of the signal. The ADV probe allowed two different orientations: downwards- and sideways-looking, where the sideways-looking orientation aligned with the vertical axis of the control volume, i.e. j direction in figure 2.6 (d), with the streamwise flow. It was found that with the two different orientations the j component of the control volume always had the least noise and could therefore measure the standard deviation most accurately. Noise was always present in the i and k directions of the ADV control volume, giving an over-estimate of the standard deviations in these directions. The Doppler noise had no clear relationship to the mean flow, contradicting previous suggestions by Lemmin & Lhermitte (1999) who reviewed ADV studies in 1999. A number of techniques were used to try to reduce the noise in Khorsandi et al. (2012), including the de-spiking method of Wahl (2003), which was adapted from Goring & Nikora (2002), using the WinADV software and also the noise reduction methods of Hurther & Lemmin (2001). Both methods reduced the standard deviations of the signal, subject to noise but insufficiently to match the values measured by the hot-film and other previous studies.

Often, results from ADV measurements have been used to verify numerical models (e.g. Harrison et al. (2010) and Batten et al., 2013). Table 5.1 lists work conducted to date using ADV in tidal energy research. ADV in particular has been extensively used in investigating wake recovery downstream of devices. All studies using ADV include measurements of the mean velocities with many also presenting higher-order statistics and turbulent time/lengthscales. Table 5.1 also details the ADV device used and probe orientation where known. Also, in table 5.2 numerical studies which compared their results to those taken by ADV are shown.

In this thesis ADV has been used to measure instantaneous flow velocities which was subsequently used to calculate, mean velocities, Reynolds normal and shear stresses plotted along with calculations of the Reynolds-

stress anisotropy tensor. ADV has also been key to a number of studies which have investigated the flow around tidal devices (e.g. Myers & Bahaj, 2009 and Neary et al., 2013).

Table 5.1: Work conducted using ADVs in tidal energy research. Where the following are defined: u', v' and w' are the Reynolds normal stresses (equations 1.5-1.7), $\overline{u'v'}$, $\overline{u'w'}$ and $\overline{v'w'}$ are the Reynolds shear stresses (equations 3.1 - 3.3), TKE = Turbulent Kinetic Energy (equation 1.4), TI =Turbulence intensity (equation 1.8), FKE = Flow Kinetic Energy $= \frac{1}{2}\sum_{i=1}^{3}\overline{(\tilde{u}_i(t)+u_i'(t))^2}$, where $\tilde{u}$ is the periodic wave-induced fluctuations and u' is the turbulent fluctuations. Olczak et al. (2013).

Author/year	ADV type & frequency	Data given
Myers & Bahaj (2009)	Nortek Vectrino $50Hz$	u, u'
Myers & Bahaj (2010)	Nortek Vectrino $50Hz$ - downwards-looking	u, $\overline{u'v'}$
Rose et al. (2011b)	$25Hz$	u, TI
Rose et al. (2011a)	$25Hz/64Hz$	u
Stallard et al. (2011, 2013)	$200Hz$	u, u'
Neary et al. (2013)	Nortek Vectrino - downwards-looking	u,u'
Chamorro et al. (2013)	$200Hz$ - downwards-looking	u, u' integral length-scales
Fleming et al. (2013)	$25Hz$	u, TI
Olczak et al. (2013)	$200Hz$ - downwards	u, $3D$ integral length-scales, FKE
Tedds et al. (2013)	Nortek Vectrino $200Hz$ - downwards-looking	u, v, w, u', v', TKE
Tedds et al. (2014)	Nortek Vectrino $200Hz$ - downwards-looking	u, v, w, u', v', w' $\overline{u'v'}$, $\overline{u'w'}$, $\overline{v'w'}$, TKE
Blackmore et al. (2014)	Norteck Vectrino $50Hz$	u, $\sqrt{\frac{\overline{u'^2}}{\bar{u}}}$, streamwise integral lengthscales

Table 5.2: Computational studies comparing results to ADV measurements

Author/year	ADV study	Data used
Harrison et al. (2010)	Myers & Bahaj (2010)	u, u'
Batten et al. (2013)	Myers & Bahaj (2010)	u, u'
Daly et al. (2013)	Myers & Bahaj (2010)	u

5.2 Velocity Measurements - ADV Issues

To investigate the issues surround the ADV technique, velocity measurements were taken with the two different ADV probes, and with LDV, both in uniform flow and at 1.5 turbine diameters (D) downstream of the turbine.

5.2.1 Means and Reynolds Normal Stresses

From previous studies (Voulgaris & Trowbridge, 1998 and Khorsandi et al., 2012) it is known that the orientation of the ADV probe has an effect on the Reynolds normal stresses obtained from the measured velocities. It is therefore important to quantify the differences between measurements taken with the two ADV probes in different orientations. To set a baseline in a simple flow with low turbulence levels, measurements were taken in the high-speed water-channel with uniform flow without the turbine present. These measurements were taken with both ADV probes. Due to the flexibility of probe B, see figure 2.6 (b) and (c), the orientation was altered so that it measured in both a 'sideways' and a 'downwards' orientation, enabling comparison of both probes A and B in the same orientation.

In addition to these orientations, measurements were taken so that the j component of the ADV control volume was aligned with the streamwise velocity (figure 2.6 (d)). In this configuration, however, when data could be obtained, the ADV itself caused a physical disruption to the mean flow resulting in a 10% reduction in the mean streamwise velocity. As a consequence of these issues, data is not shown for this configuration.

Figure 5.1 shows the three-dimensional mean velocities in uniform flow where the flow is essentially one-dimensional. In all three components a good agreement between the mean velocity measurements can be seen, small differences are probably a consequence of unavoidable minor probe misalignments. Figure 5.2 shows the Reynolds normal stresses of the three velocity components for the different probe orientations. In figure 5.2(a) the streamwise Reynolds normal stresses are presented and there is good agreement between the two probes in different orientations. It can be seen in figure 5.2(b) that for the vertical Reynolds normal stresses there is a significant discrepancy between different orientations, where in the sideways-looking orientation the normal stresses are three times greater than those in the downwards-looking orientation. Conversely, the spanwise Reynolds normal stresses (figure 5.2(c)) when the probe is downwards-looking are much greater than when the probe is in the sideways-looking orientation. The small difference between both the probes in the downwards-looking orientation in figure 5.2(c) is due to the inherent uncertainty in setting up probe B in this non-standard orientation, resulting in slight misalignment. The data shown in figure 5.2 is in agreement with Voulgaris & Trowbridge (1998) and Khorsandi et al. (2012), suggesting that there is a noise issue in at least one of the velocity components of the ADV system and the velocity component affected by this noise is dependent on the orientation of the probe.

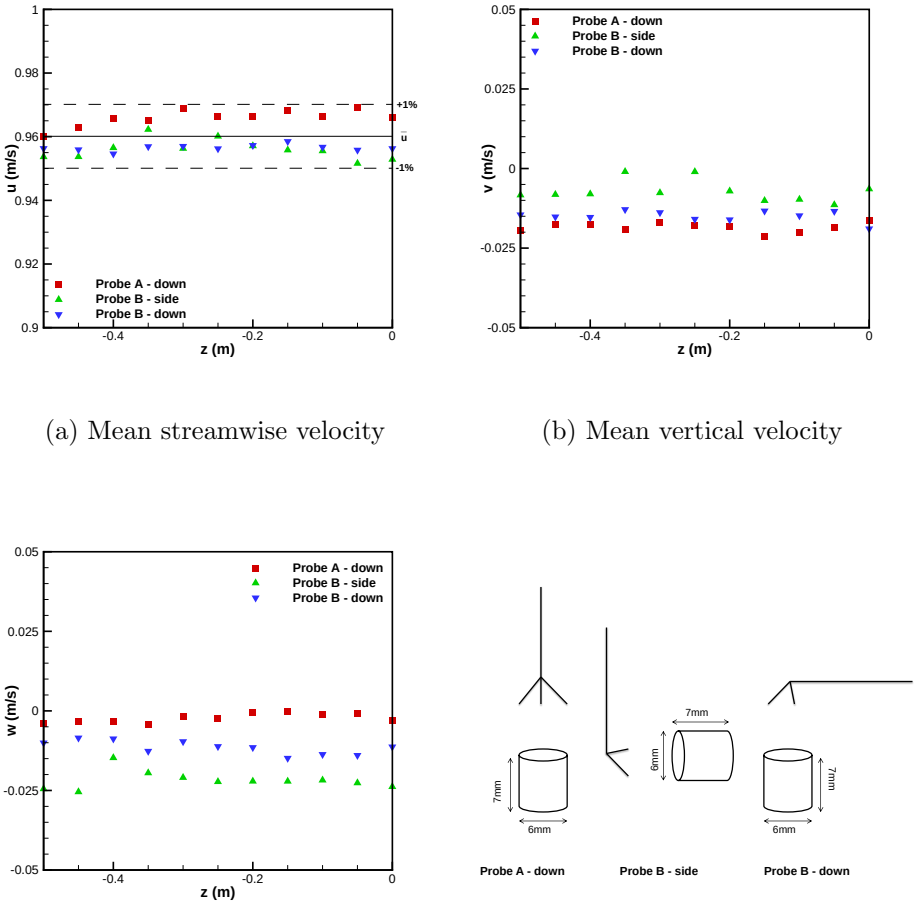

(a) Mean streamwise velocity

(b) Mean vertical velocity

(c) Mean spanwise velocity

(d) Probe orientations

Figure 5.1: Mean velocities in uniform flow

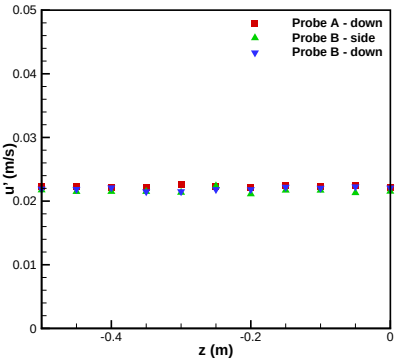

(a) Streamwise Reynolds normal stresses

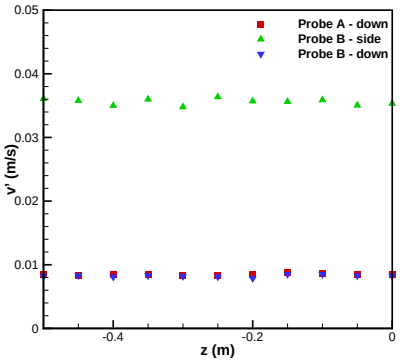

(b) Vertical Reynolds normal stresses

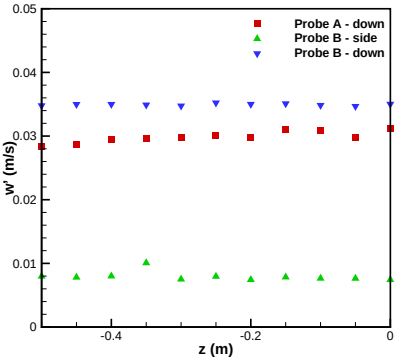

(c) Spanwise Reynolds normal stresses

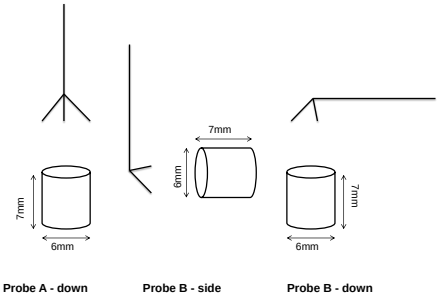

(d) Probe orientations

Figure 5.2: Reynolds normal stresses in uniform flow

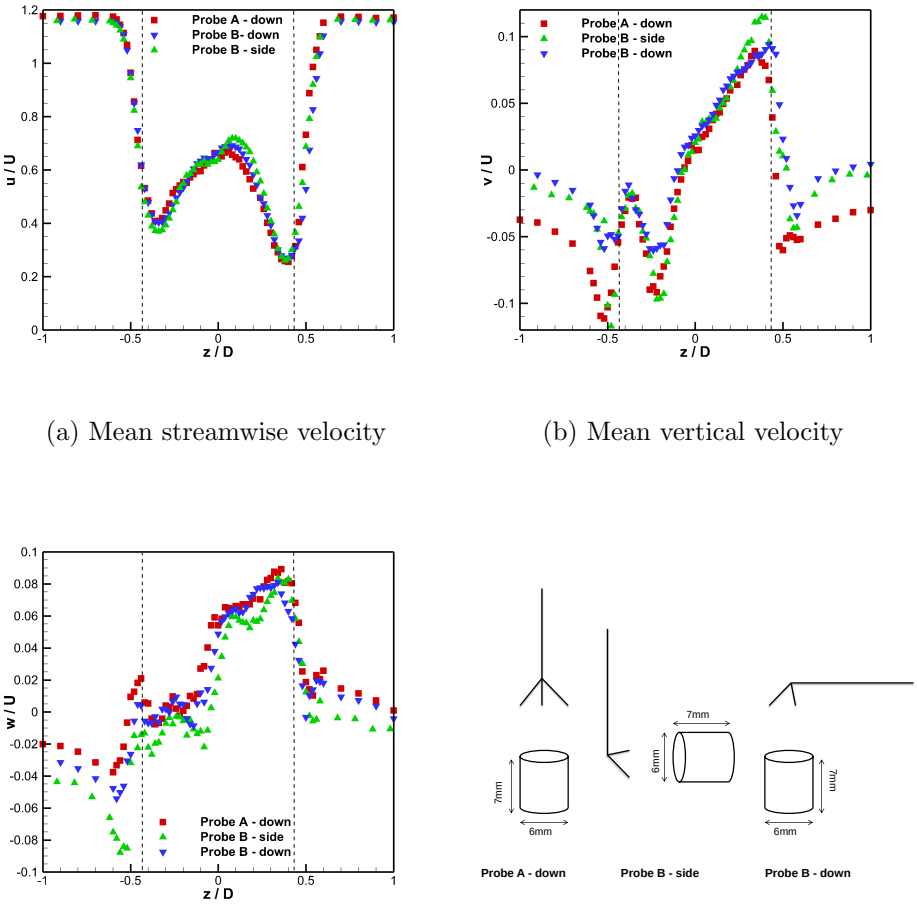

(a) Mean streamwise velocity

(b) Mean vertical velocity

(c) Mean spanwise velocity

(d) Probe orientations

Figure 5.3: Mean velocities $1.5D$ downstream of the turbine, $12.5cm$ above the centreline (dashed lines indicate turbine edge)

Having investigated the issue of ADV probe orientation with a steady uniform flow of low turbulence intensity, it is important to see the effects in a more complex flow typical of marine energy applications (e.g. Myers & Bahaj, 2009, Stallard et al., 2013 and Neary et al., 2013) and more relevant to the studies conducted in this thesis. Not only here but also within tidal energy research, ADV has been widely used particularly for investigating the wake of tidal stream turbines, as in the work described in the previous chapters. Therefore the effect of the ADV probe orientation in the wake of a turbine has been investigated here to illustrate typical effects on the results shown in the previous chapters and in the published literature. In such wakes, as shown in chapters 3 and 4, the mean flow has a complex swirling structure with sharp mean flow gradients and regions of large Reynolds normal stresses (standard deviations) and shear stresses (covariance).

Figure 5.3 shows the three velocity components at $1.5D$ downstream of the turbine at a height of $12.5cm$ above the centre of the turbine. Measurements were taken in two orientations with the two different ADV probes and once again good agreement in the mean values is observed. In particular the u and w components show very good agreement, with the small differences being associated with probe alignment and the spatial positioning of the control volume. The vertical velocities qualitatively agree, with all three data sets following the same trends, again the slightly larger differences close to the walls of the channel are most likely a consequence of the probe alignment. It can be concluded that the ADV probe orientation has little effect on the mean velocities measured. However, within the Reynolds normal stresses, figure 5.4, there are clear differences depending on the probe orientation. In figure 5.4(a) the streamwise Reynolds normal stresses are shown; consistent with the measurements in the uniform flow there is reasonable agreement with the different probe orientations. It should be borne in mind that it was not possible to configure the probe so that the streamwise velocity could be measured in the j probe direction however i.e. the low noise direction. The

differences caused by the probe orientation is most evident in the vertical and spanwise Reynolds normal stresses (figures 5.4(b) and (c) respectively). In figure 5.4(b) it can be seen that when probe B is in the sideways-looking orientation, the vertical Reynolds normal stresses are much greater than when the probe is measuring in the downwards-looking orientation. The increase is not constant across the width of the wake and is much greater in the flow from the tips of the turbine blades ($z/D = \pm 0.433$ - indicated by dashed lines) in the shear layer where turbulence production is likely to be the highest (Pope, 2011 and Tennekes & Lumley, 1972). Similarly, in figure 5.4 (c) the spanwise Reynolds normal stress appears much greater when the probe is in the downwards-looking orientation, this increase is also non-constant across the flow. Significant differences between the Reynolds normal stresses measured in different probe orientations can be observed in regions of essentially uniform mean flow with low turbulence levels (i.e. near the channel walls $0.7 < |z/D| < 1$), in the shear layer where the mean velocity gradient is highest and turbulence production is high ($|z/D| = 0.433$ - denoted by dashed lines), and at the centreline where the mean velocity gradient is essentially zero. As the noise contribution varies across the flow, it would appear that in this complex flow the noise is a function of both the mean flow and local turbulence intensity. As others have previously postulated, the increases in Reynolds normal stress could be due to a combination of Doppler noise and mean velocity gradient broadening, for example Voulgaris & Trowbridge (1998) and Khorsandi et al. (2012). Mean velocity gradient broadening will only bias the standard deviation if there is a significant shear across the control volume and this can be ruled out for the data near the walls ($0.7 < |z/D| < 1$) where there is no mean gradient.

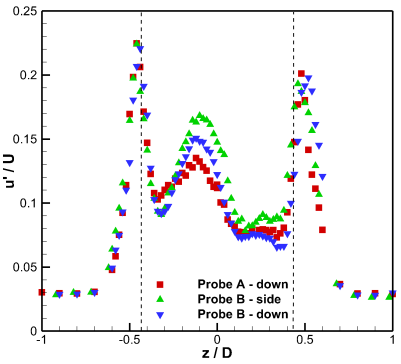

(a) Streamwise Reynolds normal stresses

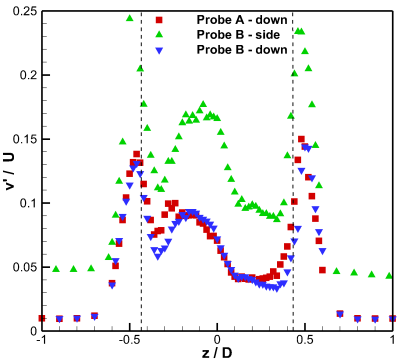

(b) Vertical Reynolds normal stresses

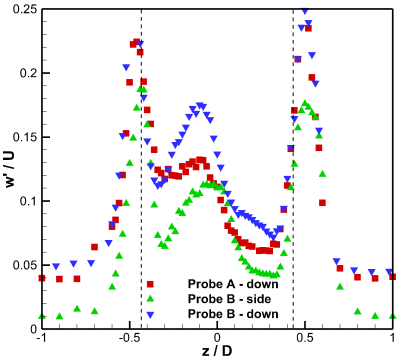

(c) Spanwise Reynolds normal stresses

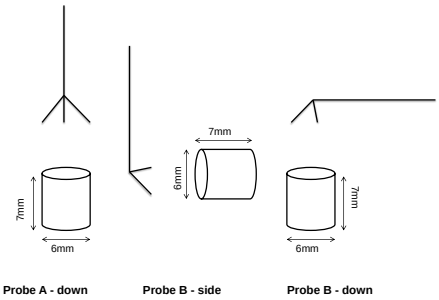

(d) Probe orientations

Figure 5.4: Reynolds normal stresses $1.5D$ downstream of the turbine (dashed lines indicate turbine edge)

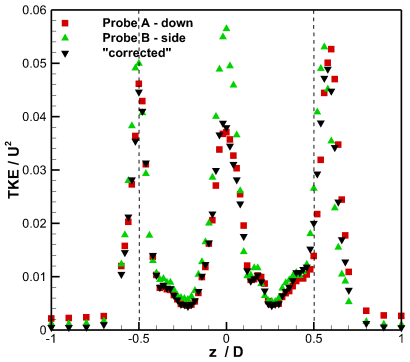

Figure 5.5: Turbulent Kinetic Energy downstream of turbine

5.2.2 Turbulent Kinetic Energy

As has been shown in the previous chapters, an important measure of the wake characteristics downstream of a turbine is Turbulent Kinetic Energy which represents all three fluctuating velocity components, where TKE is defined in equation 1.4. The results in the previous section and previous studies (Voulgaris & Trowbridge, 1998, Khorsandi et al., 2012), have shown that an individual ADV probe may overestimate two of the Reynolds normal stresses which, by definition, results in overestimation of the TKE. In an attempt to combat this overestimation, the TKE has been calculated using the streamwise and vertical Reynolds normal stresses using probe A and the spanwise Reynolds normal stresses using probe B. This data is shown in figure 5.5 as TKE 'corrected' at $1.5D$ downstream of the turbine. In addition to this 'correction' the TKE using both probe A (downwards-looking) and probe B (sideways-looking) is shown, where probe A and probe B agree with each other in most regions across the channel, except at the centre where the TKE measured by probe B is much larger than that for probe A. The 'corrected' TKE also shows little difference to the probe A measurements apart from the peaks at the edge of the blades ($z/D = \pm 0.5$) where the corrected is slightly

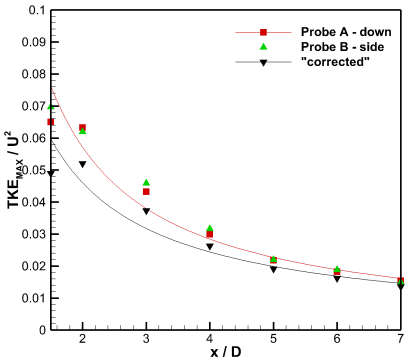

Figure 5.6: Maximum Turbulent Kinetic Energy downstream of turbine

lower. From this data set it can be concluded that even though there is a large difference in the individual Reynolds normal stresses, the TKE when corrected for two good components shows little difference, apart from the centre of the channel, compared to individual probe-measured TKE. This suggests that TKE is a fairly robust indicator of the turbulence levels in the flow even when noise is present in the measurement technique. To investigate this further the maximum TKE downstream of the turbine is plotted in figure 5.6, where both probes are shown and compared to the 'corrected' values using the approach outlined above. It is seen that the 'corrected' TKE decays with the same power-law exponent however it is shifted down slightly from the individually measured TKE, showing that maximum TKE decay gives a robust representation of the decay of the turbulent wake downstream of the turbine.

5.2.3 Reynolds Shear Stresses

ADV can measure all three velocity components simultaneously so Reynolds shear stresses, defined in equations 3.1 - 3.3, can be calculated. These Reynolds shear stresses are shown in the uniform flow in figure 5.7 and at $1.5D$ downstream of the turbine in figure 5.8. As expected in a uniform flow with no mean shear the Reynolds shear stresses are essentially zero across the entire width of the channel in all three planes. Slight variation, due to slight probe misalignment, with the orientations can be seen in the $x - z$ plane, where probe A results are constantly lower than those from probe B. In figure 5.8 the Reynolds shear stresses downstream of the turbine show reasonable agreement with some exceptions at the edge of the blades. These differences are in the region of largest shear where the probes, due to the unsteady nature of the flow, are more sensitive to effects of 'noise' and vibrations on the support structure.

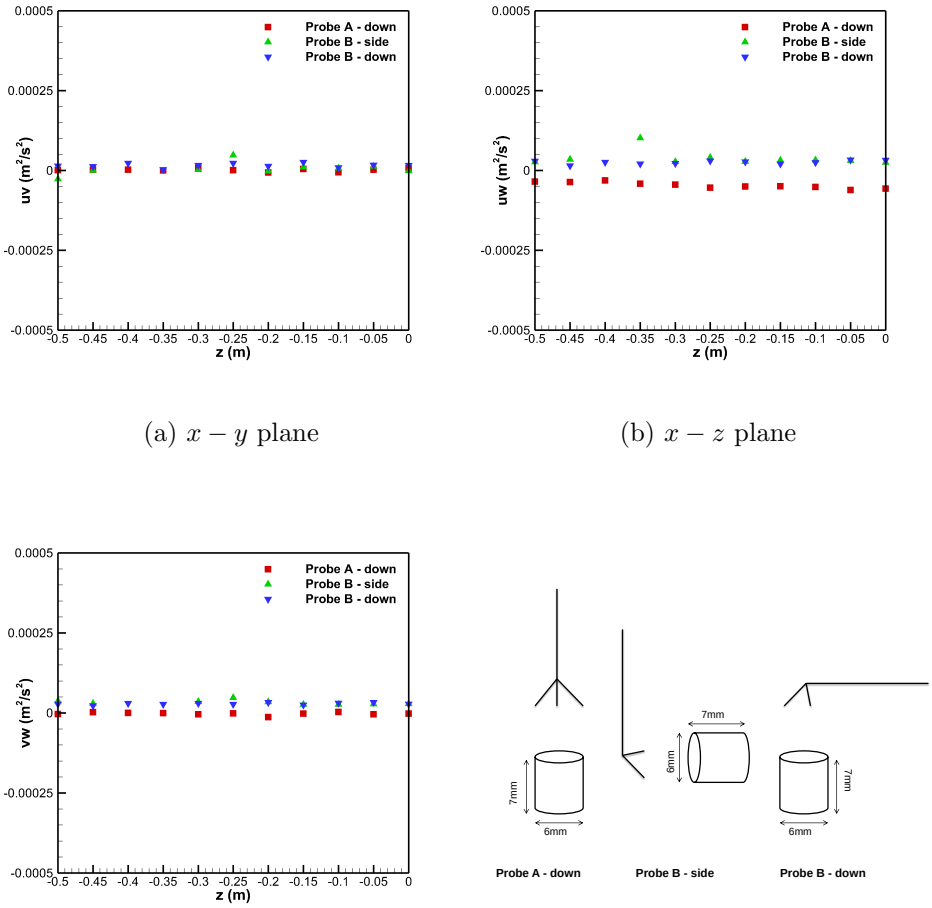

(a) $x - y$ plane

(b) $x - z$ plane

(c) $y - z$ plane

(d) Probe orientations

Figure 5.7: Reynolds shear stresses in empty channel

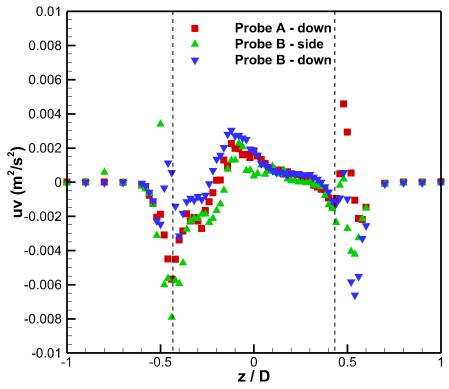

(a) $x - y$ plane

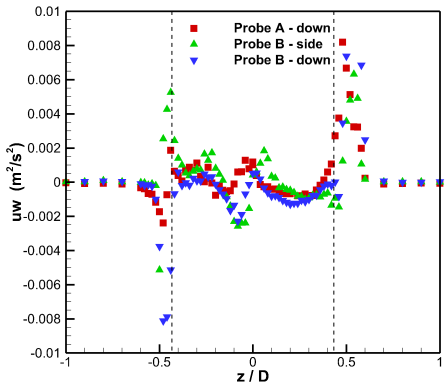

(b) $x - z$ plane

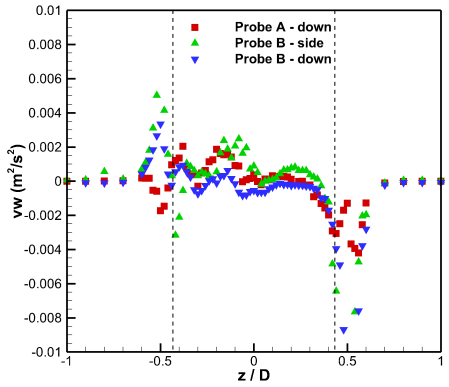

(c) $y - z$ plane

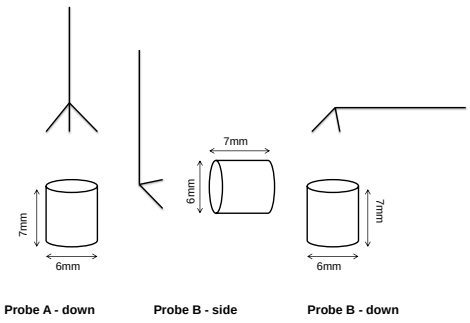

(d) Probe orientations

Figure 5.8: Reynolds shear stresses $1.5D$ downstream of the turbine at a height of $12.5cm$ above the centre of the turbine (dashed lines indicate turbine edge)

5.2.4 Reynolds Stress Anisotropy

In addition to the mean, Reynolds normal, and shear stresses the Reynolds stress anisotropy has also been calculated for the surrounding flow of a turbine in both chapters 3 and 4 and plotted by means of η and ξ on the 'Lumley Triangle'. The invariants η and ξ (equations 3.6 and 3.5) are characterised from the Reynolds-stress anisotropy tensor (3.4), which is defined in terms of both Reynolds normal and shear stresses. It is therefore expected that the ADV probe orientation will affect the calculations. Nevertheless, the Reynolds-stress anisotropy tensor was calculated using u', v', $\overline{uv}$ and $\overline{vw}$ from probe A - downwards-looking - and w' and $\overline{uw}$ from probe B - sideways-looking - in an attempt to produce invariants ξ and η that are as 'noise-free' as possible. Although this may not be the most robust method, due to the issues with precise location of measurements, it is concluded to be useful in terms of reducing 'noise' effects and assessing the effect on these parameters.

In figure 5.9(a) ξ and η for the three ADV probe set-ups are shown alongside the 'corrected' values for the uniform flow in the channel alone. It is observed that the 'corrected' points are found to be one-dimensional turbulence, which can be explained by the fact that the v' and w' used in the calculation were 'noise-free', and so the uncorrected streamwise Reynolds normal stress will be dominant as it is larger, resulting in one-dimensional turbulence. On the other hand the individually measured ADV probe data sets have two 'noisy' components, and one might expect that the results will therefore show two-dimensional turbulence, as two fluctuating velocity components will be larger than the third 'noise-free' component and this can be seen in figure 5.9(a). There are however some differences between the probe types, for instance with probe B whichever orientation, ξ is always negative whereas ξ is both negative and positive for probe A. In all probe arrangements the flow is shown to be anisotropic and this is therefore all that can be concluded from this plot about this flow field. As it was found that the two 'noise-free' normal stresses measured in the two orientations were very

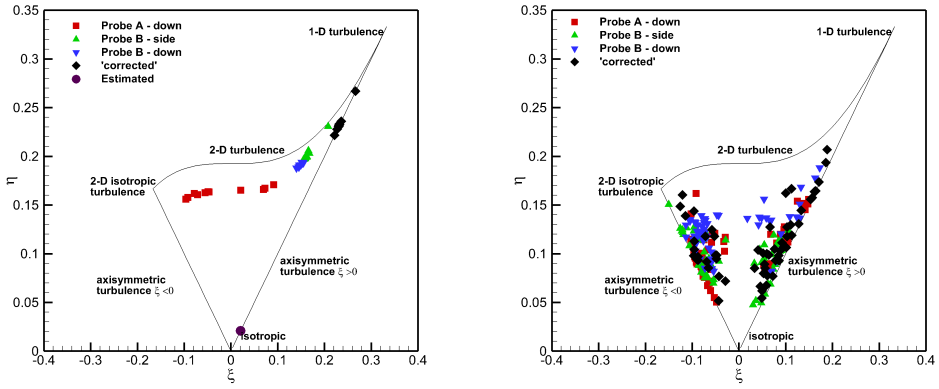

(a) No turbine (b) 1.5D downstream of the turbine

Figure 5.9: Lumley triangle showing the turbulence anisotropy with different ADV probe set-ups

similar and all three Reynolds shear stresses were of the same order, ξ and η were estimated where $u' = v' = w' = 0.009$ and $\overline{uv} = \overline{uw} = \overline{vw} = 0.000004$, as this is a possibility within the flow if we were to assume that the u' is equivalent to the 'noise-free' fluctuating component. This estimation is also plotted on figure 5.9(a) and it shows that using these rough estimations the channel-alone flow is near to isotropic. This, however, is a very crude approximation and is shown to illustrate the sensitivity of the invariants of the Reynolds-stress anisotropy tensor, and how careful one must be when using ADV measurements to calculate this measure.

In addition to the plot in the uniform flow the invariants ξ and η are plotted in figure 5.9(b) for the flow $1.5D$ downstream of the turbine with the different probe arrangements and the 'corrected' estimate. The data shown is that of the flow directly downstream of the turbine i.e $|z/D| \leq 0.7$, where the swirl effects are the dominant feature of the flow, there is little difference in the measurements which lie on the edges of the Lumley triangle where ξ is either maximum or minimum. It can therefore be seen that the flow is highly anisotropic and that all of these methods of calculating the anisotropy are effective at showing the same result for how far from isotropic the flow downstream of a turbine is. Nonetheless, it is important to consider that ADV technique is not the most robust method for undertaking such calculations but that general trends may still be observed (i.e. the absolute distance from $\xi = \eta = 0$).

5.2.5 Integral Timescales

For experimental studies and computational turbulence modelling of tidal devices, researchers are often interested in turbulent integral time and length-scales, both upstream and downstream of the turbine (Olczak et al., 2013, Blackmore et al., 2014 and Chamorro et al., 2013). Integral time and length-scales can be calculated using the autocorrelation function (Pope, 2011):

$$\rho(s) \equiv \frac{\overline{u_i(t)u_i(t+s)}}{\overline{u_i(t)^2}}, \tag{5.1}$$

where $u_i(t)$ is the time varying velocity, for increasing time increments s. The integral timescale is defined as:

$$\bar{\tau}_{ii} \equiv \int_0^\infty \rho(s)ds. \tag{5.2}$$

In practice the integration is not to $s = \infty$ but to the time at which the autocorrelation becomes negative Hinze (1975). Integral lengthscales can then

be estimated by multiplying $\bar{\tau_{ii}}$ by a typical convection velocity (Pope, 2011). Or, more precisely, by using two ADV probes at different spatial locations. In the present study the integral timescales have been calculated for uniform flow and downstream of the turbine for both sideways- and downwards-looking probes, using filtered and unfiltered time series. Having filtered the data using the de-spiking methods of Wahl (2003), to remove erroneous data caused by the acoustic signal not being reflected by the seeding particles, the missing time series data is replaced using either a simple sample-and-hold or a linear interpolation technique to ensure a suitable time series is obtained (Adrian & Yao, 1987).

Figure 5.10 shows the normalised (by the mean upstream streamwise velocity and width of the channel ($W = 1.4m$)) integral timescales for all three velocity components in uniform flow. For the streamwise integral timescale, figure 5.10(a), there is some very weak order-of-magnitude agreement between the two probes, but there are slight variations across the channel, which is probably due to the varying levels of noise in each time series. The vertical integral timescale (figure 5.10(b)) is an order-of-magnitude greater for probe A which has the least noise within the signal. The converse is true for the spanwise component, where the integral timescale measured by probe A is an order of magnitude smaller than for probe B. These differences are a consequence of the noise in the signal. If there is a large amount of random noise in a signal then the autocorrelation will rapidly decay to zero and therefore the integral timescale will become very small, where a completely uncorrelated signal will have an integral timescale equal to $\frac{1}{2} \times 1/f$ where f is the sampling frequency of the time series. For this ADV system the minimum limit of the normalised integral timescale is therefore $\frac{\bar{\tau_{ii}}U}{W} = 0.0016$, which the noisy signals, i.e. v in probe B and w in probe A, are slightly greater than showing that the noise has a very significant impact on the integral timescale making it essentially a measurement of instrument noise rather than a flow characteristic. In addition both data replacement methods, sample-and-hold

and linear interpolation, calculate integral timescales with reasonable agreement for all three velocity components, suggesting there is little bias to either method.

Although the means (Reynolds normal stresses) of the ADV velocity signal will (may) agree for different probe orientations, more complex analysis involving integral time/lengthscales show large differences. In figure 5.11 the normalised integral timescale $1.5D$ downstream of the turbine for all three velocity components is shown. For all three components it is seen that the integral timescale is much lower - by a factor of 2 - for the unfiltered data, this is due to the presence of noise. Not only is the signal much smaller for the unfiltered data but there are also differences between the two probe orientations. For instance in the streamwise component where both probes agree for mean and standard deviation, there are qualitative differences between the integral timescales (figure 5.11 (a)), i.e. they do not follow the same trends across the entire width of the channel. This highlights that the noise is non-constant for the two probes. The vertical integral timescales shown in figure 5.11 (b) are larger for probe A, due to the noise in probe B for this component. The converse is true for the spanwise integral timescale where it is much larger for probe B than probe A. The unfiltered spanwise timescales for probe B are very similar to the filtered timescales for probe A, showing that the unfiltered time series for probe B is giving a better estimation than the filtered for probe B. This result agrees with the integral timescales calculated within the uniform flow. These two data sets indicate that particular care should be used when trying to determine such scales from ADV measurements as order-of-magnitude errors may occur.

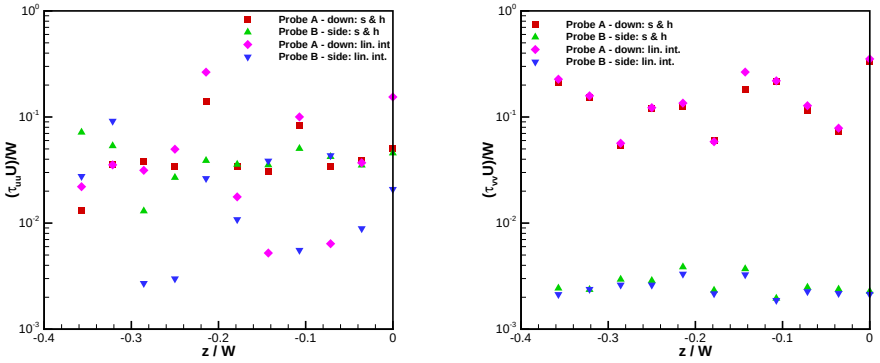

(a) Streamwise Integral Time Scale (b) Vertical Integral Time Scale

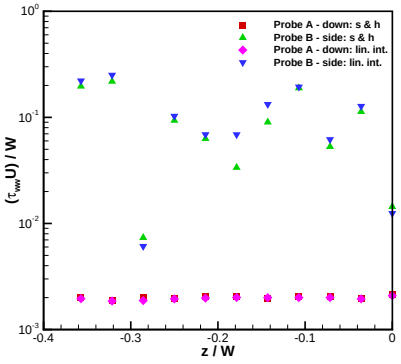

(c) Spanwise Integral Time Scale

Figure 5.10: Integral Time Scales in uniform flow (s & h: Sample and hold, lin. int.: linear interpolation)

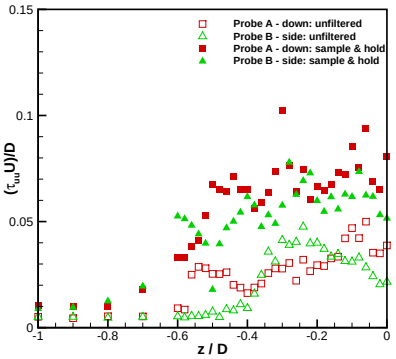

(a) Streamwise Integral Time Scale

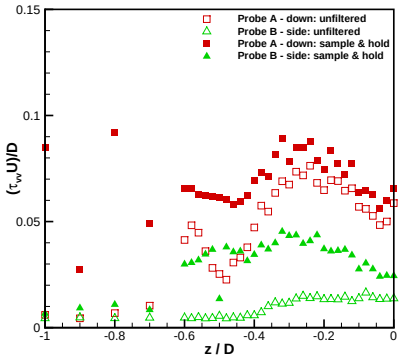

(b) Vertical Integral Time Scale

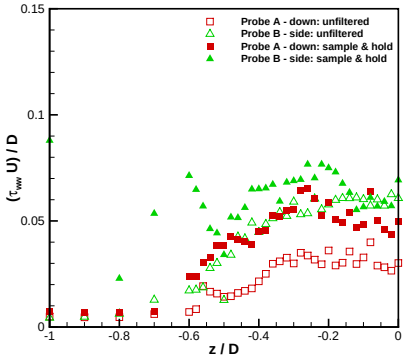

(c) Spanwise Integral Time Scale

Figure 5.11: Integral Time Scales $1.5D$ downstream of the turbine

5.2.6 Fast Fourier Transforms of ADV measurements

One possible source of noise could be from vibrations/oscillations arising from vortex shedding off the support structure holding the device. It is well known that vortex shedding from a cylindrical structure occurs at a Strouhal number (defined as $St = \frac{f_c L}{U}$, where f_c is the frequency, L is a characteristic length of the structure, i.e. the cylinder diameter and U is the mean flow velocity) of around 0.2 dependent on the Reynolds number (White, 2008). To investigate this potential source of additional noise Fast Fourier Transforms (FFTs) of the velocity signals are plotted in figures 5.12 and 5.13 for downwards- and sideways-looking probe orientations and a peak in the velocity signal was observed at measurement depths greater than $0.53m$ ($15cm$ below the centre of the turbine) for both probes. These frequency peaks correspond to a Strouhal number of approximately 0.2, suggesting that at these depths significant vortex shedding from the probe was occurring. For instance for the downwards-looking probe the peak in frequency occurs at $23Hz$ and the typical length, that of the width of the stem from the ADV probe is $8mm$ resulting in $St = 0.184$. For the sideways-looking probe the width of the supporting bar structure is $15mm$ and this peak is frequency is observed at $14Hz$ resulting in $St = 0.21$. However, for all measurements conducted within this chapter the ADV measurements are taken at depths at or above the central turbine hub height to ensure that this was not occurring when the 'noise' effects are being analysed and in these cases the FFTs revealed no peaks. Therefore vortex shedding can be ruled out as a possible mechanism for increasing the Reynolds normal stresses of the ADV measured velocities reported here. Since there are no significant peaks in the FFT of the velocity signal, it can be assumed that any noise in the signal is not a single added frequency but rather an increase in the amplitude of some or all of the measured individual velocities, in agreement with the data of Khorsandi et al. (2012). Since there are no dominant frequencies, this means that there is no simple filtering solution to removing the noise from the velocity signal.

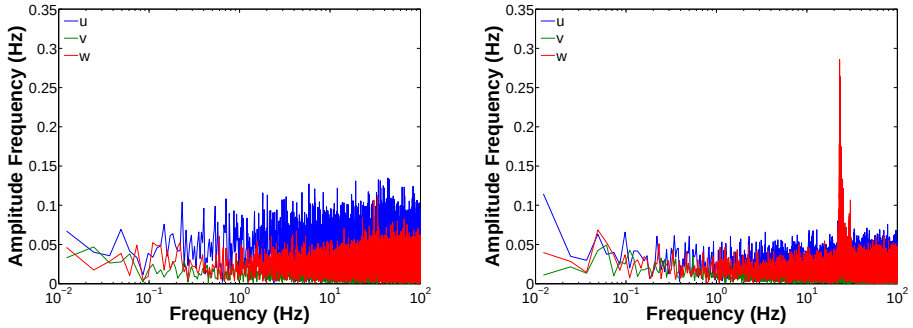

(a) centre (b) 15cm below centre

Figure 5.12: FFT of velocities with ADV downwards looking probe at a height equal to the centre of the turbine and $15cm$ below the centre

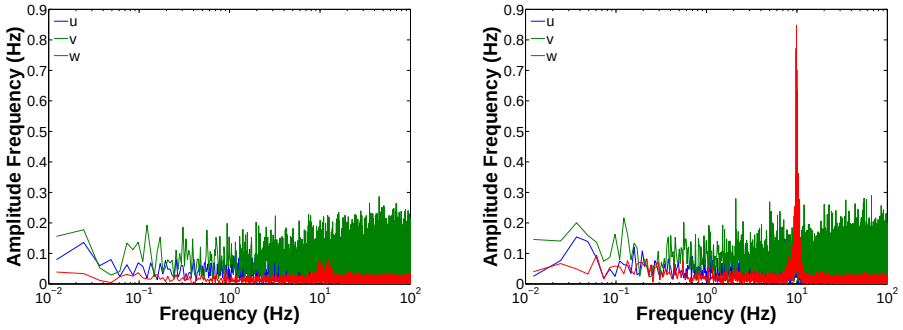

(a) centre (b) 15cm below centre

Figure 5.13: FFT of velocities with ADV sideways looking probe at a height equal to the centre of the turbine and $15cm$ below the centre

5.2.7 Effect of sampling frequency of ADV measurements

Previous studies with ADV have used different sampling frequencies (e.g. Khorsandi et al., 2012) and it was suggested by Blackmore et al. (2014) that reducing the sampling frequency reduces noise within the ADV signal. Hence, to investigate the effect of sampling frequency, measurements were taken with probe A - downwards-looking - at three locations downstream of the turbine (centre, blade edge and channel edge). At each measurement location four different sampling frequencies were used ($25, 50, 100$, and $200Hz$) with $10,000$ samples collected at each frequency. The mean velocities at the different sampling frequencies are shown in figure 5.14 and reasonable agreement is shown at all sampling frequencies. Nevertheless it is found that the sampling frequency does effect the Reynolds normal stresses, as shown in figure 5.15, as the higher the sampling frequency the greater the Reynolds normal stress (apart from at the blade edge where u' is seen to be lower). This reduction of normal stresses by reducing the sampling frequency occurs in all three components, and even reduced the 'noise-free' component suggesting that by reducing the sampling frequency real parts of the velocity signal are also lost, and, as is shown in the next section, the vertical Reynolds normal stress measured at $200Hz$ is in agreement with LDV measurements. In addition to these plots, table 5.3 shows the signal-to-noise ratios (SNR) at the four different sampling frequencies at the three measurement locations. Blackmore et al. (2014) stated that they reduced the ADV sampling frequency because above a sampling frequency of $50Hz$ they found that the SNR was at unacceptable levels ($SNR < 15$), however this was not the case here where the SNR is fairly constant at different frequencies and are not lower than 40. Hence, the SNR does not explain why there is a change in Reynolds normal stresses at different frequencies, but does support the suggestion that some data may be lost at lower sampling frequencies. It is therefore important to be aware of sampling frequencies and that, although

Table 5.3: Signal-to-noise ratios at different sampling frequencies

Sampling Frequency	Blade edge	Centre	Channel edge
25	51.7	42.4	46.1
50	51.5	42.8	46.4
100	51.1	42.9	46.3
200	52.8	43.2	53.6

they may reduce the Reynolds normal stresses, 'real' turbulent fluctuations may also be lost and this is not a suitable method to remove noise from the velocity signal as they do not reduce the normal stresses to the 'noise-free' values.

5.2.8 Comparison with Laser Doppler Velocimetry

To provide an independent benchmark for the ADV measurements, a $1D$ LDV was used to measure separately the streamwise and vertical velocity components in the channel with and without the presence of the turbine. Details of the LDV system are found in section 2.5, which had, on average, a sampling frequency of around $4Hz$. Table 5.4 compares ADV (Probe A) to LDV measurements in uniform flow. All ADV measurements were taken using probe A simultaneously with the LDV. Three independent measurements were taken for both the ADV ($10,000$ samples per location) and LDV ($10,000$ samples per location) and a good agreement can be seen in the mean velocities for all measurements. The streamwise Reynolds normal stresses measured by the ADV are in agreement with the LDV, however for the vertical Reynolds normal stresses the ADV appears to be slightly underestimating the LDV values (or the LDV is slightly overestimating). Thus, in this flow, ADVs are essentially as accurate as an LDV which is often considered as the gold-standard non-intrusive method for turbulence measurements (Adrian & Yao, 1987 and Tropea, 1995). In addition to the results in uniform flow, si-

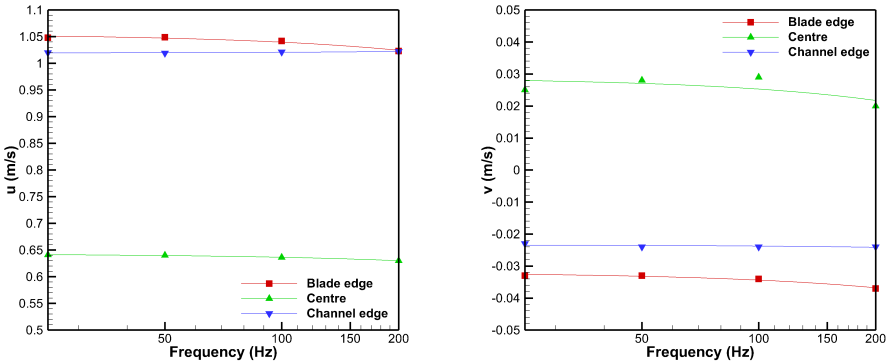

(a) u (b) v

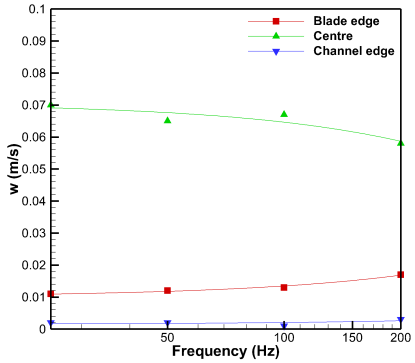

(c) w

Figure 5.14: Mean velocities measured at different sampling frequencies (plotted with linear lines of fit)

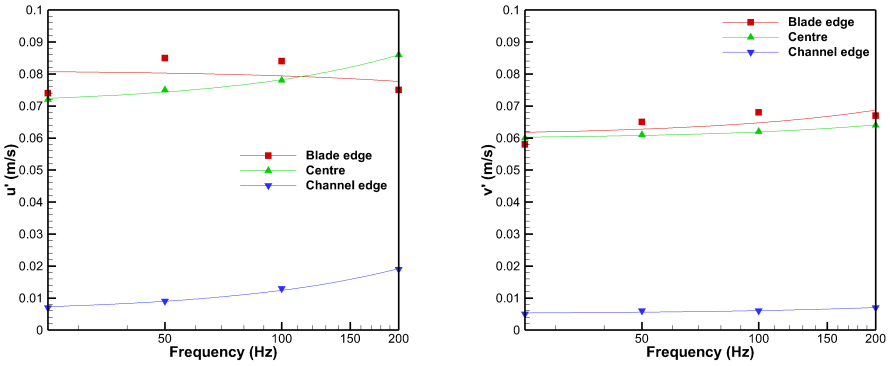

(a) u' (b) v'

(c) w'

Figure 5.15: Reynolds normal stresses measured at different sampling frequencies (plotted with linear lines of fit)

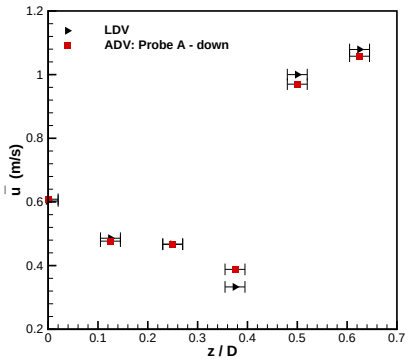

(a) Streamwise velocity

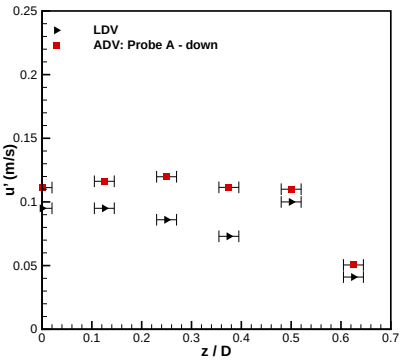

(b) Standard deviation of streamwise velocity

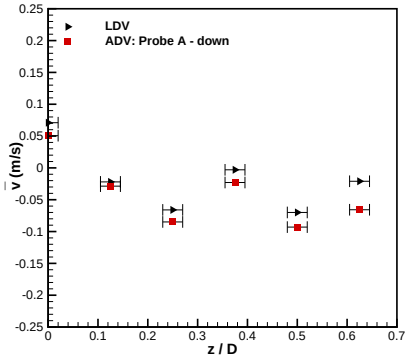

(c) Vertical velocity

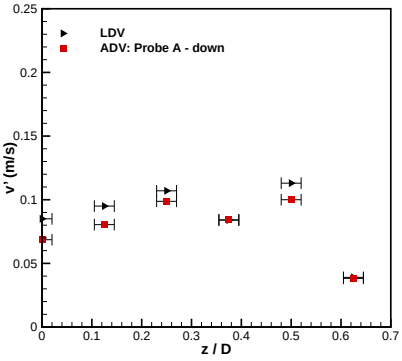

(d) Standard deviation of vertical velocity

Figure 5.16: ADV and LDV measurements downstream of the turbine

Table 5.4: ADV and LDV measurements in uniform flow

	$\bar{u}$ (m/s)	u' (m/s)	$\bar{v}(m/s)$	v' (m/s)
ADV - 1	0.98	0.019	-0.01	0.007
LDV - 1	1.00	0.019	-0.016	0.010
ADV - 2	0.98	0.019	-0.01	0.007
LDV - 2	1.00	0.018	-0.025	0.011
ADV - 3	0.97	0.023	-0.02	0.009
LDV - 3	0.98	0.018	-0.022	0.013

multaneous ADV and LDV measurements were also taken downstream of the turbine. It was only possible to measure the streamwise and vertical velocities using the LDV as the measurements were taken through the side-window of the water-channel.

These measurements were taken by keeping the ADV and LDV stationary and moving the turbine in the channel to capture the shear in the wake behind the turbine without having to move the measurement systems; this also ensured that the ADV and LDV control volumes were always centred at the same point in space. To ensure measurements were taken at the same point in space measurements were taken with the ADV and LDV in a region of high shear behind the turbine where the ADV was moved in $3mm$ increments in all three dimensions until mean velocities in ADV and LDV matched. Measurements were taken at six points $1.5D$ downstream of the turbine, where $z/D = 0$ is the centre of the turbine and $z/D = 0.5$ is the edge of the turbine blades (figure 5.16). The horizontal error bars, included in figure 5.16, indicate a maximum error of $5mm$ in the positioning of the turbine in the flow. Similar to the results in uniform flow, the mean streamwise (figure 5.16(a)) and vertical (figure 5.16(c)) velocity show good agreement for the ADV and LDV, showing that the ADV is entirely consistent with LDV when measuring the mean velocities. ADV is always overestimating the streamwise Reynolds normal stresses (figure 5.16(b)) compared with the LDV measurements and is worst at the slower mean velocities in the wake.

However, for the vertical Reynolds normal stresses (figure 5.16(d)) ADV gives a reasonable approximation to the LDV values, and in fact may be slightly underestimating the LDV measurements in some cases. Having compared ADV measurements to LDV it can be concluded that the ADV overestimates the normal stresses in at least one component, for example for probe A, downwards-looking, it is the streamwise component which is overestimated.

5.3 Summary of key results and recommendations for ADV use

Because of the issues with velocity measurements from ADV highlighted in this chapter, to estimate the effect of noise issues with ADV wake measurements presented in the previous chapters, measurements were repeated for all conditions, and are presented in Appendix A. These repeated measurements were obtained in the three different flow conditions (uniform flow ($TI \approx 2\%$), grid generated turbulence uniform flow ($TI \approx 5\%$) and non-uniform flow ($TI \approx 5\%$)) using the two probe orientations; sideways- and downwards-looking where, as in the previous chapters, the turbine was set with three blades at optimum blade-pitch-angle (6^o). Further the torque set to 20% of the motor's maximum torque resulting in tip-speed-ratio of 6.15, thrust coefficient of 1.00 and power coefficient of 0.35 for all flow conditions. These measurements were taken within two weeks to ensure conditions were as constant as possible, such as water depth (so that water was not required to be removed and evaporation was minimal), temperature, and seeding particle density. Minor repeatability errors can occur when setting the channel velocity but it is estimated that the velocity can be always set within a 1%. All the near-wake measurements shown in appendix A were taken at a height equal to the centre of the turbine.

The results shown in this section, and the repeated measurements in appendix D, show that different probe orientations give the same mean ve-

locities but different Reynolds normal stresses. The velocity component in the j direction appears to be the least effected by noise and is seen to be essentially accurate, two of the components were shown to have significant levels of noise. It is also observed that the noise in the signal changes in a non-linear and non-systematic manner and therefore no simple solution was obtained to correct for these artefacts. Therefore it is useful to measure the wake in at least two different ADV probe orientations to provide a set of data which allows us to gain 'noise-free' measurements of the vertical and spanwise velocities. Nonetheless, it was not possible to measure the streamwise component 'noise-free' due to the limitations of the ADV probe used. ADVs are good at showing trends in the flow and provide a good qualitative data set to compare general flow characteristics. However, higher order turbulence statistics should be calculated with caution, as measures such as integral time/lengthscales are very sensitive to noise where order of magnitude differences are seen between different probe orientations. On the other hand TKE was found to be a fairly robust measure, in particular the maximum TKE decay is shown to be fairly unaffected by probe orientation and is a useful measure of the turbulence downstream of the tidal turbine. It was found that in the very low turbulence levels, i.e. empty channel, the ADV (downwards-looking orientation) measurements were equally as good as LDV. In more complex shear flows - typical of tidal turbine wakes - ADV (downwards-looking orientation) was found to overestimate u' but v' was found to be equivalent if not lower than the same measurement taken with LDV. Overall ADV is quick and easy to set-up, can measure all three-dimensional velocities and is a very useful instrument to characterise the near-wake of tidal devices, but caution should be taken in regard to 'noise'.

Chapter 6

Conclusions

Scale model testing of tidal devices in well controlled laboratory environment is required before optimal development of full-scale devices. It is crucial to investigate the power output and loading on the tidal device and the effect of these in flow conditions of those experienced at sea. Additionally, characterisation of the flow field around a tidal stream turbine is important for the consideration of farms and arrays of devices. A number of studies, both experimentally and numerically, have conducted research in this area and were discussed in detail in chapter 1.

In chapter 2 the experimental facilities and instrumentation that were used throughout this thesis, including details on the production of different flow conditions within the high-speed water-channel were explained. To produce more realistic flow conditions than those produced in the water-channel alone, i.e. uniform with low TI, a uniform flow with a high TI was produced by means of a grid upstream of the working section. Furthermore a series of horizontal bars were placed upstream producing a more realistic non-uniform steady velocity profile (with high TI) representative of a $1/5th$ power-law. The power and thrust on the turbine measurements were taken in uniform flow (low TI) with numbers of blades ranging between two and six with various blade-pitch-angles. These experiments confirmed the

study by Mason-Jones (2010) in which the optimum blade-pitch-angles for this particular design of turbine were calculated using CFD. It was found at upstream velocities $< 0.78m/s$ the power coefficient did not collapse and was dependent on Reynolds number: suggesting that scaled experimental studies with this turbine should be conducted at Reynolds numbers greater than 2 x 10^5. In addition a key result of the thesis, shown in chapter 2, which confirms for the first time experimentally purely numerical results from both Mason-Jones et al. (2012) and Fleming et al. (2013), collapse of the power and thrust coefficients in both uniform and non-uniform flow was observed when normalised by the integral average velocity or velocity squared/cubed respectively.

The wake of the turbine was measured in uniform flow with low TI (2%) in chapter 3. Initially the flow field around the three-bladed turbine with optimum blade-pitch-angle and upstream velocity of $0.9m/s$ was measured using an ADV at five different heights, up to $7D$ downstream. Upstream velocity measurements showed that the turbine did not influence the uniformity of the flow at $1D$ and $2D$ upstream, but altered the mean flow by 10% at $0.5D$ upstream. By $7D$ downstream - the furthest location accessible in the water-channel - all the streamwise mean velocities had recovered to 85% of the upstream mean velocity. The main feature of the wake was found to be the large-scale swirling motions induced by the rotation of the blades which was visible in the mean vertical and spanwise velocities. It was suggested that these swirling motions had the greatest impact on the fluctuating velocities and, therefore, ultimately the TKE recovery downstream. As a consequence of the inclusion of swirl effects, the TKE downstream of the turbine was found to be very different to that downstream of the absorption disk measured by Harrison et al. (2010). These results suggested that the disk, although reasonable at capturing the streamwise mean flow, does not fully capture the complicated turbulent nature of the flow downstream of a rotating turbine. Calculations of the Reynolds stress anisotropy found that

the wake of a turbine is highly anisotropic and therefore it is recommended that turbulence models which assume isotropy are avoided when numerically modelling turbine wakes.

A number of studies have measured wakes at low Reynolds number (e.g. Stallard et al., 2013, Neary et al., 2013 and Harrison et al., 2010). In chapter 2 it was found that at velocities less than $0.78m/s$ power coefficients were dependent on Reynolds number. To probe the effect of Reynolds number on turbine wakes, the wake of the three-bladed turbine (where the tip-speed-ratio was matched to that of the study at $0.9m/s$), with optimum blade-pitch-angle (6^o), was measured with upstream velocities of $0.45m/s$ and $0.68m/s$ in section 3.2. The streamwise mean velocity in the turbine's wake was found to be similar at both $0.45m/s$ and $0.68m/s$ and the deficit was in agreement to that downstream of the turbine measured by Stallard et al. (2013) and the absorption disk by Harrison et al. (2010) after $3D$ downstream. However the mean streamwise velocity in the wake at lower upstream velocities was greater than at $0.9m/s$ and had recovered to only 70% of the mean upstream velocity by $7D$ downstream rather than 85%. The TKE decay of the wake was similar for upstream velocities of both $0.68m/s$ and $0.9m/s$, (and in the study by Stallard et al. (2013)) after $3D$ downstream. With upstream velocity of $0.45m/s$ the TKE in the very near-wake ($< 4D$) was about 50% lower. Therefore the data in this thesis indicates that caution must be taken when measuring the near-wake of turbines at low Reynolds numbers as characteristics may not be fully representative of a wake at full-scale.

Harrison et al. (2010) suggested that the thrust coefficient has the greatest impact on the wake characteristics and Chamorro et al. (2013) showed that the mean velocity in the wake was slightly dependent on tip-speed-ratio. To investigate the effect of C_T and λ on the wake, measurements were taken downstream of a two-bladed turbine at optimum and non-optimum blade-pitch-angles and compared to the results of the wake of the three-bladed turbine. The two-bladed turbine with optimum blade-pitch-angle had matching

C_P and tip-speed-ratio to the three-bladed turbine, but C_T was increased by 40%. At non-optimum blade-pitch-angle the C_T of the two-bladed turbine was half the C_T for the three-bladed turbine and the tip-speed-ratio and C_P was slightly reduced. After $3D$ downstream the maximum streamwise velocity agreed within 5% for both two-bladed turbine wakes and the three-bladed turbine wake. However the maximum streamwise velocity downstream of the two-bladed turbine with non-optimum blade-pitch-angle was much lower than those at optimum blade-pitch-angles which suggested that the reduction in power extraction or reduced thrust increased the downstream velocity in the very near-wake. Collapse of the TKE downstream of the two and three-bladed turbine with optimum blade-pitch-angles was observed, contrary to the suggestion of Harrison et al. (2010) that C_T is a dominant factor. It was observed that for different thrust coefficients, but matching C_P and λ, i.e. the two- and three-bladed turbines at optimum blade-pitch-angles, the wakes were similar. However when all three coefficients were altered (i.e. two-bladed turbine with non-optimum blade-pitch-angle) the wakes were found to be very different. As a consequence of these two results it was posited that the wake structure is more dependent on C_P and/or λ than C_T.

In all the wake studies in chapter 3 a reduction in streamwise velocity was constantly found directly downstream of the centre of the channel, and Myers & Bahaj (2009) found that the wake of the turbine support structure was significant. The wake of the turbine support structure without blades was measured with an upstream velocity of $0.9m/s$. The support structure had little impact on the mean velocities or Reynolds normal stresses after $2D$ downstream which was a smaller impact than that observed for the larger support structure in Myers & Bahaj (2009) of $3.5D$ downstream confirming that shape and size of the support structure is crucial to reduce downstream effects.

In chapter 4 the wake of a three-bladed turbine with optimum blade-pitch-angle (6^o) was measured in uniform flow with high TI (5%) and non-uniform

flow with high TI. When normalised by the integral average velocity, the wake through the centre-plane at a depth equal to the centre of the turbine was found to be very similar, for both means and turbulence statistics, in all three flow conditions. At different depths, the velocity profile with non-uniformity of the upstream flow was still present $5D$ downstream of the turbine. As there was little to distinguish the wakes in the three flow conditions it was proposed that the key feature of the wake of a turbine is the swirling motions produced by blade rotation.

Throughout this thesis and in a number of other studies (e.g. Myers & Bahaj, 2009, Stallard et al., 2013 and Neary et al., 2013) ADV has been used to measure velocities in the flow field around a tidal turbine. During the latter stages of the course of the research reported in this thesis, questions emerged about the characteristics of ADV measurements. ADV probe orientation was found to effect the velocity fluctuations and therefore in chapter 5 experiments were conducted to investigate the robustness of this measurement technique. The biggest advantage of ADV is that it is quick to set up, easy to use, and is capable of measuring mean velocities in three dimensions to a high accuracy. It was shown that the orientation of the ADV probe has little effect on these mean velocities. However, from comparison to $1D$ LDV and different probe orientations, results also showed that the Reynolds normal stresses are dependent on the probe orientation and that two of the components contain significant levels of noise. Thus the Reynolds normal stresses recorded by the ADV are always overestimated for two of the velocity components. It was observed that the noise in the signal changes in a non-linear and non-systematic manner and therefore no simple solution was obtained to correct for these artefacts. It is therefore suggested that to improve on these statistics ADV should be used in different orientations as to measure 'noise-free' velocities. The use of two different ADV set-ups allowed 'noise-free' measurements of the vertical and spanwise velocities. However, it was not possible to measure the streamwise component 'noise-free' due to the

limitations of the ADV probe used. It is suggested that ADVs are qualitatively very good at showing the trends in the flow and can be used to obtain general flow characteristics. However, when higher order statistics or integral timescales are calculated, the noise has a very significant influence. Order of magnitude differences were observed between different probe orientations and even different qualitative behaviour. When investigating the TKE, ADV is useful as a robust measure, in particular when looking at the decay of maximum TKE downstream of a turbine, the power-law decay component seems to give a robust approximation of the decay of the turbulence. It is important when comparing computational models with ADV measurements to consider the effect of noise on the velocity signal, especially when looking at higher order statistics and integral length/timescales. It is recommended that the j velocity component, e.g. vertical velocity for a downwards-looking probe, is used as the most suitable data set for comparison between experimental data and numerical predictions. Due to the issues highlighted in chapter 5, measurements of the wake of the three-bladed turbine in the three flow conditions were repeated with the two different probe orientations and were shown in appendix D. These repeated measurements therefore give data-sets that are as accurate as possible so that comparison of numerical models can be made. This solution of repeating the measurements is not optimal and as it was only possible to compare the ADV measurements to $1D$ LDV, it is therefore recommended that $2D$ or $3D$ LDV measurements are taken alongside ADV in different flow conditions to confirm these suggestions.

6.1 Future work and recommendations

The work presented in this thesis gives a large data set of wake measurements to which numerical models can be compared to. Although there are a number of numerical studies that have modelled the wakes of turbines there has been little comparison to experimental work. It is therefore recommended that to compare to this data set models should be representative of the scale model turbine and conditions found in the UoL water-channel before being expanded to full-scale devices in more realistic flows and arrays of devices. The turbulent flow downstream of the turbine was found to be highly anisotropic, therefore any turbulence models used in simulations should not assume isotropy.

In an attempt to create realistic flows a number of different well characterised flow conditions were produced with the UoL water-channel, these conditions were still relatively simple compared to those found at sea. Further experimental work on power, thrust and wakes of turbines in more complex flows is therefore required. Flows with increased shear and with waves are of particular interest as these are likely to cause uneven loading on the turbine structure possibly reducing its performance and life-span. Additionally, these more realistic flows may impact the wake and could alter the design of arrays or farms where positioning of turbines is crucial.

It is not fully clear from either the literature or this study which coefficient (thrust, power or tip-speed-ratio) has the largest impact on the wake structure which could be crucial for arrays/farms of devices in a limited space or to obtain maximum power from a particular tidal region. By changing the numbers of blades, blade-pitch-angles, and torque the coefficients can be altered therefore further well-controlled tests of turbine wakes should be taken to try to alter a single coefficient at a time.

The ADV technique has been extensively used in this thesis and throughout the literature for measuring the flow field around turbines. However, as discussed in chapter 5, when compared to $1D$ LDV the ADV overesti-

mates the velocity fluctuation in at least one component. It is therefore recommended that measurements with ADV are compared with a $3D$ LDV system in flows typical of those found in turbine wakes so that the robustness of ADV is fully studied and detailed recommendations can be made. This comparison is required to investigate turbulence statistics such as Reynolds shear stresses and the calculations of the Reynolds stress anisotropy tensor in addition to any corrections that can be made to the ADV technique.

References

M. S. Adaramola, O. G. Akinlade, D. Sumner, D. J. Bergstrom, and A. J. Schenstead. Turbulent wake of a finite circular cylinder of small aspect ratio. *J. Fluid. Struct.*, 22(67):919 – 928, 2006.

R. J. Adrian and C. S. Yao. Power spectra of fluid velocities measured by laser Doppler velocitmetry. *Exp. Fluids*, 5:17–28, 1987.

A. S. Bahaj, A. F. Molland, J. R. Chaplin, and W. M. J. Batten. Power and thrust measurements of marine current turbines under various hydrodynamic flow conditions in a cavitation tunnel and a towing tank. *Renew. Energ.*, 32(32):407–426, 2006.

A. S. Bahaj, W. M. J. Batten, and G. McCann. Experimental verifications of numerical predictions for the hydrodynamic performance of horizontal axis marine current turbines. *Renew. Energ.*, 32:2479 – 2490, 2007.

N. Barltrop, K.S. Varyani, A. Grant, D. Clelland, and X. P. Pham. Wave-current interactions in marine current turbines. In *Proceedings of the Institution of Mechanical Engineers, Part A: J. Power Energ.*, 2006.

N. Barltrop, K.S. Varyani, A. Grant, D. Clelland, and X. P. Pham. Investigation into wave-current interactions in marine current turbines. In *Proceedings of the Institution of Mechanical Engineers, Part A: J. Power Energ.*, 2007.

W. M. J. Batten, A. S. Bahaj, A. F. Molland, J. R. Chaplin, and Sustainable Energy Res Grp. Experimentally validated numerical method for the hydrodynamic design of horizontal axis tidal turbines. *Ocean Eng.*, 34(7): 1013–1020, 2007.

W. M. J. Batten, A. S. Bahaj, A. F. Molland, and J. R. Chaplin. The prediction of the hydrodynamic performance of marine current turbines. *Renew. Energ.*, 33:1085 – 1096, 2008.

W. M. J. Batten, M. E. Harrison, and A. S. Bahaj. Accuracy of the actuator disc-RANS approach for predicting the performance and wake of tidal turbines. *Philos. T. R. Soc.*, 371:20120293, 2013.

Black and Veatch Ltd. Phase II UK tidal stream energy tidal stream energy resource assessment. Technical Report 107799/D/2200/03, Carbon Trust, 2005.

T. Blackmore, W. M. J. Batten, G. U. Muller, and A. S. Bahaj. Influence of turbulence on the drag of solid discs and turbine simulators in a water current. *Exp. Fluids*, 55:1637, 2014.

P. Bucchave, W. R. George, and J. L. Lumley. The Measurement of Turbulence with the Laser-Doppler Anemometer. *Annu. Rev. Fluid Mech.*, 11: 443–503, 1979.

Carbon Trust. United Kingdom Wave and Tidal Energy Study. Variablity of UK marine resources. Final Report, 2005.

L. P. Chamorro, C. Hill, S. Morton, C. Ellis, R. E. A. Arndt, and F. Sotiropoulos. On the interaction between a turbulent open channel flow and an axial-flow turbine. *J. Fluid Mech.*, 716:658–670, 2013.

J. C. Chapman, I. Masters, M. Togneri, and J. A. C. Orme. The Buhl correction factor applied to high induction conditions for tidal stream turbines. *Renew. Energ.*, 60:472 –480, 2013.

T. Y. Chen and L. R. Liou. Blockage corrections in wind tunnel tests of small horizontal-axis wind turbines. *Exp. Therm. Fluid Sci.*, 35(3):565–569, 2011.

K. S. Choi and J. L. Lumley. The return to isotropy of homogeneous turbulence. *J. Fluid Mech.*, 436:59–84, 2001.

D. J. Cockrell and B. E. Lee. Production of Shear Profiles in a Wind Tunnel by Cylindrical Rods Placed Normal to the Stream. *J. R. Aeronaut. Soc.*, 70(7), 1966.

C. A. Consul, R. H. J. Willden, and S. C. McIntosh. Blockage effects on the hydrodynamic performance of a marine cross-flow turbine. *Phil. Trans. R. Soc.*, 371:210120299, 2013.

T. Daly, L. E. Myers, and A. S. Bahaj. Modelling of the flow field surrounding tidal turbine arrays for varying positions in a channel. *Philos. T. R. Soc.*, 371:20120246, 2013.

Department of Energy and Climate Change. UK Renewable Energy Roadmap update 2013. Technical report, DECC, 2013.

R. Devarakonda and J. A. C. Humphrey. Experimental study of turbulent flow in the near wakes of single and tandem prisms. *Int. J. Heat Fluid Fl.*, 17(3):219–227, JUN 1996.

D. A. Egarr, T. O'Doherty, T. Morris, and R. G. Ayre. Feasibility study using Computational Fluid Dynamics for the use of a turbine for extracting energy from the tide. In *15th Australasian Fluid Mechanics Conference*, The University of Sydney, Sydney, Australia, 2004.

J.W. Elder. Steady Flow Through Non-Uniform Gauzes of Arbitrary Shape. *J. Fluid Mech.*, 5:355–368, 1959.

C. F. Fleming, S. C. McIntosh, and R. H. J. Willden. Tidal Turbine Performance in Sheared Flow. In *Tenth European Wave and Tidal Energy Conference*, Aalborg, Denmark, 2013.

Fujita Research. Wave and Tidal Power. *Web version Jul 2000,* `www.fujitaresearch.com/reports/tidalpower.html`, 2011.

P.W. Galloway, L. E. Myers, and A. S. Bahaj. Quantifying wave and yaw effects on a scale tidal stream turbine. *Renew. Energ.*, 63:297–307, 2013.

C. Garrett and P. Cummins. The efficiency of a turbine in a tidal channel. *J. Fluid Mech.*, 588:243–251, 2007.

D. G. Goring and V. I. Nikora. Despiking Acoustic Doppler Velocimeter Data. *J. Hydraul. Eng.*, 128(1):117–126, 2002.

J. Hardisty. *The Analysis of Tidal Stream Power*. Wiley-Blackwell, 2009.

M. E. Harrison, W. M. J. Batten, L. E. Myers, and A. S. Bahaj. Comparison between CFD simulations and experiments for predicting the far wake of horizontal axis tidal turbines. *IET Renew. Power Gen.*, 4(6, Sp. Iss. SI): 613–627, 2010.

J. O. Hinze. *Turbulence*. McGraw-Hill Publishing Company, 2nd edition, 1975.

D. Hurther and U. Lemmin. A correction method for turbulence measurements with a 3D acoustic Doppler velocity profiler. *J. Atmos. Ocean. Tech.*, 18(3):452–463, 2001.

H. J. Hussein, S. P. Capp, and W. K. George. Velocity measurements in a high-Reynolds-number, momentum-conserving, axisymmetrical, turbulent jet. *J. Fluid Mech.*, 258:31–75, 1994.

B. Khorsandi, L. Mydlarski, and S. Gaskin. Noise in Turbulenc Measurements Using Acoustic Doppler Velocimethry. *J. Hydraul. Eng.*, 138(10): 829–838, 2012.

J. King and T. Tryfonas. Tidal Stream Power Technology - State of the Art. In *Oceans 2009 - Europe, Vols 1 and 2*, Oceans-IEEE, pages 146–153, 2009. Oceans 2009 Conference, Bremen, Germany, May 11-14, 2009.

N. C. Kraus, A. Lohrmann, and R. Cabrera. New Acoustic Meter for Measuring 3D Laboratory Flows. *J. Hydraul. Eng.*, 120(3):406–412, 1994.

U. Lemmin and R. Lhermitte. Discussion of 'ADV measurements of turbulence: Can we improve their interpretation?' by V.I. Nikora and D. G. Goring. *J. Hydraul. Eng.*, 25(3):987–988, 1999.

J.L. Livesey and J.T. Turner. The Generation of Symmetrical Duct Velocity Profiles of High Uniform Shear. *J. Fluid Mech.*, 20:201–208, 1964.

A. Lohrmann, R. Cabrera, and N. C. Kraus. Acoustic-Doppler velocimeter (ADV) for laboratory use. In C.A. Pugh, editor, *Fundamentals and advancements in hydraulic measurements and experimentation*, pages 351–365, ASCE, Reston, VA, 1994.

J. Lumley. Computational modelling of turbulent flows. *Adv. Appl. Mech.*, 18:123, 1978.

Lunar Energy. [online].`http://www.lunarenergy.co.uk/`, 2013.

L. Luznik, K. A. Flack, J. M. Walker, and M. C. V. Benthem. The influence of surface gravity waves on marine current turbine performance. *Int. J. Marine Energ.*, 3-4:27 – 40, 2013.

F. Maganga, G. Germain, J. King, G. Pinon, and E. Rivoalen. Experimental study to determine flow characteristic effects on marine current turbine be-

haviour. In *Eighth European Wave and Tidal Energy Conference*, Uppsala, Sweden, 2009.

F. Maganga, G. Germain, J. King, G. Pinon, and E. Rivoalen. Experimental characterisation of flow effects on marine current turbine behaviour and on its wake properties. *IET Renew. Power Gen.*, 4(6):498–509, NOV 2010.

R. Malki, A. J. Williams, T.N. Croft, M. Togneri, and Masters I. A coupled blade element momentum - Computational fluid dynamics model for evaluating tidal stream turbine performance. *Appl. Math. Model.*, 37:3006–3020, 2013.

Marine Current Turbines. [online]. `http://www.marineturbines.com/`, 2013.

A. Mason-Jones. *Performance assessment of a Horizontal Axis Tidal Turbine in a high velocity shear environment*. PhD thesis, Cardiff University, 2010.

A. Mason-Jones, D. M. O'Doherty, C. E. Morris, T. O'Doherty, C. B. Byrne, P. W. Prickett, R. I. Grosvenor, I. Owen, S. C. Tedds, and R. J. Poole. Non-dimensional scaling of tidal stream turbines. *Energy*, 44(1):820 – 829, 2012.

A. Mason-Jones, D. M. O' Doherty, C. E. Morris, and T. O' Doherty. Influence of a velocity profile and support structure on tidal stream turbine performance. *Renew. Energ.*, 52:23–30, 2013.

R. A. McAdam, G. T. Houlsby, M. L. G. Oldfield, and M. D. McCulloch. Experimental Testing of the Transverse Horizontal Axis Water Turbine. In *Eighth European Wave and Tidal Energy Conference*, Uppsala, Sweden, 2009.

F. R. Menter. Two-Equation Eddy- Viscosity Turbulence Models for Engineering Applications. *AIAA Journal*, 32:1598–1605, 1994.

S. J. Miley. A catalog of low Reynolds number airfoil data for wind turbine applications, DE82-021712. Technical report, National Technological Information Service, 1982.

A. Millward. The Design and Development of a Recirculating Water Channel - A Critical Assessment. Master's thesis, University of Liverpool, 2002.

A. Millward and J. Rossiter. The Design of a Multi-purpose Multi-component Strain Gauge Dynamometer. *Strain*, 19(7):27–30, 1983.

F. Murzyn and Belorgey. Experimental investigation of the grid-generated turbulence features in a free surface flow. *Exp. Therm. Fluid. Sci.*, 29: 925–935, 2005.

P. Mycek, B. Gaurier, G. Germain, G. Pinon, and E. Rivoalen. Numerical and Experimental Study of the Interaction Between Two Marin Current Turbines. In *Ninth European Wave and Tidal Energy Conference*, Southampton, UK, 2011.

P. Mycek, B. Gaurier, G. Germain, J-V. Facq, T. Bacchetti, G. Pinon, and E. Rivoalen. Characterisation of Interactions between Horizontal Axis Turbine Aligned with the Flow. In *Tenth European Wave and Tidal Energy Conference*, Aalborg, Denmark, 2013a.

P. Mycek, B. Gaurier, G. Germain, and G. Pinon. Numerical and experimental study of the interaction between two marine current turbines. *Int. J. Marine Energ.*, 1:70–83, 2013b.

L. Myers and A. S. Bahaj. Power output performance characteristics of a horizontal axis marine current turbine. *Renew. Energ.*, 31(2):197–208, 2006.

L. Myers and A. S. Bahaj. Near wake properties of horizontal axis marine current turbines. In *Eighth European Wave and Tidal Energy Conference*, Uppsala, Sweden, 2009.

L. E. Myers and A. S. Bahaj. Experimental analysis of the flow field around horizontal axis tidal turbines by use of scale mesh disk rotor simulators. *Ocean Engineering*, 37(2-3):218–227, 2010.

V. S. Neary, B. Gunawan, C. Hill, and P. Chamorro. Near and far field flow disturbances induced by model hydrokinetic turbine: ADV and ADP comparison. *Renew. Energ.*, 60:1–6, 2013.

Neptune Renewable Energy. [online]. `http://www.neptunerenewableenergy.com/`, 2013.

I. Nezu and W. Rodi. Open-Channel Flow Measurements with a Laser Doppler Anemometer. *J. Hydraul. Eng.*, 112(5):335–355, 1986.

Nortek AS. Vectrino velocimeter user guide. Technical report, Norway, 2009.

T. O'Doherty, A. Mason-Jones, D. M. O'Doherty, C. B. Byrne, I. Owen, and Y. Wang. Experimental and Computational Analysis of a Model Horizontal Axis Tidal Turbine. In *Eighth European Wave and Tidal Energy Conference*, Uppsala, Sweden, 2009.

A. Olczak, T. Stallard, and P. Stansby. The Influence of Waves on Tidal Stream Turbine Wake Recovery. In *Tenth European Wave and Tidal Energy Conference*, Aalborg, Denmark, 2013.

P.R. Owen and H.K. Zienkiewcz. The Production of Uniform Shear Flow in a Wind Tunnel. *J. Fluid Mech.*, 2:521–531, 1957.

N. R. Panchapakesan and J. L. Lumley. Turbulence measurements in axisymmetric jets of air and helium. Part 1. Airjet. *J. Fluid Mech.*, 246: 197–223, 1993.

G. Pinon, P. Mycek, G. Germain, and E. Rivoalen. Numerical simulation of the wake of marine current turbines with a particle method. *Renew. Energ.*, 46:11–126, 2012.

S. B. Pope. *Turbulent Flows*. Cambridge University Press, 2011.

Pulse Tidal. [online]. `http://www.pulsetidal.com/`, 2013.

S. Rose, A. Good, M. Atcheson, Hamill G., C. Johnstone, P. MacKinnon, D. Robinson, A. Grant, and T. Whittaker. Investigating Experimental Techniques for Measurement of the Downstream Near Wake of a Tidal Turbine. In *Ninth European Wave and Tidal Energy Conference*, Southampton, UK, 2011a.

S. Rose, S. Ordonez, K. H. Lee, C. Johnstone, C. H. Jo, T. McCombes, and A. Grant. Tidal Turbine Wakes: Small Scale Experimental and Initial Computational Modelling. In *Ninth European Wave and Tidal Energy Conference*, Southampton, UK, 2011b.

A. J. Simonsen and P. A. Krogstad. Turbulent stress invariant analysis: Clarification of existing terminology. *Phys. Fluids*, 17:88–103, 2005.

C. Soares. Tidal Power: the next wave of electricity. *Pollution Engineering, www.pollutionengineering.com*, 2011.

T. Stallard, R. Collings, T. Feng, and J. I. Whelan. Interations Between Tidal Turbine Wakes: Experimental Study of a Group of 3-Bladed Rotors. In *Ninth European Wave and Tidal Energy Conference*, Southampton, UK, 2011.

T. Stallard, R. Collings, T. Feng, and J. Whelan. Interactions between tidal turbine wakes: experimental study of a group of three-bladed rotors. *Philos. T. R. Soc.*, 371:20120159, 2013.

X. Sun, J. P. Chick, and I. G. Bryden. Laboratory-scale simulation of energy extraction from tidal currents. *Renew. Energ.*, 33(6):1267–1274, 2008.

C. Sutcliffe. *The effect of waves on the Performance of Yachts*. PhD thesis, University of Liverpool, 1995.

S. C. Tedds, T. A. de Jesus Henriques, I. Owen, and R. J. Poole. Near-wake characterisation of Horizontal Axis Tidal Stream Turbines in non-uniform steady flow. In *Tenth European Wave and Tidal Energy Conference*, Aalborg, Denmark, 2013.

S. C. Tedds, I. Owen, and R. J. Poole. Near-wake characteristics of a model horizontal axis tidal stream turbine. *Renew. Energ.*, 64:222–235, 2014.

H. Tennekes and J. Lumley. *A First Course in Turbulence*. The MIT Press, 1972.

The European Marine Energy Centre Ltd. [online]. `http://www.emec.org.uk/index.asp`, 2014.

C. Tropea. A note concerning the use of a one-component LDA to measure shear stress terms. *Exp. Fluids*, 1(4):209–210, 1983.

C Tropea. Laser-Doppler Anemometry - Recent Developments and Future Challenges. *Measure Sci. Tech*, 6(6):605–619, 1995.

M. S. Uberoi and S. Wallis. Effect of Grid Geometry on Turbulence Decay. *Phys. Fluids*, 10:1216–1224, 1967.

L. J. Vermeer, J. N. Sorensen, and A. Crespo. Wind turbine wake aerodynamics. *Prog. Aerosp. Sci.*, 39(6-7):467–510, 2003.

G. Voulgaris and J. H. Trowbridge. Evaluation of the acoustic Doppler velocimeter (ADV) for turbulence measurements. *J. Atmos. Ocean. Technol.*, 15(1, Part 2):272–289, 1998.

T. L. Wahl. Discussion of 'Despiking acoustic Doppler Velocimeter data' by Derek G. Goring and Vladimir I. Nikora. *J. Hydraul. Eng.*, 129(6):484–488, 2003.

J. I. Whelan, J. M. R. Graham, and J. Peiro. A free-surface and blockage correction for tidal turbines. *J. Fluid Mech.*, 624:281–291, 2009.

F. M. White. *Fluid Mechanics: Sixth Edition*. McGraw-Hill, 2008.

T. Wright. *Fluid Machinery: Performance, Analysis and Design*. CRC Press, Florida, 1999.

H-N. Wu, L-J. Chen, M-H. Yu, W-Y. Li, and B-F. Chen. On design and performance prediction of the horizontal-axis water turbine. *Ocean Eng.*, 50:23–30, 2012.

S. Wussow, L. Sitzki, and T. Hahm. 3D-simulation of the turbulent wake behind a wind turbine. In Hansen, M. O. L. and Hansen, K. S., editor, *Science of Making Torque from Wind*, volume 75 of *J. Phys. Conf. Ser.*, page 12033, 2007.

Appendix A

Developers and their devices

Table A.1 lists all the tidal stream developers and their devices as of early 2014 and is compiled from details given by The European Marine Energy Centre Ltd. (2014). The device type and main location of the developers are detailed.

Table A.1: Tidal developers and their devices (The European Marine Energy Centre Ltd., 2014)

Company	**Technology**	**Device Type**	**Country**
Alstom Hydro	Clean Current Tidal Turbine	Ducted	France
Aquantis Inc	C-Plane	VATT	USA
Atalantis Resources Corp	AR-1000	HATT	UK
Atlantisstrom	Atlantisstorm	HATT	Germany
Aquascientific	Aquascientific Turbine	other	UK
Balkee Tide and Wave Electricity Generator	TWPEG	HATT	Mauitius
BioPower System Pty Ltd	bioStream	Hydrofoil	Australia
Blue Energy	Blue Energy Ocean Turbine (Davis Hydro Turbine)	VATT	Canada
Bluewater	BlueTec	HATT / VATT	Netherlands
BluStream	MegaWatForce	other	France
Bourne Energy	CurrentStar / TidalStar / OceanStar	HATT	USA
Cetus Energy	Cetus Turbine	HATT	Australia
Clean Current Power Systems	Clean Current Tidal Turbine	ducted	Canada
Crest Energy		other	New Zealand
Current2Current	Tidal Turbine	VATT	UK
Current Power AB	Current Power	VATT	Sweden
Ecofys	Wave Rotor	HATT	Netherlands
Edinburgh Designs	Vertical-axis, variable pitch tidal turbine	VATT	UK
Edinburgh University	Polo	VATT	UK

Company	**Technology**	**Device Type**	**Country**
Elemental Energy Technologies Limited	SeaUrchine	ducted HATT	Australia
Fieldstone Tidal Energy Technologies Limited	Fieldstone Tidal Energy	other	USA
Firth Tidal Energy	Sea Caisson and Turbine System (SEACATS)	HATT	UK
Flumill	Flumill Power Tower	other	Norway
Free Flow 69	Osprey	HATT	USA
Free Flow Power Corporation	SmarTurbine	HATT	USA
GCK Technology	Corlov Turbine	VATT	USA
Greener Works Limited	Relentless^{TM}Turbine	other	UK
Greenheat Systems Ltd	Gentec Venturi	other	UK
Hales Energy Ltd	Hales Tidal Turbine	ducted VATT	UK
Hammerfest Strom	Tidal Stream Turbines	HATT	Norway
Hydra Tidal Energy Technology AS	Morild ©	HATT	Norway
Hydro Green Energy	Hydrokinetic	ducted	USA
Hydro-Gen	Hydro-gen	other	France
HydroCoil Power Inc	HydroCoil	other	USA
Hydrokinetic Laboratory	HyPEG	HATT	USA
Hydromine	The Hydro Mine	other	UK
Hydroventuri	Rochester Venturi	ducted	UK
Hydrovolts Inc	Hydrovolts	VATT	USA
Ing Arvid Nesheim	Waterturbine	other	Norway
Kepler Energy	Transverse Horizontal Axis Water Turbine (THWAT)	VATT	UK
Kinetic Energy Systems	Hydrokinetic Generator, KESC Bowsprit Generator, KESC Tidal Generator	HATT	USA
Lucid Energy Technologies	Gorlov Helical Turbine (GHT)	VATT	USA

Company	**Technology**	**Device Type**	**Country**
Lunar Energy	Rotech Tidal Turbine	ducted HATT	UK
Magallanes Renovables	Magallanes Project	HATT	Spain
Marine Current Turbines	SeaGen, SeaFlow	HATT	UK
Minesto	Deep Green Technology	other	Sweden
Natural Currents	Red Hawk	other	USA
Nautricity Ltd	CoRMat	HATT	UK
Neo-Aerodynamic Ltd	Neo-Aerodynamic	VATT	USA
Neptune Systems	Tide Current Converter	other	Netherlands
Neptune Renewable Energy Ltd	Proteus	VATT	UK
New Energy Corp.	EnCurrent Vertical Axis Hydro Turbine	VATT	Canada
Norwegian Ocean Power	The Pulsus Turbine	other	Norway
Ocean Flow Energy	Evopod	HATT	UK
Ocean Renewable Power Company	OCGen	other	USA
Oceana Energy Company	TIDES	HATT	USA
Offshore Islands Ltd	Current Catcher	HATT	USA
OpenHydro	Open Centre Turbine	HATT	Ireland
Ponte di Archimede	Kobold Turbine / Enermar	VATT	Italy
Pulse Tidal	Pulse-Stream	Hydrofoil	UK
Robert Gordon University	Sea Snail	HATT	UK
Roteh	Rotech Tidal Turbine (RTT)	HATT	UK
Rugged Renewables	Savonius turbine	other	UK
SABELLA SAS	Hyrdo-Helix	HATT	France
Scotrenewables	SR250	HATT	UK

Company	**Technology**	**Device Type**	**Country**
SMD Hydrovision	TiDEL	HATT	UK
Sustainable Marine Technologies (SMT)	PLAT-O	HATT	UK
Starfish Electronics Ltd	StarTider	HATT	UK
Statkraft	Tidevanndkraft	HATT	Norway
Swanturbines	Swan Turbine	HATT	UK
Teamwork Tech	Torcado	HATT	Netherlands
The Engineering Business	Stingray	Hydrofoil	UK
Tidal Electric	Tidal Lagoons	other	UK/USA
Tidal Energy Ltd	Delta Stream	HATT	UK
Tidal Energy Systems Corporation	Foil Rotor III	ducted	USA
Tidal Energy Pty Ltd	DHV Turbine	VATT	Australia
Tidal Generation Limited	Deep-gen	HATT	UK
Tidal Sails	Tidal Sails AS	other	Norway
TidalStream	TidalStream Triton Platform	HATT	UK
Tidebg	Tideng	HATT	Denmark
Tocardo BV	Tocardo Turbines	HATT	Netherlands
UEK Corporation	Underwater Electric Kite	hydrofoil	USA
University of Southampton	Southampton Integrated Tidal Generator	HATT	UK
Verdant Power	Various	HATT	USA
Voith Hydro	Hytide	HATT	Germany
Vortex Hydro Energy	VIVACE (Vortex Induced Vibrations Aquatic Clean Energy)	other	USA
Water Wall Turbine	WWTurbine	other	USA
Woodshed Techologies - CleanTechCom Ltd	Tidal Delay	other	Australia / UK

Appendix B

Design of 'velocity profiler'

A velocity profile within the high-speed water-channel was produced by placing a series of horizontal rods at differing depths using the method used by Cockrell & Lee (1966) from wind tunnel experiments. This method arises from basic theory by Elder (1959). For discussion of this method the following variables are used:

B	=	lift coefficient $(-)$
d_r	=	rod diameter (m)
K	=	drag coefficient $(-)$
l	=	rod centre-line spacing (m)
s	=	resistance parameter $(-)$
U	=	maximum velocity at given section (m/s)
$\bar{U} = U_\infty$	=	mean velocity (m/s)
u	=	local velocity at height y (m/s)
V	=	$\frac{u_0}{U_\infty}$ $(-)$
δ_c	=	height of channel (m)

To apply Elder's theory we assume that the upstream velocity U_∞ is uniform, ADV measurements confirm this is true within the high-speed water-channel. Applying Elder's theory we use a number of specific relationships, these are:

$$B = \frac{d_r}{l}, \tag{B.1}$$

$$K = K_0(1+s) = \left[\frac{\frac{d_r}{l}}{(1-\frac{d_r}{l})}\right]^2, \tag{B.2}$$

and

$$s = \frac{2}{(1-A)}(1-V). \tag{B.3}$$

Where A is a constant and can be defined in the form

$$A = \frac{(2-K_0-B(1-K_0))}{(2+K_0-B)}. \tag{B.4}$$

These equations can be reduced to give

$$V = \frac{2(2+K_0-\frac{d_r}{l})(1-\frac{d_r}{l}) - (2-\frac{d_r}{l})((\frac{d_r}{l})^2 - K_0(1-\frac{d_r}{l})^2)}{2(2+K_0-\frac{d_r}{l})(1-\frac{d_r}{l})^2}. \tag{B.5}$$

The rod diameter d_r is considered to be constant and if K_0 is known then we can get l in terms of V. To put a value to K_0 as used by Owen & Zienkiewcz (1957) and further used by Livesey & Turner (1964), it is argued that $\frac{d_r}{l} = 0$ for $y = \delta_c$.

Therefore, for the case of power-law velocity profiles, equation (B.5) becomes

$$\frac{n+1}{n}\left(\frac{y}{\delta_c}\right)^{\frac{1}{n}} = \frac{2(2+K_0-\frac{d_r}{l})(1-\frac{d_r}{l}) - (2-\frac{d_r}{l})((\frac{d_r}{l})^2 - K_0(1-\frac{d_r}{l})^2)}{2(2+K_0-\frac{d_r}{l})(1-\frac{d_r}{l})^2}. \tag{B.6}$$

Using the argument above (i.e. $\frac{d_r}{l} = 0$ for $y = \delta_c$) this reduces to

$$\frac{n+1}{n} = \left[\frac{1+K_0}{1+\frac{K_0}{2}}\right]. \tag{B.7}$$

The value for K_0 can then be found for any value of the power n, for example for $n = 7$, $K_0 = 0.\dot{3}$. However Owen & Zienkiewcz (1957), to avoid rapid rates of change, state a value of $K_0 = 0.4$ should be used, similarly for a $1/4th$ power law $K_0 = 0.7$ should be used instead of the calculated value of $K_0 = 0.\dot{6}$.

Thus to calculate the spacing for the relevant power-law velocity profile we use the following:

$$\left(\frac{u}{U}\right)_0 = \left(\frac{y}{\delta_c}\right)^{\frac{1}{n}}. \tag{B.8}$$

Then to calculate a $\frac{1}{7}th$ power-law $n = 7$ and $d = 16mm$ (where $\delta_c = 0.8m$) we get

$$u_0 = \frac{U_0 y^{\frac{1}{7}}}{0.969}, \tag{B.9}$$

by continuity

$$\bar{U} = U_\infty = \frac{n}{n+1}U_0 = \frac{7}{8}U_0, \tag{B.10}$$

$\Rightarrow$

$$V = \frac{u_0}{U_\infty} = \frac{8u_0}{7U_0} = \frac{8}{7}\frac{y^{\frac{1}{7}}}{0.969} = 1.179y^{\frac{1}{7}}. \tag{B.11}$$

Similarly for a $\frac{1}{4}th$ power-law we get

$$V = \frac{u_0}{U_\infty} = \frac{5u_0}{4U_0} = \frac{5}{4}\frac{y^{\frac{1}{4}}}{0.946} = 1.322y^{\frac{1}{4}}. \tag{B.12}$$

Using these results and equation (B.5), where $K_0 = 0.4$ for $\frac{1}{7}th$ power-law and $K_0 = 0.7$ for $\frac{1}{4}th$ power-law we get the relationship between y and l, this is shown in figure B.1. Further we are able to fit a polynomial to the order of 6 to this relationship using the least squares fitting method and thus

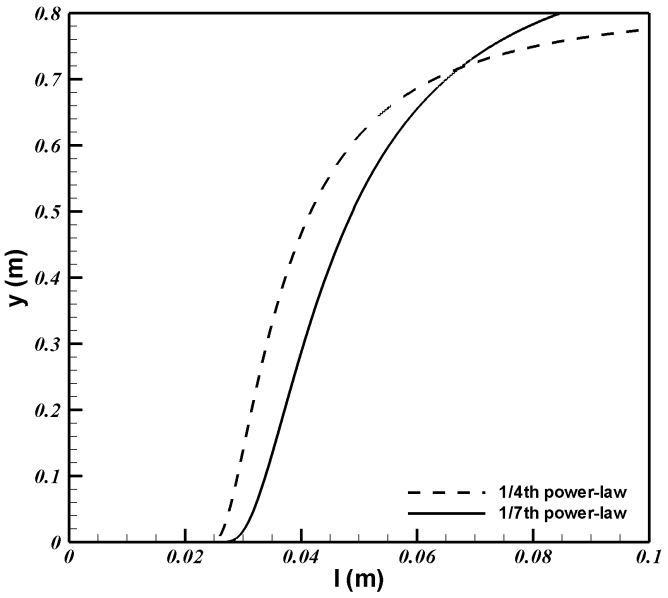

Figure B.1: Rod spacing configuration curves for $1/4th$ and $1/7th$ power-laws for 16mm rods

calculate the number of rods and the spacing required between the rods.

Figure B.2 shows the expected velocities at the corresponding normalised height for two different velocity profiles. Using these calculations based on the $1/7th$ power-law, the heights at which the $16mm$ bars were centred at are given in table B.1

Height from bottom of the channel (m)
0.018
0.063
0.0110
0.159
0.209
0.260
0.312
0.365
0.419
0.474
0.531
0.589
0.648
0.709
0.772

Table B.1: Heights at which 16mm bars are centred

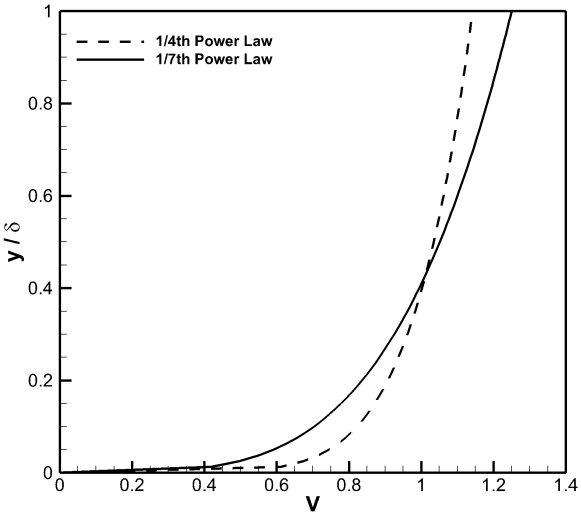

Figure B.2: Velocity profiles for $1/4th$ and $1/7th$ power-laws for 16mm rods

Appendix C

Blockage Correction of Bahaj et al. (2006)

To investigate the blockage correction for power, thrust coefficients and tip-speed-ratio the methods of Bahaj et al. (2006) are used. The blockage correction is based on an actuator disk model of the flow through the turbine. The flow is assumed to be uniform across any section of the stream tube enclosing the turbine disk. Pressure is presumed to be discontinuous across the disk and directly related to the thrust on the turbine. The layout of these assumptions are shown in figure C.1, where plane A is far upstream and plane B is far downstream of the disk so that pressures are uniform across the channel. The T and F subscripts denote the tunnel and free-stream conditions, respectively.

Using the principles of continuity and momentum balance on the water between planes A and B the following relations are obtained between various velocities and the ratio of the disk area (A) and channel area (C):

$$\frac{U_1}{U_2} = \frac{-1 + \sqrt{1 + (A/C)\left((U_3/U_2)^2 - 1\right)}}{(A/C)\left(U_3/U_2\right) - 1)}, \tag{C.1}$$

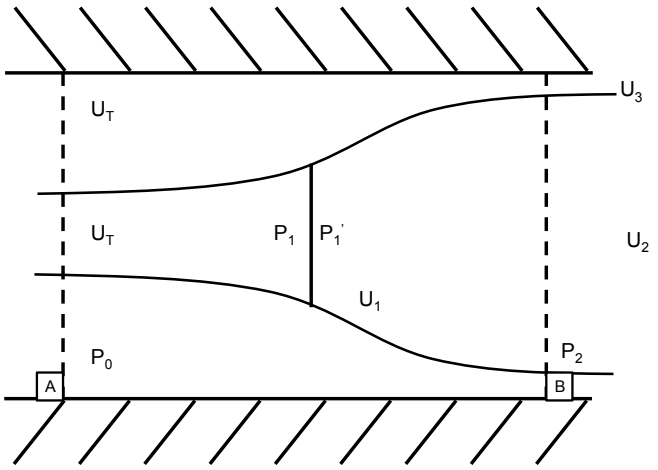

Figure C.1: Layout of assumptions in blockage correction

$$\frac{U_T}{U_2} = \frac{U_3}{U_2} - \frac{A}{C}\frac{U_1}{U_2}\left(\frac{U_3}{U_2} - 1\right). \tag{C.2}$$

Whilst the thrust coefficient is obtained as:

$$C_{T_T} = \frac{T}{1/2\rho A U_T^2} = \left(\frac{U_2}{U_T}\right)^2 \left(\left(\frac{U_3}{U_2}\right)^2 - 1\right), \tag{C.3}$$

rearranged as

$$\frac{U_T}{U_2} = 1/\sqrt{\frac{C_T}{((u_3/U_2)^2 - 1)}}. \tag{C.4}$$

By assuming a range of values of $\frac{U_3}{U_2}$ the equations are solved using iteration such that values of $\frac{U_T}{U_2}$ obtained from equations C.1 and C.2 are equal. Therefore $\frac{U_1}{U_T}$ is then obtained using equation C.1 and C.4.

To find the equivalent water speed U_F in open water the assumptions that disk flow speed, the turbine rotational speed and the turbine thrust are

the same in channel conditions to open water conditions is made. Leading to:

$$\frac{U_T}{U_F} = \frac{U_1/U_T}{(U_1/U_T)^2 + C_{T_T}/4}. \tag{C.5}$$

This blockage factor ($\frac{U_T}{U_F}$) is then used to calculate the corrections to tip-speed-ratio, power and thrust coefficients as following:

$$C_{P_F} = C_{P_T}\left(\frac{U_T}{U_F}\right)^3, \tag{C.6}$$

$$C_{T_F} = C_{T_T}\left(\frac{U_T}{U_F}\right)^2, \tag{C.7}$$

$$\lambda_F = \lambda_T\left(\frac{U_T}{U_F}\right). \tag{C.8}$$

Appendix D

Near-wake repeat measurements using two probe orientations

Due to the issues with velocity measurements from ADV highlighted in chapter 5, to estimate the effect of noise issues with ADV wake measurements presented in the previous chapters, measurements were repeated for all three flow conditions, and are henceforth presented.

D.1 Uniform flow - $TI \approx 2\%$

Initially velocity measurements of the turbine's near-wake were taken in the uniform flow conditions, essentially repeating with the two probes some of the experiments conducted in section 3.1. These measurements were taken using both probes across the width of the channel, with a maximum of $50mm$ spacing between measurements, up to $7D$ downstream.

D.1.1 Mean velocity contours

As discussed in section 5.2 the ADV is good at measuring mean velocities, which is highlighted further in the contour plots in figure D.1. In figures D.1(a) and (d) the normalised mean streamwise velocity contours are shown for the two different probe orientations, where good agreement is observed. There are a couple of minor differences of the order of 1% of the mean upstream velocity and can be attributed to probe alignment. The vertical and spanwise velocity contours, shown in figures D.1(b), (c), (e) and (f), show agreement with the two different probe orientations, however it can be seen that there is some slight discrepancies in the maximum and minimum velocities in that they are slightly larger for probe B. This effect is due to probe alignment which has a greater impact on these smaller velocities as they are typically of an order of magnitude smaller than the streamwise component. These differences are around $0.01 - 0.02m/s$, which is the expected range for the ADV to measure means (Nortek AS, 2009), i.e. 1% of the mean streamwise velocity.

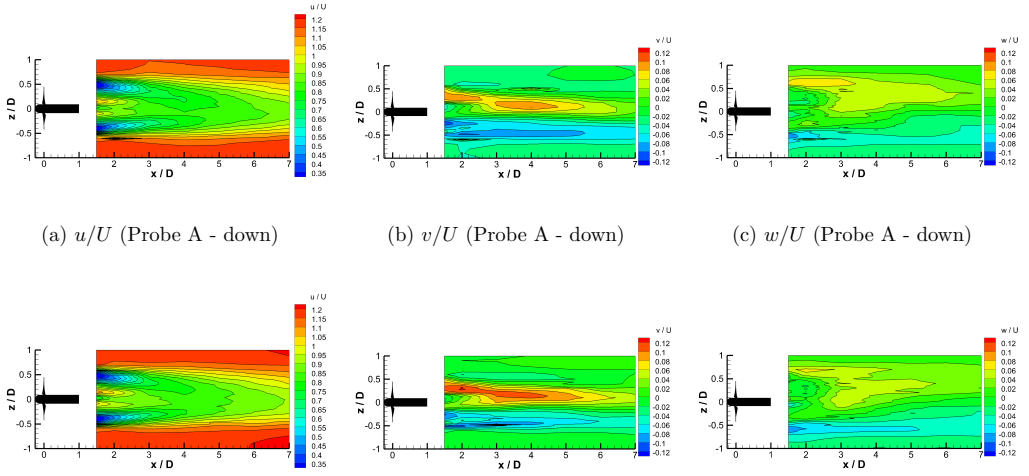

(a) u/U (Probe A - down) (b) v/U (Probe A - down) (c) w/U (Probe A - down)

(d) u/U (Probe B - side) (e) v/U (Probe B - side) (f) w/U (Probe B - side)

Figure D.1: Mean velocity contours downstream of the three-bladed turbine in uniform flow ($TI \approx 2\%$)

D.1.2 Reynolds Normal Stresses

The Reynolds normal stresses have been found to only be accurate in one component which is dependent on the probe orientation, it is therefore important to use the different orientations so as to produce an accurate set of data as possible (where two velocity components are measured in the 'noise-free' j direction). Figure D.2 shows the normalised streamwise Reynolds normal stress (by mean upstream velocity)downstream of the three-bladed turbine in uniform flow. It was observed in the previous section that the streamwise Reynolds normal stress is overestimated in both probe orientations - sideways and downwards looking - therefore quantitative analysis should be made with caution. When comparing the two probe orientations it can be seen in figure D.2 that both probes show the same qualitative results with peaks always occurring at the blade edges (denoted by dashed lines), with a third central peak at $1.5D$ downstream. Quantitatively the Reynolds normal stresses are similar for both probes after $3D$ downstream, at $1.5D$ and $2D$ downstream the maximum values are greater for probe B, this difference is fairly minimal and could be due to slight probe misalignment or the difference in ADV probe support structure effects of the two different probe heads.

The differences between the two orientations are more obvious in the vertical and spanwise Reynolds normal stresses. The vertical component is found to be 'noise-free' in probe A and the spanwise is 'noise-free' in probe B. The vertical Reynolds normal stresses shown in figure D.3 shows this difference, where at the blade edges (maximum velocity fluctuations) probe B results are nearly double those from probe A at $1.5D$ downstream, and at the outside of the turbine's wake ($|z/D| > 0.7$) the Reynolds normal stresses are five times greater for probe B than for probe A. The component which is 'noise-free' is the j component shown in figure 2.6 (d), which is consistent in that probe A gives lower values for the vertical Reynolds normal stresses. Although there is an overestimation of the vertical Reynolds normal stress by probe B, qualitatively the trends are the same as for probe A. Conversely, the

opposite is true for the spanwise Reynolds normal stresses which are found to be 'noise-free' in probe B in the sideways-looking orientation. Again at the edge of the blades the 'noisy' spanwise Reynolds normal stresses measured by probe A are found to be up to twice that measured by probe B at the blade edges ($z/D = 0.5$ - dashed lines on figure D.4) and up to ten times greater at the edge of the channel ($|z/D| > 0.7$). Again general trends can be observed by the 'noisy' component, so the data qualitatively indicates regions of high fluctuations.

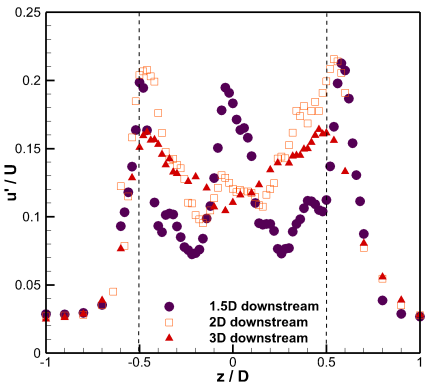

(a) Probe A - down

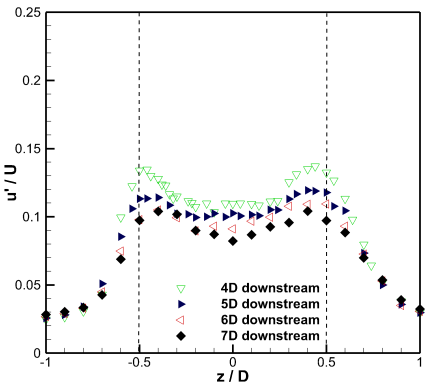

(b) Probe A - down

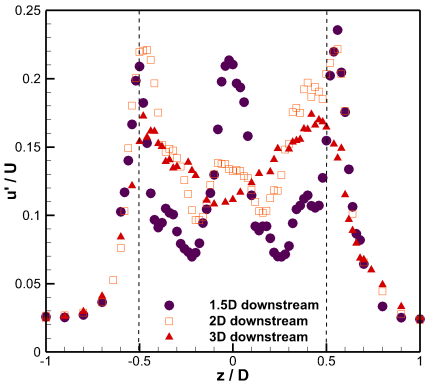

(c) Probe B - side

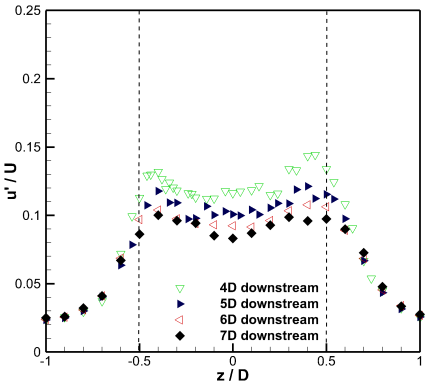

(d) Probe B - side

Figure D.2: Streamwise Reynolds normal stresses downstream of the three-bladed turbine in uniform flow ($TI \approx 2\%$)

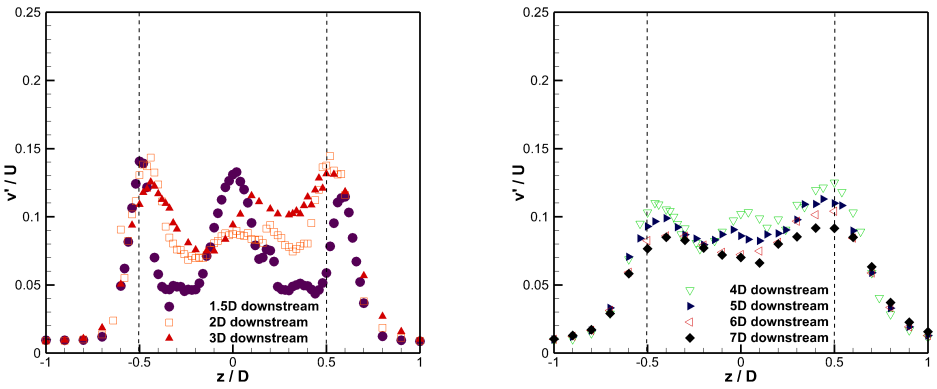

(a) Probe A - down

(b) Probe A - down

(c) Probe B - side

(d) Probe B - side

Figure D.3: Vertical Reynolds normal stresses downstream of the three-bladed turbine in uniform flow ($TI \approx 2\%$)

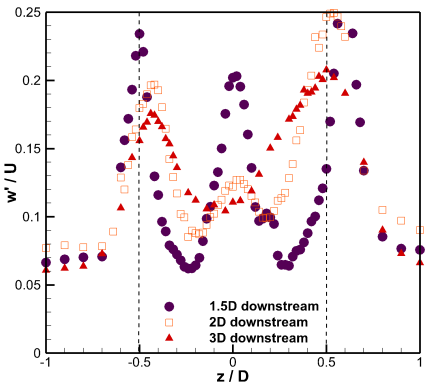

(a) Probe A - down

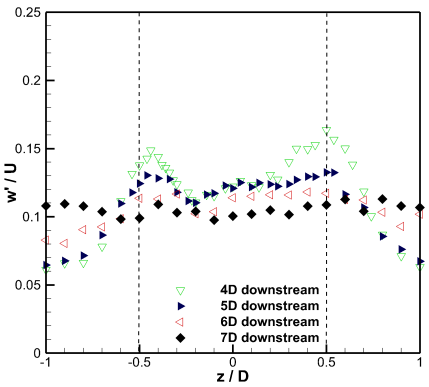

(b) Probe A - down

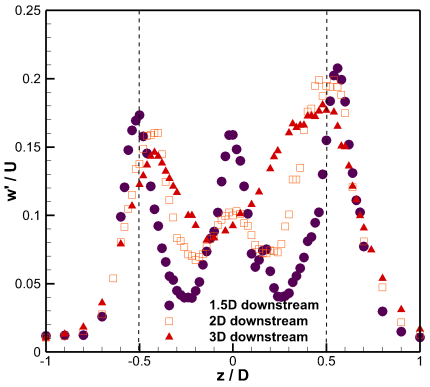

(c) Probe B - side

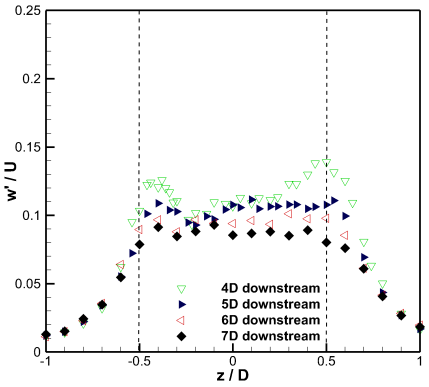

(d) Probe B - side

Figure D.4: Spanwise Reynolds normal stresses downstream of the three-bladed turbine in uniform flow ($TI \approx 2\%$)

D.1.3 Turbulent Kinetic Energy

Turbulent Kinetic Energy is a second-order turbulence statistic like the Reynolds normal stresses, however it is has the advantage that as a three-dimensional measurement 'noise' effects may potentially be minimised as noise is not spatially correlated. When two probe orientations are used, as the two components that have been found to be 'noise-free' (i.e. v' in probe A downwards-looking and w' in probe B sideways-looking) can be used to calculate the TKE rather than all three components from a single probe measurement a useful comparison can also be performed. Firstly the TKE is shown downstream of the turbine calculated using individual probe measurements, shown in figure D.5. Both probes show nearly identical results, apart from at $1.5D$ downstream where the third central peak is much greater in probe B than for probe A, which could be due to the instability of the support structure used for probe B which at this region could be effected more by the standing wave produced by the turbine in the flow. Also at the edge of the channel ($|z/D| > 0.7$) there are small differences where the TKE calculated using probe A is slightly greater than that from probe B, this stems from the differences in w' which were greater at the edge of the channel (seen in figure D.4). Although these differences are within the repeatability of the measurements when compared to the results in section 3.1, specifically figure 3.22, where the TKE is measured using probe A downwards-looking configuration highlighting minor differences to the nominally identical measurement here.

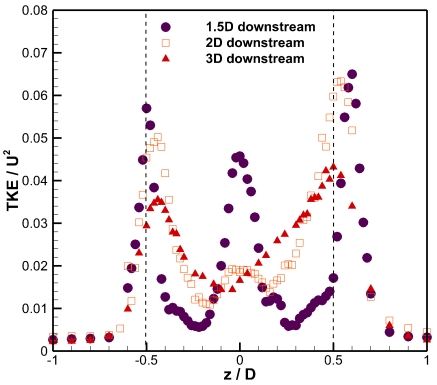

(a) Probe A - down

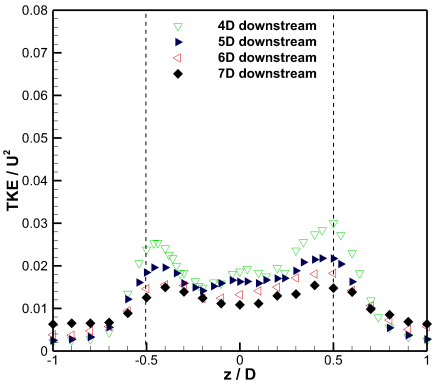

(b) Probe A - down

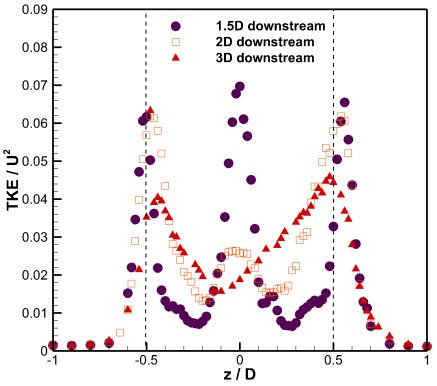

(c) Probe B - side

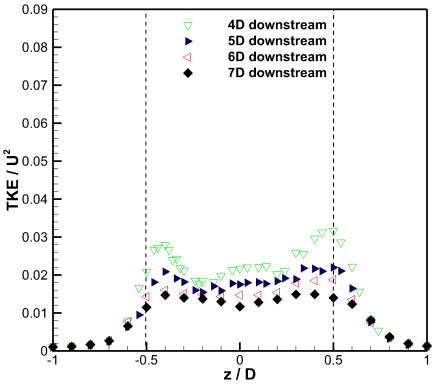

(d) Probe B - side

Figure D.5: Turbulent Kinetic Energy downstream of the three-bladed turbine in uniform flow ($TI \approx 2\%$)

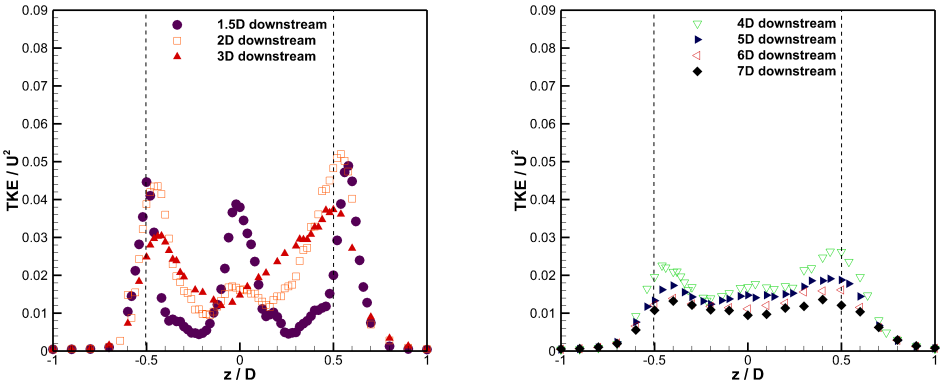

(a) $1.5 - 3D$ downstream

(b) $4 - 7D$ downstream

Figure D.6: Turbulent Kinetic Energy 'corrected' downstream of the three-bladed turbine in uniform flow ($TI \approx 2\%$)

Figure D.6 shows the TKE calculated from both probes, where u' and v' are taken from probe A (downwards-looking) and w' form probe B (sideways-looking) hence using two components that have been found to be 'noise-free'. Calculated in this manner means that TKE is reduced throughout the width of the channel, where this reduction is clearest at the peaks at the edge of the blades (dashed lines on the figure). As already highlighted in chapter 5, the decay of TKE is also a very robust method. However, it can be seen that qualitatively this method of calculating TKE is similar to that calculated from a single probe measurement (figure D.5), but if comparing to numerical models it would be preferable to use the TKE from two ADV probes as this is more representative of real conditions.

D.1.4 Reynolds Shear Stresses

It was found in section 5.2.3 that the Reynolds shear stresses are not seemingly effected by ADV probe orientation, which is again seen in figures D.7

- D.9. Any differences between the Reynolds shear stresses are minimal and are of the same order of differences seen in the repeatability of the measurements. The biggest visible difference is at $1.5D$ downstream in figures D.7(a) and (c), where at the centre of the channel the shear stress is near to zero for the downwards-looking probe and is ≈ -0.008 which can be attributed to the effect of the standing wave produced by the turbine having a different impact on the support structures for the differing ADV probes.

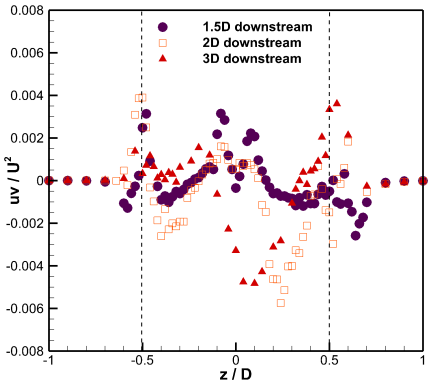

(a) Probe A - down

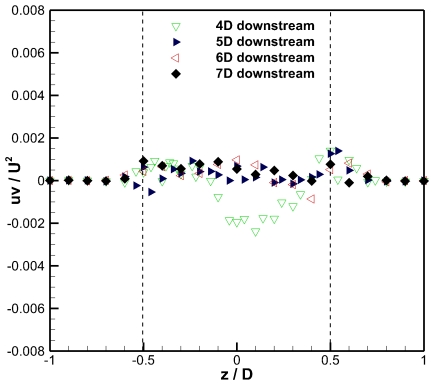

(b) Probe A - down

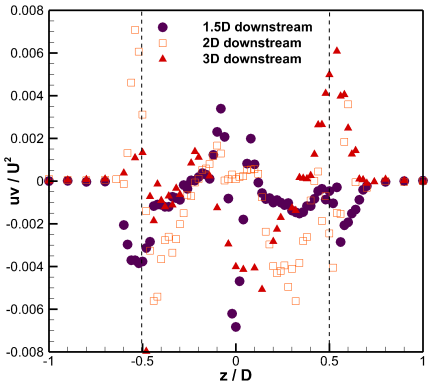

(c) Probe B - side

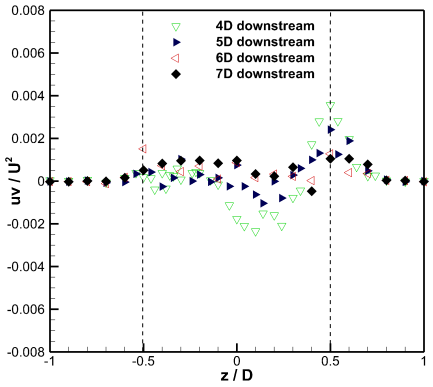

(d) Probe B - side

Figure D.7: Reynolds shear stresses in the $x - y$ plane downstream of the three-bladed turbine in uniform flow ($TI \approx 2\%$)

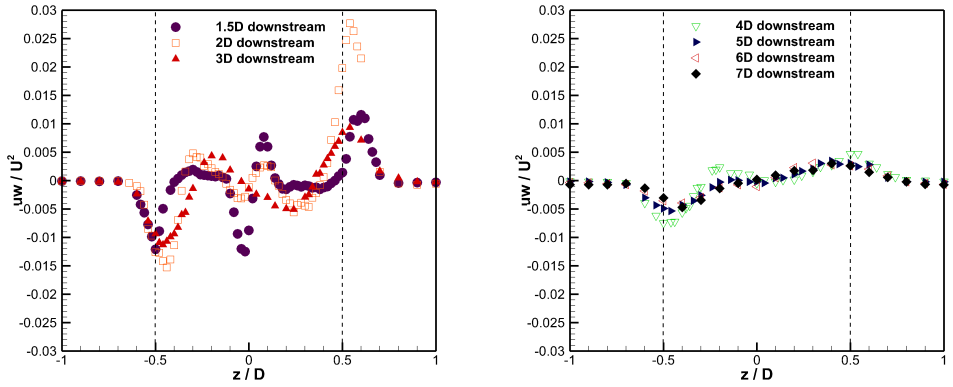

(a) Probe A - down

(b) Probe A - down

(c) Probe B - side

(d) Probe B - side

Figure D.8: Reynolds shear stresses in the $x - z$ plane downstream of the three-bladed turbine in uniform flow ($TI \approx 2\%$)

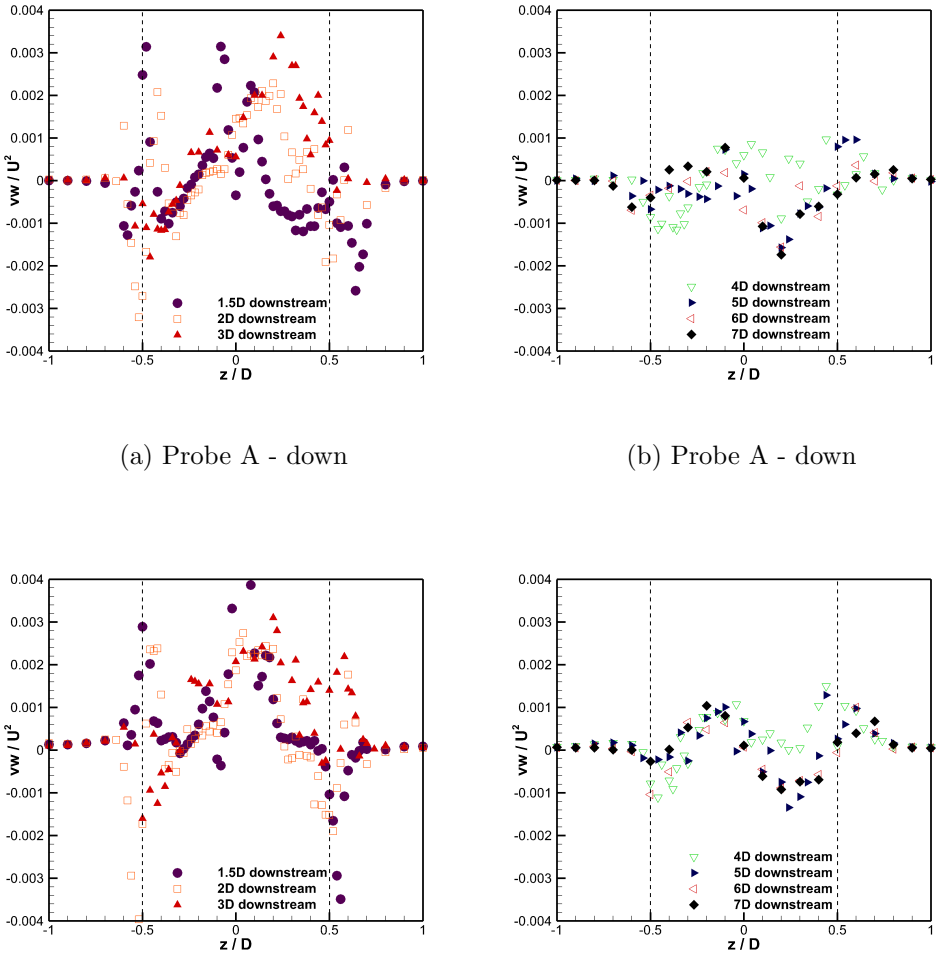

(a) Probe A - down

(b) Probe A - down

(c) Probe B - side

(d) Probe B - side

Figure D.9: Reynolds shear stresses in the $y - z$ plane downstream of the three-bladed turbine in uniform flow ($TI \approx 2\%$)

D.2 Uniform flow - $TI \approx 5\%$

Following wake measurements in uniform flow with low turbulence intensity (ADV measured, 2%), the near-wake measurements were repeated downstream of the three-bladed turbine at optimum blade-pitch-angle (6^o) in the flow downstream of the turbulence grid using both ADV probes. As described in section 2.6 the grid upstream produced a uniform steady flow throughout the channel but increased the turbulence levels. The turbine was placed $0.25m$ downstream of the grid and the wake measurements were taken between $1.5D$ and $6D$ downstream in the centreplane.

D.2.1 Mean velocity contours

The mean velocity contours are shown in figure D.10 measured with both probes. Akin to the mean velocity contours shown in section D.1.1, there is very little to distinguish the measurements taken with the two different probe orientations. Any small differences are attributed to the slight probe misalignment and are of the order of 1% of the mean upstream streamwise velocity. In addition these contours match those in section 4.1 showing the repeatability of the experimental technique.

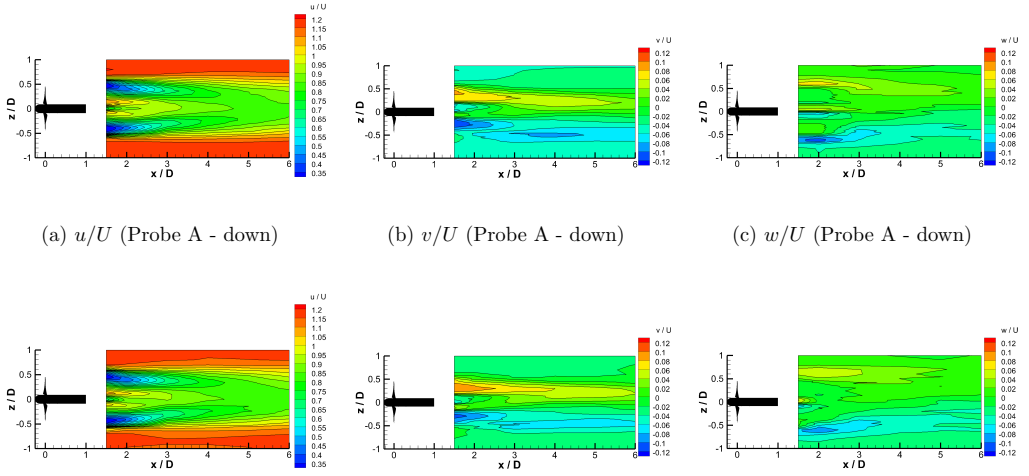

(a) u/U (Probe A - down) (b) v/U (Probe A - down) (c) w/U (Probe A - down)

(d) u/U (Probe B - side) (e) v/U (Probe B - side) (f) w/U (Probe B - side)

Figure D.10: Mean velocity contours downstream of the three-bladed turbine in uniform flow ($TI \approx 5\%$)

D.2.2 Reynolds Normal Stresses

The Reynolds normal stresses measured by ADV are found to contain 'noise' in two of the three components, which components is dependent on the probe orientation. It has been found that probe A (downwards-looking) is 'noise-free' in the vertical component and probe B (sideways-looking) is 'noise-free' in the spanwise component. It is found that in the streamwise Reynolds normal stresses both probes show similar results, unlike in the lower turbulence level in the previous section where small differences can be seen between the measurements in the two probes. Likewise to the mean velocity contours the streamwise Reynolds normal stresses also show a good replication of the results shown in section 4.1. The vertical Reynolds normal stress is shown to be lower when measured using probe A and the difference is more prominent closer to the turbine. At the edges of the channel, $|z/D| > 0.7$, the difference is less than that found in the previous section of the wake in the channel alone, this is probably due to the Reynolds normal stresses being greater upstream due to grid and that the 'noise' is dependent on the turbulence levels in the flow. Again the differences are visible between the different probe orientation measurements of the spanwise Reynolds normal stress. The differences between the spanwise Reynolds normal stresses are of the same order as the differences of the vertical Reynolds normal stresses between $|z/D| < 0.7$. At the channel edges, $|z/D| > 0.7$ the spanwise normal stresses were found to be an order of magnitude greater in the downwards-looking orientation than for the sideways-looking orientation.

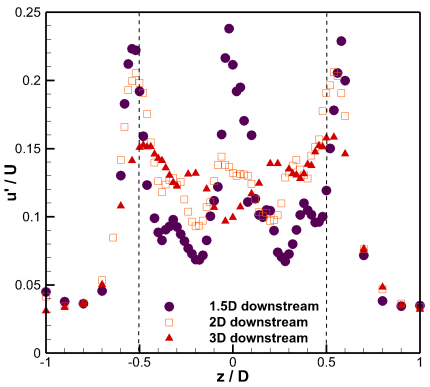

(a) Probe A - down

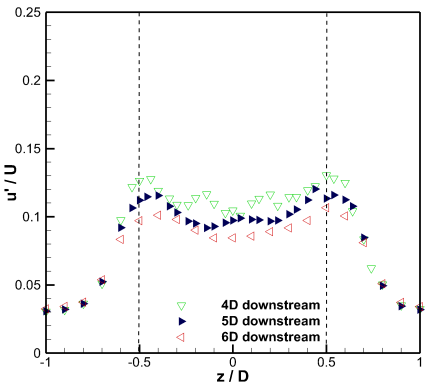

(b) Probe A - down

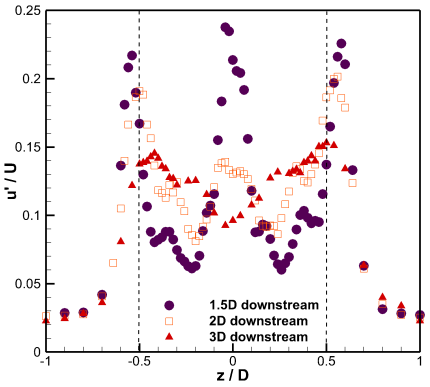

(c) Probe B - side

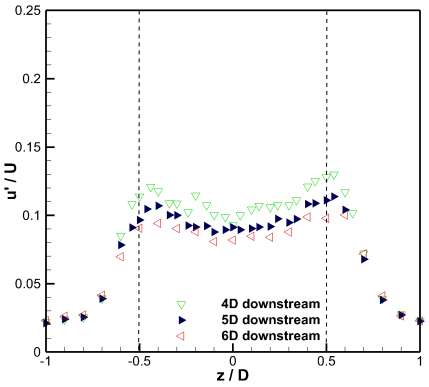

(d) Probe B - side

Figure D.11: Streamwise Reynolds normal stresses downstream of the three-bladed turbine in uniform flow ($TI \approx 5\%$)

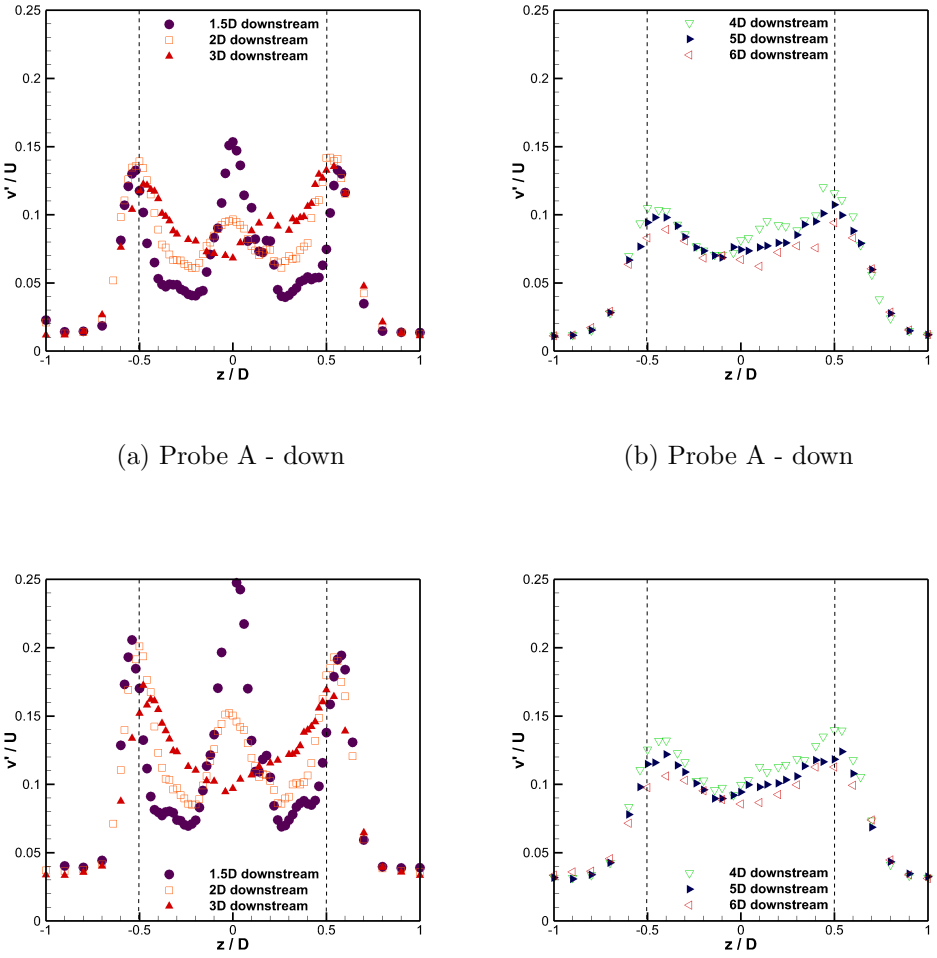

(a) Probe A - down

(b) Probe A - down

(c) Probe B - side

(d) Probe B - side

Figure D.12: Vertical Reynolds normal stresses downstream of the three-bladed turbine in uniform flow ($TI \approx 5\%$)

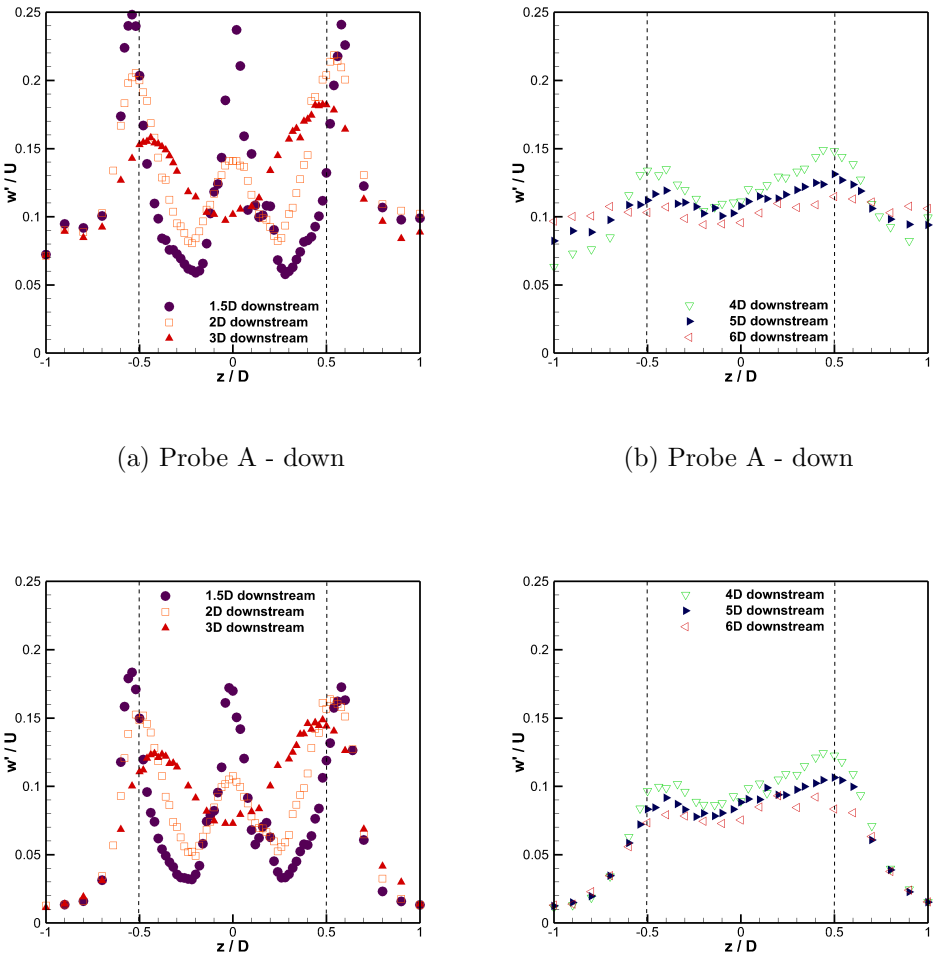

(a) Probe A - down

(b) Probe A - down

(c) Probe B - side

(d) Probe B - side

Figure D.13: Spanwise Reynolds normal stresses downstream of the three-bladed turbine in uniform flow ($TI \approx 5\%$)

D.2.3 Turbulent Kinetic Energy

The Turbulent Kinetic Energy is a useful measure of the turbulence in all three dimensions. It has been shown that TKE is a useful measure to minimise individual component 'noise' effects. Figure D.14 shows the TKE measured with different probe orientations, and collapse is observed for both. There appears to be small differences at the edge of the channel ($|z/D| > 0.7$) and this is due to the large 'noise' effect found in the spanwise component in the downwards-looking orientation. To reduce the 'noise' effects further the TKE is plotted in figure D.15 where two components u' and v' are measured with the downwards-looking probe, and the third component, w', with the sideways-looking probe. Calculated in this way the TKE is reduced slightly, in particularly in the area of greatest shear at the blade edges (denoted by dashed lines), but qualitatively the data is the same to that of the individual probe calculated TKE.

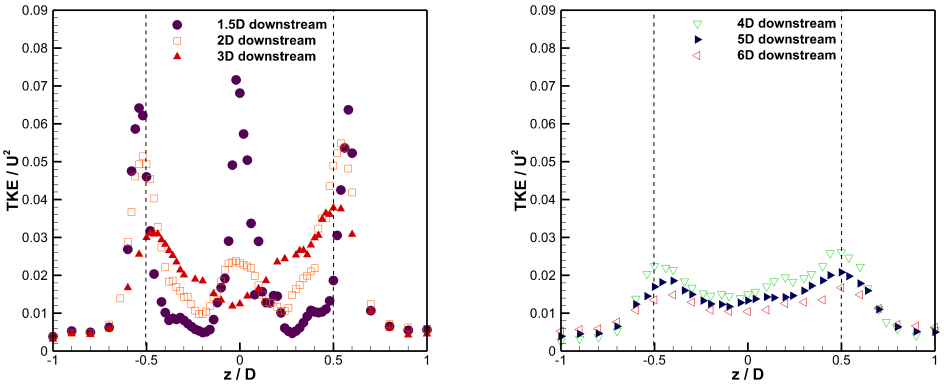

(a) Probe A - down

(b) Probe A - down

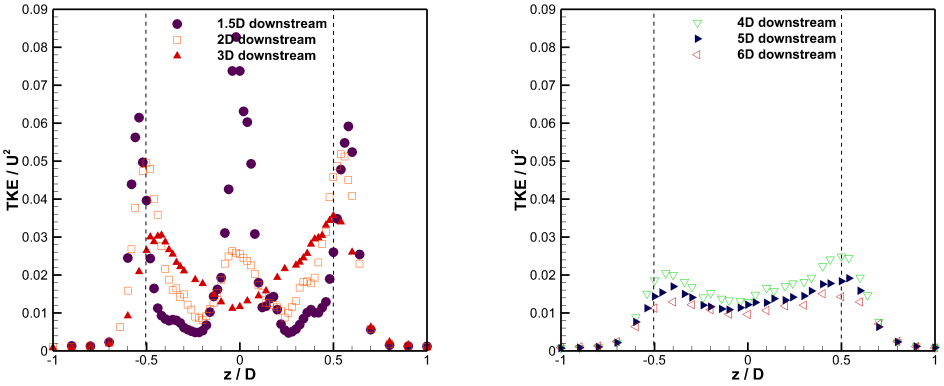

(c) Probe B - side

(d) Probe B - side

Figure D.14: Turbulent Kinetic Energy downstream of the three-bladed turbine in uniform flow ($TI \approx 5\%$)

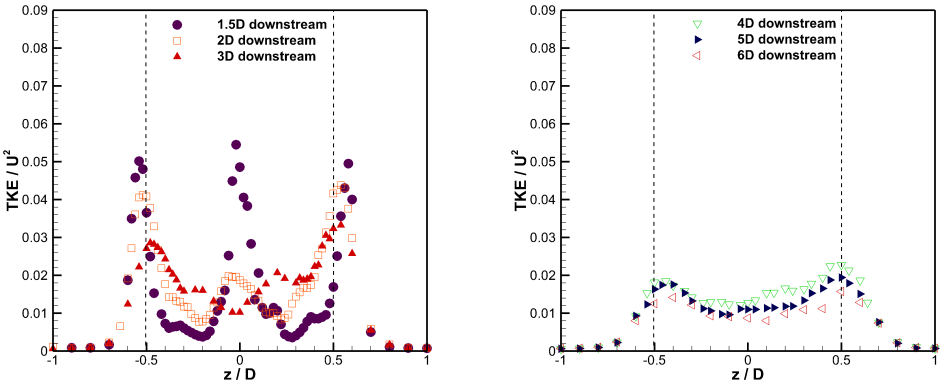

(a) $1.5 - 3D$ downstream

(b) $4 - 6D$ downstream

Figure D.15: Turbulent Kinetic Energy 'corrected' downstream of the three-bladed turbine in non-uniform flow ($TI \approx 5\%$)

D.2.4 Reynolds Shear Stresses

In chapter 5 it was observed that the Reynolds shear stresses measured by ADV appear not to be dependent on the probe orientation. This is noticed again in this flow condition and is shown in figures D.16 - D.18 where both probe orientations are shown. The only difference observed is at $1.5D$ downstream in the $x - y$ plane (figures D.16(a) and (c)) at the centre of the channel in the normalised Reynolds shear stress highly negative for the sideways-looking probe orientation, but positive for the downwards-looking probe, this could be a result of effects from the stanchion and that the support structures differ, especially as there is a similar discrepancy in uniform flow in the previous section.

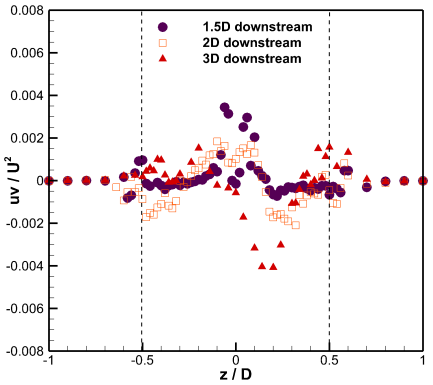

(a) Probe A - down

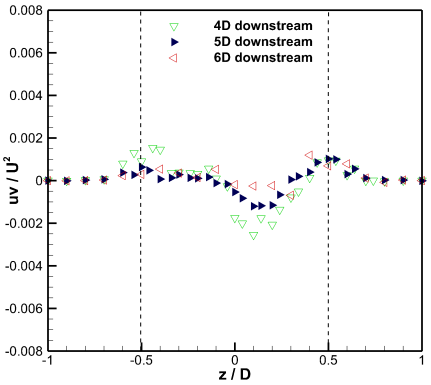

(b) Probe A - down

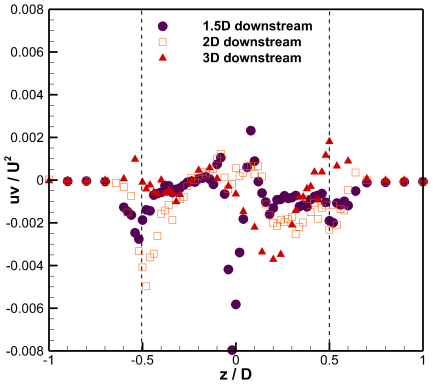

(c) Probe B - side

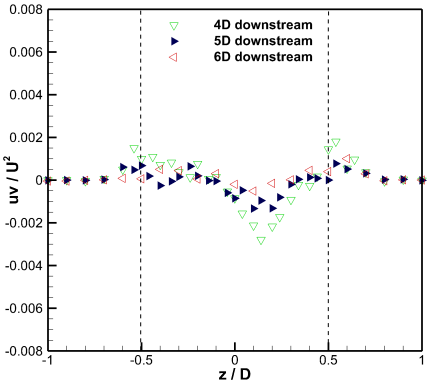

(d) Probe B - side

Figure D.16: Reynolds shear stresses in the $x - y$ plane downstream of the three-bladed turbine in uniform flow ($TI \approx 5\%$)

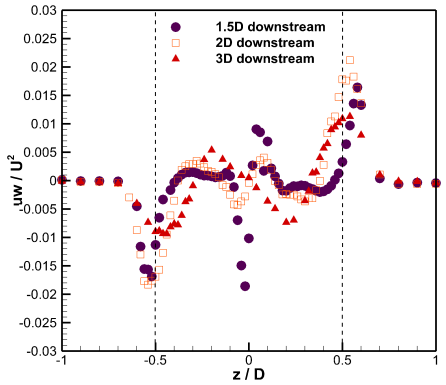

(a) Probe A - down

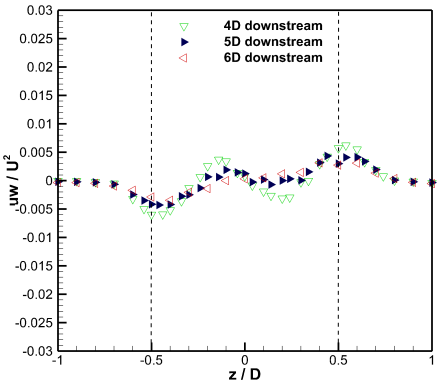

(b) Probe A - down

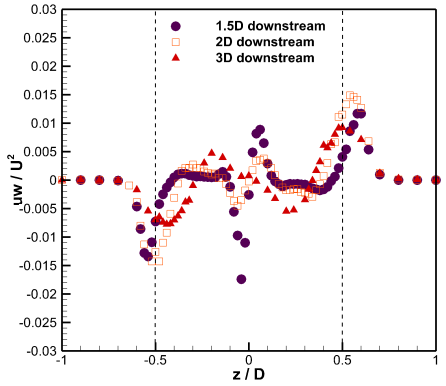

(c) Probe B - side

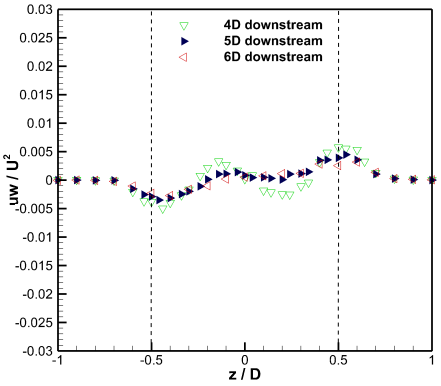

(d) Probe B - side

Figure D.17: Reynolds shear stresses in the $x - z$ plane downstream of the three-bladed turbine in uniform flow ($TI \approx 5\%$)

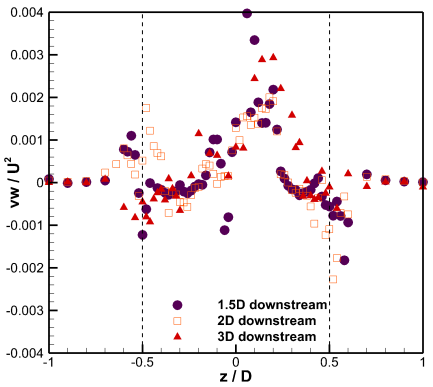

(a) Probe A - down

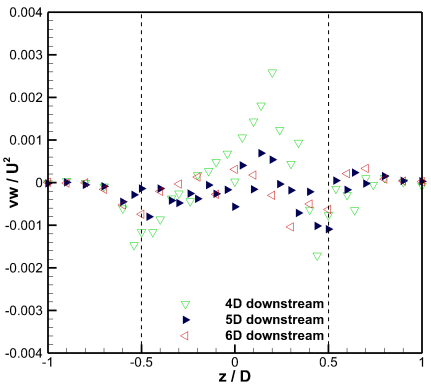

(b) Probe A - down

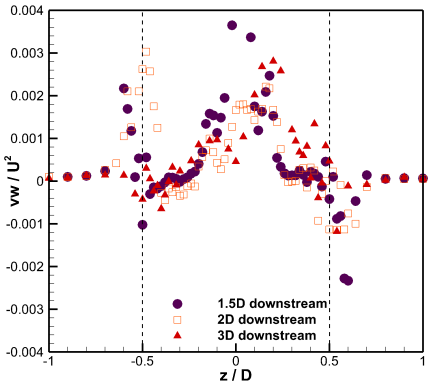

(c) Probe B - side

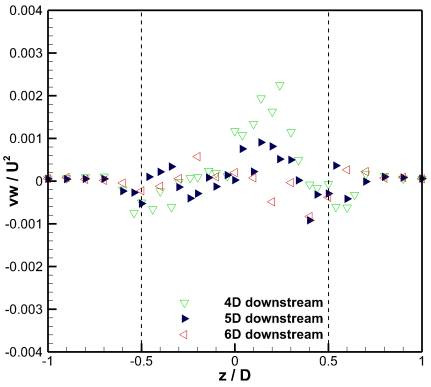

(d) Probe B - side

Figure D.18: Reynolds shear stresses in the $y - z$ plane downstream of the three-bladed turbine in uniform flow ($TI \approx 5\%$)

D.3 Non-uniform flow - $TI \approx 5\%$

Having repeated the experiments in the two uniform flow conditions it was therefore important to replicate the measurements of the near-wake in the non-uniform steady flow. Hence the wake of the three-bladed turbine with optimum blade pitch angle (6^o) was measured at a depth equal to the centre of the turbine from $1.5D$ to $5D$ downstream across the channel at least every $50mm$ using both sideways- and downwards-looking ADV probes.

D.3.1 Mean Velocity Contours

Reiterating the mean velocity contours in the uniform flows, the mean velocity contours in figure D.19 show good agreement for both probe orientations. With small differences of the order of 1% of the mean upstream velocity due to slight probe misalignment.

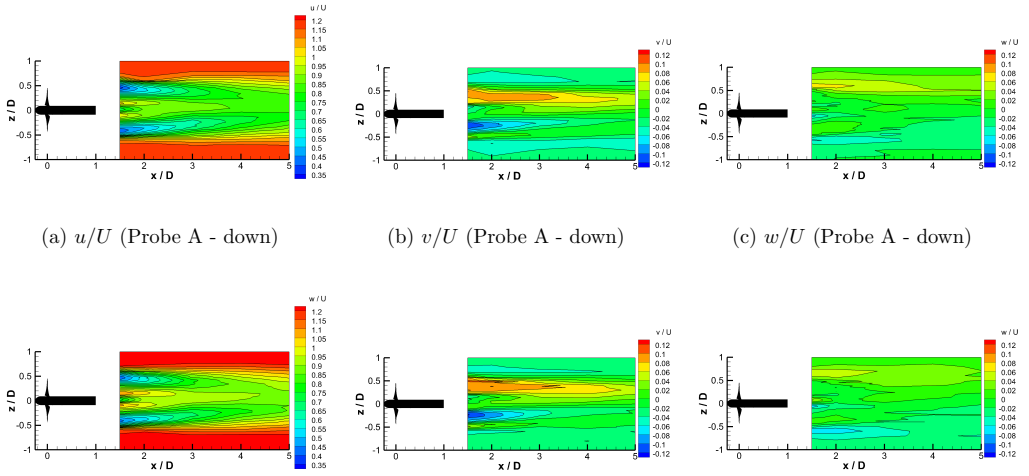

(a) u/U (Probe A - down) (b) v/U (Probe A - down) (c) w/U (Probe A - down)

(d) u/U (Probe B - side) (e) v/U (Probe B - side) (f) w/U (Probe B - side)

Figure D.19: Mean velocity contours downstream of the three-bladed turbine in non-uniform steady flow ($TI \approx 5\%$)

D.3.2 Reynolds Normal Stresses

ADV probe orientation greatly effects the measured values of Reynolds normal stresses, hence the importance of these repeated experiments. The streamwise Reynolds normal stresses are shown in figure D.20 and there is good agreement between the different probe measurements concurring with the results in the uniform flow conditions. The vertical Reynolds normal stresses are overestimated with probe B (sideways-looking), where at the blade edges the stresses are measured to be 50% greater in the sideways-looking orientation than the downwards-looking orientation. At the edge of the channel ($|z/D| > 0.7$) the streamwise normal stresses from the sideways-looking probe are twice those from the downwards-looking probe, noting that this is a smaller increase than that in the other flow conditions. Moreover at the centre of the channel at $1.5D$ downstream the peak in streamwise normal stress due to the presence of the stanchion, is much greater in the sideways-looking probe and is much greater than the peaks at the blade edges. In contrast the central peak in the streamwise normal stresses measured by the downwards-looking probe is equal to the peaks at the blade edges. Conversely the spanwise Reynolds normal stresses are overestimated by the downwards-looking probe orientation, which are found to be up to three times greater at the edge of the channel, but it can be seen that the peaks are found to be qualitatively similar.

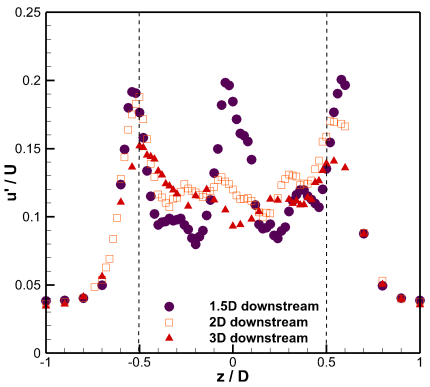

(a) Probe A - down

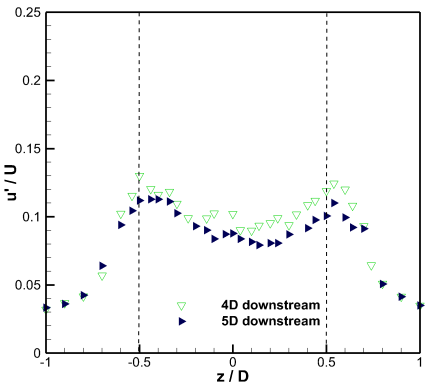

(b) Probe A - down

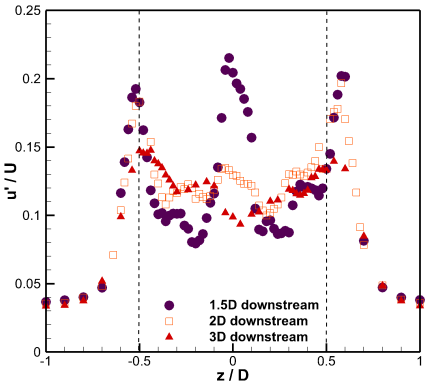

(c) Probe B - side

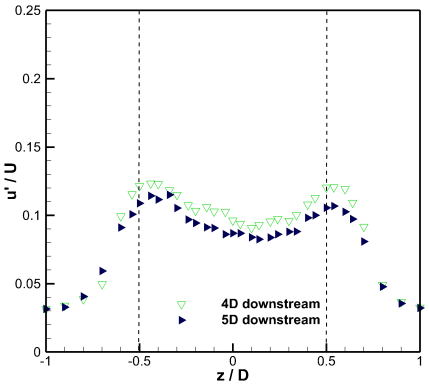

(d) Probe B - side

Figure D.20: Streamwise Reynolds normal stresses downstream of the three-bladed turbine in non-uniform flow ($TI \approx 5\%$)

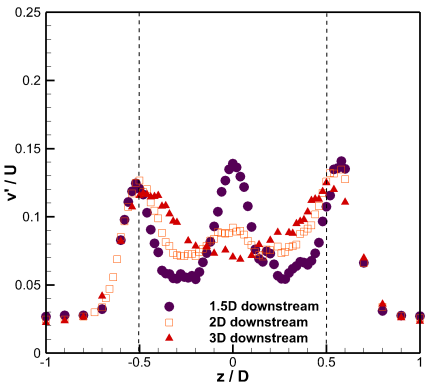

(a) Probe A - down

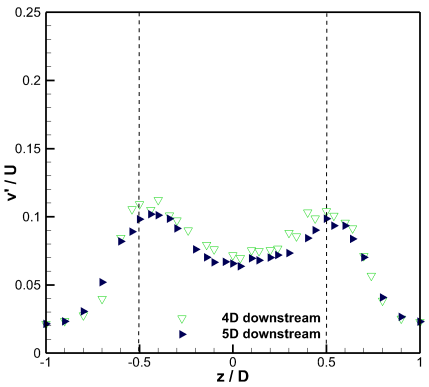

(b) Probe A - down

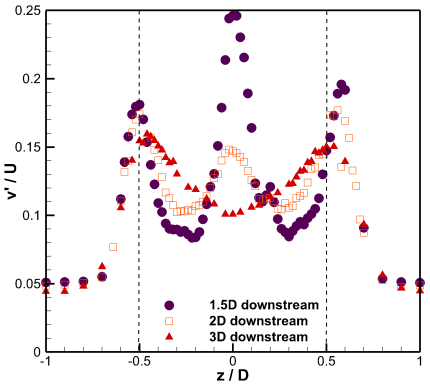

(c) Probe B - side

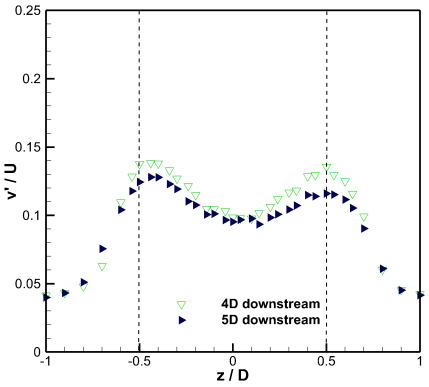

(d) Probe B - side

Figure D.21: Vertical Reynolds normal stresses downstream of the three-bladed turbine in non-uniform flow ($TI \approx 5\%$)

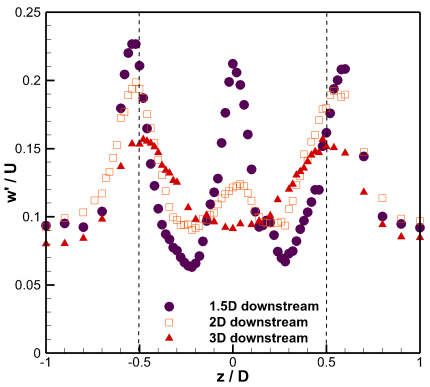

(a) Probe A - down

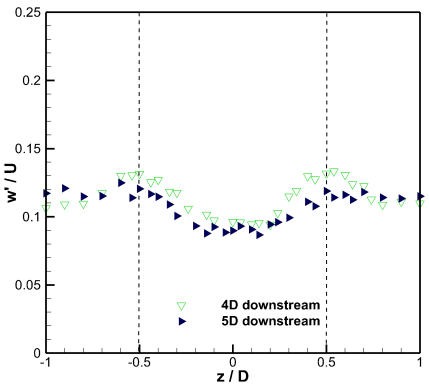

(b) Probe A - down

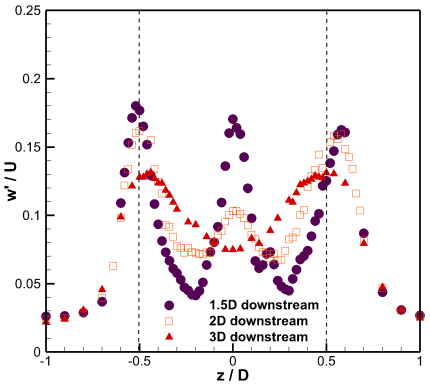

(c) Probe B - side

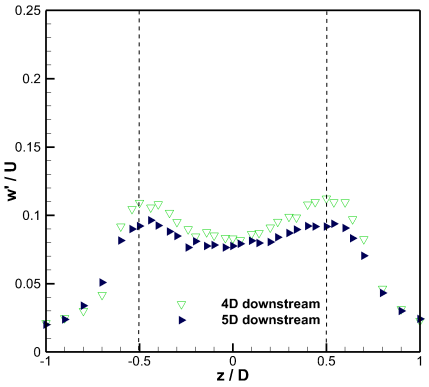

(d) Probe B - side

Figure D.22: Spanwise Reynolds normal stresses downstream of the three-bladed turbine in non-uniform flow ($TI \approx 5\%$)

D.3.3 Turbulent Kinetic Energy

Turbulent Kinetic Energy has been found to be an effective measure of turbulence downstream of the turbine, in particular when using ADV as it considers all three velocity components. Initially the individually probe measured TKE is plotted in figure D.23. The two probes are generally consistent for both probes, with some small differences found at the edge of the channel, where the TKE is slightly greater for probe A - downwards-looking orientation - which stems from the larger overestimation of the spanwise Reynolds normal stresses. Another difference between the two probe measured TKE is at the central peak, due to the presence of the stanchion, is found to be much greater in the measurement from probe B (sideways-looking) which will be as a result of the larger peak in u' and v'. To minimise the ADV noise effects, the TKE is plotted where u' and v' are from probe A (downwards-looking) and w' from probe B (sideways-looking) in figure D.24. The differences between this 'corrected' and single probe measured TKE are seen at the peaks, which are reduced up to a third. Nonetheless, it can be seen that the 'corrected' and single-probe measured TKE are qualitatively the same, i.e. that the shear from the blade edges is the most prominent feature of the wake and the wake recovery length is not effected.

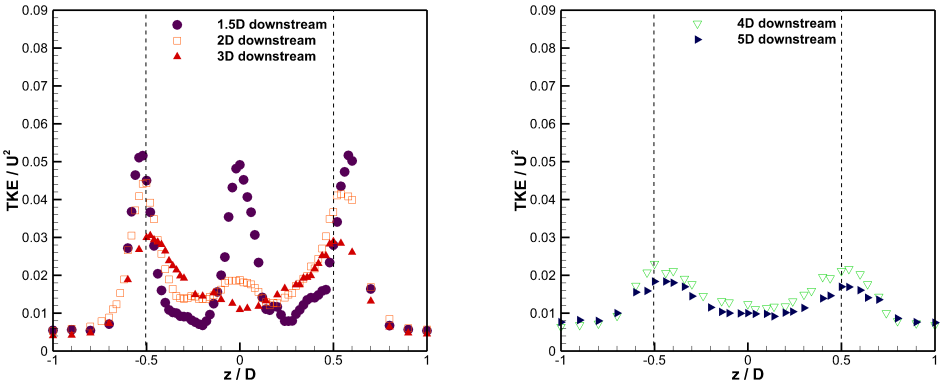

(a) Probe A - down

(b) Probe A - down

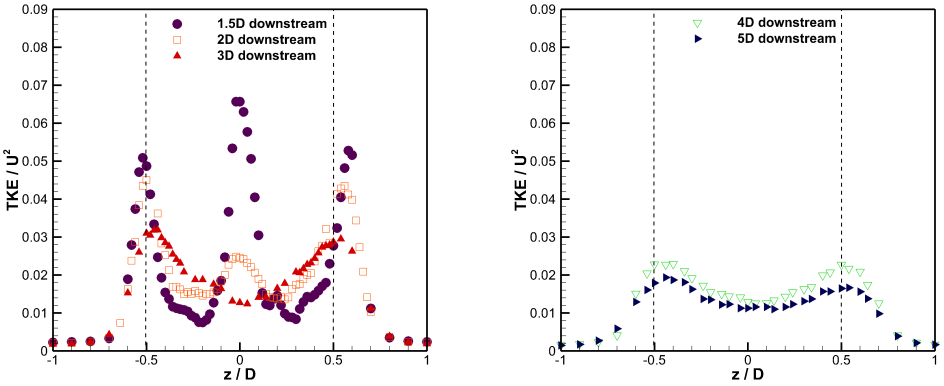

(c) Probe B - side

(d) Probe B - side

Figure D.23: Turbulent Kinetic Energy downstream of the three-bladed turbine in non-uniform flow ($TI \approx 5\%$)

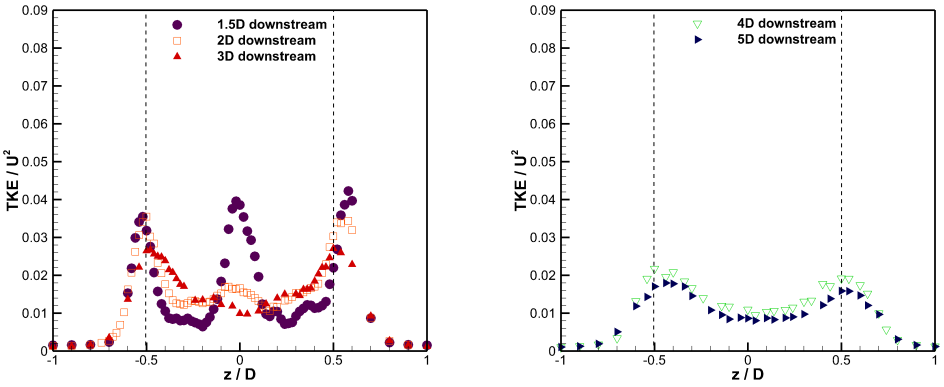

(a) $1.5 - 3D$ downstream

(b) $4 - 5D$ downstream

Figure D.24: Turbulent Kinetic Energy 'corrected' downstream of the three-bladed turbine in non-uniform flow ($TI \approx 5\%$)

D.3.4 Reynolds Shear Stresses

In addition to the Reynolds normal stresses and TKE the Reynolds shear stresses are shown in figures D.25 - D.27. In conjunction with the measurements in the uniform flow conditions the Reynolds shear stresses are fairly similar in both probe orientations, in fact there are fewer differences which are of a smaller magnitude than in uniform flow conditions.

From these repetitions of results it can be seen that it is important to use at least two ADV probe orientations to get more quantitatively meaningful higher order statistics. It is shown that the means are the same for either probe orientation and qualitative trends are found from any ADV orientation.

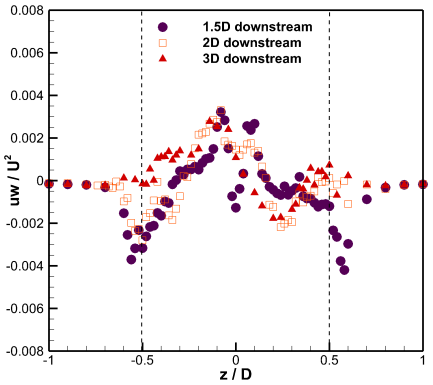

(a) Probe A - down

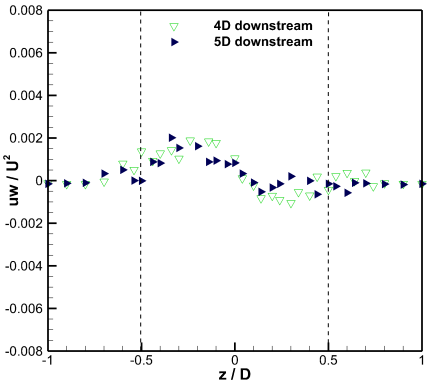

(b) Probe A - down

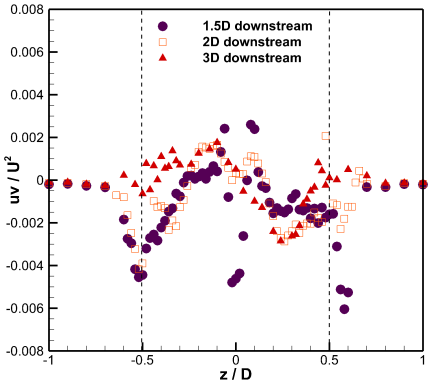

(c) Probe B - side

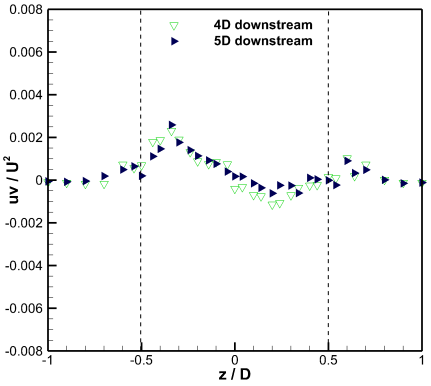

(d) Probe B - side

Figure D.25: Reynolds shear stresses in the $x-y$ plane downstream of the three-bladed turbine in non-uniform flow ($TI \approx 5\%$)

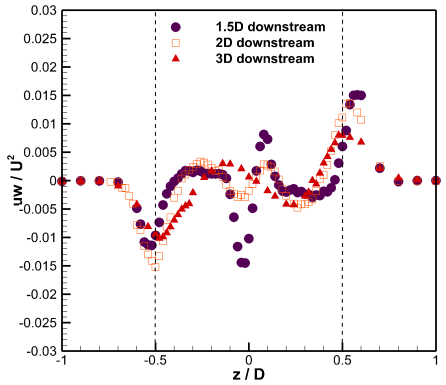

(a) Probe A - down

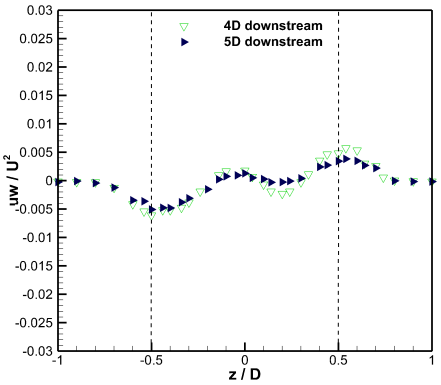

(b) Probe A - down

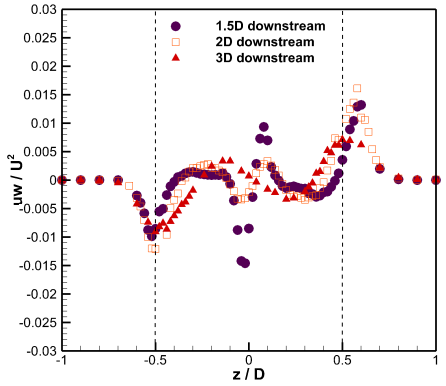

(c) Probe B - side

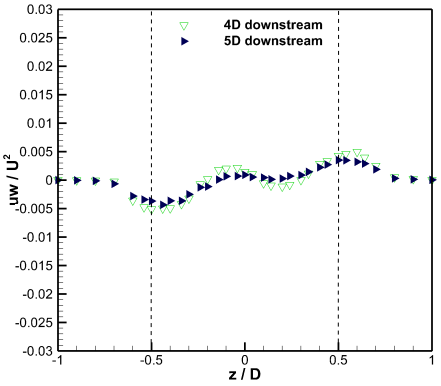

(d) Probe B - side

Figure D.26: Reynolds shear stresses in the $x - z$ plane downstream of the three-bladed turbine in non-uniform flow ($TI \approx 5\%$)

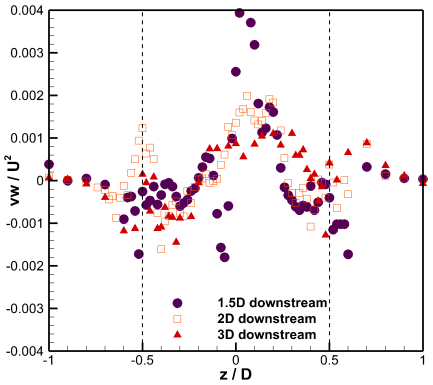

(a) Probe A - down

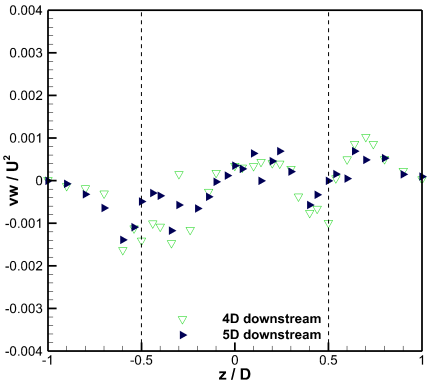

(b) Probe A - down

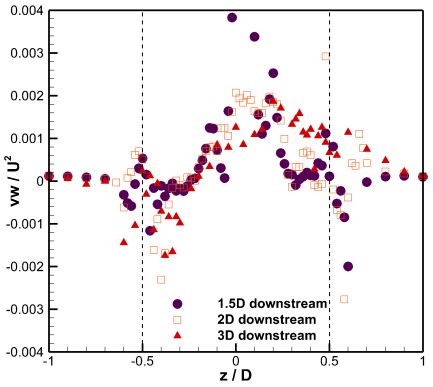

(c) Probe B - side

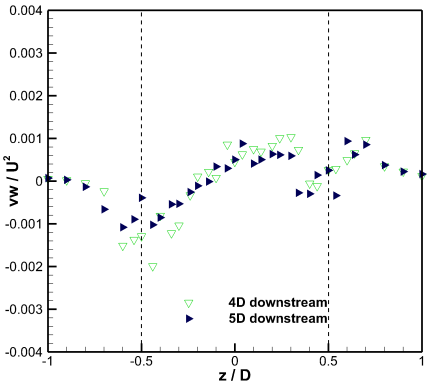

(d) Probe B - side

Figure D.27: Reynolds shear stresses in the $y - z$ plane downstream of the three-bladed turbine in non-uniform flow ($TI \approx 5\%$)

Appendix E

Publications

The work from this thesis has lead to a number of journal and conference publications which are henceforth attached.

Journal publications:

Mason-Jones, A., O'Doherty, D.M., Morris, C.E., O'Doherty, T., Byrne, C.B., Prickett, P.W., Grosvenor, R.I., Owen, I., **Tedds, S.C.**, Poole, R.J. 2012. *Non-dimensional scaling of tidal stream turbines.* Energy 44 (1). 820-829.

Tedds, S.C., Owen, I., Poole, R.J., 2014. *Near-wake characteristics of a model Horizontal Axis Tidal Stream Turbine.* Renewable Energy 63. 222-235.

Tedds, S.C., de Jesus Henriques, T.A., Whalley, R.D., Owen, I., Poole, R.J., 2014. *A cautionary note when using Acoustic Doppler Velocimetry for turbulence measurements in marine energy applications.* (submitted to International Journal of Marine Energy)

Conference publications:

Tedds, S.C., Poole, R.J., Owen, I., Naja?an, G., Bode, S., Mason-Jones, A., Morris, C.E., ODoherty, T. and ODoherty D.M. *Experimental Investigation*

Of Horizontal Axis Tidal Stream Turbines, The Ninth European Wave and Tidal Energy Conference, September 2011, Southampton, UK.

Tedds, S.C., Poole, R.J., Owen, I. *Wake characteristics of Horizontal Axis Tidal Stream Turbines in uniform and non-uniform steady flows.* The International Conference on Ocean Energy, October 2012, Dublin, Ireland.

Tedds, S.C., de Jesus Henriques, T.A., Owen, I., Poole, R.J. *Near-wake characterisation of Horizontal Axis Tidal Stream Turbines in uniform and non-uniform steady flows.* The Tenth European Wave and Tidal Energy Conference, September 2013, Aalborg, Denmark.